

ÉCOLE DE TECHNOLOGIE SUPÉRIEURE  
UNIVERSITÉ DU QUÉBEC

MANUSCRIPT-BASED THESIS PRESENTED TO  
ÉCOLE DE TECHNOLOGIE SUPÉRIEURE  
AND  
NATIONAL UNIVERSITY OF SCIENCE AND TECHNOLOGY “MISIS”  
(CO-TUTORSHIP)

IN PARTIAL FULFILLMENT OF THE REQUIREMENTS FOR  
THE DEGREE OF DOCTOR OF PHILOSOPHY  
Ph. D.

CO-TUTORSHIP RUSSIA-QUÉBEC

BY  
Alena KREITCBERG

IMPROVEMENT OF THE FUNCTIONAL PROPERTIES OF NANOSTRUCTURED  
Ti-Ni SHAPE MEMORY ALLOYS BY MEANS OF  
THERMOMECHANICAL PROCESSING

MONTREAL, 4 DECEMBER 2014



ALENA KREITCBERG, 2014



This [Creative Commons](https://creativecommons.org/licenses/by-nc-nd/4.0/) licence allows readers to download this work and share it with others as long as the author is credited. The content of this work may not be modified in any way or used commercially.

**BOARD OF EXAMINERS (THESIS PH.D.)**  
**THIS THESIS HAS BEEN EVALUATED**  
**BY THE FOLLOWING BOARD OF EXAMINERS**

Mr. Vladimir Brailovski, Thesis Supervisor  
Département de génie mécanique at École de Technologie Supérieure

Mr. Sergey D. Prokoshkin, Thesis Co-supervisor  
Department of Plastic Deformation of Special Alloys at National University of Science and Technology “MISiS” (Moscow, Russia)

Mr. Omar Chaallal, Chair, Board of Examiners  
Département de génie de la construction at École de technologie supérieure

Mr. Victor Songmené, Member of the jury  
Département de génie mécanique at École de technologie supérieure

Mr. Mohammad Jahazi, Member of the jury  
Département de génie mécanique at École de technologie supérieure

Mr. Sylvain Turenne, External Evaluator  
Département de génie mécanique at École Polytechnique de Montréal

**THIS THESIS WAS PRESENTED AND DEFENDED**  
**IN THE PRESENCE OF A BOARD OF EXAMINERS AND THE PUBLIC**

**27 NOVEMBER 2014**

**AT ÉCOLE DE TECHNOLOGIE SUPÉRIEURE**



## **ACKNOWLEDGMENTS**

First and foremost, I would like to express my sincere gratitude to my research supervisors, Vladimir Brailovski and Sergey Prokoshkin, for their assistance, guidance, continuous support, understanding, attention to detail and involvement in every step throughout the process. Over these past years, I have enjoyed working with you.

I would also like to show my gratitude to Drs. Karine Inaekyan, Elena Ryklina, Irina Khmelevskay and Andrey Korotitskiy for their helpful discussions during the various stages of this study.

To the entire team at École de technologie supérieure: Charles Simoneau, Yann Facchinello, Jonathan Rivard, Simon Lacasse, Pierre-Luc Vachon, Jean-René Poulin and Victor Urlea, thank you for the friendship, as well as personal and professional support during this time. It was a pleasure working together.

I am grateful to my colleagues at the National University of Science and Technology “MISIS”: Kristina Vachiyana, Vadim Sheremetiev, Yulia Zhukova, Sergey Dubinskiy and Victor Komorov, who were always open for discussions and made my time in the Ph.D. program more fun and interesting.

Most importantly, none of this could have happened without my family. My sincere thanks to my parents for their understanding, endless love and for supporting me spiritually throughout my life.

And finally, a big thanks to my love, Charles, who was worried about me during all this time. Your love, support and good humor made that period of my life more enjoyable.



# **AMÉLIORATION DES PROPRIÉTÉS FONCTIONNELLES DES ALLIAGES À MÉMOIRE DE FORME Ti-Ni NANOSTRUCTURÉS À L'AIDE DE TRAITEMENTS THERMOMÉCANIQUES**

Alena KREITCBERG

## **RÉSUMÉ**

Les méthodes de déformation plastique sévère sont fréquemment employées pour la mise en forme d'alliages à mémoire de forme (AMF) Ti-Ni nanostructurés. Toutefois, ce type de traitement thermomécanique augmente les risques d'endommagement du matériau et a donc pour effet de détériorer leur résistance en fatigue. Conséquemment, l'objectif principal de ce projet est d'étudier l'influence des conditions des traitements thermomécaniques (TMT) sur la microstructure, les propriétés fonctionnelles et l'endommagement des AMF Ti-Ni durant ces traitements. En d'autres mots, il est attendu que l'optimisation des conditions des TMT de ces alliages peut améliorer leurs propriétés en fatigue.

Les premiers travaux de cette thèse ont porté sur l'étude de la microstructure et des propriétés en fatigue des AMF Ti-Ni assujettis aux différentes combinaisons de TMT : laminage à froid sévère (CR), laminage à tiède (WR), recuit intermédiaire (IA) et recuit post-déformation (PDA). Les résultats obtenus ont permis de démontrer que tout comme la diminution de l'intensité du CR, l'introduction du WR et du IA au sein des différents TMT a pour effet d'augmenter la durée de vie en fatigue de l'alliage, conséquence d'un endommagement moins important. Une accentuation de la densité d'une texture favorable à la réalisation de l'effet de mémoire de forme (austénite-B2) a également été notée. Néanmoins, les modifications apportées aux TMT (température plus élevée et moins grande intensité de laminage) ont eu pour effet de grossir la microstructure, ayant comme conséquence directe d'affecter négativement la stabilité des propriétés fonctionnelles durant le cyclage thermomécanique. De plus, au terme de ces travaux, il n'était pas possible de séparer l'influence des différentes caractéristiques liées aux TMT sur les propriétés fonctionnelles des alliages Ti-Ni : la taille des grains et sous-grains, la texture et le niveau des défauts induits par le TMT.

Dans le but d'isoler la contribution de la taille des grains et sous-grains de la contribution liée à la texture sur les propriétés fonctionnelles des AMF Ti-Ni, la limite théorique cristallographique de déformation récupérable obtenue après différents TMT (menant aux différentes textures) a été calculée et comparée avec les résultats expérimentaux. Cette analyse comparative a permis de démontrer que les facteurs structuraux (la taille des grains et sous-grains) ont prévalence sur la texture. Par conséquent, afin de maximiser les propriétés fonctionnelles des Ti-Ni, il est nécessaire d'avoir une structure exclusivement nanocristalline et donc d'employer les techniques de déformation plastique sévère (SPD) à froid. Enfin, étant donné que la déformation plastique sévère à froid augmente le risque d'apparition des défauts lors de la mise en forme, il a été jugé nécessaire de comparer la tolérance aux dommages des alliages Ti-Ni avec une taille de grain/sous-grains différente, allant de quelques dizaines jusqu'à quelques centaines de nanomètres.

À cet effet, une analyse détaillée de l'interaction entre la durée de vie en fatigue des alliages Ti-Ni et leur niveau d'endommagement lors du laminage à froid sévère et/ou à tiède (caractérisé par la taille et la densité des microfissures en bordure des échantillons) a été réalisée. Cette étude a démontré que l'alliage avec une taille nanométrique de grains (structure nanocristalline) offre une meilleure tolérance à la propagation des petites fissures comparativement à son équivalent avec une taille nanométrique de sous-grains, ce qui devrait lui offrir une meilleure performance en fatigue. Aussi, afin de pouvoir obtenir les structures nanocristallines tout en diminuant la quantité de défauts de fabrication, il a été jugé essentiel d'étudier la déformabilité de ces alliages à différentes températures.

Afin d'approfondir les connaissances de la déformabilité des AMF Ti-Ni, une étude de sensibilité du taux de déformation a été conduite. Différentes microstructures possédant des grains allant de grossiers à ultrafins ont préalablement été créées à l'aide de la technologie d'extrusion dans les canaux déviés (ECAP). Ces dernières ont ensuite été assujetties à une analyse de sensibilité du taux de déformation. Ces travaux ont prouvé que peu importe la température de déformation, une microstructure à grains ultrafins comparée à une autre à grains grossiers démontre une meilleure déformabilité. Par ailleurs, il a été aussi établi que plus petite est la taille des grains, plus basse est la température et plus élevé est le taux de déformation qui mènent à la superplasticité. En se basant sur ces résultats, une séquence technologique incluant l'ECAP à température élevée, permettant d'affiner la microstructure et donc d'améliorer la déformabilité de l'alliage, suivi par laminage à froid sévère, permettant d'obtenir une structure nanocristalline, a été proposée et validée.

### **Contributions scientifiques**

Ce projet a contribué à l'avancement des connaissances dans le domaine des alliages à mémoire de forme (AMF) Ti-Ni principalement au niveau de l'interaction entre les traitements thermomécaniques, la structure et les propriétés fonctionnelles de ces alliages. Les conclusions principales de ce projet doctoral peuvent être résumées comme suit :

- L'amplitude et la stabilité des propriétés fonctionnelles d'alliages Ti-Ni avec une taille nanométrique de grains (nanocristallins) sont supérieures à celles d'alliages avec une taille nanométrique de sous-grains. Le principal facteur affectant la durée de vie en fatigue d'alliages nanocristallins est leur endommagement lors de la mise en forme.
- Lorsque comparée à la texture, la structure d'alliages Ti-Ni joue un rôle plus significatif dans la réalisation de leur potentiel de fonctionnement.
- En termes de résistance en fatigue, la structure nanocristalline est moins sensible à la propagation des petites fissures par rapport à celle avec sous-grains de taille nanométrique.



- Le raffinement de la taille de grains permet d'améliorer la déformabilité des AMF Ti-Ni et ce, peu importe la température de déformation.
- Dans le but de minimiser le risque d'apparition des défauts lors de la mise en forme des AMF Ti-Ni nanostructurés, une nouvelle séquence de traitement thermomécanique à trois étapes est proposée (ECAP+CR+PDA): 1) raffinement des grains par déformation plastique sévère à haute température (ECAP), 2) création d'une structure amorphe par déformation plastique sévère à basse température (CR) et 3) obtention d'une structure nanocristalline par recuit post-déformation (PDA).

**Mots-clés :** alliage à mémoire de forme, laminage, extrusion dans les canaux déviés, structure nanocristalline, superplasticité.



# **IMPROVEMENT OF THE FUNCTIONAL PROPERTIES OF NANOSTRUCTURED Ti-Ni SHAPE MEMORY ALLOYS BY MEANS OF THERMOMECHANICAL PROCESSING**

Alena KREITCBERG

## **ABSTRACT**

Severe plastic deformation (SPD) is commonly used for nanostructure formation in Ti-Ni shape memory alloys (SMAs), but it increases the risk of damage during processing and, consequently, negatively affects functional fatigue resistance of these materials. The principal objective of this project is, therefore, to study the interrelations between the processing conditions, damageability during processing, microstructure and the functional properties of Ti-Ni SMAs with the aim of improving long-term functional performances of these materials by optimizing their processing conditions.

First, microstructure and fatigue properties of Ti-Ni SMAs were studied after thermomechanical treatment (TMT) with different combinations of severe cold and warm rolling (CR and WR), as well as intermediate and post-deformation annealing (IA and PDA) technological steps. It was shown that either when WR and IA were introduced into the TMT schedule, or CR intensity was decreased, the fatigue life was improved as a consequence of less processing-induced damage and higher density of the favorable B2-austenite texture. This improvement was reached, however, at a price of a lower multi-cycle functional stability of these materials, the latter being a direct consequence of the microstructure coarsening after higher-temperature lower-intensity processing. At the end of this study, however, it was not possible to distinguish between contributions to the functional performances of Ti-Ni SMAs from different processing-related features: a) grain/subgrain size; b) texture; and c) level of rolling-induced defects.

To be capable of separating contributions to the functional properties of Ti-Ni alloys from grain/subgrain size and from texture, the theoretical crystallographic resource of recovery strain after different TMTs and, therefore, different textures, were calculated and compared with the experiment. The comparative analysis showed that the structural factors (grain/subgrain size) strongly dominate the texture contributions, and therefore, there is no real alternative to having nanocrystalline Ti-Ni alloys, if one needs to maximize the Ti-Ni alloys functional properties. Since the creation of such a microstructure requires the use of severe cold deformation techniques and neither of these techniques can be completely exempt from defects, it was deemed necessary to compare the damage tolerance of nanocrystalline Ti-Ni alloys to that of their nanosubgrained and mixed nanocrystalline/nanosubgrained counterparts.

With this objective in mind, a detailed analysis of interrelations between the level of the CR/WR-induced damage (edge microcrack size and concentration) and the fatigue life of Ti-Ni SMAs was carried out. It was shown that nanocrystalline structure provides higher tolerance to small-crack propagation than nanosubgrained or mixed nanocrystalline/

nanosubgrained structures, and that low-temperature deformability of these alloys has to be improved to benefit from the property-enhancement potential of nanocrystalline structure.

To broaden our knowledge in the field of Ti-Ni alloy deformability, the strain-rate sensitivity of these alloys was studied. Different microstructures, varying from the coarse- to ultrafine-grained, were created by means of equal-channel angular pressing (ECAP) and subjected to strain-rate sensitivity testing. As a result, the material with ultrafine-grained microstructure demonstrated an improved deformability as compared to the coarse-grained structure, at any deformation temperature. Moreover, it was determined that the smaller the grain size, the lower the temperature and the higher the strain-rate at which superplasticity occurs. Based on the results obtained, combined thermomechanical processing (ECAP at elevated temperatures followed by CR) was proposed and validated in terms of structural refinement with reduced level of processing-induced defects.

### **Scientific contributions**

This thesis contributes to the advancement of knowledge in the field of Ti-Ni SMAs' processing-structure-properties interactions, and the main conclusions of this study can be summed-up as follows:

- Nanocrystalline Ti-Ni alloys significantly outperform nanosubgrain Ti-Ni alloys in terms of the absolute values and stability of their single- and multiple-cycle functional properties (superelasticity and shape memory characteristics). The main factor limiting the number of cycles to failure of the nanocrystalline alloys is the processing-related damage.
- The structure of Ti-Ni alloys plays significantly higher role in the realization of their functional potential than does their texture.
- In terms of fatigue life, the nanocrystalline structure has lower small-crack sensitivity than does the nanosubgrained structure.
- Grain refinement makes it possible to improve deformability of Ti-Ni alloys at any temperature.
- To produce nanocrystalline Ti-Ni SMAs free of processing-induced-defects, a novel three-step processing is proposed (ECAP+CR+PDA): grain-refining severe plastic deformation at elevated temperatures (ECAP), followed-up by amorphizing SPD at low temperatures (CR), and ended-up by nanocrystallizing post-deformation heat treatment (PDA).

**Keywords:** shape memory alloys, rolling, equal-channel angular pressing, nanocrystalline structure, superplasticity.

## TABLE OF CONTENTS

	Page
INTRODUCTION .....	1
CHAPTER 1 LITERATURE REVIEW .....	5
1.1 TMT of Ti-Ni SMA by rolling.....	6
1.1.1 Cold rolling.....	6
1.1.2 Warm rolling.....	8
1.1.3 Structural analysis of Ti-Ni alloy.....	8
1.1.4 Thermomechanical characterization of nanostructured Ti-Ni alloy .....	10
1.1.5 Effect of TMT by rolling on the texture and properties of Ti-Ni SMAs ..	12
1.2 TMT of Ti-Ni SMA by ECAP .....	18
1.2.1 Formation of the ultrafine-grained structure.....	21
1.2.2 Formation of nanostructures .....	23
1.3 Functional properties of Ti-Ni alloys after ECAP and CR processes.....	24
1.4 Research objectives.....	25
1.5 Methodology.....	27
1.5.1 Materials and thermomechanical treatments .....	27
1.5.2 Mechanical and microstructural characterization .....	31
CHAPTER 2 ARTICLE #1: MICROSTRUCTURE AND FUNCTIONAL FATIGUE OF NANOSTRUCTURED Ti-50.26 at.%Ni ALLOY AFTER THERMOMECHANICAL TREATMENT WITH WARM ROLLING AND INTERMEDIATE ANNEALING .....	35
2.1 Summary .....	35
2.2 Abstract.....	36
2.3 Introduction.....	36
2.4 Methodology.....	38
2.5 Experimental results.....	43
2.6 Discussion .....	56
2.7 Conclusions.....	59
2.8 Acknowledgments.....	60
2.9 References.....	60
CHAPTER 3 ARTICLE #2 ROLE OF THE STRUCTURE AND TEXTURE IN THE REALIZATION OF THE RECOVERY STRAIN RESOURCE OF THE NANOSTRUCTURED Ti-50.26 at.%Ni ALLOY .....	65
3.1 Summary .....	65
3.2 Abstract.....	66
3.3 Introduction.....	66
3.4 Experimental .....	70
3.5 Results.....	79
3.6 Discussion.....	102

3.7	Conclusions.....	104
3.8	Acknowledgments.....	108
3.9	References.....	108
CHAPTER 4	ARTICLE #3 INFLUENCE OF THERMOMECHANICAL TREATMENT ON STRUCTURE AND CRACK PROPAGATION IN NANOSTRUCTURED Ti-50.26 at.%Ni ALLOY .....	113
4.1	Summary.....	113
4.2	Abstract.....	114
4.3	Introduction.....	114
4.4	Experimental.....	116
4.5	Experimental results.....	122
4.6	Discussion.....	130
4.7	Conclusions.....	134
4.8	Acknowledgments.....	135
4.9	References.....	136
CHAPTER 5	ARTICLE #4 EFFECT OF THE GRAIN/SUBGRAIN SIZE ON THE STRAIN-RATE SENSITIVITY AND DEFORMABILITY OF Ti-50 at.%Ni ALLOY .....	141
5.1	Summary.....	141
5.2	Abstract.....	142
5.3	Introduction.....	143
5.4	Experimental methodology .....	145
5.5	Results.....	148
5.6	Discussion.....	161
5.7	Conclusions.....	163
5.8	Acknowledgments.....	163
5.9	References.....	164
CONCLUSION.....		169
RECOMENDATIONS .....		171
APPENDIX I	EFFECT OF INITIAL RECOVERY STRESS ON THE FATIGUE LIFE OF Ti-50.26 at.%Ni ALLOY .....	173
LIST OF REFERENCES .....		181

## LIST OF TABLES

	Page
Table 1.1	ECAP conditions and the proposed deformation mechanisms that occurred during processing of Ti-49.8 at.%Ni alloy [4] .....21
Table 1.2	Structure and functional properties of Ti-Ni alloys after various treatment [4, 43, 46].....25
Table 1.3	Samples designation and corresponding TMT routes.....27
Table 1.4	Specimens designation and corresponding processing routes .....31
Table 2.1	Samples designation and corresponding TMT routes.....40
Table 2.2	Crack parameters after different TMT routes .....50
Table 2.3	Results of the stress-free recovery testing: recovery strain in 1 <sup>st</sup> cycle ( $\Delta\epsilon_r$ ), recovery strain degradation rate for the first 500 cycles ( $\Delta\epsilon_r^{500}$ ) and number of cycles to failure ( $N_f$ ).....51
Table 2.4	Results of the constrained recovery testing: recovery stress generated in 1 <sup>st</sup> cycle ( $\Delta\sigma_r$ ) recovery stress degradation rate for the first 500 cycles ( $\Delta\sigma_r^{500}$ ), and the number of cycles to failure ( $N_f$ ) .....52
Table 2.5	Results of superelastic testing: transformation yield stress in 1 <sup>st</sup> cycle ( $\Delta\sigma_{tr}^I$ ); transformation stress evolution rate and irrecoverable strain accumulated during the first 1000 cycles ( $\Delta\sigma_{tr}^{1000}$ and $\epsilon_{1000}$ ), and number of cycles to failure ( $N_f$ ) .....53
Table 3.1	Designations and schemes of treatments .....71
Table 3.2	Martensite lattice parameters and the maximum lattice strain upon the martensitic transformation of the Ti-50.26 at.%Ni alloy (measurements at room temperature).....86
Table 3.3	Relative pole density <100>, (110) and <111> and the corresponding crystallographic resource of the recovery strain of the Ti-50.26 at.%Ni alloy after different regimes (calculated according to [20]) .....91
Table 3.4	Resource of the recovery strain of the polycrystalline Ti-50.26 at.%Ni alloy calculated by different methods.....92

Table 3.5	Characteristics of the recovery strain of the Ti-50.26 at.%Ni SMA depending on the regimes of TMT and total induced strain $\varepsilon_t$ (%).....	96
Table 3.6	Parameters of the loading-unloading diagram of the Ti-50.26 at.%Ni SMA after TMT according to different regimes.....	101
Table 5.1	Specimen designation and corresponding processing routes.....	145
Table 5.2	Strain-rate sensitivity exponent $m$ measured by the strain-rate-jump compression test.....	155
Table 5.3	Yield stresses of B2-austenite at 400 and 500°C (0.2% offset).....	157
Table 5.4	Strain-rate sensitivity exponent $m$ measured by stress-jump creep compression test.....	159



## LIST OF FIGURES

	Page
Figure 1.1	Grain size of Ti-Ni SMA as a function of the strain rate and temperature (adapted from [5]) ..... 7
Figure 1.2	TEM images of Ti-50.26 at.%Ni alloy after different TMT routes: a) route CR( $e=1.2$ ), b) route CR( $e=0.3$ )+WR( $e=0.9$ ); c) CR( $e=1$ )+IA+CR( $e=0.2$ ); and d) WR( $e=1$ )+IA+WR( $e=0.2$ ). From left to right: bright-field image, dark-field image, microdiffraction pattern [9] ..... 9
Figure 1.3	Stress-strain plots: a) stress-free recovery testing and b) constrained recovery testing; both for N=1 (Ti-50.26 at.%Ni alloy after CR( $e=1.2$ )+PDA 400°C, 1h) [3] ..... 11
Figure 1.4	Influence of the TMT on the texture components and recoverable strains (adapted from [19]) ..... 18
Figure 1.5	Schematic representation of the ECAP processing: (a) 90°-angle ECAP; (b) schematic representation of the angle determination [26, 27] ..... 19
Figure 1.6	(a) Cross-section of billet [45] and (b) TEM image of Ti-49.8 at.%Ni alloy after ECAP at room temperature and PDA at 400°C [4] ..... 23
Figure 1.7	Typical tensile stress-strain plot to failure ..... 24
Figure 1.8	Four-high FENN laboratory rolling mill ..... 28
Figure 1.9	Schematic view of the: a) rolling mill and pulling tension system; b) electric heating system [9] ..... 29
Figure 1.10	Representation of the infrared sensor-wire alignment device [8] ..... 30
Figure 2.1	Stress-strain plots (Ti-50.26 at.%Ni alloy after $e=1.2$ CR+PDA 400°C, 1h): (a) stress-free recovery testing and (b) constrained recovery testing; both for N=1 cycle; and (c) superelastic testing ..... 42
Figure 2.2	Structure of Ti-50.26%Ni alloy after selected TMT routes: a) CR(1.2); b,c) CR(0.75); d) WR(1)+IA+WR(0.2); and e,f) CR(1)+IA+WR(0.2). Left to right: bright-field image, dark-field image, electron diffraction pattern ..... 46
Figure 2.3	ODF section at $\phi_2=0$ and 90° for six processing routes ..... 47

Figure 2.4	Inverse pole figures corresponding to the normal direction (ND) and rolling direction (RD) for all the processing routes. x – [uvw] pole, o – [011]B2 pole .....48	48
Figure 2.5	Orientation density of {100}<110>B2 texture component as a result of different TMT routes applied to Ti-50.26at.%Ni alloy .....49	49
Figure 2.6	Loading-unloading diagrams during superelastic testing after different TMT routes.....54	54
Figure 2.7	Evolution of transformation yield stress and accumulated strain (for the longest test for each TMT route) during superelastic testing.....55	55
Figure 2.8	(a) Processing-induced damage (crack size, plain bars, and concentration, hatched bars) after different processing routes, and fatigue functional properties obtained by (b) stress-free recovery, (c) constraint recovery stress generation, and (d) superelastic testing (number of cycles to failure, plain bars and stability, hatched bars) .....58	58
Figure 3.1	Crystallographic relationships corresponding to the changes in the systems of translations upon the transformation of the tetragonal cell of the B2-austenite into an orthorhombic cell with a monoclinic distortion of the B19'-martensite .....73	73
Figure 3.2	Scheme of the determination of the maximum deformation of the martensite transformation in polycrystalline austenite. Subscripts 1 and 2 correspond to two different grains of the polycrystal and to two (of equivalent length) sequential segments in the direction $\langle uvw \rangle \varepsilon_{max}$ of a single crystal.....75	75
Figure 3.3	Inverse pole figure of the B2-austenite of the Ti-50.26 at.%Ni alloy after thermomechanical treatment according to the regime WR(1)+IA+WR(0.2) (see Table 3.1).....76	76
Figure 3.4	(a) Scheme of the determination of the parameters of the loading-unloading diagram of a sample of the Ti-50.26 at.%Ni alloy and (b) of the maximum recovery strain $\varepsilon_r^{\max}$ and the maximum completely recoverable strain $\varepsilon_{r,1}^{\max}$ .....78	78
Figure 3.5	Structures of Ti-50.26 at.%Ni alloy after TMT under different conditions: (a, b) CR(0.75); (c) CR(1.2); (d) CR(1)+IA+CR(0.2); (e, f) CR(1)+IA+WR(0.2); (g) WR(1)+IA+WR(0.2). Left-hand panel: bright-field images; right-hand panel: dark-field images with the diffraction patterns in the insets .....82	82

Figure 3.6	Widths of the XRD lined $\{110\}$ and $\{211\}$ of the austenite of the Ti-50.26 at.%Ni alloy as function of the regime of TMT.....	85
Figure 3.7	$\varphi_2 = 0^\circ$ and $\varphi_2 = 90^\circ$ sections of the ODF for different regimes of thermomechanical treatments .....	87
Figure 3.8	Inverse pole figures corresponding to the direction of the normal to the rolling plane (ND) and to the rolling direction (RD) for different regimes of TMT. O - the position of the pole $[011]B_2$ ; x - the position of the maximum of the ODF .....	88
Figure 3.9	Orientation density of the textural component $\{100\}<110>_{B_2}$ and the calculated (by different methods) resources of the recovery strain of the Ti-50.26 at % Ni alloy after TMT under different conditions .....	89
Figure 3.10	Characteristic loading-unloading diagrams of the Ti-50.26 at.%Ni alloy after different regimes of TMT .....	94
Figure 3.11	Variations in the induced ( $\varepsilon_i$ ), recovery ( $\varepsilon_r$ ) and residual ( $\varepsilon_f$ ) strains of the Ti-50.26 at.%Ni SMA with an increase in the total induced strain ( $\varepsilon_t$ ) after TMTs. The regimes of the TMT are indicated in the appropriate figures .....	97
Figure 3.12	Comparison of the experimental values of the recovery strain (Table 3.5), its theoretical resource (calculated by different methods, Table 3.4), and recovery stress (borrowed from [24]) after TMT under different conditions .....	99
Figure 4.1	Schematic representation of the three processing routes .....	118
Figure 4.2	Example of sample width reduction .....	119
Figure 4.3	Example of crack measurement after CR(1.2)+PDA .....	120
Figure 4.4	Stress-strain plots for the $N=1$ and $N^{\text{th}}$ cycles of Ti-50.26%Ni samples: a) superelastic testing after CR(1.2)+PDA (400°C, 1h), and b) stress generation-relaxation testing after CR(1.0)+IA+WR(0.2)+PDA (400°C, 1h).....	121
Figure 4.5	Structure of Ti-50.26%Ni alloy after selected TMT routes: a, b) CR(0.75); c) CR(1.2); and d, e) CR(1)+IA+WR(0.2). Left to right: bright-field image, dark-field image, electron diffraction pattern .....	124
Figure 4.6	Texture of Ti-50.26 at.%Ni after CR(1.2), CR(0.75), and CR(1)+IA+WR(0.2): inverse pole figures corresponding to the	

	normal direction (ND) and rolling direction (RD): x - [uvw] pole, o - [011]B2 pole .....	125
Figure 4.7	Variation of crack length and concentration after mechanical polishing of Ti-50.26 at.%Ni samples processed by different TMTs: CR(0.75), CR(1.2) and CR(1)+IA+WR(0.2) .....	126
Figure 4.8	Distribution of crack length of Ti-50.26 at.%Ni alloy after CR(0.75), CR(1.2) and CR(1)+IA+WR(0.2): a) as-processed; b) after polishing to a 1.0 mm width .....	127
Figure 4.9	Fatigue life of Ti-50.26 at.%Ni samples as a function of the sample width (mechanical polishing): (a) superelastic testing; b) constrained recovery testing .....	128
Figure 4.10	Evolution of crack length of the Ti-50.26 at.%Ni 1mm-width CR(0.75), CR(1.2) and CR(1)+IA+WR(0.2) - processed samples: a) before superelastic cycling; b) after 500 cycles of superelastic cycling .....	130
Figure 4.11	Schematic representation of a mixed nanocrystalline (NC) + nanosubgrained (NS) structure .....	131
Figure 4.12	Number of superelastic cycles to failure as a function of the average crack length (to facilitate the observation, this figure is obtained from Figure 4.9a using only the average values of crack length and the numbers of cycles to failure) .....	133
Figure 5.1	Plane-strain compression testing specimen at various preparation stages: a) ECAP-processed billet; (b) specimen before testing and (c) specimen after testing .....	146
Figure 5.2	Alloy structure after TMT: a) RQ (optical microscopy); b) ECAP-400, c) ECAP-500 and d) ECAP-400 after creep test at 400°C (electron microscopy). In b, c and d: bright-field images are on the left, dark-field images on the right; SAED patterns are inserted into the dark-field images .....	150
Figure 5.3	DSC plots after reference quenching and different TMT routes .....	151
Figure 5.4	X-ray diffractions at RT (a) and 150°C (b) after RQ, ECAP-400 and ECAP-500 .....	153
Figure 5.5	Strain-rate-jump tensile diagrams at 20, 150, 250 and 400°C in the $[10^{-3} - 10^{-4}] \text{ s}^{-1}$ strain rate range: RQ (a) – (d) and ECAP-400 (e) – (h) .....	154

Figure 5.6	Strain-rate-jump compression diagrams: RQ (a, d); ECAP-500 (b, e); ECAP-400 (c).....	155
Figure 5.7	Stress-jump creep test diagrams: RQ (a, d), ECAP-500 (b, e), and ECAP-400 (c).....	157
Figure 5.8	The $\log(\sigma)$ vs $\log(\epsilon)$ plots after RQ (a, d), ECAP-500 (b, e), and ECAP-400 (c).....	158
Figure 5.9	Microcracking after additional cold rolling. (a) Average length and concentration of microcracks for RQ and ECAP-400-processed specimens subjected to final CR( $\epsilon=2$ ); microcrack views: (b) after RQ+CR( $\epsilon=2$ ) and (c) after ECAP+CR( $\epsilon=2$ ).....	160
Figure 5.10	Strain-rate sensitivity exponent $m$ as a function of strain rate and testing temperature after RQ, ECAP-400 and ECAP-500 .....	161



## LIST OF ABBREVIATIONS

SMA	Shape Memory Alloy
at. %	Atomic percent
B2	CsCl lattice
B19'	Monoclinic lattice
R	Rhombohedral lattice
A	Austenite
M	Martensite
bcc	Body-centered cubic lattice
$M_s$	Start temperature of the direct martensitic transformation
$M_f$	Finish temperature of the direct martensitic transformation
$A_s$	Start temperature of the reverse martensitic transformation
$A_f$	Finish temperature of reverse martensitic transformation
$T_m$	Melting temperature
SE	Superelastic effect
SME	Shape memory effect
TWSM	Two-way shape memory effect
ND	Normal to the rolling plane
RD	Rolling direction
TD	Transverse direction
PF	Pole figure
IPF	Inverse pole figure
ODF	Orientation Distribution Function

SST	Standart stereographic triangle
TMT	Thermomechanical treatment
PDA	Post-deformation annealing
IA	Intermediate annealing
RT	Room temperature
SPD	Severe plastic deformation
CR	Cold rolling
WR	Warm rolling
HR	Hot rolling
CGS(CG)	Coarse-grained structure
UFG	Ultrafine-grained structure
NSS(NS)	Nanosybgained structure
NCS(NC)	Nanocrystalline structure
DSC	Diffraction Scanning Calorimetry
SEM	Scanning Electron Microscope
TEM	Transmission electron microscopy
BF	Bright field image
DF	Dark field image
ECAP	Equal channel angular pressing
HTP	High pressure torsion



## LIST OF SYMBOLS

$e (\varepsilon)$	True strain
$\sigma_y$	Yield stress
$\sigma_{cr}$	Critical stress for martensite reorientation
$\sigma_{tr}$	Transformation yield stress
$\sigma_r (\sigma_r^{max})$	Recovery stress (maximum recovery stress)
$\Delta\sigma_r^{500}$	Degradation rate of recovery stress during first 500 cycles
$\Delta\sigma_{tr}^{1000}$	Degradation rate of transformation yield stress during first 1000 cycles
$\varepsilon_t, \%$	Total induced strain
$\varepsilon_i, \%$	Induced strain
$\varepsilon_r (\varepsilon_r^{max})$	Recovery strain (maximum recovery strain)
$\Delta\varepsilon_r^{500}$	Degradation rate of recovery strain during first 500 cycles
$\varepsilon_{r,1}^{max}$	Maximum completely recoverable strain
$\varepsilon_r^{SME}$	Recovery strain of shape memory effect
$\varepsilon_r^{SE}$	Recovery strain of superelastic effect
$\varepsilon_{TW}$	Strain of two-way shape memory effect
$\varepsilon_f (\varepsilon_p)$	Residual (permanent) strain
$\varepsilon_d (\varepsilon_{1000})$	Accumulated residual strain to failure (during first 1000 cycles)
$\varepsilon_{poly}^{max}$	Maximum macroscopic deformation of isotropic polycrystal (resource of recovery strain for polycrystal)
$\varepsilon_{mono}^{max}$	Crystallographic resource of recovery strain in single-crystal
$\varepsilon_i^{\langle uvw \rangle}$	Lattice strain along $\langle uvw \rangle$ crystallographic direction

$\rho$	Lattice defect concentration
$N_f$	Number of cycles to failure (fatigue life)
$N_c$	Crack concentration
$B_{hkl}$	X-ray peak mid-high width
$\Delta K_{th}$	Fatigue threshold
$d_w$	Average size of weighted structural element
$R$	Relative density of orientation
$E_{unload}$	Elasticity modulus of unloading branch of deformation diagram
$m$	Strain-rate superplasticity exponent
$\dot{\epsilon}$	Strain rate

## INTRODUCTION

Ti-Ni shape memory alloys (SMAs) are used as heat-sensitive elements and thermomechanical actuators (shape memory property), and medical implants and tools (superelasticity effect). These applications require extended fatigue life and adequate stability of the SMAs' functional properties. It has been shown that obtaining nanocrystalline structures can significantly improve the functional properties of Ti-Ni SMAs [1].

One of the methods of obtaining such structures consists of severe cold rolling (CR) followed by post-deformation annealing (PDA). This technique finds its limits in terms of the alloys' fatigue life because of the processing-induced material damage [2]. It was hypothesized that the problem of forming nanocrystalline structures in Ti-Ni alloys, while decreasing damage during processing, can be solved by using warm plastic deformation and intermediate annealing technological steps [3].

It was hypothesized also that the introduction of warm rolling (WR) and intermediate annealing (IA) technological steps will create a specific texture in the material, which will improve further functional properties of the alloy. As a consequence, the possible control over the texture formation in Ti-Ni alloys and the detailed analysis of the texture–functional property interrelations were the first problems which were deemed necessary to address.

Second, an in-depth analysis of deformability of Ti-Ni SMAs can be the key to successful manufacturing of nanocrystalline structure formation with a limited number of processing-induced defects. It was hypothesized that preliminary structural refinement of Ti-Ni alloys can improve their deformability. Equal-channel angular pressing (ECAP) appeared to be the suitable technique for such a preliminary structural refinement since it does not modify the sample cross-section, which is an asset for subsequent processing.

From this point of view, the principal research objectives of this project were to study a) the interaction between the thermomechanical treatment (TMT), structure/texture and functional

properties of Ti-Ni SMAs; and b) to optimize the technological parameters of this thermomechanical treatment with the aim of obtaining the best combination of static and dynamic (fatigue) functional properties of Ti-Ni SMAs.

According to the principal research objectives, the work presented in this thesis is focused on the influence of TMT conditions on the microstructure, damageability, static and fatigue functional properties of Ti-Ni SMAs. First, it studies the particularities of structure and crystallographic texture formation in Ti-Ni alloys under conditions of severe CR and/or WR with the objective to obtain the best combination of their static and fatigue functional properties. It investigates next the influence of the microstructure resulting from this processing on the resistance of these alloys to small-crack propagation. Finally, comparing the strain-rate sensitivity and deformability of Ti-Ni SMAs with coarse- and ultrafine-grained microstructures at different temperatures and strain rates, the author proposes a new sequence of thermomechanical processing of these alloys capable of improving their deformability at low temperatures, and, therefore, their capacity to be nanostructured with the minimum risk of the processing-induced damage.

## **Thesis organization**

The main results of the research have been published in four journal articles and are presented in Chapters 2, 3, 4, 5. Then, the important points of this research and some recommendations are presented in the conclusion. Annex I includes the detailed analysis of the fatigue life dependence on the initial recovery stress under recovery stress generation-relaxation tests.

### **Part 1: The influence of TMT including CR/WR and intermediate, PDA on the structure, texture, functional fatigue properties and processing-induced defects.**

This part is presented in Chapter 2 of this thesis. It contains the first article entitled: *“Microstructure and functional fatigue of nanostructured Ti-50.26 at.%Ni alloy after*

*thermomechanical treatment with warm rolling and intermediate annealing*” by A. Kreitchberg, V. Brailovski, S.D. Prokoshkin, Y. Facchinello, K. Inaekyan and S.M. Dubinskiy, and published in the journal Materials Science and Engineering A, 2013, v. 562, pp. 118-127.

**Part 2: The contributions from structure and texture to the single-cycle recovery strain value of nanostructured Ti-Ni alloys.**

This part is presented in Chapter 3 of this thesis and contains the second article entitled: *“Role of the structure and texture in the realization of the recovery strain resource of the nanostructured Ti-50.26 at.%Ni alloy”* by A.Y. Kreitchberg, S.D. Prokoshkin, V. Brailovski, A.V. Korotitskiy, and published in the journal The Physics of Metals and Metallography, 2014, v.115, no.9, pp. 926-947.

**Part 3: An analysis of interrelations between the processing-induced microcracks, structure and fatigue life of nanostructured Ti-50.26 at.%Ni alloy.**

This part is presented in Chapter 4 of this thesis and contains the third article entitled: *“Influence of thermomechanical treatment on structure and crack propagation in nanostructured Ti-50.26 at.%Ni alloy”* by A. Kreitchberg, V. Brailovski, S. Prokoshkin, K. Inaekyan, and published in the journal Metallography, Microstructure, and Analysis, 2014, v. 3, no. 1, pp. 46-57.

**Part 4: The finding of the processing parameters such as deformation temperature, strain-rate and initial structure to improve manufacturability of Ti-Ni alloys.**

This part is presented in Chapter 4 of this thesis and contains the fourth article entitled: *“Effect of the grain/subgrain size on the strain-rate sensitivity and deformability of Ti-50 at.%Ni alloy”* by A. Kreitchberg, V. Brailovski, S.D. Prokoshkin, D. Gunderov, M.

Khomutov, K. Inaekyan, and published in the journal Materials Science and Engineering A, 2015, v. 622, pp. 21-29.

## **CHAPTER 1**

### **LITERATURE REVIEW**

Fundamental functional characteristics of SMAs are recoverable strain and recovery stress, both characteristics depending on the alloys' structure and texture.

Thermo and thermomechanical treatments (TMTs) of Ti-Ni alloys make it possible to form in these alloys nano- and ultrafine-grained structures thus to improve their functional properties. One of the TMT techniques is a combination of severe plastic deformation (SPD) and post-deformation annealing (PDA). The ideal SPD+PDA processing of Ti-Ni SMA should allow: (1) creating of uniformly distributed nano- and ultrafine-grained structures; (2) processing of large-size specimens; (3) minimizing the risk of material damage during processing.

There are a number of SPD techniques which allow the nano- and ultrafine-grained structures to be obtained, such as rolling, high pressure torsion (HPT), equal-channel angular extrusion or pressing (ECAP), multiple forging, etc. In this work, we will consider two of the most frequently used SPD methods for nanostructure formation: rolling and ECAP.

#### **Marforming and ausforming**

Depending on the Ti-Ni alloy transformation temperatures, it can be deformed in either martensitic (marforming) or austenitic (ausforming) states. The process of SPD has three main stages.

During stage I of marforming, elastic deformation of martensite occurs. During stage II, detwinning of martensite occurs, favoring growth of some variants at the expense of others. During stage III, plastic deformation of the reoriented martensite and martensite stabilization take place; the latter is caused by high dislocation density stored in the material. During stage

I of ausforming, elastic deformation of austenite occurs. During stage II, stress-induced martensitic transformation takes place. During stage III, plastic deformation of martensite occurs as in the case of marforming. When either ausforming or marforming of Ti-Ni SMAs are performed with sufficiently high strain levels, partial material amorphization takes place [4].

## **1.1 TMT of Ti-Ni SMA by rolling**

### **1.1.1 Cold rolling**

Deformation by rolling at room temperature followed by post-deformation annealing (CR + PDA) represent the simplest sequence of TMT applied to Ti-Ni SMAs to refine their microstructure and improve functional properties. Concurrent SPD technologies imply deformation at higher temperatures using more complex processing techniques: HPT and ECAP. Figure 1.1 illustrates the influence of the deformation intensity and temperature on the grain size of Ti-Ni SMAs after post-deformation annealing.



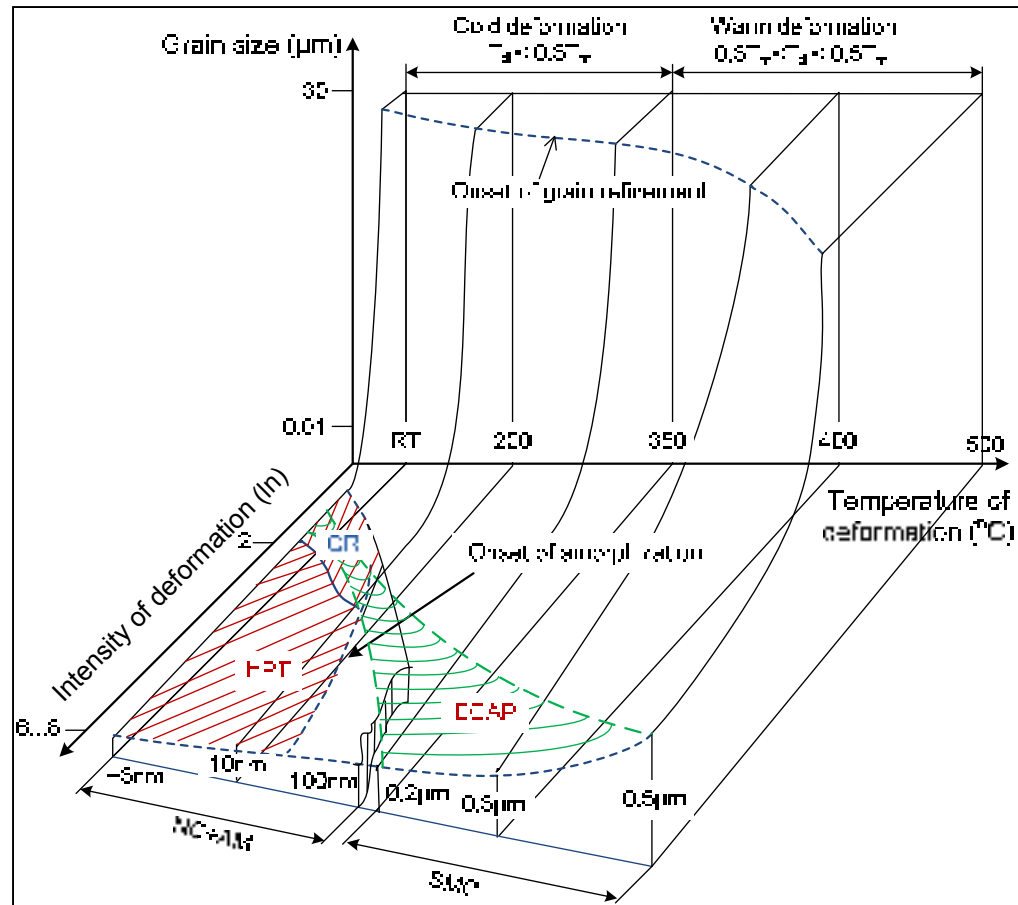


Figure 1.1 Grain size of Ti-Ni SMA as a function of the strain rate and temperature (adapted from [5])

After moderate CR (up to  $e=1.0$ ), the austenite structure after PDA is mainly a polygonized substructure with a small fraction of nanocrystalline structure. Severe cold plastic deformation leads to the strain-induced grain refinement and amorphization [6, 7], and the greater the deformation, the greater the quantity of the amorphized material (Figure 1.1). When CR ( $e>1.0$ ) is followed by PDA, the nanograins grow, the amorphized phase crystallizes, and the material consists of nanosize grains almost entirely exempt of dislocations.

The formation of the nanocrystalline structure in Ti-Ni alloys leads to higher transformation yield stresses (1500-1600 MPa), than in the case of the polygonized substructure (1100-1200 MPa). The difference between the yield and the transformation onset stresses in the case of

nanocrystalline structure is also higher [1]. These factors determine higher values of reactive stresses and recoverable strains. However, the negative side of this processing consists in a higher level of defects created in the material during severe CR, and, as a consequence, a decreased fatigue life of the processed material. Therefore, to increase the number of cycles to failure, authors [8, 9] suggested cold rolling to be replaced by warm rolling. Since the cited works are precursors to my thesis, a short summary of the results obtained are given in sections 1.1.1.2 to 1.1.1.4.

### **1.1.2 Warm rolling**

Generally, WR is carried out at  $T_{WR}=0.25...0.5 \cdot T_m$ , where  $T_m$  [K] is melting temperature [10]. For Ti-Ni SMAs, melting temperature is 1200°C; therefore  $T_{WR}$  corresponds to 300-600°C. A previous study [9] showed that limiting Ti-50.26 at.%Ni WR temperature to 150°C ( $\sim 0.15 \cdot T_m$ ) and thickness reduction to  $e=1.2$  allows the manufacture of mainly nanocrystalline (but partially nanosubgrained) material, while decreasing the processing-induced damages (microcracks).

### **1.1.3 Structural analysis of Ti-Ni alloy**

In [9], structure of Ti-Ni alloy after SPD was investigated by transmission electron microscopy (TEM). Ti-50.26 at.%Ni alloy samples were rolled down with pulling tension corresponding to 10% of the material's yield stress at the roll mill entry. The total cumulative deformation corresponded to  $e=1.2$ . Temperature of the PDA was chosen as 400°C.

The purpose of this section is to discuss the structural changes caused by warm rolling, WR ( $T_{WR}=150^\circ\text{C}$ ) and intermediate annealing, IA (400°C, 1h). The CR( $e=1.2$ ) route is selected as a reference for processing leading to nanocrystalline structure. The results of TEM are presented in Figure 1.2.

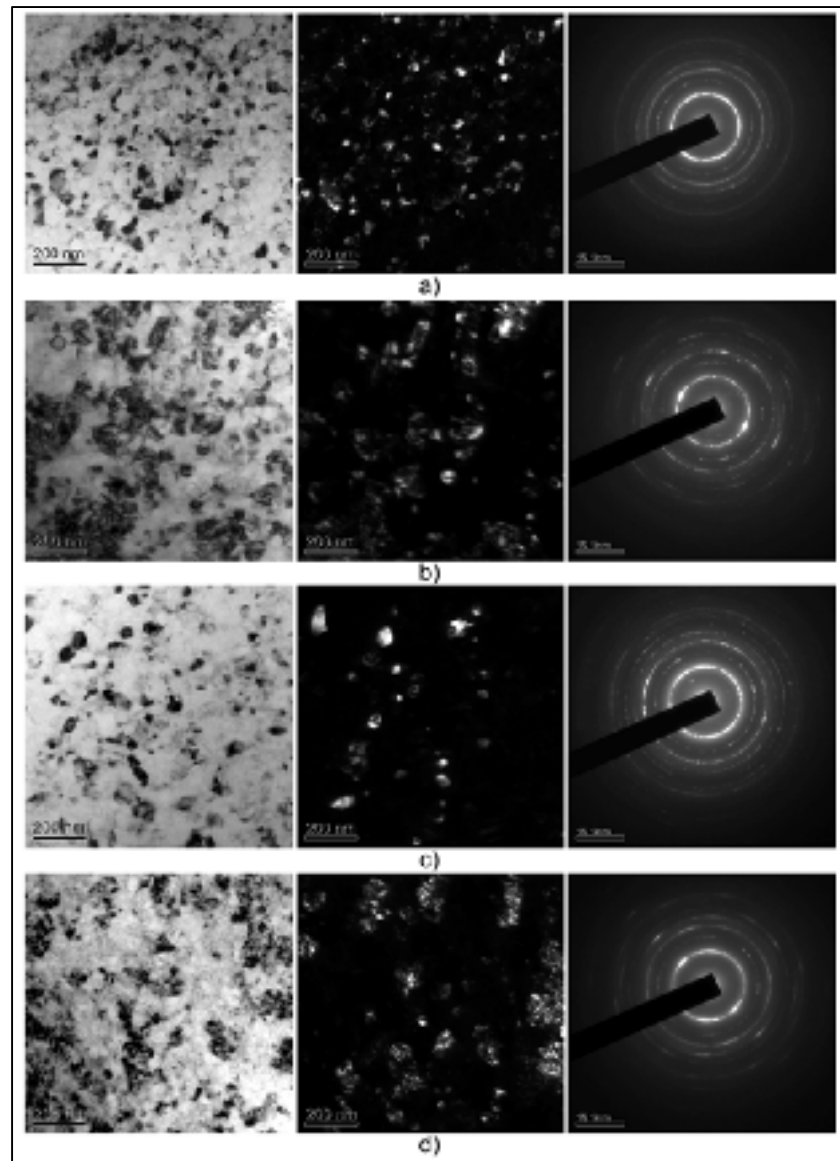


Figure 1.2 TEM images of Ti-50.26 at.%Ni alloy after different TMT routes: a) route CR( $e=1.2$ ), b) route CR( $e=0.3$ )+WR( $e=0.9$ ); c) CR( $e=1$ )+IA+CR( $e=0.2$ ); and d) WR( $e=1$ )+IA+WR( $e=0.2$ ). From left to right: bright-field image, dark-field image, microdiffraction pattern [9]

According to Figure 1.2a, after CR( $e=1.2$ ) and PDA (400°C), the structure of Ti-50.26 at.%Ni alloy is a mixed nanocrystalline (NC) and nanosubgrained (NS) structure. The size of the NC grains is 15-70 nm (Figure 1.2a). From the dark field, the quantity of the NS structure corresponds to 10-15% with mean subgrain size up to 150 nm [9].

Combination of CR and WR,  $CR(e=0.3)+WR(e=0.9)$ , creates grains with size up to 80-150 nm. The quantity of the NS structure is greater than the NC structure (Figure 1.2b). Intermediate annealing at 400°C,  $CR(e=1)+IA+CR(e=0.2)$ , leads to 60-120 nm grain size (Figure 1.2c), which is 1.5-2 times larger than after reference processing. Quantity of the NS structure is limited, because it is not detectable on the bright- and dark-field images and on the microdiffraction pattern [9].

Finally, structure after  $WR(e=1)+IA+WR(e=0.2)$  is mostly NS with grain size up to 200 nm (Figure 1.2d). However, NC structure is also present. An increased density of dislocation can be mentioned, and this structure is characterized as a polygonized dislocation substructure.

Accordingly, different combinations of CR and WR and IA create the mixture of NC and NS structures. Although changes in grain size are observed, this structure remains in a NC and NS size range. Therefore, WR at 150°C and IA at 400°C can be applied to obtain nanocrystalline structures and to study their influence on the mechanical properties and fatigue life of Ti-Ni SMA. This methodology will be used in this work for testing.

#### 1.1.4 Thermomechanical characterization of nanostructured Ti-Ni alloy

##### Stress-free recovery testing

Stress-free recovery testing was carried out using *Enduratec ELF 3200 (Bose)* testing equipment [3, 9]. The sample was first strained up to 9% (Figure 1.3a: O-A). Stress was then released to allow elastic springback (A-B). The initial strain was then set at about  $\varepsilon_i = 6-7\%$  for all the processing routes. When state B was reached, the sample was heated up to a 100°C (complete shape recovery) (B-C). After the sample was free air-cooled down to RT (C-E), the test was repeated up to the sample's failure.

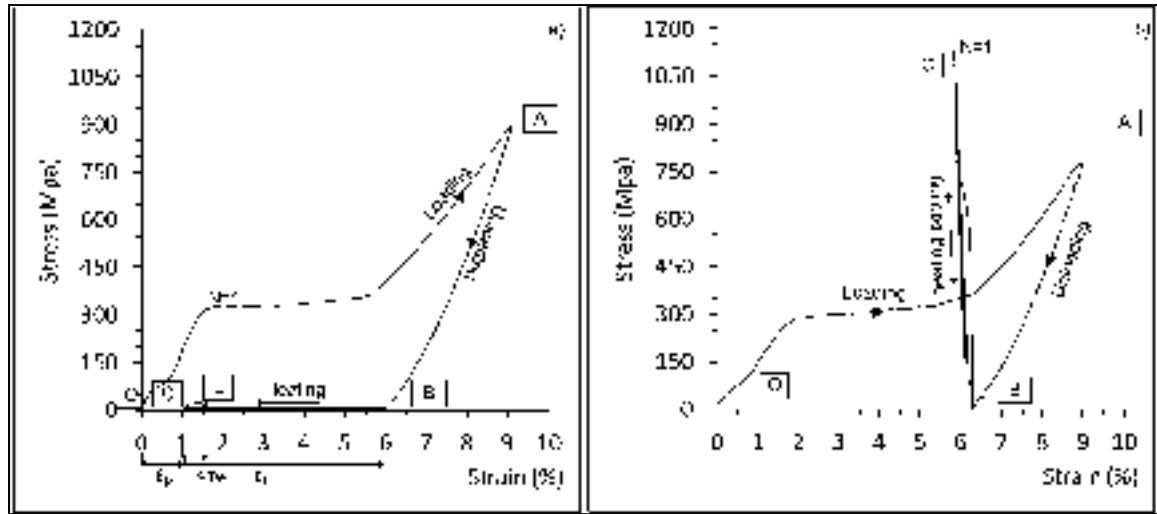


Figure 1.3 Stress-strain plots: a) stress-free recovery testing and b) constrained recovery testing; both for N=1 (Ti-50.26 at.%Ni alloy after CR( $\epsilon=1.2$ )+PDA 400°C, 1h) [3]

Stress-free recovery testing was carried out for Ti-50.26 at.%Ni alloy using the six following routes: CR( $\epsilon=1.2$ ), CR( $\epsilon=1$ )+WR( $\epsilon=0.2$ ), CR( $\epsilon=0.3$ )+WR( $\epsilon=0.9$ ), CR( $\epsilon=1$ )+IA+CR( $\epsilon=0.2$ ), CR( $\epsilon=1$ )+IA+WR( $\epsilon=0.2$ ), WR( $\epsilon=1$ )+IA+WR( $\epsilon=0.2$ ).

The recoverable strain remains constant (around 5.5%) for all the cases. However, the greater heat energy supplied to the material during processing, the higher the two-way strain  $\epsilon_{TW}$ . Also, it is worth noting that the number of cycles to failure increases with processing routes containing WR or IA. The highest number of cycles to failure is observed after CR( $\epsilon=1$ )+IA+WR( $\epsilon=0.2$ ) and WR( $\epsilon=1$ )+IA+WR( $\epsilon=0.2$ ), whereas the lowest number of cycles is observed after reference processing, CR( $\epsilon=1.2$ ) [9].

### Constrained recovery testing

Constrained recovery testing was carried out on a custom testing bench [9] using the same processing routes. Sample was strained up to 9% (Figure 1.3b: O-A), then released to allow elastic springback (A-B). The initial strain was then set at  $\epsilon_i=6-7\%$ . After that, the sample

was heated from room temperature to 200°C to allow the almost complete reverse martensitic transformation (B-C) and finally air-cooled to room temperature.

As in the previous test, the number of cycles to failure increases with increasing heat energy provided to the specimen during processing, but at the expense of the functional stability. The greatest fatigue life was observed after  $WR(e=1)+IA+WR(e=0.2)$ , 2028 cycles, which is 2.5 times higher than after reference processing  $CR(e=1.2)$ , 782 cycles. However during cycling, recovery stress after  $WR(e=1)+IA+WR(e=0.2)$  decreased more than after  $CR(e=1.2)$  (degradation rate of 24% towards 17%). The exact mechanism of this influence is not clear and may be a combination of stress relaxation resulting from IA and a specific deformation texture created by deformation of the mainly nanosubgrained material and also the greater damage of Ti-Ni alloys after entirely cold rolling.

#### **1.1.5 Effect of TMT by rolling on the texture and properties of Ti-Ni SMAs**

The shape memory effect in Ti-Ni alloys also depends on texture; therefore, the texture formation and its influence on the functional properties (recovery strain) is described in this chapter.

Texture forms when there is a preferential orientation of the external forces acting on the sample, for example in cases of plastic deformation, compacting and other technological processes [11]. Depending on the sequence of the technological processing, three types of texture could be considered: recrystallization (generally taken as a reference texture), deformation texture and annealing textures [12].

### **Effect of CR on the austenite texture**

Authors [12] in their study identified the recrystallization texture of Ti-Ni austenite after heat treatment at 500°C and subsequent quenching in water at room temperature such as  $\{110\}\langle 110 \rangle$ , where  $\{hkl\}$  is a rolling plane and  $\langle uvw \rangle$  is rolling direction (RD).

The low-intensity CR does not affect this recrystallization austenite texture; after CR up to 30%, austenite texture remains  $\{110\}\langle 110 \rangle$ B2 [12-14]. However, during CR and PDA, other texture components can appear. For example, after 30% of CR and thermal treatment at 500°C (30 min), two components of austenite texture were observed in Ti-49 at.%Ni alloy: principal  $\{110\}\langle 110 \rangle$  and secondary  $\{001\}\langle 110 \rangle$  [14].

Severe CR contributes to the appearance of a multicomponent texture. For example,  $\alpha$ -fiber II B2-texture –  $\{110\}\langle 110 \rangle + \{111\}\langle 110 \rangle$  – was obtained in a Ti-45Ni-5Cu sample after multiple-pass CR with IA at 500°C (10 min) and final annealing at 500°C (1.5 h) [15]. The  $\{110\}\langle 110 \rangle$  component intensity and density were higher than those of the  $\{111\}\langle 110 \rangle$  component, which allows the obtained texture to be identified as mainly  $\{110\}\langle 110 \rangle$ B2.

### **Effect of the heat treatment temperature after CR on the austenite texture**

Rolling and annealing affect the deformation texture as well as the recrystallization texture. Usually heat treatment temperature for shape memorization is slightly below the recrystallization temperature, which is about 500°C. In this case, heat treatment only causes recovery without changing the crystallite orientation distribution appreciably, so that the deformation texture remains and affects the shape memory characteristics of the rolled plates. Since the rolled plates are generally subjected to multiple IA, the annealing texture is also involved in the technological process. Therefore, control of the annealing texture is also of importance for the purpose of tailoring the final texture of TiNi-based SMA rolled plates [16].

As said, PDA after a low level of CR (up to 30%) does not change austenite texture. But when CR intensity is higher, texture depends on the PDA temperature. There are three levels of temperature to be considered: below, above and around the recrystallization temperature ( $\sim 500^\circ\text{C}$ ).

In [16], the influence of the annealing temperature on the austenite texture was analyzed. Texture of the Ti-50.5Ni-0.4Fe alloy samples after CR and annealing at  $400^\circ\text{C}$  was identified as being similar to the  $\gamma$ -fiber  $\{111\}\langle 110 \rangle + \{111\}\langle 112 \rangle$  texture.  $400^\circ\text{C}$  is below the recrystallization temperature, so that the deformation texture with high dislocation density, thermally rearranged by recovery, was retained.

Increasing the temperature up to  $600^\circ\text{C}$ , led to the  $\{221\}\langle 110 \rangle$  B2-texture formation.  $600^\circ\text{C}$  is slightly higher than the recrystallization temperature, and sub-micron sized grains were formed in this situation [16]. After subsequent heating at  $1000^\circ\text{C}$ , texture was composed of two components  $\{332\}\langle 110 \rangle$  and  $\{111\}\langle 011 \rangle$ , and this texture formation was accompanied by intensive growth of recrystallized grains.

### **Effect of hot rolling on the austenite texture**

The authors [17] found  $\{112\}\langle 110 \rangle$  texture in the parent phase of Ti-50.0 at.%Ni subjected to hot rolling (HR).

$\{111\}\langle 110 \rangle$  austenite texture was measured in Ti-49.2 at.%Ni alloy after annealing at  $400^\circ\text{C}$  and final recrystallization annealing after 50% of HR [13].

Ti-50.5 at.%Ni samples after HR at a temperature not exceeding  $1000^\circ\text{C}$  and then annealed, rolled at  $500^\circ\text{C}$  and quenched from  $800^\circ\text{C}$  in water had a recrystallization B2-phase texture of  $\{110\}\langle 110 \rangle$  [18].



### **Combined influence of CR and HR on the austenite texture**

The deformation mechanisms which operate in austenite during HR are related to the deformation mechanisms in martensite during CR by a specific orientation relationship [13, 19]. For example, after HR of Ti-50.4 at.%Ni alloy at 850°C, annealing at 800°C (30 min) and CR at room temperature, austenite texture was an  $\alpha$ -fiber I like texture:  $\{001\}\langle 110 \rangle + \{112\}\langle 110 \rangle, \{111\}\langle 110 \rangle$ , extended from the orientation (885)[110] to (112)[110], the fiber axis [110] being parallel to the RD, and the maximum orientation density of 7.15 at (885)[110] orientation [20, 21].

### **Effect of annealing time on the austenite texture**

Long annealing changes the austenite texture. For Ti-51.5 at.%Ni alloy, rolled and annealed at 820°C (10 min) and then aged at 500°C (1.5 h), B2-texture was  $\{111\}\langle 112 \rangle$ , but after annealing for 500°C (5 h) and aging under the same conditions, B2-texture was  $\{111\}\langle 213 \rangle$  [22]. Texture of Ti-50.45 at.%Ni alloy after HR and aging at 500°C (10 h) was  $\{112\}\langle 110 \rangle$  and  $\{001\}\langle 110 \rangle$  [19].

The single-component texture is more likely to occur after the one-step deformation process. In particular,  $\{110\}\langle 110 \rangle$  and  $\{111\}\langle 110 \rangle$  ( $\alpha$ -fiber II texture) is generally observed after CR of Ti-Ni SMAs. The higher the rolling intensity, the greater the chances that both textures appear at the same time. The more complicated the processing route is, the more components could be present in the austenite texture.

### **Martensite texture evolution during CR**

Martensite lattice is monoclinic, and therefore texture analysis is complex. To simplify the martensite texture analysis, pole figures are frequently compared with the standard projection of the cubic system, which contributes to error and incorrect texture definition [23, 24].

As known, 12 martensite variants correspond to one crystal of austenite. Therefore, even when austenite texture doesn't change, martensite texture may be evaluated. For example, martensite texture changes in the case of conventional (low-intensity) CR contrary to the austenite texture. For example, B19'-martensite texture containing the following variants: 3,  $(120)[\bar{2}11]$ , and 5,  $(120)[00\bar{2}]$ , after CR was replaced by 2,  $(10\bar{2})[211]$ , 4,  $(10\bar{2})[\bar{2}1\bar{1}]$  and 6,  $(10\bar{2})[0\bar{2}0]$  after PDA [12]. All these martensite texture components correspond to the single  $\{111\}\langle 110 \rangle$  component of the austenite texture.

### **Texture versus properties for polycrystalline Ti-Ni SMAs**

Based on the results of the literature review, a generalized austenite texture in Ti-Ni SMAs might be represented by the following components:  $\{110\}\langle 110 \rangle$ ,  $\{111\}\langle 110 \rangle$ ,  $\{001\}\langle 110 \rangle$  and  $\{112\}\langle 110 \rangle$ .

Texture component  $\{110\}\langle 110 \rangle$  (recrystallization texture according to [12]) occurs more frequently than other components in Ti-Ni SMAs. One can observe it after recrystallization annealing, CR and HR. However, the more complicated the thermomechanical processing is, the more probable the appearance of other texture components.

$\{110\}\langle 110 \rangle$  austenite texture leads to the highest transformation (lattice) strain corresponding to maximum deformation of the crystallographic lattice [15, 25]. But taking into account the grain accommodation phenomena in polycrystalline material, very high planar anisotropy results from this texture with very low recoverable strain in rolling direction (RD), ~3% [19]. No experimental results related to the  $\{110\}\langle 110 \rangle$  single-component austenite texture were found.

Texture component  $\{111\}\langle 110 \rangle$  is the next one after  $\{110\}\langle 110 \rangle$  in the order of frequency in textured Ti-Ni alloys. Authors [23] called the  $\{111\}\langle 110 \rangle$  texture the deformation texture of B2-austenite. In fact, it is present after complex deformation processes: for example, after

moderate and severe cold or hot deformation with IA, when temperature doesn't exceed the recrystallization temperature ( $\sim 500^{\circ}\text{C}$ ). According to the calculation,  $\{111\}\langle 110\rangle$  leads to high lattice (8.4%) and recoverable ( $\sim 5.5\%$ ) strains with moderate anisotropy [15, 19]. However, no experimental confirmation was found for this case.

Texture component  $\{001\}\langle 110\rangle$  has not been observed as a single-component austenite texture. It was always present in combination with other texture components, after complex deformation routes, such as CR and HR and aging. The theoretically predicted recovery strain for this texture doesn't exceed 5.5% at 0 and  $90^{\circ}$  to RD, and there is a drop to 3.1% at  $45^{\circ}$  to RD ( $\langle 010\rangle$ ) [19]. Thus, this texture leads to high planar anisotropy of recoverable strain.

Texture component  $\{112\}\langle 110\rangle$  was observed after HR, as well as after combined CR and HR plus aging. Frequently, this component accompanies the  $\{001\}\langle 110\rangle$  texture after HR and aging. No any calculated transformation (lattice) strain values were not found for this case: neither for single crystals, nor for polycrystalline materials. At  $0^{\circ}$  to RD, the measured recoverable strain was close to 5.5%, similar to this value for  $\{111\}\langle 110\rangle$  and  $\{001\}\langle 110\rangle$  components. This texture leads to a significant anisotropy of measured recoverable strains: at  $90^{\circ}$  to RD ( $\langle \bar{1}1\bar{1}\rangle$ ), recoverable strain was about 7%, whereas at  $45^{\circ}$ , it was around 3.5% [19].

Based on the literature data, the following scheme could be used to illustrate the influence of the thermomechanical processing on the texture components and recoverable strains in RD (Figure 1.4).

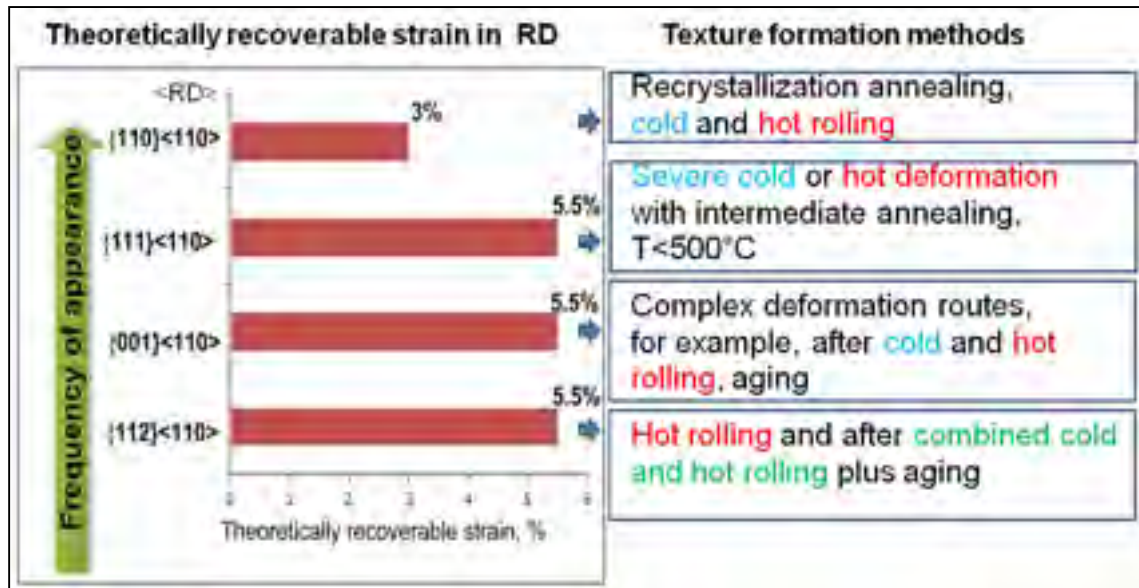


Figure 1.4 Influence of the TMT on the texture components and recoverable strains (adapted from [19])

## 1.2 TMT of Ti-Ni SMA by ECAP

Equal channel angular pressing is the SPD process that permits application of a large amount of uniform strain without a reduction in a cross-section area. ECAP is superior to other techniques because of the formation of uniform microstructures, control over the development of grain morphology and texture. This method realizes deformation of massive billets via pure shear. Figure 1.5 shows a schematic representation of the ECAP process. The cross-section of the billet can be a circle, square or rectangle cross-sections. The billet is pressed down by a plunger from the top of the vertical channel and it is deformed in the shear zone and extruded from the horizontal channel with the same diameter. The angle between two intersected channels ranges between  $90^{\circ}$  and  $120^{\circ}$ . In the case of hardly-deformed materials, the deformation can be carried out at high temperature and/or greater extrusion angle. Every pass at angle of  $90^{\circ}$  corresponds to a total strain equal to 1, which is equivalent to 70% of CR.

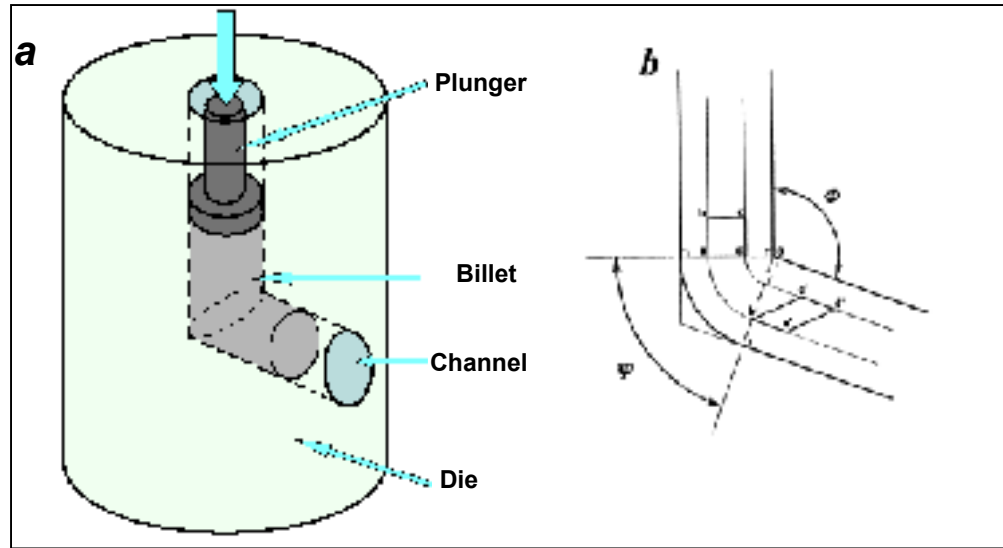


Figure 1.5 Schematic representation of the ECAP processing: (a) 90°-angle ECAP; (b) schematic representation of the angle determination [26, 27]

To calculate the accumulated shear strain applied to a billet during N-pass ECAP processing, the following formula can be used [26]:

$$e_N = N \left[ \frac{2 \operatorname{ctg}(\phi / 2 + \psi / 2) + \psi \operatorname{cosec}(\phi / 2 + \psi / 2)}{\sqrt{3}} \right] \quad (1.1)$$

where N – number of passes;  $\phi$  – inner angle;  $\psi$  – outer angle.

The ECAP treatment is controlled through five process parameters:

1. Angle between the channels;
2. Temperature during treatment;
3. Pressing rate (strain per pass);
4. Number of passes;

## 5. Rotation of the material between passes.

Rotation of the material between pressings is possible because the material retains its initial cross-section. The following routes can be considered: (1) billet orientation remains constant for each pass (route A); (2) after each pass, the billet is rotated around its longitudinal axis by  $90^\circ$  (route B); (3) after each pass, the billet is rotated around its longitudinal axis by  $180^\circ$  (route C) [28]. Authors [29] showed that for pure titanium, a uniform microstructure with high quality of surface forms after  $2n$  or  $4n$  passes ( $n$  – whole number) in the case of route B. Shear deformation during uneven pass of route B leads to grain elongation, although every even pass returns a cubic element in the working piece to its original cubic shape. It provides uniform equiaxed structure [30].

### **Influence of the ECAP strain rate on the Ti-Ni alloys' deformation mechanisms**

Experiments at high strain rates lead to shear localization arising from adiabatic heat dissipation and local thermal softening of the material [4, 28, 31-33]. Localized shear is an important mode of deformation. It results in catastrophic failure during high strain-rate deformation. Consequently, one of the purposes is to control strain-rate and, correspondingly, localized shear deformation and formation of shear bands. Also, at high strain-rates, strong local heating can occur and, consequently, strain-induced austenite formation (in the case of the marforming process) provokes appearance of macroshear bands. Observed transformation bands lead to a strong deformation localization and to strong local heating.

Therefore, during marforming (deformation of martensite structure), the pressing rate is generally kept sufficiently small to minimize deformation heating. At higher temperatures (ausforming), where no martensite/austenite transformation can occur, the rate can be higher. And if the specimen has been heated in a furnace and then placed in the ECAP die, the specimen temperature decreases with time at a low strain-rate, which should be taken into account. For example, authors [4] carried out ECAP at room temperature in martensite state

with extremely small rate (0.127 mm/s) to avoid local heating. The increase of ECAP temperature up to 450°C allowed application of strain-rates as high as 8 mm/s [4, 34-43].

A combined influence of the strain-rate and temperature on the deformation mechanisms (one ECAP pass with 90° angle) of Ti-49.8 at.%Ni alloy is presented in Table 1.1.

Table 1.1 ECAP conditions and the proposed deformation mechanisms that occurred during processing of Ti-49.8 at.%Ni alloy [4]

Processing temperature	Initial phase	Pressing rate (mm/s)	Deformation mechanisms
RT	martensite	0.127	Martensite reorientation and plastic deformation by dislocation slip
50°C (close to $A_s$ )	martensite	0.25	Dislocation slip in martensite and local formation of strain-induced B2 phase
150°C	austenite	0.25	Stress-induced martensite formation and plastic deformation by dislocation slip

### **Influence of ECAP parameters on the Ti-Ni alloys' microstructure**

The stress-strain state during ECAP differs from the stress-strain state during rolling; one should therefore expect different microstructures after the same level of total deformation strain. In the case of ECAP, along with tensile and compression strains, shear strain contributes to the structure formation.

#### **1.2.1 Formation of the ultrafine-grained structure**

The microstructure formation is affected by the processing temperature and total ECAP strain. The higher the pressing temperature, the higher the total strain required for achievement of the desired microstructure.

Microstructure of Ti-50.2 at.%Ni alloy after ECAP at 450°C with total strain  $e = 0.81$  showed reduction of grain size down to 600 nm compared to the as-quenched state (80  $\mu\text{m}$ ) [34]. If the total strain increases to 3.2, the grain size decreases to 450 nm and after  $e = 6.5$ , it is 200-300 nm [34-39]. However, reduction of the grain size to this low limit (230 nm) was achieved by lowering of the ECAP temperature to 400°C, whereas enlargement of the grain size to 300 nm was achieved by increase of the ECAP temperature to 500°C [34]. If the total ECAP strain increases to 9.2, no effect on the grain size was found [34-38]. Finally, the finest submicrocrystalline structure (100-200 nm) was obtained in Ti-50.6 at.%Ni alloy after ECAP at 350°C with  $e = 4.9$  [43].

The high-temperature ECAP processing with even number of cycles (and  $e=4.9-9.2$ ) results in the formation of equiaxed ultracrystalline structure. However, high stresses and lattice distortions are measured inside of the grains and in their boundaries. Non-equilibrium grains contain well-developed substructure with high dislocation density. We can conclude that an increase in ECAP temperature is not the best-suited solution for the microstructure refinement, because it requires application of higher total strains (greater pressing angle and/or more number of passes) to reach the same grain size.

### **Influence of post-ECAP annealing on the ultrafine-grained structure**

During PDA of the ECAP-processed samples, structural recovery takes place. After annealing at 300°C, 20 min, the average grain size changes are not significant: they remain of about 200-300 nm in size. However, non-equilibrium grain boundaries become more contrasted. Following high-temperature annealing (500°C), grain size increases up to 400-500 nm. Further temperature rise (550-600°C, 1h) results in grain growth to up to 600-800 nm [41, 42].



### 1.2.2 Formation of nanostructures

It is reasonable to expect that further structural refinement of Ti-Ni SMAs down to nano-scale could be obtained if ECAP was conducted at temperatures lower than 350°C-300°C [43-46]. However, the results of the ECAP processing of Ti-Ni alloys at low-temperature can be found in only two reports [44, 45], where the authors pretend detecting the presence of nanostructures after ECAP of Ti-49.8 at.%Ni and Ti-50.8 at.%Ni alloys billets at room temperature (one pass with  $\epsilon=1.15$ ). However, the photo published in one of these works exhibits a billet with large macrocracks [45], which should have made it useless for subsequent passes and testing (Figure 1.6a). Moreover, the results of microstructural analysis presented in [44, 45] raise serious doubts of whether a true nanocrystalline structure have indeed been obtained after  $\epsilon=1.15$  in this works, since the presented TEM images and X-Ray diffractograms are more characteristic of the nanosubgrained and, certainly, none of the nanocrystalline structure (Figure 1.6b).

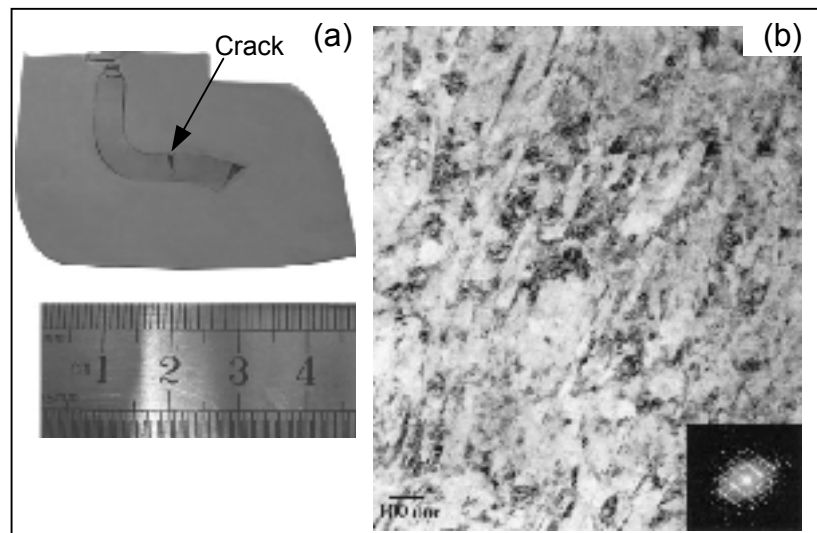


Figure 1.6 (a) Cross-section of billet [45] and (b) TEM image of Ti-49.8 at.%Ni alloy after ECAP at room temperature and PDA at 400°C [4]

### 1.3 Functional properties of Ti-Ni alloys after ECAP and CR processes

Since the stress-strain states during CR and ECAP processing are different, it is interesting to compare the functional properties of the submicrocrystalline and nanocrystalline structures after these TMTs. The maximum recovery stress ( $\Delta\sigma$ ) was calculated from the stress-strain diagrams as a difference between the critical stress for martensite reorientation (stress-induced martensitic phase transformation) and the true yield stress of martensite (Figure 1.7). The maximum recovery stress and austenite microstructure after CR and ECAP processing are presented in Table 1.2.

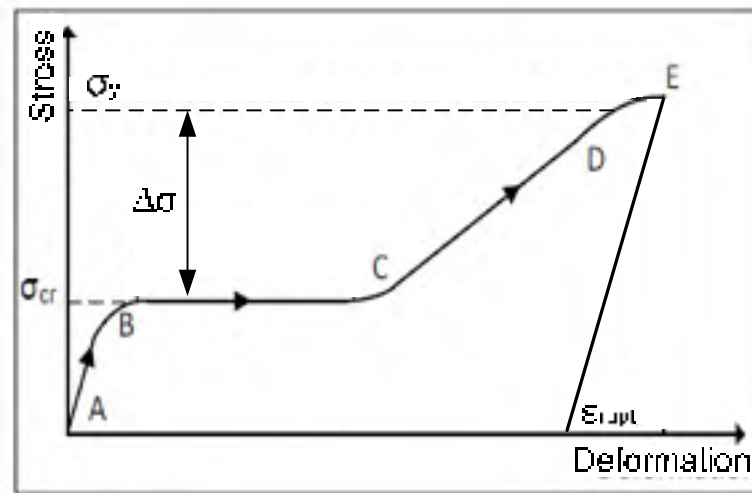


Figure 1.7 Typical tensile stress-strain plot to failure

Table 1.2 Structure and functional properties of Ti-Ni alloys after various treatment [4, 43, 46]

Alloy	Treatment	Structure of austenite	$\Delta\sigma$ , MPa
Ti-50.0 at.%Ni	CR( $e=0.3$ )+350-400°C	Recovered and polygonized	900
	CR( $e=0.88$ )+350-400°C	Nanosubgrained and nanocrystalline	1100
Ti-50.26 at.%Ni	CR( $e=1.2$ )+400°C	Nanocrystalline (15-50 nm)	1500
Ti-50.2 at.%Ni	ECAP (450°C, $e=3.2-9.2$ )	Submicrocrystalline (200-400 nm)	800-1100
Ti-50.6 at.%Ni	ECAP (450°C, $e=6.5$ )	Submicrocrystalline (200-400 nm)	720
	ECAP (350°C, $e=4.9$ )	Submicrocrystalline (100-200 nm)	780

Comparing the maximum  $\Delta\sigma$  of the ultrafine-grained Ti-Ni alloys after CR and ECAP processing, it can be noted that the smaller the grain (or subgrain) size, the higher the  $\Delta\sigma$ . The maximum comparable  $\Delta\sigma$  is observed in the case of nanostructures resulting from CR. However, considering the differences between ECAP and rolling of Ti-Ni alloy, ECAP allows formation of a mainly ultrafine-grained structure with  $d \geq 200$  nm; on the other hand, this method makes it possible to deform massive billets without changing their cross-section, which provides the net advantage for the preliminary structural refinement.

#### 1.4 Research objectives

As was shown by the literature review, first, a specific combination of CR, WR and IA leads to a significantly increased fatigue life with high level of functional properties [9].

One of the supposed reasons for this high performance is a favorable texture resulting from

thermomechanical processing. Even though it has been already shown that texture influences recoverable strain of Ti-Ni alloys, the texture formation during SPD including CR and WR was not studied.

Second, ECAP keeps the initial cross-section of samples constant and preserves the material integrity even at high degrees of deformation at elevated temperatures. Therefore, it appears attractive to use this method for the initial structural refinement of bulk Ti-Ni alloys prior to severe cold deformation.

Therefore, two main objectives are:

- 1) To understand the interrelations between the processing conditions to manufacture nanostructured Ti-Ni SMAs and their structure, texture, functional properties and processing-induced damage;
- 2) To optimize the technological processing conditions of nanostructured Ti-Ni SMAs with the aim of obtaining the best combination of their static and dynamic (fatigue) functional properties.

According to the first objective, characterization of the “statistic” and “dynamic” functional properties of nanostructured Ti-50.26 at.%Ni alloy after different TMTs including CR, WR, intermediate annealing and PDA will be performed. This study should clarify the influence of the TMT conditions on the alloys’ structure, texture and functional properties, including fatigue resistance.

According to the second objective of this project, the technological processing of Ti-Ni alloys to produce nanocrystalline material free of processing-induced damage will be optimized. This study should be focused on the influence of the temperature, strain rate and microstructure on the strain-rate sensitivity of Ti-Ni alloys with the aim to improve their deformability.

## 1.5 Methodology

The methodology used in this project is described in each article (Chapters 2-5). However, below a brief overview of materials, TMTs, and mechanical and microstructure characterization is provided.

### 1.5.1 Materials and thermomechanical treatments

Two Ti-Ni shape memory alloys' compositions were used in this study: Ti-50.0 at.%Ni and Ti-50.26 at.%Ni. Ti-50.0 at.%Ni alloy was supplied by *Johnson Matthey* as as-drawn 19 mm diameter bars, the finish temperature of reverse martensitic transformation corresponds to 98°C. For the strain-rate sensitivity and deformability study after different TMTs including ECAP, Ti-50.0 at.%Ni alloy was chosen. This alloy is no-age-hardenable and therefore has higher plasticity at elevated temperatures than Ti-50.26 at.%Ni alloy.

Ti-50.0 at.%Ni alloy was subjected to homogenization annealing (800°C, 1h) and cut into 100 mm long bars. Some bars underwent ECAP at different temperatures (400°C and 500°C) with  $e=5.44$  for eight passes at Ufa State Aviation Technical University, Ufa, Russia (Table 1.3). The ECAP temperatures and true strains were selected based on the literature review. PDA was performed using a SNOL-6/11 electrical furnace.

Table 1.3 Samples designation and corresponding TMT routes

Route	Identification	Step 1	Step 2	Step 3
1	Reference quenching (RQ)	Heating at 800°C (1h) followed by water quenching	-	-
2	ECAP-400		ECAP (400°C, $e=5.44$ )	PDA (350°C, 1 h)
3	ECAP-500		ECAP (500°C, $e=5.44$ )	PDA (450°C, 1 h)

Ti-50.26 at.%Ni alloy was supplied by *SAES Getters* as an as-drawn (30% of cold work) 1mm diameter wire, the start and finish temperatures of reverse martensitic transformation correspond to 74 and 91°C respectively. This alloy was chosen from the previous work [8] for further study of interactions between the thermomechanical treatment, structure/texture and functional properties and also possesses a certain advantage compared to Ti-50.0 at.%Ni alloy since it allows room-temperature superelasticity (its  $M_s$  temperature is lower than that of equiatomic alloy). The wire was primarily subjected to homogenization annealing (700°C, 1 h), and then rolled using four-high *FENN* laboratory rolling mill (Figure 1.8).



Figure 1.8 Four-high FENN laboratory rolling mill

For warm rolling, a four-high FENN laboratory rolling mill was combined with a spooler, a take-up reel system and a continuous direct electric current resistance heating system ([8, 9], Figure 1.9).

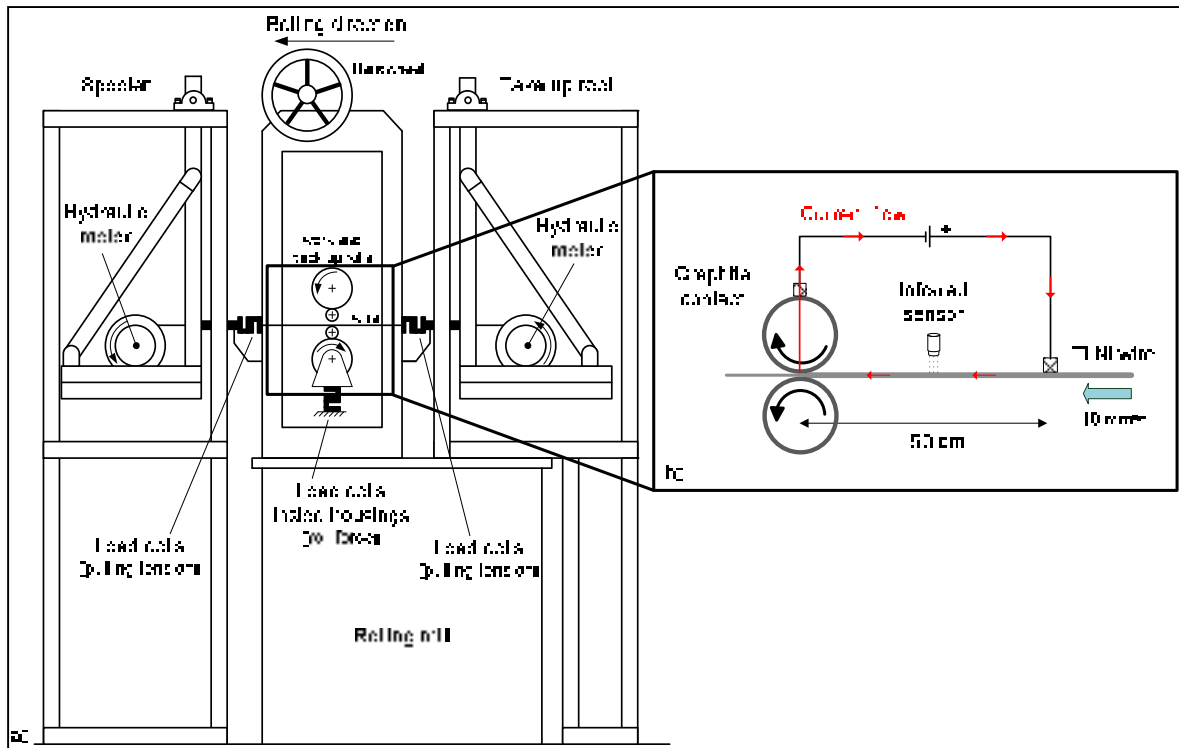


Figure 1.9 Schematic view of the: a) rolling mill and pulling tension system; b) electric heating system [9]

Direct Joule heating was used to increase the temperature of the material during the rolling process. The resistivity of the Ti-Ni alloy being high compared to conventional metals; the Joule heating was easy to implement by applying moderate current densities, of the order of  $1\text{A/mm}^2$ , to reach the desired deformation temperature. The heating system consisted of a current generator (*Sorensen*, DLM 40-15 Series) that can provide up to 15 A at 40 V, and the current flows between two graphite connectors, one on the wire and another, on the roller (Figure 1.9). It allowed heating of the material in the deformation zone. An infrared temperature sensor (CT 20/1, *Optris*) capable of measuring the temperature of a  $\varnothing 0.6\text{ mm}$  target at a distance of 10 mm in the  $-40^\circ\text{C}$  to  $900^\circ\text{C}$  range was used to control the wire temperature at the rolling mill entry [8].

A guide was placed under the support of the thermometer to follow the wire movement during rolling. Therefore, the wire temperature was continuously monitored by the

temperature sensor to provide reliable and consistent deformation conditions. The device is shown in Figure 1.10.

An interface was developed in the *Labview* environment to allow real-time monitoring of various parameters, such as rolling force, voltage and wire temperature. Recording of these parameters ensured maintenance of the conditions under which the samples were produced.

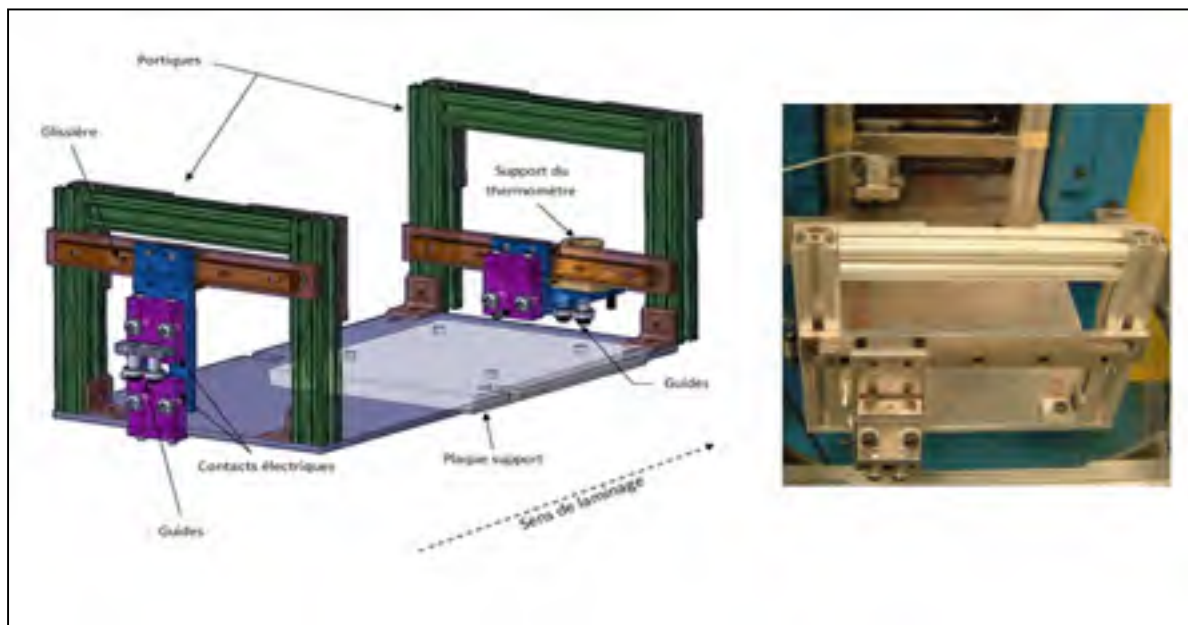


Figure 1.10 Representation of the infrared sensor-wire alignment device [8]

Six processing routes were chosen for this study (Table 1.4). Route 3 is the reference route and Routes 4, 5, 6 are routes which showed the best functional properties during previous stress-free recovery and constrained recovery testing (section 1.1.1.4). Routes 3-6 corresponded to a total logarithmic thickness reduction of  $e=1.2$ . Also, samples after CR( $e=0.75$ ) and CR( $e=1.0$ ) with combined nanosubgrained and nanocrystalline structure were chosen for comparison of their functional properties with those of entirely nanocrystalline alloys.



A pulling tension corresponded to 10% of the material's yield stress, and a rolling speed corresponded to 10 mm/s. WR was carried out at  $150\pm 5^{\circ}\text{C}$  ( $0.15\cdot T_m$ ). Four rolling routes with different combinations of CR and WR and IA were tested (Table1.4).

Table1.4 Specimens designation and corresponding processing routes

Routes	Identification	Step 1	Step 2	Step 3	Step 4
1	CR( $e=0.75$ )	CR, $e=0.75$	PDA $400^{\circ}\text{C}$ , 1h	-	-
2	CR( $e=1.0$ )	CR, $e=1.0$	PDA $400^{\circ}\text{C}$ , 1h	-	-
3	CR( $e=1.2$ )	CR, $e=1.2$	PDA $400^{\circ}\text{C}$ , 1h	-	-
4	CR( $e=1$ )+IA+ CR( $e=0.2$ )	CR, $e=1$	IA $400^{\circ}\text{C}$ , 1h	CR, $e=0.2$	PDA $400^{\circ}\text{C}$ , 1h
5	CR( $e=1$ )+IA+ WR( $e=0.2$ )	CR, $e=1$	IA $400^{\circ}\text{C}$ , 1h	CR, $e=0.2$	PDA $400^{\circ}\text{C}$ , 1h
6	WR( $e=1$ )+IA+ WR( $e=0.2$ )	WR, $e=1$	IA $400^{\circ}\text{C}$ , 1h	WR, $e=0.2$	PDA $400^{\circ}\text{C}$ , 1h

PDA was carried out at  $400^{\circ}\text{C}$ , 1h using the *PYRADIA* heating furnace, with subsequent water-quenching to room temperature.

### 1.5.2 Mechanical and microstructural characterization

#### Electron microscopy

The transmission electron microscopy (TEM) study was carried out using *JEOL-2100* and *Tesla BS-540* microscopes. TEM was operated in three modes: bright-field, dark-field and electron diffraction pattern.

#### X-ray diffractometer

The X-ray diffraction analysis (XRD) was conducted using an *X'pert PRO PANalytical* X-ray diffractometer operating at 40kV/45mA with  $\text{CuK}_{\alpha}$ -radiation (wavelength  $\lambda=0.15406$

nm). A *TTK450* thermal chamber made it possible to conduct XRD analyses in the  $-150$  to  $450^{\circ}\text{C}$  temperature range. The control unit, the data acquisition and processing were managed by the *X'pert PRO PANalytical* software. The *X'pert PRO PANalytical* program allowed calculation of the inverse pole figures and orientation distribution functions, with an ultimate goal to determine texture components and to calculate the theoretical transformation strain resource taking into account the austenite texture.

#### *Enduratec ELF 3200*

The following shape memory properties were measured using an *Enduratec ELF 3200 (Bose)* testing equipment controlled by a *Wintest* software: recovery ( $\epsilon_r$ ) and residual (permanent) ( $\epsilon_p$ ) strains, two-way shape memory (TWSM) strain ( $\epsilon_{TW}$ ) and number of cycles during thermomechanical cycling. The sample heating was performed by Joule effect, and the testing temperature was measured by thermocouple of type K, fixed on the sample and isolated by a PTFE ribbon.

#### *Custom-made testing bench*

The custom-made testing bench capable of applying the maximum force of 3 kN and the maximum displacement of 50 mm made it possible to measure recovery forces upon heating of the deformed samples (reverse martensitic transformation). The temperature, force and displacement were controlled by a dedicated *Labview* program. *LVDT (Transtek)* and *LC-101-750lbs (Omega)* sensors were used to measure force and displacement variations respectively. The samples heating was performed by Joule effect followed by free cooling, and the sample temperature was measured by a fixed and isolated K-type thermocouple.

#### *MTS MiniBionix 858*

Cycling at a constant temperature was carried out on an *MTS MiniBionix 858* machine. Heating of samples was enabled by thermal chamber in the  $-400$  to  $400^{\circ}\text{C}$  temperature range. Loading and unloading were undertaken with up to a  $1-0.0001\text{ s}^{-1}$  rate. The *Station Manager* software was used to control the force, displacement and temperature of the test.

*Gleeble System 3800*

Strain-rate jump test and creep tests were performed using *Gleeble System 3800* under a plane strain mode). This system is capable of providing homogenous distribution of temperature in a sample volume, with maximum heating rate of 14000 K/s. Loading can be realized in the 10 to  $0.00001 \text{ s}^{-1}$  strain rate range, with maximum applied force of 100 kN (tension) and 200 kN (compression).



## CHAPTER 2

### ARTICLE #1: MICROSTRUCTURE AND FUNCTIONAL FATIGUE OF NANOSTRUCTURED Ti-50.26 at.%Ni ALLOY AFTER THERMOMECHANICAL TREATMENT WITH WARM ROLLING AND INTERMEDIATE ANNEALING

A. Kreitzberg<sup>a,b</sup>, V. Brailovski<sup>b</sup>, S.D. Prokoshkin<sup>a</sup>, Ya. Facchinello<sup>b</sup>, K. Inaekyan<sup>b</sup>,  
S.M. Dubinskiy<sup>a,b</sup>

<sup>a</sup>National University of Science and Technology “MISIS”, Moscow, Russia

<sup>b</sup>Ecole de technologie supérieure, Montreal, Canada

This article was published  
in *Materials Science and Engineering A*, 2013, v. 562, pp. 118-127.

#### 2.1 Summary

The main objective of this article was to study the effect of the TMTs, which combine cold rolling (CR), warm rolling (WR), intermediate annealing (IA, T=400°C, 1h), and post-deformation annealing (PDA, T=400°C, 1h), on the structure, texture, processing-induced damage and functional fatigue properties of 50.26 at.%Ni % alloy. The specimens were subjected to the following TMTs: CR( $\epsilon=0.75$ ), CR( $\epsilon=1$ ), CR( $\epsilon=1.2$ ), CR( $\epsilon=1$ )+IA+CR( $\epsilon=0.2$ ), CR( $\epsilon=1$ )+IA+WR( $\epsilon=0.2$ ), WR( $\epsilon=1$ )+IA+WR( $\epsilon=0.2$ ) and WR( $\epsilon=1.2$ ). The features of the structure formation after all the TMTs were studied using TEM; X-ray diffraction analysis was carried out to quantify the B2-austenite texture. The functional fatigue properties were determined using the stress-free recovery, constrained recovery and superelastic multi-cycle testing modes.

The electron microscopy analysis showed that all TMTs followed by PDA resulted in nanostructure formation. The greater the CR contribution, the larger the fraction of

nanocrystalline structure compared to the nanosubgrained structure, and the lower the average dislocation density. When the WR contribution increases, the nanosubgrained structure becomes dominant and less processing-induced damage is observed. The main texture component of B2-austenite after all the processing routes is  $\{100\}\langle 110 \rangle$ B2, and it is the sharpest after CR( $e=1$ )+IA+WR( $e=0.2$ ). Improved functional fatigue performances were observed in two cases: after CR( $e=1$ )+IA+WR( $e=0.2$ ) and after CR( $e=0.75$ ) as a consequence of the processing-induced damage reduction combined with the development of a favorable B2-austenite texture.

## 2.2 Abstract

The effect of different thermomechanical treatments (TMTs) on the microstructure and functional fatigue of Ti-50.26 at.%Ni alloy was studied. The TMTs evaluated were severe cold rolling (CR) in a strain range of  $e=0.75$  to 1.2, and a combination of CR with warm rolling at 150°C (WR) and intermediate annealing at 400°C, 1h (IA). The final step of all the TMT routes tested consisted of post-deformation annealing at 400°C, 1h (PDA). The resulting microstructure and crystallographic textures were studied using transmission electron microscopy and X-ray diffractometry. The processing-induced material damage was assessed by comparing edge cracks' length and concentration measurements. Functional fatigue properties were measured after all the TMT routes using three multicycle testing modes: a) stress-free strain recovery, b) constraint stress recovery and c) superelastic testing. The results of this study point to some promising technological avenues to improve the fatigue functional properties of Ti-Ni SMA.

**Keywords:** titanium alloys, nanostructured materials, shape memory alloys, fatigue, thermomechanical processing.

## 2.3 Introduction

Ti-Ni alloys are used as heat-sensitive elements and thermomechanical actuators (shape memory effect, SM), and flexible elements such as medical implants and tools (superelastic

effect, SE). These applications require the continuous improvement of SMAs' functional properties, especially in terms of their multiple-cycle recovery strain and stress generation capabilities. It has been shown that the formation of specific nanostructures by means of appropriate thermomechanical treatments (TMTs) can significantly improve the functional properties of binary Ti-Ni SMA [1-3]. One of these TMT routes implies the use of severe plastic deformation and post-deformation annealing technological steps [4-8]. During cold rolling (CR) with strain levels under  $e=0.5$  ( $e$ , logarithmic thickness reduction), a well-developed dislocation substructure forms, and when CR intensity increases, this structure is gradually replaced by a mixture of nanocrystalline and amorphous phases, the latter becoming predominant at  $e > 1$ . Post-deformation annealing (PDA) leads to polygonization of the dislocation substructure, to grain growth of the nanocrystalline structure and to nanocrystallization of the amorphous phase [1, 9].

According to the previous work [9], after  $e=0.75$ +PDA (400°C, 1h) of Ti-50.26 at.%Ni alloy, a ~50%-50% mixture of nanocrystalline (NC) structure and polygonized nanosubgrained (NS) structure is observed. When CR intensity increases to  $e=1.0$ +PDA (400°C, 1h), the quantity of NC structure becomes greater than that of NS structure, and when CR intensity reaches  $e=1.5$ +PDA (400°C, 1h), NC structure becomes predominant.

For Ti-Ni alloys, NC structure formed as a result of TMT comprising CR ( $e=1.5 \div 2.0$ ) and PDA (400°C, 1h) was found to be the most effective microstructure in terms of their functional properties, but only for a very limited number of recovery stress and strain generation-relaxation cycles ( $N < 10^3$ ) [1-3]. On the other hand, the best fatigue characteristics ( $N \gg 10^3$ ) were obtained in the case of a mixed NC+NS structure resulted from CR ( $e=0.75 \div 1$ )+PDA(400°C, 1h) processing routes [3, 10]. This phenomenon is explained by the fact that the higher the CR intensity, the greater the processing-induced damage of the material with evident negative impact on functional fatigue life [3]. In this respect, increasing rolling temperature and/or the introduction of intermediate annealing in the TMT multi-pass schedule seem to be promising avenues [11, 12].

From another perspective, SMAs' functional properties depend not only on structure but also on their crystallographic texture developed during processing. Three main types of the processing-related texture are generally distinguished: recrystallization texture (usually considered as a reference texture), deformation texture and annealing texture [13, 14]. The main components of the austenite texture in binary Ti-Ni SMAs are presented here in order of decreasing frequency of their occurrence:  $\{110\}\langle 110\rangle$ ,  $\{111\}\langle 110\rangle$ ,  $\{001\}\langle 110\rangle$  and  $\{112\}\langle 110\rangle$  [13, 15-23]. The  $\{110\}\langle 110\rangle$  texture component is called the recrystallization texture, and it is observed also after cold and hot rolling [13, 15, 18]. The  $\{111\}\langle 110\rangle$  texture component is called the deformation texture, and it generally appears after severe cold or hot deformation with intermediate annealing [15,18-20]. The  $\{001\}\langle 110\rangle$  texture component is generally observed in combination with other components after cold or hot rolling and aging [18-21, 24]. The  $\{112\}\langle 110\rangle$  component appears after hot rolling and when cold and hot rolling are combined with aging [18-21, 24].

In this work we studied the effect of different TMT routes, which combine severe cold and warm rolling, intermediate and post-deformation annealing, on structural features and the functional fatigue of binary Ti-Ni SMA.

## 2.4 Methodology

A Ti-50.26 at.%Ni alloy was studied. A 1 mm diameter as-drawn (30% of cold work) wire supplied by "SAES Getters" was primarily subjected to a homogenization annealing (700°C, 1 h) and then to various TMTs, which included cold rolling (CR), warm rolling (WR), intermediate annealing (IA) and post-deformation annealing (PDA) steps in different combinations. The rolling was performed using a four-high "FENN" laboratory rolling mill under pulling tension corresponding to 10% of the material's yield stress at the mill's entry; the rolling speed was 10 mm/s. Warm rolling was carried out at 150°C ( $\sim 0.15 \cdot T_m$  [K]). This temperature does not correspond to the conventionally-accepted temperature of warm deformation (generally above  $0.3T_m$ ), but it is the highest deformation temperature for this alloy, which allows initiation of strain-induced amorphization and therefore the creation of



nanocrystalline microstructure after post-deformation annealing [12]. To reach this temperature, the wire was in-line heated by electrical current (Joule effect) using a custom heating unit described in detail in [12]. Both the IA and PDA heat treatments were performed at 400°C (1h) using a “PYRADIA” heating furnace, with subsequent water-quenching to room temperature.

The following seven TMT routes were tested (Table 2.1):

-Routes 1-3, CR  $\epsilon=0.75$  (4 passes), 1 (5 passes) and 1.2 (6 passes):  $CR(0.75)$ ,  $CR(1.0)$ ,  $CR(1.2)$ ;

-Route 4, CR  $\epsilon=1$  (5 passes)+IA+CR  $\epsilon=0.2$  (one pass):  $CR(1)+IA+CR(0.2)$ ;

-Route 5, CR  $\epsilon=1$  (5 passes)+IA+WR  $\epsilon=0.2$  (one pass):  $CR(1)+IA+WR(0.2)$ ;

-Route 6, WR  $\epsilon=1$  (5 passes)+IA+WR  $\epsilon=0.2$  (one pass):  $WR(1)+IA+WR(0.2)$ ;

-Route 7, WR  $\epsilon=1.2$  (6 passes):  $WR(1.2)$ .

Identical PDA (400°C, 1h) was carried out following each of the TMT routes.

Table 2.1 Samples designation and corresponding TMT routes

Route	Identification	Step 1	Step 2	Step 3	Step 4
1	CR(0.75)	CR, $e=0.75$	...	...	PDA, 400°C(1h)
2	CR (1.0)*	CR, $e=1.0$	...	...	PDA, 400°C(1h)
3	CR (1.2)	CR, $e=1.2$	...	...	PDA, 400°C(1h)
4	CR (1.0)+IA+ CR (0.2)	CR, $e=1.0$	IA, 400°C(1h)	CR, $e=0.2$	PDA, 400°C(1h)
5	CR (1.0)+ IA +WR(0.2)	CR, $e=1.0$	IA, 400°C(1h)	WR, $e=0.2$	PDA, 400°C(1h)
6	WR (1.0)+ IA + WR(0.2)	WR, $e=1.0$	IA, 400°C(1h)	WR, $e=0.2$	PDA, 400°C(1h)
7	WR (1.2)*	WR, $e=1.2$	...	...	PDA, 400°C(1h)

\*The CR(1.0) and WR(1.2) routes were selectively used for verification.

The electron microscopy study was carried out using “JEOL-2100” and “Tesla BS-540” microscopes. Thin foils were cut by the electro-erosion method and then thinned by mechanical and electrolytic polishing.

The texture analysis was carried out using a “PANalytical X’pert Pro” X-ray diffractometer with  $\text{CuK}\alpha$ -radiation. Samples were cut along the rolling direction and the surface layer was etched. The scanning for  $(110)_{\text{B2}}$ ,  $(200)_{\text{B2}}$ ,  $(211)_{\text{B2}}$  pole figures was carried out at  $A_f+10^\circ\text{C}$  temperature with  $\Delta\alpha = \Delta\beta = 5^\circ$  azimuthal steps and with the radial angle of inclination  $\alpha_{\text{max}}$  varying from 0 to  $75^\circ$ . Both direct and inverse pole figure methods were used. Furthermore, the orientation distribution functions (ODF) were built in accordance with [26]. Since the

width of each individual sample was about 1.7 mm, a side-by-side stack of 4-5 parallel samples was used for each measurement.

To assess the degree of the processing-induced material damage (edge microcracks caused by rolling), the metallographic analysis of the mechanically polished samples was performed using a “Union” optical microscope. For each TMT route, 30-40 mm length samples were prepared and analyzed with the number of counted cracks varying from 300 to 520. The average crack size (depth) and concentration were measured.

The stress-free strain recovery testing was carried out using an “Enduratec ELF 3200 (Bose)” testing machine. The 50 mm-long samples were first strained up to  $\varepsilon_t = 9\%$  (Figure 2.1a: O-A), then unloaded to allow elastic springback (A-B). As a result, an initial (induced) strain of about  $\varepsilon_i = 6-7\%$  was set for all the samples. After the state B was reached, the sample was heated up to  $100^\circ\text{C}$  (above  $A_f$ , the austenite formation finish temperature) to allow strain recovery (B-C). Recovery ( $\varepsilon_r$ ) and residual (permanent) ( $\varepsilon_p$ ) strains were then measured. After the sample was free air-cooled to room temperature (RT), (C-E), it changed its shape again due to the two-way shape memory effect (TWSM), and the corresponding TWSM strain ( $\varepsilon_{TW}$ ) was measured. The test was repeated up to sample failure. Four samples were used for this test. For the first 500 testing cycles, a degradation rate of recovery strain generation ( $\Delta\varepsilon_r^{500}$ ) was calculated:

$$\Delta\varepsilon_r^{500} = \frac{(\varepsilon_i - \varepsilon_{500})}{\varepsilon_i} \cdot 100\% \quad (2.1)$$

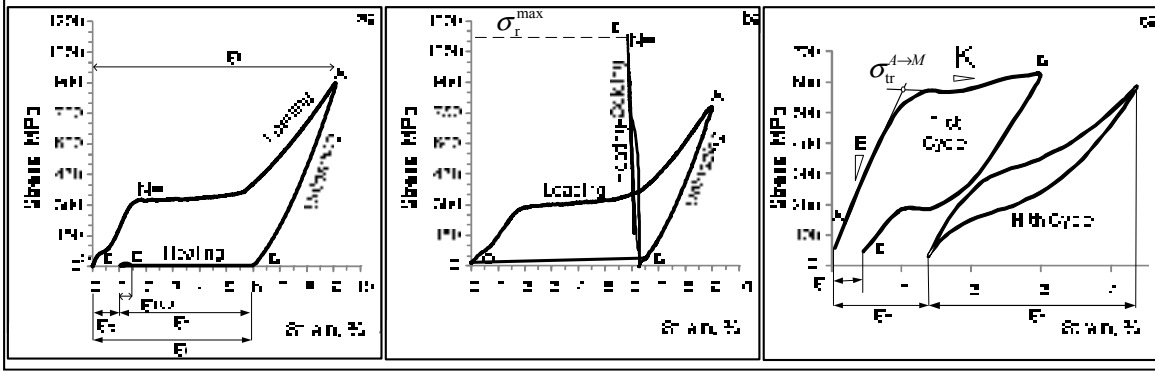


Figure 2.1 Stress-strain plots (Ti-50.26 at%Ni alloy after  $\epsilon=1.2CR+PDA$  400°C, 1h): (a) stress-free recovery testing and (b) constrained recovery testing; both for  $N=1$  cycle; and (c) superelastic testing

The recovery stress  $\sigma_r$  generation-relaxation (constrained recovery) testing was carried out using the custom-made testing bench [10]. A sample was strained up to  $\epsilon_t = 9\%$  (Figure 2.1b: O-A), then released to allow the elastic springback (A-B), as in the previous test. The initial (induced) strain was thus set at  $\epsilon_i = 6-7\%$ . Afterwards, the sample was kept fixed and then heated from room temperature to 200°C to allow an almost complete reverse martensitic transformation (B-C) and recovery stress generation,  $\sigma_r$  (B-C), and finally air-cooled to room temperature. The test was repeated until sample failure. Four samples were used for this test. For the first 500 cycles, a degradation rate of the recovery stress generation ( $\Delta\sigma_r^{500}$ ) was calculated:

$$\Delta\sigma_r^{500} = \frac{(\sigma_i - \sigma_{500})}{\sigma_i} \cdot 100 \% \quad (2.2)$$

Finally, the superelastic testing was carried out using “MTS’ MiniBionix 858” machine and thermal chamber. The 70 mm-long samples were heated up to  $A_f + 10^\circ\text{C}$  temperature, then strained up to  $\epsilon_f = 3\%$  (Figure 2.1c: A-B), then unloaded (B-C). The test was repeated until sample failure. The following superelastic loop features were determined:  $\sigma_{tr}$  – transformation yield stress,  $\epsilon_r$  – superelastic recovery strain,  $\epsilon_f$  – residual strain in one SE-

cycle, and  $\varepsilon_d$  – accumulated residual strain to failure. Three samples were used for this testing.

For the first 1000 superelastic cycles, the evolution of the transformation yield stress ( $\Delta\sigma_{tr}^{1000}$ ) was calculated:

$$\Delta\sigma_{tr}^{1000} = \frac{(\sigma_{tr}^I - \sigma_{tr}^{1000})}{\sigma_{tr}^I} \cdot 100\% \quad (2.3)$$

Equations (2.1)-(2.3) were used to assess the stability of the alloy's functional properties in conformity with the approach adopted in [12]. The confidence error for all the measurements was calculated<sup>1</sup>:

$$\delta_{\bar{X}} = \frac{t_{0.95,(n-1)}}{\sqrt{n}} \cdot \left( \frac{\sum_{i=1}^n (\bar{X} - X_i)^2}{n-1} \right)^{\frac{1}{2}} \quad (2.4)$$

where  $X_i$  is the measured value of  $X$  in the  $i$ -th cycle,  $\bar{X}$  is the mean value,  $n$  is the number of measurements, and  $t_{0.95,(n-1)}$  is the Student's confidence coefficient for  $P=0.95$  probability, and  $\kappa=n-1$  degrees of freedom.

## 2.5 Experimental results

### Electron microscopy study

---

<sup>1</sup> D. Montgomery, Applied statistics and probability for engineers. 2006

As electron microscopy study shows, different nanostructures are formed after each of the processing routes. Particular features of these nanostructures are discussed below.

*Route CR(1.2)*, Figure 2.2a. According to the bright- and dark-field images, mainly nanocrystalline (NC) structure with grain size in the 15-70 nm range is observed. Dark-field images indicate the presence of a relatively small amount (about 10-15%) of nanosubgrained (NS) structure, which is indentified as sparse “shining” nanosized (up to 150 nm) agglomerations containing several closely-oriented (and therefore simultaneously shining) subgrains. Electron microdiffraction patterns contain dotted rings with a rather uniform orbital distribution of point-wise reflections, which is typical for NC structure. In general, this structure is similar to that observed in the same alloy after CR ( $e=1.5$ ) + PDA (400°C, 1h) [9].

*Route CR(0.75)*, Figure 2.2b, c. With this processing, which also serves as a reference treatment, a mixed nanostructure is present after PDA. This structure includes alternating NS and NC regions (Figure 2.2b and c, respectively) in approximately equal quantities. Nanosized subgrains contain high dislocation density. The both observations are consistent with [9]. The microdiffraction pattern consists of fragmented arcs with higher concentrations of point-wise reflections (NS) and of a relatively small amount of individual reflections between them (NC) (Figure 2.2b).

*Route CR(1)+IA+CR(0.2)* (not shown in Figure 2.2). In this case, mainly NC structure is observed, which is similar to CR(1.2). However, grain size after this route is 1.5-2 times larger than after the CR(1.2) route.

*Route WR(1)+IA+WR(0.2)*, Figure 2.2d. According to the bright- and dark-field images, NS structure is mainly present, but a notable quantity of NC structure is still observable. The grains, subgrains and subgrain groups (polygonized regions) are larger, than in the case of CR(1.2). High dislocation density is observed inside the subgrains. The diffraction pattern features confirm this character of the structure: arc-like concentrations of point-wise reflections are observed, which is typical for a polygonized dislocation substructure [1, 9].

*Route CR(1)+IA+WR(0.2)*, Figure 2.2e, f. This TMT route occupies an intermediate position between  $CR(1)+IA+CR(0.2)$  and  $WR(1)+IA+WR(0.2)$ , but is still closer to the first. This processing produces mainly NC structure, but NS structure is also present (conglomerates of subgrains sized under 200 nm).

*Route WR(1.2)* (not shown in Figure 2.2). The structure is similar to that after  $WR(1)+IA+WR(0.2)$ .

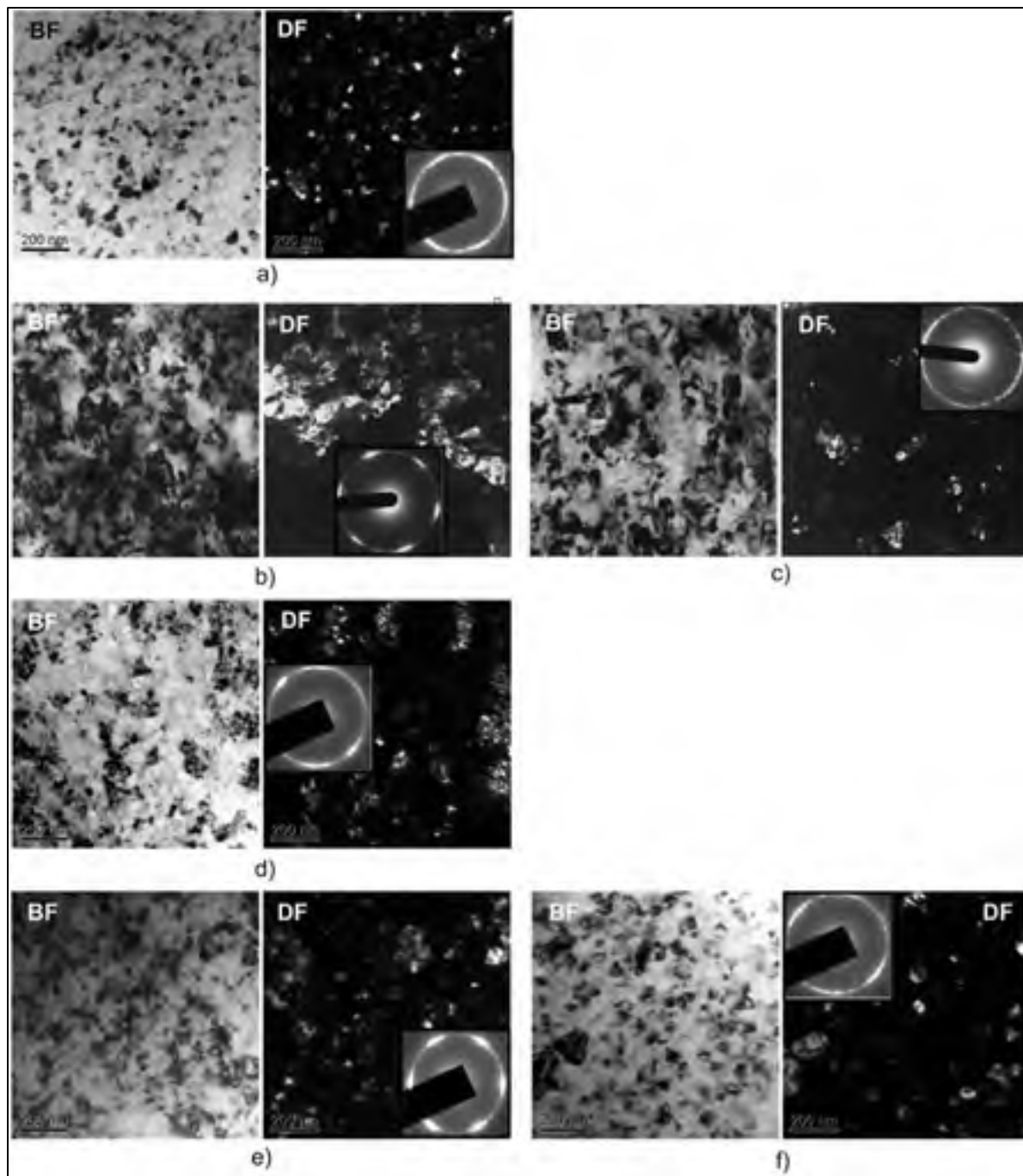


Figure 2.2 Structure of Ti-50.26%Ni alloy after selected TMT routes: a) CR(1.2); b,c) CR(0.75); d) WR(1)+IA+WR(0.2); and e,f) CR(1)+IA+WR(0.2). Left to right: bright-field image, dark-field image, electron diffraction pattern



## Texture analysis

Orientation distribution function (ODF) was calculated on the basis of three pole figures: (110), (200) and (211) using standard "X'pert texture" software. In Figure 2.3, ODF sections corresponding to the  $\phi_2=0^\circ$  or  $90^\circ$  Euler angles are shown for six processing routes: after simple CR and combined CR, WR and IA, each with final PDA at  $400^\circ\text{C}$ , 1h. In all the cases, the texture components  $\{hkl\}\langle uvw \rangle$  were qualitatively analyzed in terms of their orientation densities using classical relationships between the Euler angle coordinates  $\{\phi_1, \Phi, \phi_2\}$  and  $\{hkl\}\langle uvw \rangle$  [25].

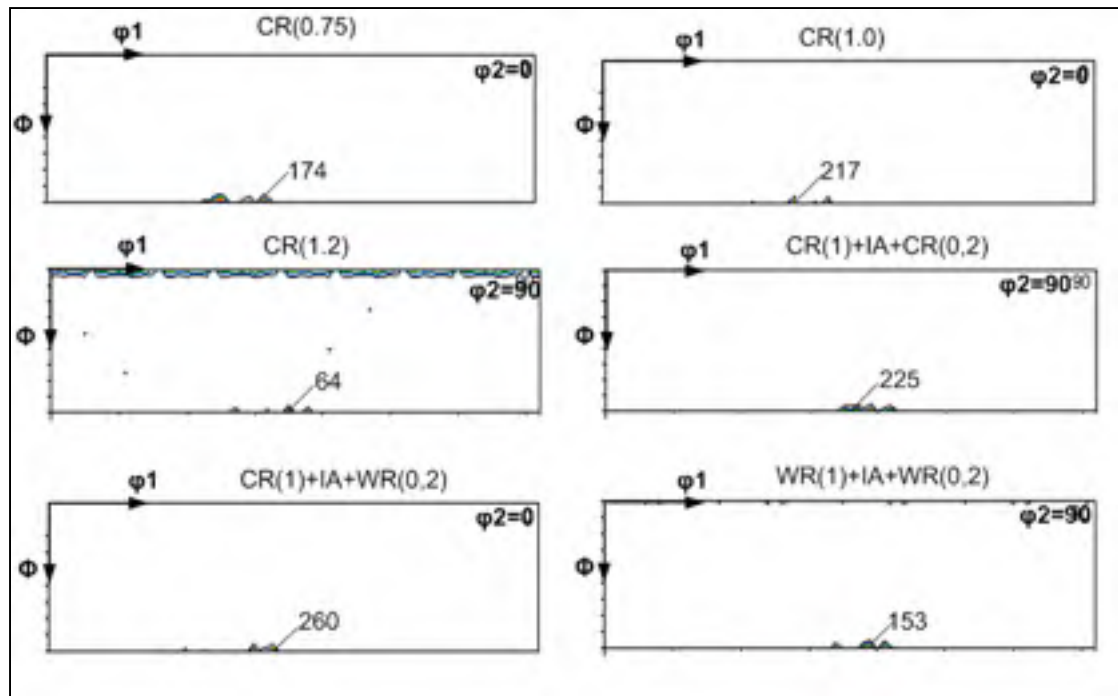


Figure 2.3 ODF section at  $\phi_2=0$  and  $90^\circ$  for six processing routes

In the ODF is taken at  $\phi_2=0^\circ$  (or  $90^\circ$ ) and  $\Phi=90^\circ$ , the main texture component of B2-austenite corresponds exactly to the  $\{100\}$  plane with small deviations from the  $\langle 011 \rangle$  direction. For a more detailed analysis, the inverse pole figures (IPF) are shown in Figure 2.4. It follows from the IPF analysis that the  $\langle 011 \rangle$  B2 direction is very close to the IPF

maximum. Thus, the main austenite texture component in Ti-50.26 at.%Ni alloy after all the processing routes is  $\{100\}\langle 011\rangle$ .

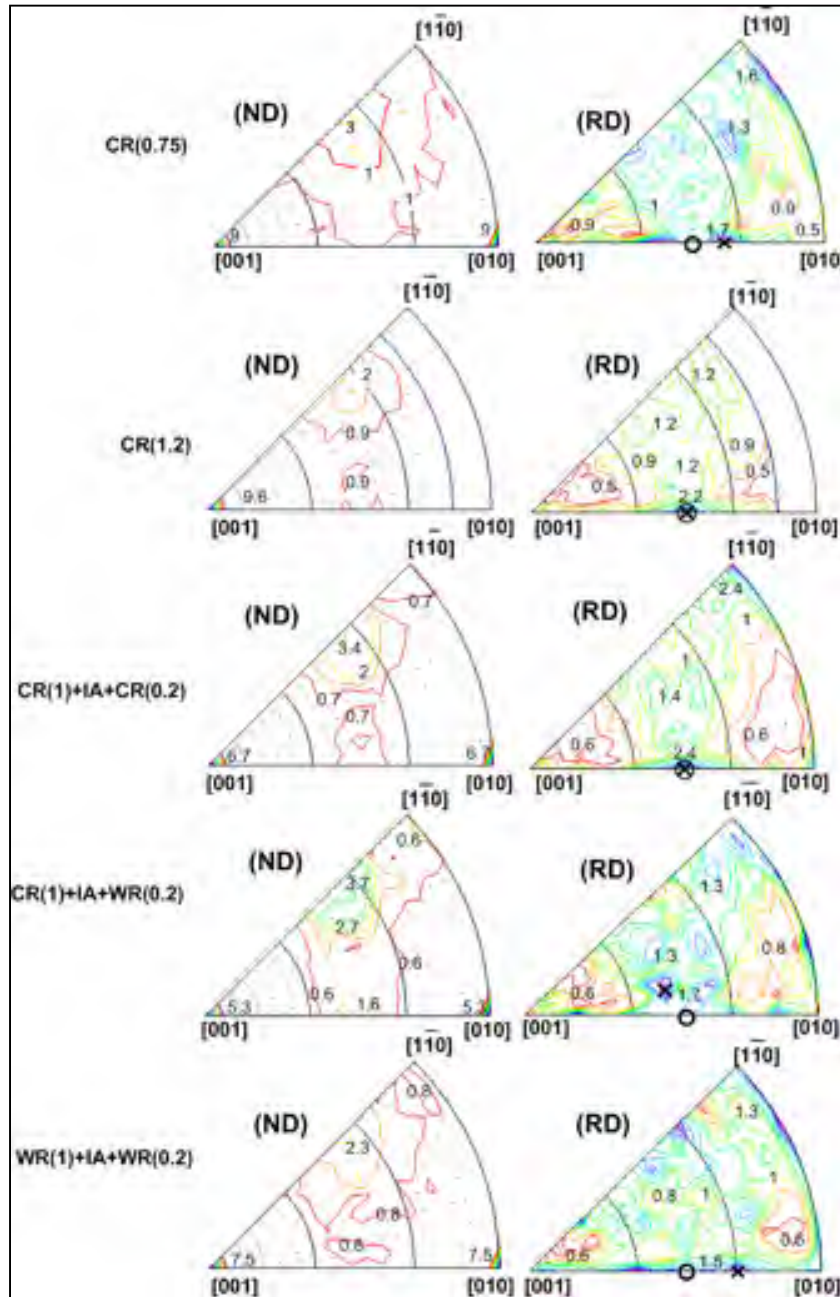


Figure 2.4 Inverse pole figures corresponding to the normal direction (ND) and rolling direction (RD) for all the processing routes. x –  $[uvw]$  pole, o –  $[011]B2$  pole

In Figure 2.5, the orientation density of the main texture component  $\{100\}\langle 011 \rangle$  is shown for each processing route. It follows from Figure 2.5 that the orientation density of the  $\{100\}\langle 011 \rangle$ B2 component increases when CR strain increases from  $e=0.75$  to  $e=1$ , while when CR strain increases from  $e=1$  to  $e=1.2$ , it drastically decreases. When IA and WR technological steps are introduced in the processing, CR(1)+IA+CR(0.2) and CR(1)+IA+WR(0.2), while keeping the same accumulated strain of  $e=1.2$ , a significant enhancement of the orientation density is observed as compared to the reference CR(1.2) processing. Finally, when all the deformation is conducted at a higher temperature, WR(1)+IA+WR(0.2), the texture sharpness degrades again.

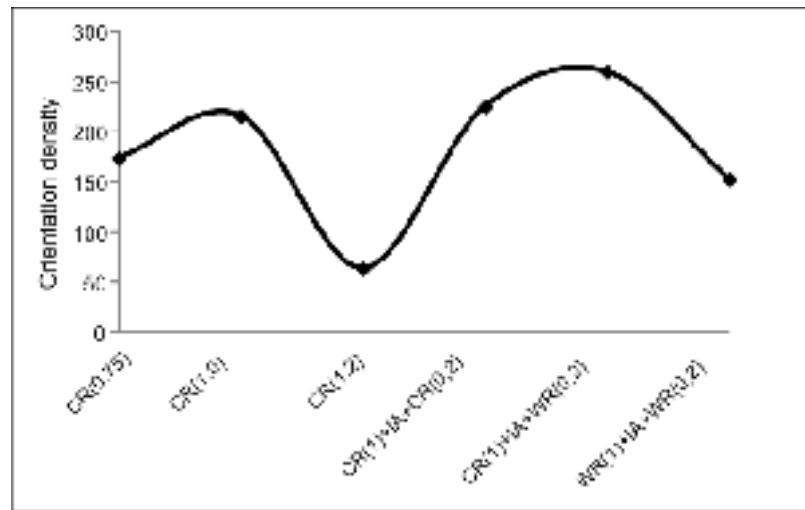


Figure 2.5 Orientation density of  $\{100\}\langle 110 \rangle$ B2 texture component as a result of different TMT routes applied to Ti-50.26at.%Ni alloy

### **Metallographic analysis of processing-related material damage (edge microcracks)**

The metallographic analysis of the edge microcracks' size (depth) and concentration after following TMT routes was completed: CR(0.75), CR(1.0), CR(1.2), CR(1)+IA+CR(0.2), CR(1)+IA+WR(0.2), WR(1)+IA+WR(0.2), and WR(1.2). The results of this analysis are collected in Table 2.2. After CR(0.75), the average surface crack size is  $21 \pm 2 \mu\text{m}$  and the crack concentration is  $10 \pm 1$  cracks/mm. The crack size (concentration) increases to  $31 \pm 3 \mu\text{m}$

( $13 \pm 1$  cracks/mm) when CR intensity reaches  $e=1.0$ , and to  $32 \pm 4$   $\mu\text{m}$  ( $13 \pm 1$  cracks/mm) when it reaches  $e=1.2$ . When intermediate annealing is included in the TMT sequence, CR(1)+IA+CR(0.2), the crack size (concentration) decreases to  $25 \pm 3$   $\mu\text{m}$  ( $12 \pm 2$  cracks/mm). Further increase in the heat energy input leads to an even greater reduction of the processing-induced damage: it becomes  $22 \pm 2$   $\mu\text{m}$  ( $10 \pm 1$  cracks/mm) and  $21 \pm 3$   $\mu\text{m}$  ( $10 \pm 2$  cracks/mm) after respectively CR(1)+IA+WR(0.2) and WR(1)+IA+WR(0.2), finally reaching  $18 \pm 2$   $\mu\text{m}$  ( $10 \pm 2$  cracks/mm), after completely warm rolling, WR(1.2).

Table 2.2 Crack parameters after different TMT routes

Route	Identification	Crack size (depth), $\mu\text{m}$	Crack concentration, cracks/mm
1	CR(0.75)	$21 \pm 2$	$10 \pm 1$
2	CR(1.0)	$31 \pm 3$	$13 \pm 1$
3	CR(1.2)	$32 \pm 4$	$13 \pm 1$
4	CR(1)+IA+CR(0.2)	$25 \pm 3$	$12 \pm 2$
5	CR(1)+IA+WR(0.2)	$22 \pm 2$	$10 \pm 1$
6	WR(1)+IA+WR(0.2)	$21 \pm 3$	$10 \pm 2$
7	WR(1.2)	$18 \pm 2$	$10 \pm 2$

### Multi-cycle thermomechanical and superelastic testing

#### *Stress-free recovery testing and constrained recovery testing*

Stress-free recovery. The results of the multi-cycle stress-free recovery testing after selected TMT routes (1, 3, 4, 5 and 6) are collected in Table 2.3. It can be noted that the number of cycles to failure decreases as the initial CR intensity increases, and the fatigue life becomes the shortest after the CR(1.2) reference route. On the contrary, the fatigue life increases significantly when WR and IA are included in the TMT sequence. The highest fatigue life is

observed after two routes with a total accumulated strain of  $e=1.2$ , CR(1)+IA+WR(0.2) and WR(1)+IA+WR(0.2) being comparable with that after CR(0.75).

Table 2.3 Results of the stress-free recovery testing: recovery strain in 1<sup>st</sup> cycle ( $\Delta\epsilon_r$ ), recovery strain degradation rate for the first 500 cycles ( $\Delta\epsilon_r^{500}$ ) and number of cycles to failure ( $N_f$ )

Route	Identification	$\Delta\epsilon_r$ , (%)	$\Delta\epsilon_r^{500}$ , (%)	$N_f$
1	CR(0.75)	5.6±0.3	11.2±2.8	7770±550
3	CR(1.2)	5.3±0.1	2.4±1.3	4020±1650
4	CR(1)+IA+CR(0.2)	5.6±0.1	6.2±1.4	5040±600
5	CR(1)+IA+WR(0.2)	5.6±0.1	7.3±0.8	6550±1310
6	WR(1)+IA+WR(0.2)	5.5±0.1	6.0±1.4	6300±1200

Despite the recovery strain in the 1<sup>st</sup> cycle ( $\Delta\epsilon_r$ ) remaining approximately the same (about 5.5% regardless of the TMT sequence), the functional stability is the lowest after CR(0.75) route. The recovery strain degradation rate ( $\Delta\epsilon_r^{500}$ ) in this last case is almost twice as high as it is after other processing routes.

Constrained recovery testing. The results of the multiple-cycle constrained recovery stress generation-relaxation after selected TMT routes (1, 3, 4, 5 and 6) are shown in Table 2.4. It can be observed that fatigue life after CR( $e=0.75$ ) is the longest (3870 cycles) among all the processing routes, whereas it is the shortest (780 cycles) after CR( $e=1.2$ ). TMT routes including WR and IA result in an intermediate length of cycling life.

The greatest recovery stress in the first cycle  $\Delta\sigma_r$  (1170 MPa) is measured after the reference CR(1.2) route. This is comparable with all the processing routes that have a total deformation of  $e=1.2$ , except only WR(1)+IA+WR(0.2). After this last route, the recovery stress decreases significantly (940 MPa) to become comparable with that after CR (0.75). The lower recovery

stress generation capability observed with these two cases is accompanied by the lowest functional stability during multi-cycle activation ( $\Delta\sigma_{tr}^{500}$ ).

Table 2.4 Results of the constrained recovery testing: recovery stress generated in 1<sup>st</sup> cycle ( $\Delta\sigma_i$ ) recovery stress degradation rate for the first 500 cycles ( $\Delta\sigma_{tr}^{500}$ ), and the number of cycles to failure ( $N_f$ )

Route	Identification	$\Delta\sigma_i$ , (MPa)	$\Delta\sigma_{tr}^{500}$ , (%)	$N_f$
1	CR(0.75)	940±40	25±1	3870±700
3	CR(1.2)	1170±50	17±2	780±150
4	CR(1.0)+IA+CR(0.2)	1110±40	20±3	1370±340
5	CR(1.0)+IA+WR(0.2)	1040±30	22±2	1820±290
6	WR(1.0)+IA+WR(0.2)	940±30	24±1	2030±200

### Superelastic testing

Results of the superelastic testing after selected TMT routes (1, 3, 4, 5 and 6) are shown in Table 2.5. A more detailed representation of the superelastic behavior after all of the processing routes is made using loading–unloading diagrams of Figure 2.6. Furthermore, the transformation yield stress in the first cycle ( $\sigma_{tr}^1$ ) and its evolution rate ( $\Delta\sigma_{tr}^{1000}$ ) are plotted for all the processing routes in Figure 2.7.

Table 2.5 Results of superelastic testing: transformation yield stress in 1<sup>st</sup> cycle ( $\Delta\sigma_{tr}^I$ ); transformation stress evolution rate and irrecoverable strain accumulated during the first 1000 cycles ( $\Delta\sigma_{tr}^{1000}$  and  $\varepsilon_{1000}$ ), and number of cycles to failure ( $N_f$ )

No.	Identification	$\Delta\sigma_{tr}^I$ , (MPa)	$\Delta\sigma_{tr}^{1000}$ , (%)	$\varepsilon_{1000}$ , %	$N_f$
1	CR(0.75)	480±20	54±2	2.5±0.1	2440±260
3	CR(1.2)	580±30	41±3	0.6±0.04	1680±50
4	CR(1)+IA+CR(0.2)	550±40	45±2	1±0.1	1710±190
5	CR(1)+IA+WR(0.2)	520±50	53±4	2.2±0.5	2940±380
6	WR(1)+IA+WR(0.2)	560±30	53±2	1.4±0.19	1360±80

It can be noted that the maximum numbers of cycles to failure are concurrently observed after CR(0.75) and CR(1)+IA+WR(0.2). In both cases however, a pronounced amount of irrecoverable strain appears after 1000 actuation cycles: 2.5% after CR(0.75) and 2.2% after CR(1)+IA+WR(0.2).

The number of cycles to failure and the accumulated strain are significantly lower after CR(1.2) and CR(1)+IA+CR(0.2). The highest functional stability belongs to the CR(1.2) route, with the smallest  $\varepsilon_{1000}$ =0.6% (Figure 2.7). The specimens subjected to WR(1)+IA+WR(0.2) processing show the shortest fatigue life ( $N_f$ =1360) and intermediate level of accumulated strain after 1000 cycle of actuation ( $\varepsilon_{1000}$ =1.4%).

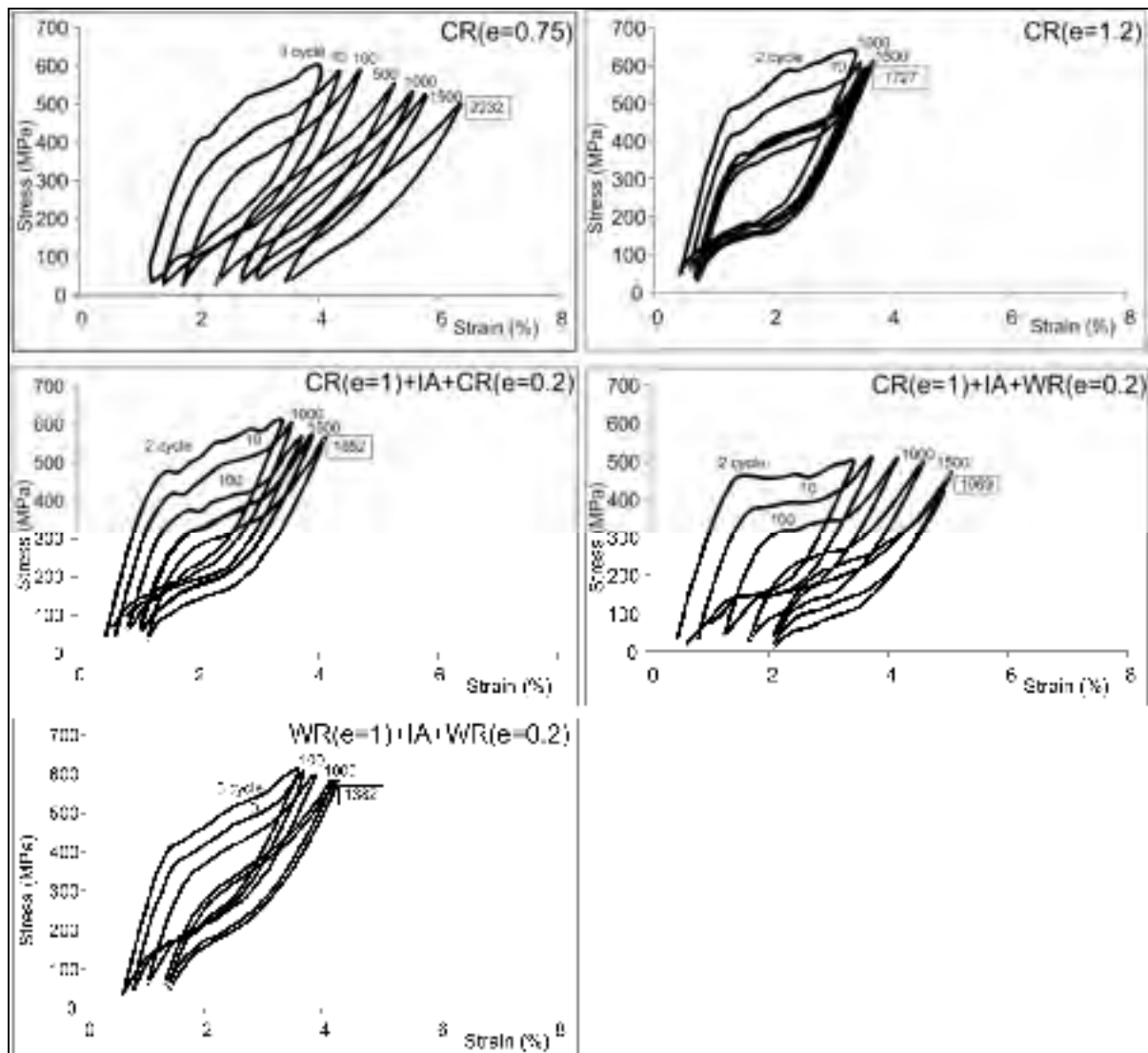


Figure 2.6 Loading-unloading diagrams during superelastic testing after different TMT routes



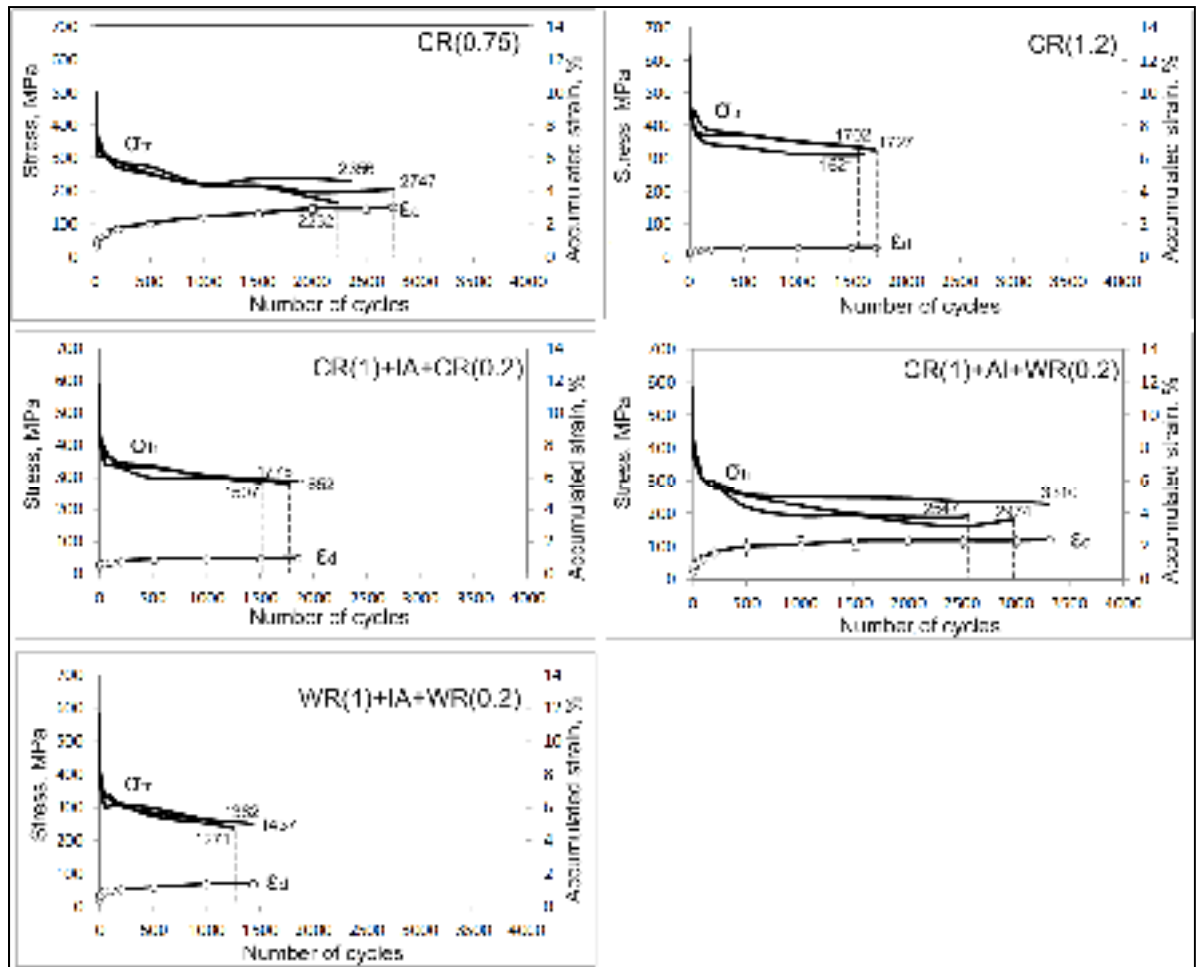


Figure 2.7 Evolution of transformation yield stress and accumulated strain (for the longest test for each TMT route) during superelastic testing

In the first cycle of testing, the transformation yield stress  $\Delta\sigma'_{tr}$  is similar for all the processing routes within the error limits. During superelastic cycling,  $\Delta\sigma'_{tr}$  decreases. The greatest stability of  $\Delta\sigma'_{tr}$  is observed after CR(1.2) with somewhat reduced fatigue life. Again, the longest fatigue life is observed concurrently after CR(1)+IA+WR(0.2) and CR(0.75), but at the expense of the lower functional stability. Finally, WR(1)+IA+WR(0.2) combines the lowest fatigue life with an intermediate functional stability.

## 2.6 Discussion

The electron microscopy study identified the following specificity of the B2-phase structure formation in Ti-50.26%Ni alloy subjected to different TMTs (in all the cases, the observations were made after final PDA): (1) The greater the CR contribution, the larger the fraction of NC structure compared to the NS structure, and the lower the average dislocation density; (2) When the WR contribution increases, the NS structure becomes dominant, and the larger grains, subgrains and polyzonized regions are observed; and (3) Including intermediate annealing (400°C, 1h) in the technological sequence results in overall structure coarsening, i.e., in an increase of the NC grain size and NS subgrain size. These regularities can be explained as follows. On one hand, the deformation-induced amorphization promotes NC structure formation (crystallization of nanosize grains during PDA) [8]. On the other hand, the fraction of the amorphized alloy is greater after CR than it is after WR [8]. Consequently, after CR+PDA, the dominant structure is NC (a small amount of NS structure is still observed), whereas after WR+PDA, the dominant structure is NS, because in this case, polygonization with nanosubgrain formation will dominate nanograin growth and nanocrystallization [1]. An intermediate annealing leads to a natural increase in grain and subgrain size and to a decrease in lattice defect concentration, since  $d \sim \rho^{-1/2}$  ( $d$  is the grain/subgrain size and  $\rho$  is the lattice defect concentration [27, 28]).

The observed variations in the orientation density of the  $\{100\}\langle 110 \rangle_{B2}$  texture component after different TMTs of Ti-50.26 at.%Ni alloy can be explained as follows. After CR(1.2), the quantity of amorphous phase formed during cold rolling is greater than after CR(0.75) and CR(1.0) [1, 2, 9]. Post-deformation annealing results in nanocrystallization of the amorphous structure with random grain orientation. As a result, the orientation density of the  $\{100\}\langle 110 \rangle_{B2}$  texture in the material processed by the CR(1.2)+PDA(400°C, 1h) route is lower than after lower intensity CR. In the case of CR(1)+IA+CR(0.2), the austenite texture again becomes sharper. It is believed that the moderate CR(0.2) of the nanostructured alloy resulted from the first two steps, CR(1)+IA, favors austenite lattice orientation in the  $\langle 110 \rangle$  direction. When the last  $\epsilon=0.2$  deformation step is performed at a higher temperature,

CR(1)+IA+WR(0.2), the orientation capacity of the final rolling procedure is further enhanced, and this TMT route results in the sharpest  $\{100\}\langle 110 \rangle_{B2}$  texture. Finally, when all the deformation is conducted at higher temperature, WR(1)+IA+WR(0.2), the quantity of NC structure decreases, which results in a certain decrease of the texture sharpness as compared to CR(1)+IA+WR(0.2).

The evolution of the processing-induced damage (microcrack size and concentration) as a function of TMT conditions correlates well with the results obtained from fatigue tests (Figure 2.8 combines in a graphic form the results presented in Tables 2.2-2.5). For a total strain of  $\epsilon=1.2$ , the CR(1)+IA+WR(0.2) route results in a relatively smaller level of processing-induced damage and in relatively higher fatigue life under all the testing conditions. This processing route also provides a decent functional stability as compared to the most stable, but the most damaged CR(1.2)-processed samples. Therefore, the level of processing-induced damage (edge microcracks) definitely works as the most significant regulator of the functional fatigue life.

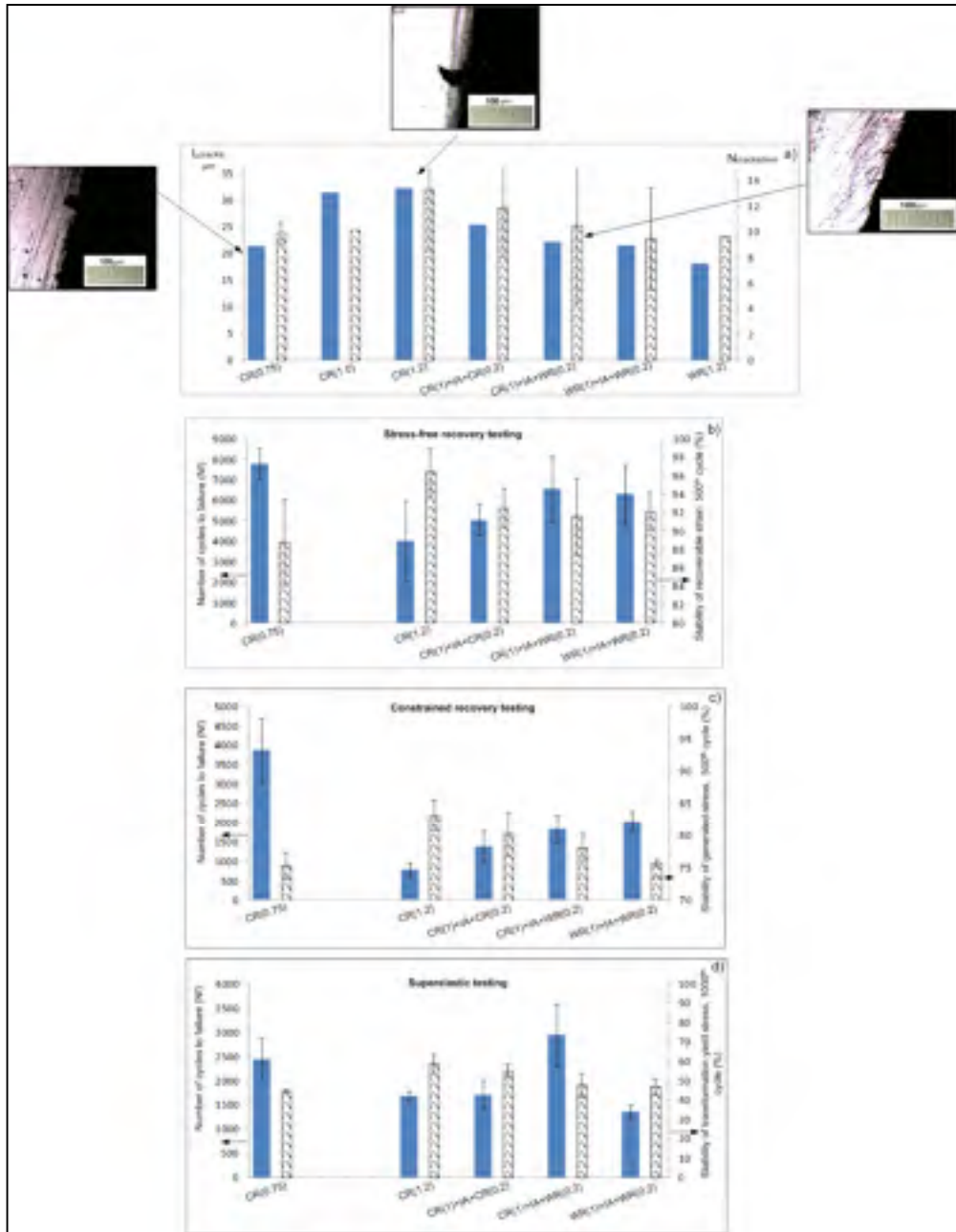


Figure 2.8 (a) Processing-induced damage (crack size, plain bars, and concentration, hatched bars) after different processing routes, and fatigue functional properties obtained by (b) stress-free recovery, (c) constraint recovery stress generation, and (d) superelastic testing (number of cycles to failure, plain bars and stability, hatched bars)

To summarize, fatigue performances of Ti-50.26 at.%Ni alloy are improved in the two following cases: when CR strain decreases from  $\epsilon=1.2$  to 0.75, or when WR and IA are

introduced in the TMT schedule for the same level of total plastic strain of  $e=1.2$ . In both cases, a decrease of mechanical damage (cracking) and formation of a mixed NSS+NCS microstructure are observed. Even though CR(0.75) and CR(1)+IA+WR(0.2) are comparable in terms of their static and fatigue functional properties, the overall functional stability for CR(0.75)–processed alloy remains significantly lower than that for CR(1)+IA+WR(0.2).

Consequently, CR(0.75) can be recommended as the best-suited processing route for an application requiring a maximum number of operation cycles and when functional stability is not a major issue. However, if the goal is to obtain the best combination of fatigue life and stability characteristics, the CR(1)+IA+WR(0.2) route appears to be preferable. Finally, when the highest functional stability is required for a limited number of working cycles, CR(1.2) is still an appropriate choice.

Note that the given results were obtained using flat rolling deformation technology. If the same intensity of low-temperature plastic deformation could be achieved by other technological means with a higher than rolling level of hydrostatic stresses, such as extrusion or forging, it would become possible to further reduce the processing-induced damage while creating textured NSS+NCS microstructures. In those circumstances, the fatigue life and functional stability of Ti-Ni SMA could simultaneously be improved.

## 2.7 Conclusions

The microstructure and functional properties of Ti-50.26%Ni SMA were studied after the following TMT routes: CR( $e=0.75$ ), CR( $e=1.02$ ), CR( $e=1.2$ ), CR( $e=1$ )+IA+CR( $e=0.2$ ), CR( $e=1$ )+IA+WR( $e=0.2$ ), WR( $e=1$ )+IA+WR( $e=0.2$ ), WR( $e=1.2$ ), with final post-deformation annealing at 400°C, 1h. The following results were obtained.

1. The greater the heat energy input during processing (WR/IA), the greater the quantity of nanosubgrain substructure at the expense of nanocrystalline structure, and the larger the

size of grain, subgrain and polygonized areas, and the lower the processing-induced damage.

2. The main texture component of austenite after all the processing routes corresponds to  $\{100\}\langle 110 \rangle_{B2}$ , and after CR( $\epsilon=1$ )+IA+WR( $\epsilon=0.2$ ) the austenite texture sharpness reaches its maximum.
3. The functional fatigue testing showed that the fatigue performances of Ti-50.26 at.%Ni alloy are significantly improved in two cases: either when CR strain is decreased from  $\epsilon=1.2$  to 0.75 or when WR/IA are introduced in the TMT schedule, for the same level of total plastic strain of  $\epsilon=1.2$ .
4. The reasons for improvement of the Ti-50.26 at.%Ni alloy fatigue performances can be summarized as follows (in descending order of importance): introduction of WR and IA promotes formation of a mixed NS+NC material microstructure, reduces processing-induced damage and promotes development of the favorable B2-austenite texture.

## 2.8 Acknowledgments

The authors are grateful to the Natural Sciences and Engineering Research Council of Canada and to the Ministry of Education and Science of the Russian Federation for financial support of the present work.

## 2.9 References

- [1] V. Brailovski, S.D. Prokoshkin, I.Y. Khmelevskaya, K.E. Inaekyan, V. Demers, S.V. Dobatkin, E.V. Tatyannin, Mater. Trans. 47 (3) (2006) 795-804.
- [2] S.D. Prokoshkin, V. Brailovski, K.E. Inaekyan, V. Demers, I.Y. Khmelevskaya, S.V. Dobatkin, E.V. Tatyannin, Mater. Sci. Eng. A 481-482 (2008) 114-118.

- [3] V. Demers, V. Brailovski, S.D. Prokoshkin, K.E. Inaekyan, Mater. Sci. Eng. A 513-514 (2009) 185-196.
- [4] V.B. Fedorov, V.G. Kurdyumov, D.K. Khakimova, E.V. Tat'yanin, Dokl. Akad. Nauk SSSR 269 (4) (1983) 885-888.
- [5] E.V. Tat'yanin, V.G. Kurdyumov, V.B. Fedorov, Fiz. Met. Metalloved 62 (1) (1986) 133-137.
- [6] H. Nakayama, K. Tsuchiya, M. Umemoto, Scr. Mater. 44 (8-9) (2001) 1781-1785.
- [7] A.V. Sergueeva, C. Song, R.Z. Valiev, A.K. Mukherjee, Mater. Sci. Eng. A 339 (2003) 159-165.
- [8] S.D. Prokoshkin, I.Y. Khmelevskaya, S.V. Dobatkin, I.B. Trubitsyna, E.V. Tatyannin, V.V. Stolyarov, E.A. Prokofiev, Acta Materialia, 53 (2005) 2703-2714.
- [9] S.D. Prokoshkin, V. Brailovski, A.V. Korotitskiy, K.E. Inaekyan, A.M. Glezer, Phys. Met. Metallogr. 110 (3) (2010) 289-303.
- [10] V. Brailovski, S. Prokoshkin, K. Inaekyan, V. Demers, J. Alloy Compd. 509 (5) (2011) 2066-2075.
- [11] Y. Facchinello, V. Brailovski, T. Georges, S.D. Prokoshkin, Advanced Materials, THERMEC'2011, Quebec City, QC, Canada, 2012 615-620.
- [12] Y. Facchinello, V. Brailovski, Sergey D. Prokoshkin, K. Inakeyan, S. M. Dubinskiy.. J. Mater. Proc. Technol. 212 (11) (2012) 2299-2304.

- [13] A.S. Paula, K.K. Mahesh, N. Schell, F.M.B. Fernandes, *Mater. Sci. Forum* 636-637 (2010) 618-623.
- [14] S.S. Gorelik, S.V. Dobatkin, L.M. Kaputkina, MISIS Publ., Moscow, 2005, pp. 432.
- [15] J.H. Mulder, P.E. Thoma, J. Beyer, *Z. Metallk.*, 84 (7) (1993) 501-508.
- [16] A.S. Paula, K.K. Mahesh, F.M.B. Fernandes, in: 8-th European Symposium of Martensitic Transformation, 06025 (2009) <http://dx.doi.org/10.1051/esomat/200906025>.
- [17] V.I. Zel'dovich, G.A. Sobyana, O.S. Rinkevich, V.M. Gundyrev, *Tech. Phys.* 41 (11) (1996) 1158-1162.
- [18] H. Inoue, N. Miwa, N. Inakazu, *Acta Mater.* 44 (1996) 4825-4834.
- [19] L. Zhao, P.F. Willemse, J.H. Mulder, J. Beyer, W. Wei, *Scr. Materialia*, 39 (9) (1998) 1317-1323.
- [20] A. Khantachawana, S. Miyazaki, H. Iwai, M. Kohl, *Mater. Sci. Eng. A* 273 (1999) 763-768.
- [21] W.Q. Yuan, S.Q. Yang, *J. Mater. Sci. Lett.* 21 (2002) 443-445.
- [22] Y. Liu, Z.L. Xie, J. Van Humbeeck, L. Delaey, *Acta Mater.* 47 (2) (1999) 645-660.
- [23] V.M. Gundyrev, V.I. Zel'dovich, *Phys. Met. Metallogr.* 96 (1) (2003) 86-91.
- [24] W.Q. Yuan, S. Yi, *Mater. Sci. Eng. A* 271 (1999) 439-448.



- [25] H.J. Bunge, Texture analysis in materials science mathematical methods, Butterworths, London, 1982.
- [26] Y.S. Umanskiy, Y.A. Skakov, A.N. Ivanov, L.N. Rastorguev, Crystallography, X-ray diffraction and electron microscopy, Metallurgy Publ, Moscow, 1983.
- [27] M.L. Bernshtein, S.V. Dobatkin, L.M. Kaputkina, S.D. Prokoshkin, Diagrams of hot deformation structure and properties of steels, Metallurgy Publ, Moscow, 1989.
- [28] D.L. Holt, Jour. Appl. Phys., 41 (8) (1970) 3197-3201.



## CHAPTER 3

### ARTICLE #2

#### **ROLE OF THE STRUCTURE AND TEXTURE IN THE REALIZATION OF THE RECOVERY STRAIN RESOURCE OF THE NANOSTRUCTURED Ti- 50.26 at.%Ni ALLOY**

A.Yu. Kreitchberg<sup>a,b</sup>, S.D. Prokoshkin<sup>a</sup>, V. Brailovski<sup>b</sup> and A.V. Korotitskiy<sup>a</sup>

<sup>a</sup> MISIS National University of Science and Technology, Leninskii pr. 4, Moscow, 119049  
Russia.

<sup>b</sup> École de technologie supérieure, 1100 Rue Notre-Dame Ouest, Montreal, Canada.

This article was originally written in Russian, then officially translated and published  
in *The Physics of Metals and Metallography*, 2014, v.115, no.9, pp. 926-947  
in both Russian and English.

### **3.1 Summary**

The principal objective of this article was to determine the contributions to the functional performance of Ti-50.26 at.%Ni alloy subjected to CR and/or WR and IA (400°C, 1h) stemmed from their structure and texture. The influence of the texture on the recovery strain value was studied by calculating the theoretical resource of recovery strain using two different approaches: (1) when one single crystal of parent B2-phase transforms to one single crystal of B19'-martensite; (2) when B2-polycrystal is textured. The calculated maximum recovery strains were compared with their experimentally-measured values to isolate the effect of structure from that of texture on the recovery strain and make an evaluation of the adequacy of the proposed calculation approaches.

It was found that the nanocrystalline structure promotes the higher value of recovery strain than a mixed nanocrystalline and nanosubgrained. Moreover, for Ti-Ni alloys, the main

influence on the practical realization of their theoretical limit of transformation strain is brought by the alloy grain/subgrain size (structure), texture plays a secondary role.

### 3.2 Abstract

In this work, we have studied the nanostructure, the crystallographic texture, and the crystal lattice of the martensite of the Ti–50.26 at.%Ni alloy subjected to a thermomechanical treatment, which includes cold rolling, warm (at 150°C) rolling, intermediate and post-deformation annealings (400°C, 1h) in different combinations. To calculate the resource of the recovery strain in the approximation of a polycrystal, we suggested and employed a method based on the sufficiently complete allowance for the orientation distribution function of the initial B2-austenite and on the assumption on the realization of the most favorable orientational variant of martensite in each grain. The calculated values of the resource of the recovery strain have been compared with the experimental data and have been analyzed along with the results of the determination of the recovery stresses and parameters of the loading–unloading diagram. Estimations have been made of the role of the structural and textural factors in the realization of the recovery strain of the nanostructured Ti–50.26 at.%Ni alloy. To achieve the maximally high recovery strain, one should focus on obtaining a nanocrystalline structure in combination with a sharp texture, which ensures the maximum transformation deformation in the direction of tension.

**Keywords:** shape memory alloys, titanium nickelide, thermomechanical treatment, cold rolling, warm rolling, microstructure, crystal structure, texture, recovery strain, recovery stress.

### 3.3 Introduction

Titanium nickelide-based shape memory alloys (SMA) are used in medicine and technology in view of their ability to impart effects of shape memory and superelasticity [1–5]. The expanding fields of application require an improvement in the functional properties of SMA, in particular an increase in the values of the recovery strain and recovery stress, their stability

and mean longevity upon mechanical and thermomechanical cycling. The recovery strain is a structurally sensitive property; therefore, any changes in the degree of deformation and in the temperature of post-deformation annealing (PDA) upon the thermomechanical treatment (TMT) lead to changes in the grain structure and substructure, crystallographic resource of the recovery strain, and the degree of its realization [6–14]. This assertion is also correct with respect to recovery stress [6, 7, 9, 10].

The theoretical (crystallographic) resource of the recovery strain of an SMA is determined by the maximum deformation of crystal lattice upon martensitic transformation. Different methods of the evaluation of the resource of the recovery strain are used taking into account different features of the crystal structure and its changes upon the martensitic transformation, taking as such a resource the following quantities:

- (1) the maximum lattice strain upon the martensitic transformation in the single-crystal approximation (austenite single crystal  $\leftrightarrow$  martensite single crystal transformation) [12, 15, 16];
- (2) the maximum macrodeformation in the isotropic-polycrystal approximation, when the austenite grains are oriented chaotically, but either (a) the lattice deformation is averaged over all orientations in the limits of the standard stereographic triangle (SST) or (b) only the most favorable orientation variant of martensite is realized in each grain [14];
- (3) the lattice deformation in the assigned direction relative to the axes of the sample (scheme of deformation) taking into account the texture of the initial austenite [17–20];
- (4) the deformation of the shape of the transformed region upon the transformation of austenite into martensite upon a specific variant of an orientation relationship taking into account the twinning of martensite variants in the martensite crystal [18–21].

The value of the resource of the recovery strain according to the variant (3) can be either less or greater than that according to the variant (2).

The maximum lattice deformation upon the martensitic transformation in the single-crystal approximation calculated for the case of a martensitic transformation in recrystallized austenite (according to the variant 1) decreases from 11.85 to 10.4% with an increase in the nickel concentration from 50.0 to 51.05 at.% in the Ti–Ni alloys [14]. Thus, the passage from nickel-hyper-equiatomic to nickel-equiatomic alloys leads to a noticeable increase in the theoretical limit of the recovery strain. The calculation of the maximum macroscopic deformation of an isotropic polycrystal according to the method 2b shows a decrease in the resource of the recovery strain by  $\sim 0.8\text{--}0.7\%$  compared with that of a single crystal. The corresponding interval of values of  $\varepsilon_{poly}^{max}$  was 11.05–9.7% [14]. The resource of the recovery strain upon the formation of martensite from polycrystalline austenite with a higher concentration of lattice defects (such as dislocations, subboundaries, grain boundaries) decreases. Thus, as the microstructure of austenite changes from recrystallized to nanocrystalline (NC) or nanosubgrained (NS) structure, the crystallographic resource of the recovery strain decreases approximately to 1% [14]. At the same time, the extent of the realization of the resource of the recovery strain upon the martensitic transformation of a more imperfect (e.g., NCS or NSS) austenite is much higher. Thus, the maximum completely recoverable strain  $\varepsilon_{r,1}^{max}$  in the case of the formation of martensite from the B2-austenite with an NC or NS structure formed as a result of a TMT approaches the resource of the recovery strain because of a sharp increase in the dislocation yield stress of austenite [7, 9].

The maximum value of the completely recoverable strain (upon the thermomechanical tensile tests) of the polygonized NSS Ti–50.0 at.%Ni alloy after cold rolling to a moderate true strain ( $e = 0.3$ ) and post-deformation annealing (PDA) is  $\varepsilon_{r,1}^{max} = 6\%$ , which considerably exceeds  $\varepsilon_{r,1}^{max} = 2\%$  of the recrystallized alloy subjected to a control treatment (PDA at  $700^\circ\text{C}$ ) [9]. In the case of severe cold deformation by rolling ( $e = 1.9$ ) and PDA at  $400^\circ\text{C}$ , the average size of grains was 65 nm and the maximum value of the completely recoverable

strain reached  $\varepsilon_{r,1}^{\max} = 7\%$  [9]. The combination of the highest dislocation yield stress and a comparatively low transformation yield stress in the case of the NC structure favorably influences the magnitude of the completely recoverable strain of the SME and the shape recovery rate because of the later start of the irreversible plastic deformation [1, 3, 9]. The greater the difference between the dislocation and transformation yield stresses, the higher the amount of completely recoverable strain [1, 3, 9].

An important factor is the opportunity of retaining the favorable deformation texture of the B2 phase necessary for obtaining the greatest recovery strain. The calculation of the resource of the recovery strain with allowance for texture gave values to 10.3% in the polycrystal [20]; however, the influence of structure on its realization was not traced. On the other hand, in works [7–12, 14] devoted to studying the influence of the nanostructure and dislocation substructure on the amount of recovery strain of the Ti–Ni SMAs, the possible influence of the crystallographic texture has not been taken into account. The calculation performed with allowance for the twinning of the orientational variants of martensite showed that the recovery strain upon the martensitic transformation in the polycrystal does not exceed 8.5% [18–20].

With regard to the recovery stress, the situation is substantially simpler. An approximate measure of its maximum value is dislocation yield stress, and the crystallographic resource of the recovery strain plays a secondary role here.

When proceeding to the optimization of dynamic (fatigue) functional properties, the situation is complicated by need to take into account the mechanical imperfection of the material arising during the deformation in the cycle of TMT as one of the basic factors that affect the material behavior. In this case, we mean the effects of an increase in the amount and sizes of microscopic cracks arising with an increase in the degree of the initial deformation, which are not removed in the course of the PDA that forms the nanostructure and the final properties. This leads to a situation where, with an increase in the initial deformation upon the TMT, the static functional characteristics of the material continue growing while the

functional longevity begins decreasing [6, 22]. An optimum combination of the functional longevity and stability was achieved in the case of the formation of a mixed NS + NC structure as a result of TMT that includes cold rolling (CR) with true (logarithmic) strain  $e = 0.75$  and PDA at 400°C for 1h [6, 22].

Thus, the impression is formed that the potential of the fatigue functional properties inherent in the NC structure is realized far not completely. In connection with this, to decrease the influence of the factor of mechanical defects while retaining the final nanostructured state, we included two additional steps into the scheme of TMT, namely, a warm rolling (WR) and an intermediate annealing (IA), which led to an improvement in the combination of fatigue functional properties of the Ti–Ni SMAs [23, 24]. However, in this case, along with a decrease in the mechanical defectiveness, the final structure and the crystallographic texture that are formed as a result of PDA [24] have changed as well. The problems of crack formation under these conditions have been considered in [25]; here, we examine in more detail the structural aspects of the problem in comparison with the main functional characteristics of the Ti–Ni SMAs.

In this work, we have investigated the influence of the nanostructured states and of the changes in the intensity of the basic components of the  $\{001\}\langle 110 \rangle_{B2}$  texture of the Ti-50.26 at.%Ni alloy that are formed upon TMT on the recovery strain and recovery stress. The TMT scheme included severe plastic deformation by rolling and post-deformation annealing in combination with a warm deformation and intermediate annealing.

### 3.4 Experimental

We investigated a Ti–50.26 at.%Ni alloy supplied by SAES GETTERS (United States) in the form of a wire with a diameter of 1 mm after cold drawing to 30% and homogenizing annealing at 700°C for 1 h. The wire was subjected to TMT, which included cold rolling (CR) at room temperature, warm rolling (WR) at a temperature of  $150 \pm 5^\circ\text{C}$  ( $0.25T_m$ ), intermediate annealing (IA), and post-deformation annealing (PDA) in different



combinations. The rolling was carried out on a FENN four-high laboratory rolling mill. The tension during rolling corresponded to 10% of the dislocation yield stress of the material, the rolling speed was 10 mm/s, and the complete accumulated logarithmic strain was  $e = 1.2$ . In the case of the warm rolling, the wire was heated by passing electric current through it. The IA and PDA were carried out at 400°C for 1h in an electric furnace with the subsequent cooling in water. The TMT was conducted according to the schemes presented in Table 3.1: (1, 2) reference CR in 4 and 6 passes with the accumulated strain  $e = 0.75$  and 1.2, respectively; (3) CR (in 5 passes) to  $e = 1$  + IA + CR in 1 pass: CR(1) + IA + CR(0.2); (4) CR(1) in 5 passes + IA + WR in 1 pass,  $e = 0.2$ : CR(1) + IA + WR(0.2); (5) WR in 5 passes,  $e = 1$  + IA + WR in 1 pass,  $e = 0.2$ : WR(1) + IA + WR(0.2). In all of the schemes, the final step of the TMT is PDA at 400°C for 1h.

Table 3.1 Designations and schemes of treatments

№	Scheme of TMT	Step 1	Step 2	Step 3	Step 4
1	CR(0.75)	CR, $e=0.75$	PDA 400°C, 1h		
2	CR(1.2)	CR, $e=1.2$	PDA 400°C, 1h	-	-
3	CR(1)+IA+ CR(0.2)	CR, $e=1$	IA 400°C, 1h	CR, $e=0.2$	PDA 400°C, 1h
4	CR(1)+IA+WR(0.2)	CR, $e=1$	IA 400°C, 1h	WR, $e=0.2$	PDA 400°C, 1h
5	WR(1)+IA+ WR(0.2)	WR, $e=1$	IA 400°C, 1h	WR, $e=0.2$	PDA 400°C, 1h

The electron-microscopic examination of the structure of thin foils were carried out using a JEOL-2100 device (at the Center of Collaborative Access “Materials Science and Metallurgy” at the MISIS National University of Science and Technology) and a Tesla BS-540” device (Kurdyumov Institute of Metal Physics, Bardeen Central Research Institute for Ferrous Metallurgy). The samples for preparing thin foils were cut out by electroerosion method and thinned by electrolytic polishing using the window method.

The X-ray diffraction research of the samples after grinding and chemical etching away of the damage surface layer were performed using a PANalytical X’pert Pro diffractometer in

monochromatized  $\text{CuK}\alpha$  radiation at room temperature and at  $100^\circ\text{C}$  (above the temperature of the finish temperature  $A_f$  of the reverse transformation). The conditional width of the X-ray lines  $\{110\}$  and  $\{211\}$  of the B2-austenite was measured at the half-height of the X-ray diffraction peak.

The lattice parameters  $a$ ,  $b$ , and  $c$  of the monoclinic B19'-martensite and the parameter  $a_{\text{B2}}$  of the B2-austenite were calculated using the method described in [11, 12, 14].

The textural analysis was carried out on a PANalytical X'pert Pro X-ray diffractometer in  $\text{CuK}\alpha$  radiation. The samples were cut out along the rolling direction; the surface layer was etched away in an  $\text{HF} : 3\text{HNO}_3 : 6\text{H}_2\text{O}_2$  solution until the appearance of a metallic luster. The  $(110)_{\text{B2}}$ ,  $(200)_{\text{B2}}$ , and  $(211)_{\text{B2}}$  pole figures were constructed using samples in the completely austenitic state at a temperature of  $A_f + 10^\circ\text{C}$  with an azimuthal step  $\Delta\alpha = \Delta\beta = 5^\circ$  and with a change in the radial angle of the inclination  $\alpha_{\text{max}}$  from  $0^\circ$  to  $75^\circ$ . Following analysis, the methods of direct and inverse pole figures were used, as well as the orientation distribution functions (ODFs) [26]. Since the width of the samples was 1.7 mm, a packet of several parallel samples was used during the X-ray diffraction study.

The theoretical estimations of the resource of the recovery strain with allowance for the texture of the initial austenite were obtained using the method presented below.

The lattice of the B2-austenite in the tetragonal representation upon the martensite transformation experiences deformation, being converted into the monoclinic lattice of the B19'-martensite (Figure 3.1).

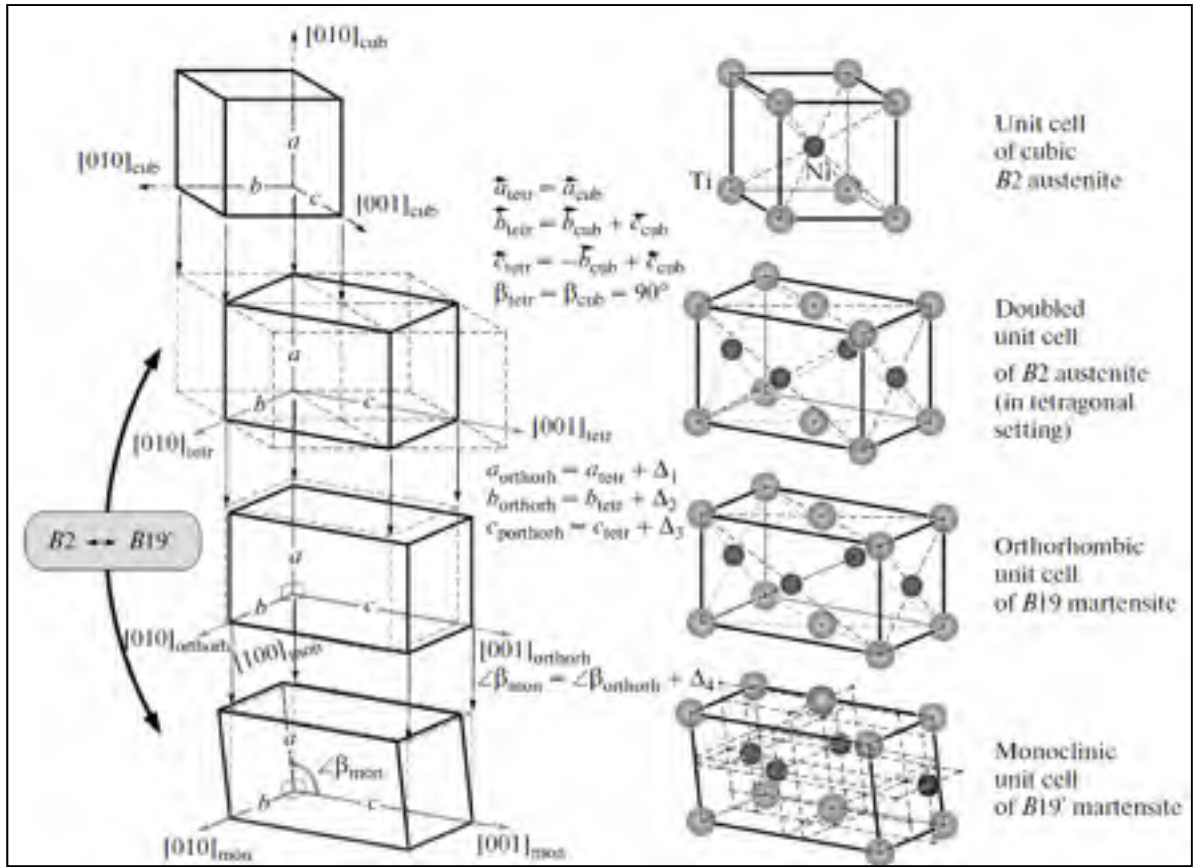


Figure 3.1 Crystallographic relationships corresponding to the changes in the systems of translations upon the transformation of the tetragonal cell of the B2-austenite into an orthorhombic cell with a monoclinic distortion of the B19'-martensite

The lattice deformation  $\mathcal{E}_i^{<uvw>}$  along any  $i$ th direction from the entire set of crystallographic orientations  $<uvw>$  was calculated as the relative change in the distance between the lattice sites that lie in a given direction:

$$\mathcal{E}_i^{<uvw>} = (r_i^{mono} - r_i^{tetr}) / r_i^{tetr} \quad (3.1)$$

Here,  $r_i^{tetr}$  is the position vector in the tetragonal coordinate system, which is determined from the relationship  $(r_i^{tetr})^2 = (x_i^2 + y_i^2)a^2 + z_i^2c^2$ , where  $a$  and  $c$  are the parameters of the

tetragonal lattice of the B2 austenite, and  $r_i^{mono}$  is the radius vector in the monoclinic system determined from the relationship  $(r_i^{mono})^2 = x_i^2 a^2 + y_i^2 b^2 + z_i^2 c^2 + 2x_i z_i a c \cdot \cos \beta$ , where  $a$ ,  $b$ ,  $c$ , and  $\beta$  are the parameters of the monoclinic lattice of the B19'-martensite.

By assigning the matrix of the transition from the orthorhombic into cubic system of translations and calculating  $\mathcal{E}_i^{uvw}$  for all possible variants of the crystallographic orientations of  $\langle uvw \rangle$ , we constructed the stereographic distribution of the lattice strains in the crystallographic setting of the cubic lattice of the B2-austenite. From this distribution, the indices of the crystallographic orientations corresponding to the basic components of the strain tensor were determined. Thus, the crystallographic resource of the recovery strain in the single-crystal approximation (B2-single-crystal  $\leftrightarrow$  B19'-single-crystal transformation), which is determined as the maximum deformation of the lattice upon the martensite transformation  $\mathcal{E}_{mono}^{max}$  and its crystallographic direction  $\langle uvw \rangle_{\mathcal{E}_{max}}$ .

The estimation of the resource of the recovery strain for the case of the transformation of polycrystalline austenite into polycrystalline martensite and back was conducted with allowance for the texture, using inverse pole figures obtained in the experiment under the assumption that in each separate grain the orientation of the optimum crystallographic orientation, along which the lattice deformation is maximum, in the general case does not coincide with the direction of external tensile stress. Since we consider the transformation under uniaxial tension, the following condition, which was adopted as the basis for calculations, seems to be closest to the real condition. In each grain upon martensitic transformation there will be realized 24 possible orientation variants of the martensite, for which the direction of the maximum deformation of the lattice is closest to the direction of external tensile stress  $\langle uvw \rangle_{\sigma}$  i.e., it lies within the limits of the same standard stereographic triangle (see scheme in Figure 3.2).

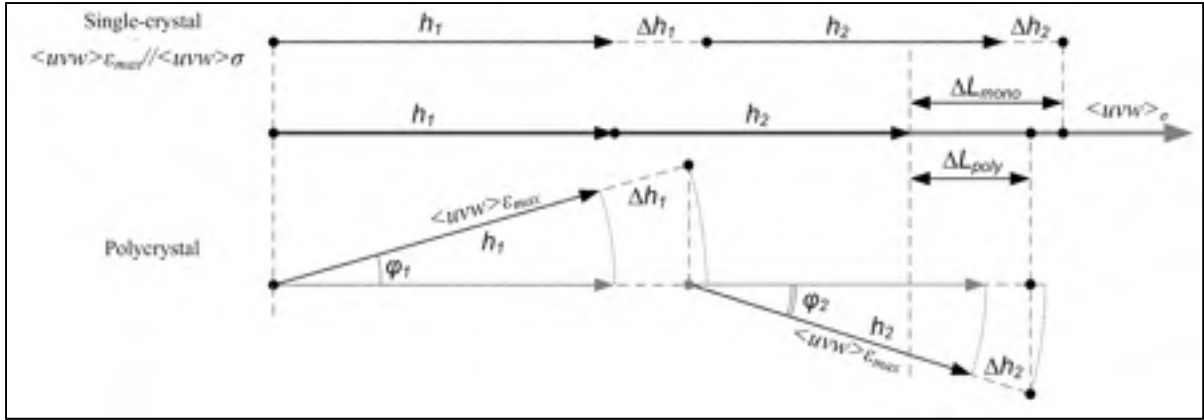


Figure 3.2 Scheme of the determination of the maximum deformation of the martensite transformation in polycrystalline austenite. Subscripts 1 and 2 correspond to two different grains of the polycrystal and to two (of equivalent length) sequential segments in the direction  $\langle uvw \rangle_{\epsilon_{max}}$  of a single crystal

With such idealized representation, the magnitude of the maximum possible macroscopic strain  $\epsilon_{poly}^{max}$  along the preferred direction (in our case, this is the rolling direction) upon the martensite transformation in polycrystalline B2-austenite was calculated as follows:

$$\epsilon_{poly}^{max1} = \frac{\epsilon_{mono}^{max}}{n} \sum_i^n R(g_i) \cdot \cos(\varphi_i) \approx \frac{\epsilon_{mono}^{max}}{4\pi/48} \int_0^{4\pi/48} R(g) \cdot \cos(\varphi) d\Omega \quad (3.2)$$

where  $\epsilon_{mono}^{max}$  is the maximally possible lattice deformation, which corresponds to the most favorable orientation of a single crystal, and  $R$  is the orientation distribution function  $R(g) = \frac{1}{V} \cdot \frac{dV(g_i)}{dg}$ , which reflects the pole density or the volume fraction  $\frac{dV(g_i)}{V}$  of grains with a definite orientation  $g$ . This orientation, which is equivalent to a concrete crystallographic orientation  $\langle uvw \rangle_i$  can be obtained from an analysis of the set of pole figures or diffraction spectra;  $\varphi_i$  is the angle between the preferred direction  $\langle uvw \rangle_{\sigma}$  along the external tensile stress in the  $i$ th grain and the crystallographic orientation  $\langle uvw \rangle_{\epsilon_{max}}$ , in which the maximum possible relative lattice strain is realized in the  $i$ th grain from many grains that lie along this chosen direction; and  $\Omega_i$  is the solid angle that corresponds to the

fraction of the  $i$ th orientation from the infinite number of possible orientations inside one standard stereographic triangle whose size corresponds to the solid angle  $4\pi/48$ . In the crystallographically isotropic polycrystal,  $R = 1$  irrespective of  $g$ .

The numerical integration was performed based on 12500 crystallographic orientations, which were spherically uniformly distributed inside one standard stereographic triangle. In the case of a textured polycrystal, the calculation was conducted taking into account their pole density. An example of the distribution of pole density  $R(g)$  within the limits of one standard stereographic triangle is given in Figure 3.3.

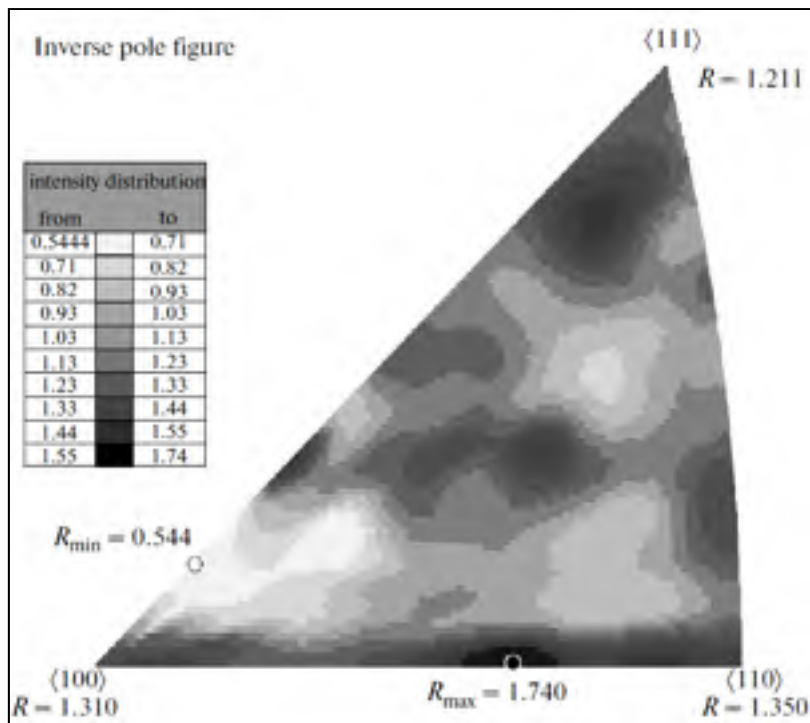


Figure 3.3 Inverse pole figure of the B2-austenite of the Ti-50.26 at.%Ni alloy after thermomechanical treatment according to the regime WR(1)+IA+WR(0.2) (see Table 3.1)

For comparison, the calculation of the resource of the recovery strain was carried out by two additional methods:

(1) by the simple spatial averaging of the lattice strain in the limits of the standard stereographic triangle

$$\varepsilon_{poly}^{\max 2} \approx \frac{1}{4\pi/48} \int_0^{4\pi/48} R(g) \cdot \varepsilon(g) d\Omega \quad (3.3)$$

(2) by a method based on the use of pole density and amounts of the lattice strain corresponding to crystallographic orientations  $\langle 100 \rangle$ ,  $\langle 110 \rangle$ , and  $\langle 111 \rangle$  of the B2-austenite [20]:

$$\varepsilon_{poly}^{\max 3} = \frac{R_{\langle 100 \rangle} \cdot \varepsilon_{mono}^{\langle 100 \rangle} + R_{\langle 110 \rangle} \cdot \varepsilon_{mono}^{\langle 110 \rangle} + R_{\langle 111 \rangle} \cdot \varepsilon_{mono}^{\langle 111 \rangle}}{R_{\langle 100 \rangle} + R_{\langle 110 \rangle} + R_{\langle 111 \rangle}} \quad (3.4)$$

Here,  $\varepsilon_{poly}^{\max 3}$  is the lattice macrodeformation in the direction of tension,  $\varepsilon_{mono}^{\langle uvw \rangle}$  is the lattice strain in the direction  $\langle uvw \rangle$  and  $R_{\langle uvw \rangle}$  is the pole density of the reflection  $\langle uvw \rangle$  in the direction of the tensile axis. For the Ti–50.26 at.%Ni alloy,  $\varepsilon_{mono}^{\langle 100 \rangle} = 2.94\%$ ,  $\varepsilon_{mono}^{\langle 110 \rangle} = 8.86\%$ , and  $\varepsilon_{mono}^{\langle 111 \rangle} = 10.71\%$  [14]. The direction  $\langle uvw \rangle_{\varepsilon_{max}}$  coincides with  $\langle 355 \rangle$  to a good accuracy, and  $\varepsilon_{mono}^{\max} = 11.48\%$ .

The calculations of  $\varepsilon_{poly}^{\max 1}$ ,  $\varepsilon_{poly}^{\max 2}$  and  $\varepsilon_{poly}^{\max 3}$  were conducted using specially developed computer programs.

For the experimental determination of the maximum recovery strain  $\varepsilon_r^{\max}$  and maximum completely recoverable strain  $\varepsilon_{r,1}^{\max}$  (to an accuracy of 0.2%) using the tensile loading–unloading scheme (Figure 3.4), an *INSTRON 3360* tensile machine was used. The samples with the gage part with a length of 100 mm were deformed to different values of the total deformation  $\varepsilon_t = 7\text{--}11\%$  in steps of 0.5–1% (Figure 3.4a, trajectory O–A). Then, the sample

was unloaded; after unloading, the sample shape was partially restored along the trajectory A–B. The induced strain  $\varepsilon_i$  was determined by drawing a tangent A–E to the initial segment of the unloading branch until the intersection with the horizontal axis (axis of deformation) at point E, as shown in Figure 3.4. This made it possible to take into account the contribution from the superelastic unloading, which leads to a bend of the lower part of the unloading branch toward smaller deformations) ( $\varepsilon_r^{SE}$ ).

Then, the sample was subjected to a short-term heating in the furnace at 250°C. This led to the restoration of the initial shape by the SME mechanism, either complete, along the trajectory B–O, or partial, along the trajectory B–C. Finally, the recovery strain  $\varepsilon_r^{SME}$  was measured as the distance between the markers on the gage part of the sample. Part of the deformation after heating could remain unrecoverable ( $\varepsilon_f$ ).

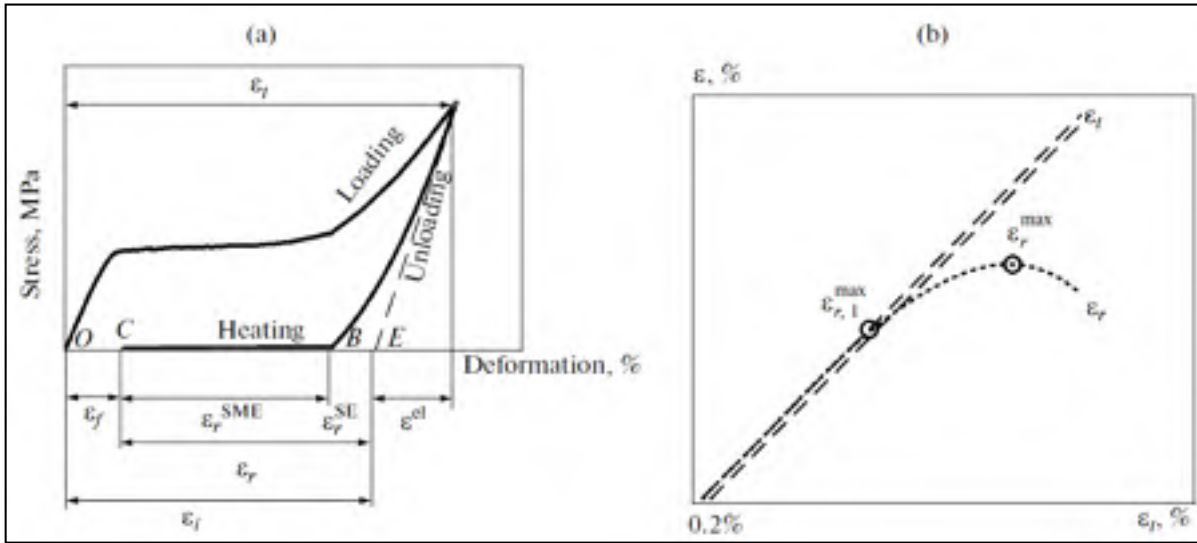


Figure 3.4(a) Scheme of the determination of the parameters of the loading-unloading diagram of a sample of the Ti-50.26 at.%Ni alloy and (b) of the maximum recovery strain  $\varepsilon_r^{max}$  and the maximum completely recoverable strain  $\varepsilon_{r,1}^{max}$

The total recovery strain  $\varepsilon_r$  was calculated as the sum of the recovery strain realized by the SME mechanism upon heating ( $\varepsilon_r^{SME}$ ) and the recovery superelastic strain ( $\varepsilon_r^{SE}$ ) as follows:



$$\varepsilon_r = \varepsilon_r^{SME} + \varepsilon_r^{SE} \quad (3.5)$$

### 3.5 Results

#### Structural studies

*Electron-microscopic examination.* The electron-microscopic examination has shown that the PDA at 400°C for 1h results in a nanostructured state of the Ti–50.26 at.%Ni alloy after TMT performed by all regimes. The average size of individual structural elements surrounded by low-angle or high-angle boundaries, i.e., of subgrains or grains, does not exceed 100 nm. Below, we consider the main features of this structural state depending on the regime of TMT. Note that the final stage of TMT in each regime is PDA at 400°C for 1h, which produces the final structure and properties of the SMA. The sequence of the TMT regimes is as follows: the first two regimes include only cold rolling (CR), the third regime is a combination of CR with an intermediate annealing (IA), the fourth regime is a combination of CR with IA and warm rolling (WR), and the fifth regime is a combination of WR with IA.

*Regime CR(0.75), Figure 3.5a, b.* In the case of this regime, after PDA at 400°C for 1h, a mixed nanostructure is observed that consists of alternating regions of submicron size predominantly with an NS or NC structure, as was also observed in [27]. A schematic representation of such a mixture of structures is shown in [25]. The subgrains of the NS structure exhibit a high dislocation density, which agrees with the data of [7, 27]. Figure 3.5a displays bright-field and dark-field images of the structure characteristic of NS regions, while Figure 3.5b shows the same for NC regions; the insets show corresponding diffraction patterns. In all of the cases, the NS and NC regions are not completely uniform in their structure. In the first case, individual nanodimensional grains are encountered and, in the second case, small groups of subgrains are observed, as in [25, 27]. The selected-area electron diffraction (SAED) patterns of NC regions consist of point rings with a sufficiently uniform distribution of reflections. The diffraction rings from the NS regions consist of relatively short, frequently fragmented arcs-crowdings of reflections, and a small number of

individual reflections from NC regions between them. The crystallographic orientation of the lattice in NS regions is imperfect, but the average orientation on a selected area after the formation of an NS structure as a result of a polygonization of the dislocation substructure is retained. For example, in Figure 3.5a, the zone axis of the region with an NS structure is obviously  $\langle 111 \rangle_{B2}$  (as follows from the positions of the centers of reflection crowdings).

*Regime CR(1.2)*, Figure 3.5c. An increase in the degree of deformation upon CR from  $e = 0.75$  to 1.2 leads to the intense development of an NC structure and an increase in the fraction of amorphous structure [27]. Therefore, after PDA at 400°C for 1h, which leads to a nanocrystallization of the amorphous structure and to grain growth in the NC structure [27], in the bright-field and dark-field images there are mainly observed NC regions with a grain size of 15–70 nm. Judging from the dark-field images, a small amount (10–15%) of an NS structure is also present, which is identified as luminous regions up to 150 nm in size that consist of several subgrains with close orientations. The SAED patterns represent point rings typical of NC structures with a fairly uniform distribution of separate point-like reflections. The crowdings of reflections, which serve as a sign of the existences of NS regions [7, 27], are weak. On the whole, this structure is similar to that observed for the same alloy subjected to CR to  $e = 1.5$  after a PDA at 400°C for 1 h [27].

*Regime CR(1)+IA+CR(0.2)*, Figure 3.5d. In the bright- and dark-field images, an NC structure is mainly observed, as in the case of regime CR(1.2) with the same accumulated deformation but without IA. In this case, the NC grains are approximately 1.5-2 times larger than in the case of the CR(1.2) regime. This follows also from a more rarefied arrangement of point-like reflections in the ring of the SAED pattern compared to the case of CR(1.2). On the whole, the intensity is distributed fairly uniformly along the point electron diffraction ring without the sharp crowding of reflections; the number of clearly pronounced regions with an NS structure in the bright-field and dark-field images is small. Consequently, the structures after TMT with an identical degree of deformation ( $e = 1.2$ ) accumulated upon CR are similar and only differ in the size of grains of B2-austenite. In the final analysis, the grain

size increased as a result of using IA in the TMT schedule and, correspondingly, because of the smaller accumulation of lattice defects before PDA.

*Regime CR(1)+IA+WR(0.2)*, Figure 3.5e, 5f. The structure after TMT by this regime is as if intermediate between the structures that are formed as a result of TMT by regimes CR(1)+IA+CR(0.2) and WR(1)+IA+WR(0.2) (the latter is shown in Figure 3.5g), but is nearer to the first. It mainly contains NC regions (with the corresponding annular point diffraction pattern, Figure 3.5e), but also a fairly large amount of NS regions (conglomerates of subgrains with a size to 200 nm and the regular crowdings of reflections in the annular electron diffraction pattern, Figure 3.5f). The amount of NS regions is noticeably less than after TMT by the regime WR(1)+IA+WR(0.2). The size of structural elements (grains, subgrains) is approximately the same as after CR(1)+IA+CR(0.2), i.e., is greater than after the simple CR(1.2), and the distribution of point reflections in the diffraction ring is more rarefied.

*Regime WR(1)+IA+WR(0.2)*, Figure 3.5g. Judging from the bright- and dark-field images, this regime yields mainly NS structures, but there are also a fairly large number of NC regions. The grains, subgrains, and groups of subgrains (polygonized regions) are larger than in the case of the CR(1.2) regime. Inside the subgrains, an enhanced dislocation density is observed. The diffraction pattern confirms this character of the structure; clearly pronounced arc-shaped crowdings of the intensity in diffraction rings are observed, which are characteristic of a polygonized dislocation substructure [7, 27].

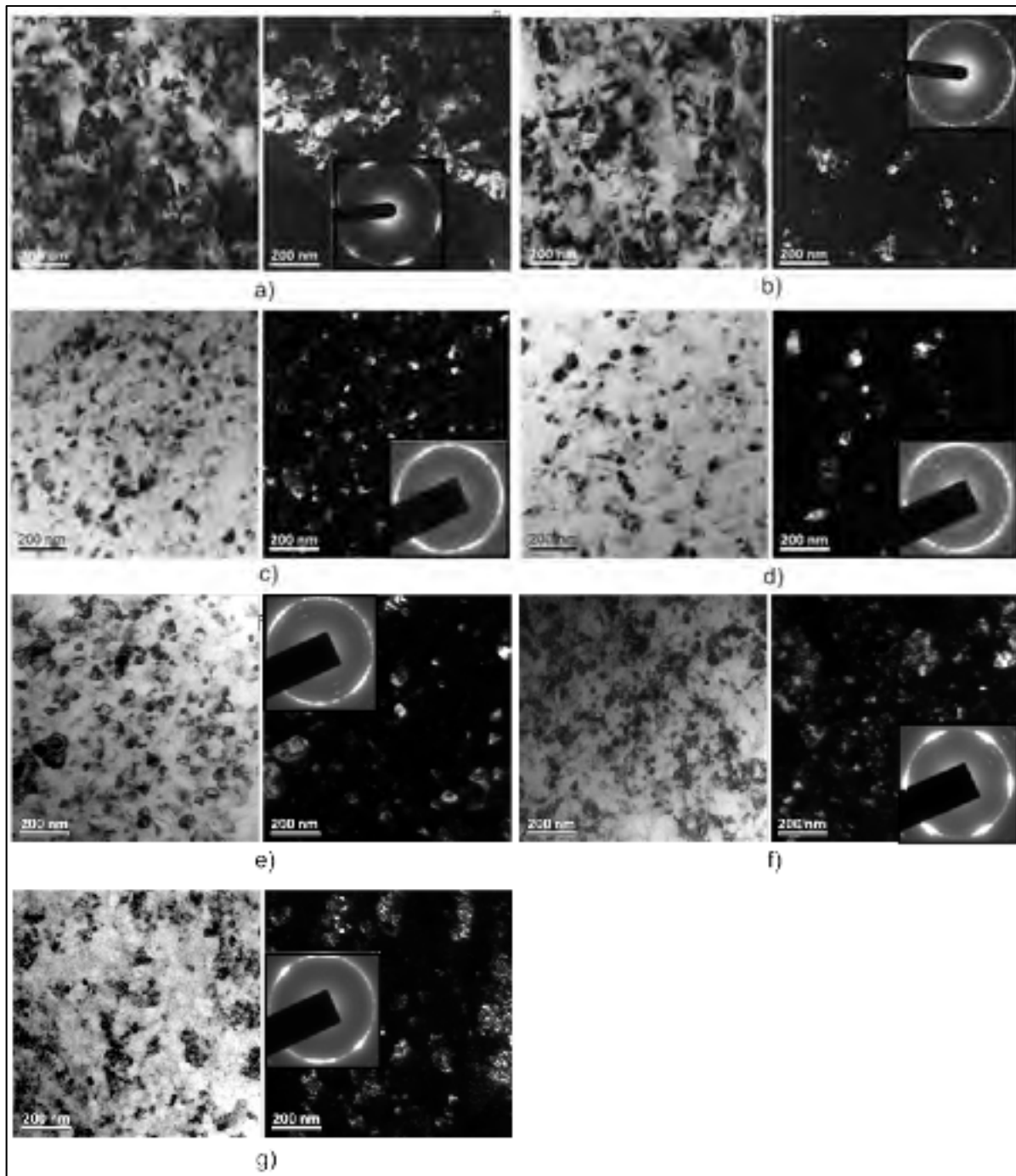


Figure 3.5 Structures of Ti-50.26 at.%Ni alloy after TMT under different conditions: (a, b) CR(0.75); (c) CR(1.2); (d) CR(1)+IA+CR(0.2); (e, f) CR(1)+IA+WR(0.2); (g) WR(1)+IA+WR(0.2). Left-hand panel: bright-field images; right-hand panel: dark-field images with the diffraction patterns in the insets

Thus, the electron-microscopic examination revealed the following features characteristic of the processes of formation of the structure of the B2-phase of the Ti–50.26 at.%Ni alloy:

- (1) the greater the contribution from CR to the accumulated deformation, the greater the fraction of NC regions in comparison with NS regions, and the lower the average dislocation density after PDA at 400°C for 1h;
- (2) the greater the contribution from WR to the accumulated deformation, the greater the fraction of NS regions in comparison with NC regions and the larger the grains, subgrains, and polygonized regions with an NS structure;
- (3) the addition of a step of intermediate annealing at 400°C for 1h into the regime of the TMT leads to a coarsening of the structural elements, i.e., to an increase in the size of NC grains and subgrains, as well as to an increase in the fraction of NS regions.

These regularities can be explained as follows. The amorphization of the structure upon the deformation of Ti–Ni alloys favors the formation of NC regions (as a result of nanocrystallization) in the course of subsequent PDA, and the fraction of the amorphous structure after CR is higher than after WR at 150°C [28]. Consequently, if after CR (for example, to  $e = 1.2$ ) and PDA at 400°C for 1h the structure must be mainly nanocrystalline with a small amount of NS regions, then after WR and PDA at 400°C for 1h, the fraction of NS regions must be substantially greater. In this case, in many regions, upon the PDA, polygonization will be observed with the formation of nanosubgrains with an enhanced dislocation density inside them rather than the nanocrystallization and growth of nanograins [7]. An intermediate annealing naturally leads to an increase in the final dimension of grains and subgrains, since its temperature is much higher than the temperatures of the CR and WR. Consequently, the concentration of lattice defects, which is inversely proportional to the size of subgrains and grains ( $d \sim \rho^{-1/2}$ , where  $d$  is the size of the grain/subgrain, and  $\rho$  is the dislocation density) [29, 30], is lower.

Thus, the incorporation of an intermediate annealing and warm deformation into the process of TMT together with a cold deformation leads not only to a decrease in the mechanical damage, but also to a change in the nature of the nanostructure of the Ti–Ni SMA after PDA at 400°C, namely, to an increase in the fraction of NS regions and to a decrease in the NC regions, an increase in the size of structural elements (grains and subgrains), and an increase in the average density of free dislocations.

*X-ray diffraction analysis.* The integral estimation of the structural states of the Ti-50.26 at.%Ni alloy based on the conditional width of the X-ray diffraction lines  $B_{hkl}$  agrees with the results of local electron-microscopic analysis.

It follows from Figure 3.6 that, with an increase in the degree of initial deformation upon CR from  $e = 0.75$  to  $e = 1.2$ , the width of the B2-austenite lines measured after PDA grows noticeably. The incorporation into the TMT schedule with the initial deformation  $e = 1.2$  of an intermediate annealing at 400°C for 1 h in different combinations with CR and WR, does not lead to a further broadening of the lines. It seems that the width of the austenite line, i.e., the lattice imperfection, after PDA at 400°C for 1h is determined only by the degree of the induced deformation irrespective of the combination of CR, WR, and IA treatments (the greater the  $e$ , the greater the  $B_{hkl}$ ). In our case, the basic contribution to the line width is introduced by two factors: the density of free dislocations (not entering into boundaries or subboundaries) and the size of the grains/subgrains (the stresses of the 2nd kind after PDA at 400°C for 1 h (microscopic stresses) are to be neglected): the greater the dislocation density and the smaller the size of the grains/subgrains, the greater the  $B_{hkl}$ . According to [14], if the PDA of the Ti–50.26 at.%Ni alloy is performed at low temperatures, the contribution from the small grain size predominates; at high temperatures, the contribution from the dislocation density is prevailing. This conclusion follows from the comparison of the dependence of widths of  $B_{110}$  lines of austenite on the temperature of the PDA after CR to  $e = 0.3$  and 1.9, when at some stages of the PDA, pure NS and NC structures were formed, respectively. The transitional temperature range of the PDA, where the contributions to the width of lines of both factors are close, for the Ti–50.26 at.%Ni alloy is exactly 350–400°C [14], which does

explain the equality of the  $B_{hkl}$  of austenite after all regimes of TMT with an accumulated deformation 1.2.

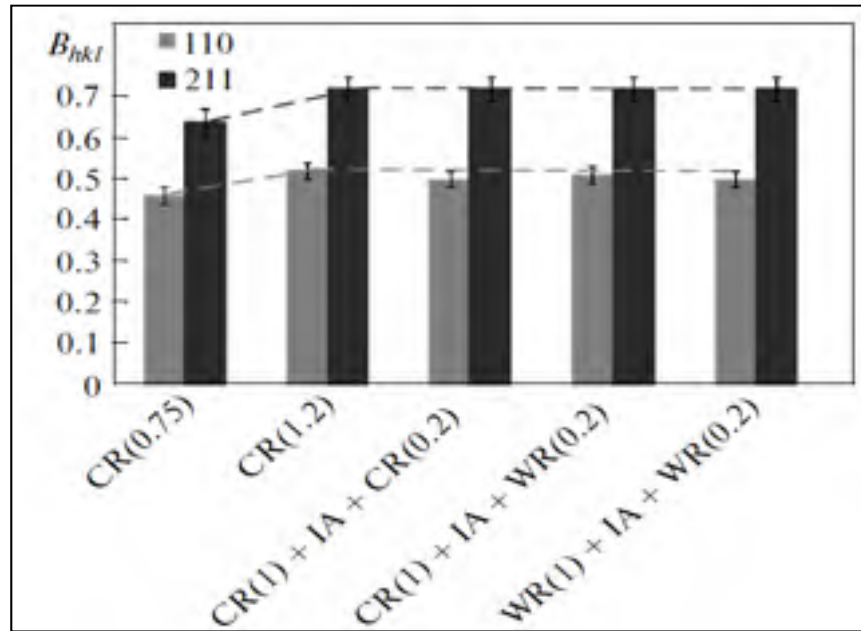


Figure 3.6 Widths of the XRD lined  $\{110\}$  and  $\{211\}$  of the austenite of the Ti-50.26 at.%Ni alloy as function of the regime of TMT

The angular coordinates of the XRD lines of the B19'-martensite of the Ti-50.26 at.%Ni alloy after TMT in all regimes do not differ substantially. Correspondingly, the lattice parameters of the B19'-martensite after different TMT regimes calculated from these coordinates also do not differ within the experimental error (Table 3.2). At the same time, their values change compared to the corresponding parameters of the quenched martensite to the same directions and by the same amounts as in the previous studies, where the martensite was formed from nanocrystalline or polygonized (nanosubgranular) austenite [11, 12, 14].

Table 3.2 Martensite lattice parameters and the maximum lattice strain upon the martensitic transformation of the Ti-50.26 at.%Ni alloy (measurements at room temperature)

Treatment	Lattice parameters of martensite				$\epsilon_{mono}^{\max}$ %
	$a$ , Å	$b$ , Å	$c$ , Å	$\beta$ , deg	
Quenching from 700°C [14]	2.8969 ±0.0014	4.1228 ±0.0026	4.6435 ±0.0012	97.47 ±0.08	11.48±0.06
CR(0.75) + PDA (400°C, 1h)	2.8898 ±0.012	4.1195 ±0.0044	4.6265 ±0.0035	96.99 ±0.26	10.89±0.17
CR(1)+IA+ CR(0.2)+ PDA (400°C, 1h)	2.886 ±0.0106	4.122 ±0.0044	4.6311 ±0.0034	97.16 ±0.23	10.88±0.16
CR(1)+IA+WR(0.2)+ PDA (400°C, 1h)	2.8827 ±0.0075	4.1187 ±0.0045	4.622 ±0.0038	96.88 ±0.17	10.50±0.13
WR(1)+IA+ WR(0.2)+ PDA (400°C, 1h)	2.8878 ±0.0082	4.1249 ±0.0045	4.6268 ±0.0037	96.83 ±0.20	10.71±0.14

The maximum lattice strain upon martensite transformation (crystallographic resource of the recovery strain in the single-crystal approximation)  $\epsilon_{mono}^{\max}$  has a maximum value if the martensite is formed from recrystallized austenite during the usual quenching as follows:  $\epsilon_{mono}^{\max} = 11.48\%$  (Table 3.2). These resources are less after TMT in all regimes, which agrees with the data of [11, 12, 14], and do not differ between themselves essentially (Table 3.2).

*Textural analysis.* The orientation distribution function (ODF) of the B2-austenite was determined based on the pole figures (110), (200), and (211) using an X'pert Texture computer program for textural analysis. Figure 3.7 displays sections of the ODF at the values of the Euler angle  $\varphi_2 = 0^\circ$  or  $90^\circ$  for the samples after TMT with an intense CR and combinations of CR, WR, and IA. In all cases, the texture components  $(hkl)[uvw]$  can be qualitatively determined based on the values of the density of their orientations using the relationships between the Euler angles  $\{\varphi_1, \Phi, \varphi_2\}$  [26].



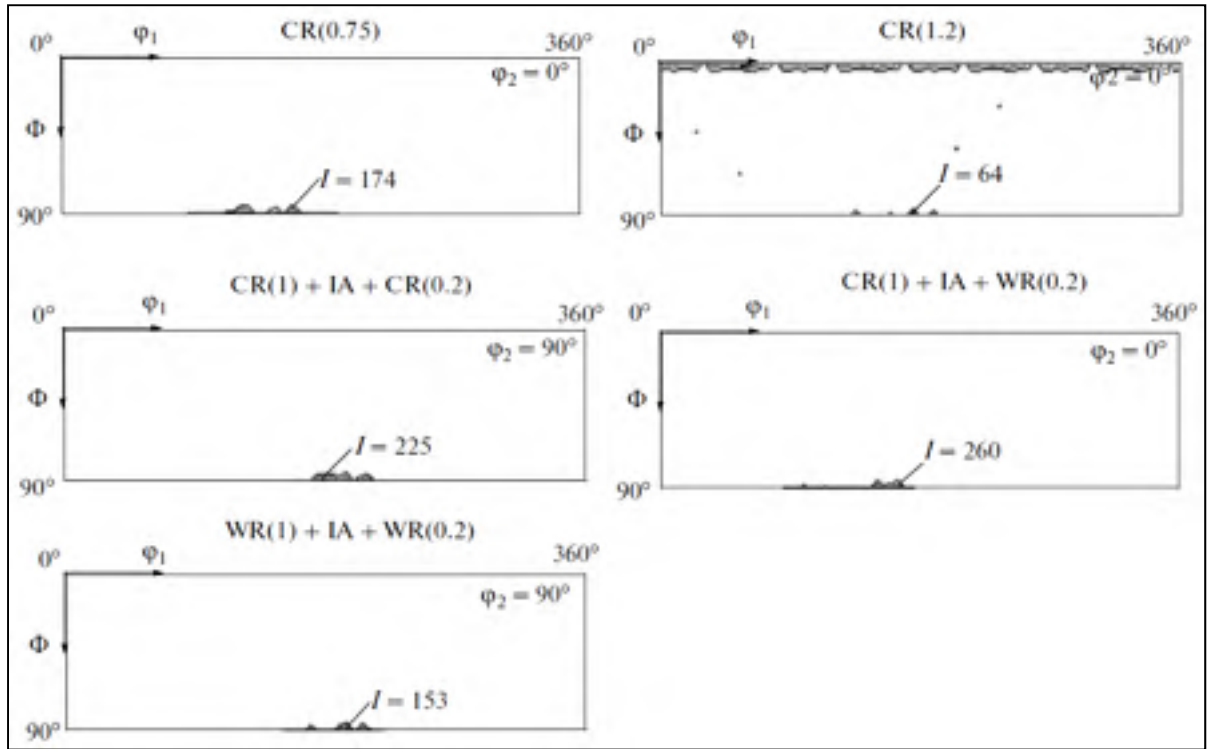


Figure 3.7  $\varphi_2 = 0^\circ$  and  $\varphi_2 = 90^\circ$  sections of the ODF for different regimes of thermomechanical treatments

At  $\varphi_2 = 0^\circ$  (or  $90^\circ$ ) and  $\Phi = 90^\circ$ , the calculated component of the texture exactly corresponds to the plane  $\{100\}$  and with a small deviation, to the direction  $[011]$ . For a more detailed analysis, let us examine the related inverse pole figures (Figure 3.8).

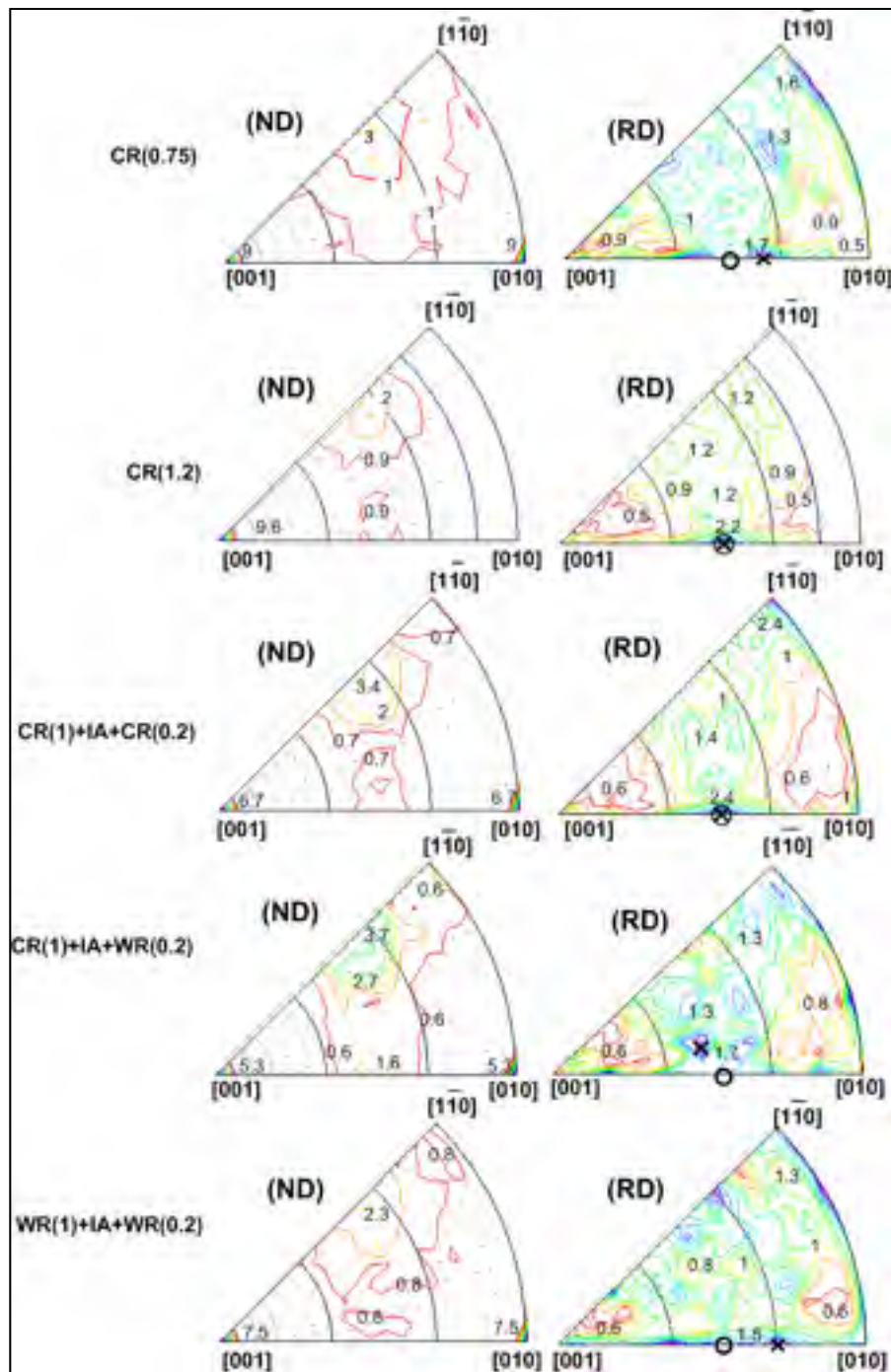


Figure 3.8 Inverse pole figures corresponding to the direction of the normal to the rolling plane (ND) and to the rolling direction (RD) for different regimes of TMT. O - the position of the pole  $[011]B2$ ; x - the position of the maximum of the ODF

It follows from the analysis of these inverse pole figures (IPFs) that the direction closest to the maxima of the IPF is  $[011]_{B2}$ . Thus, the texture of the austenite of the Ti–50.26 at.%Ni alloy after TMT in all regimes corresponds to  $\{100\}\langle 011\rangle_{B2}$ . Figure 3.9 shows the ODF for the textural component  $\{100\}\langle 011\rangle$  depending on the regime of TMT.

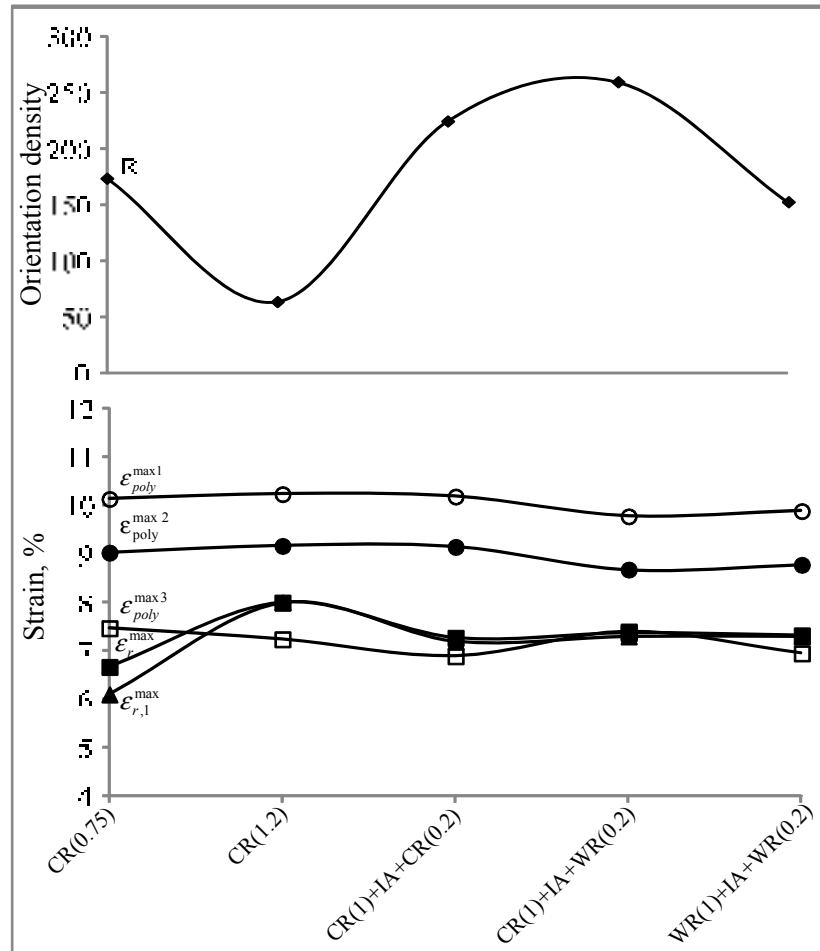


Figure 3.9 Orientation density of the textural component  $\{100\}\langle 110\rangle_{B2}$  and the calculated (by different methods) resources of the recovery strain of the Ti-50.26 at % Ni alloy after TMT under different conditions

After TMT via the CR(0.75) regime, the  $\{100\}\langle 110\rangle_{B2}$  component is very sharp. With an increase in the accumulated cold strain to  $e = 1.0$ , the texture of the austenite becomes sharper, while at  $e = 1.2$  its sharpness is reduced rapidly. The following explanation of this change can be suggested. After cold strain with  $e = 1.2$ , the amount of the amorphous phase

is greater than that after  $e = 0.75$  and  $1.0$  [27]. Upon the nanocrystallization of the amorphous phase in the course of PDA at  $400^{\circ}\text{C}$  the orientations of the arising grains is arbitrary; as a consequence, after TMT by the regime of CR(1.2), a reduction occurs in the orientational density.

In the case of TMT, according to the regime CR(1)+IA+CR(0.2), the texture of the austenite again becomes sharper. After the CR(1.0)+IA regime, the texture is additionally oriented in the direction  $\langle 110 \rangle$  at the stage of CR to  $e = 0.2$ , since the amorphous structure is crystallized after IA. Upon the replacement of the second step, CR, by WR, the rotation of the lattice of grains can be facilitated and, therefore, the regime CR(1)+IA+WR(0.2) gives the sharpest texture. As for the decrease in the orientation density with a further increase in the contribution from the thermal energy in the process of rolling (regime WR(1)+IA+WR(0.2)), we can so far only assume that it may be connected with a change in the relationship between the NS and NC structures in favor of the NS structure.

The textural analysis makes it possible to estimate the crystallographic resource of the recovery strain of the polycrystalline Ti–50.26 at.%Ni after TMT performed via different regimes with allowance for the specific features of texture (Figure 3.9; Table 3.3, Table 3.4). The relative density of the orientations  $R_{\langle hkl \rangle}$  in the directions  $\langle 100 \rangle$ ,  $\langle 110 \rangle$ , and  $\langle 111 \rangle$  calculated from the inverse pole figures and the crystallographic resource of the recovery strain calculated according to [20] are presented in Table 3.3 for five regimes of TMT. The values of the crystallographic resource of the recovery strain calculated with allowance for the ODF based on 12500 orientations in the limits of the standard triangle, i.e.,  $\varepsilon_{poly}^{\max 1}$ , under the assumption of the realization of the most favorable orientational variant of martensite in each grain, and  $\varepsilon_{poly}^{\max 2}$ , calculated by simple averaging over all orientations, are given in Table 3.4.

Table 3.3 Relative pole density  $\langle 100 \rangle$ ,  $\langle 110 \rangle$  and  $\langle 111 \rangle$  and the corresponding crystallographic resource of the recovery strain of the Ti-50.26 at.%Ni alloy after different regimes (calculated according to [20])

$R_{\langle 100 \rangle}$	$R_{\langle 110 \rangle}$	$R_{\langle 111 \rangle}$	Calculated resource of recovery strain $\varepsilon_{poly}^{\max 3}$ , %
<b>CR(0.75)</b>			
0.74	0.96	0.97	7.47
<b>CR(1.2)</b>			
1.28	2.61	0.83	7.24
<b>CR(1)+IA+CR(0.2)</b>			
1.82	2.77	1.05	6.89
<b>CR(1)+IA+WR(0.2)</b>			
0.52	1.47	0.61	7.40
<b>WR(1)+IA+WR(0.2)</b>			
1.31	1.35	1.21	6.95

Table 3.4 Resource of the recovery strain of the polycrystalline Ti-50.26 at.%Ni alloy calculated by different methods

Treatment	Calculated resource of recovery strain, %		
	$\epsilon_{poly}^{\max 1}$	$\epsilon_{poly}^{\max 2}$	$\epsilon_{poly}^{\max 3}$
Quenching from 700°C	10.56	9.26	-
CR(0.75) + PDA (400°C, 1h)	10.14	9.03	7.47
CR(1.2) + PDA (400°C, 1h)	10.24	9.17	7.24
CR(1)+IA+CR(0.2)+ PDA (400°C, 1h)	10.19	9.15	6.89
CR(1)+IA+WR(0.2)+ PDA (400°C, 1h)	9.78	8.68	7.40
WR(1)+IA+WR(0.2)+ PDA (400°C, 1h)	9.89	8.78	6.95

Based on analysis of Figure 3.9 and Table 3.3 and Table 3.4, the following conclusions can be drawn:

(1) The values of the resource of the recovery strain calculated with taking into account the texture of the polycrystalline austenite by different methods, differ substantially. For the different regimes of TMT, the calculation by the method which takes into account that under stress in each grain there arises a most favorable orientational variant of martensite, gives  $\epsilon_{poly}^{\max 1}$  of about 10%; the simple averaging of orientational variants gives a value of about 9%; the allowance for only polar densities of directions  $\langle 100 \rangle$ ,  $\langle 110 \rangle$  and  $\langle 111 \rangle$  gives  $\epsilon_{poly}^{\max 3}$  in limits of 6.92–7.45%.

(2) Despite the large differences in the orientational density of the textural component  $\{100\}\langle 110 \rangle_{B2}$  after TMT according to different regimes, the differences in the theoretical resource of the recovery strain of a polycrystal (in the limits of one method of its calculation) are small and hardly exceed the experimental error.

A more accurate analysis of these results can be made by comparing them with the realization of the resource of the recovery strain in the experiment described below.

### Functional Tests

*Determination of the recovery strain.* A sharp increase in the maximum completely recoverable strain  $\varepsilon_{r,l}^{\max}$  upon the formation of NS and, especially, NC structures was explained in [6, 7, 9] by a sharp increase in the difference between the dislocation and transformation yield stresses. But this explained only the influence of structural features introduced by TMT and did not take into consideration the specific features of the austenite texture. In this work, the comparison of the experimental values of the maximum recovery strain and the completely recoverable strain after TMT under different conditions with those predicted theoretically and between themselves allowed us to estimate the relative influence of the textural and structural factors on these quantities. The tests according to the tensile deformation–unloading scheme were performed after TMT according to the following regimes: CR(0.75), CR(1.2), CR(1)+IA+CR(0.2), CR(1)+IA+WR(0.2), and WR(1)+IA+WR(0.2).

The loading–unloading diagrams obtained are given in Figure 3.10. The straight line under each curve designates the amount of the recovery strain due to the SME determined after complete unloading and heating at 250°C ( $\varepsilon_r^{SME}$ ). The case when the straight line of the recovery strain does not reach the zero indicates the presence of a residual strain  $\varepsilon_f$ .

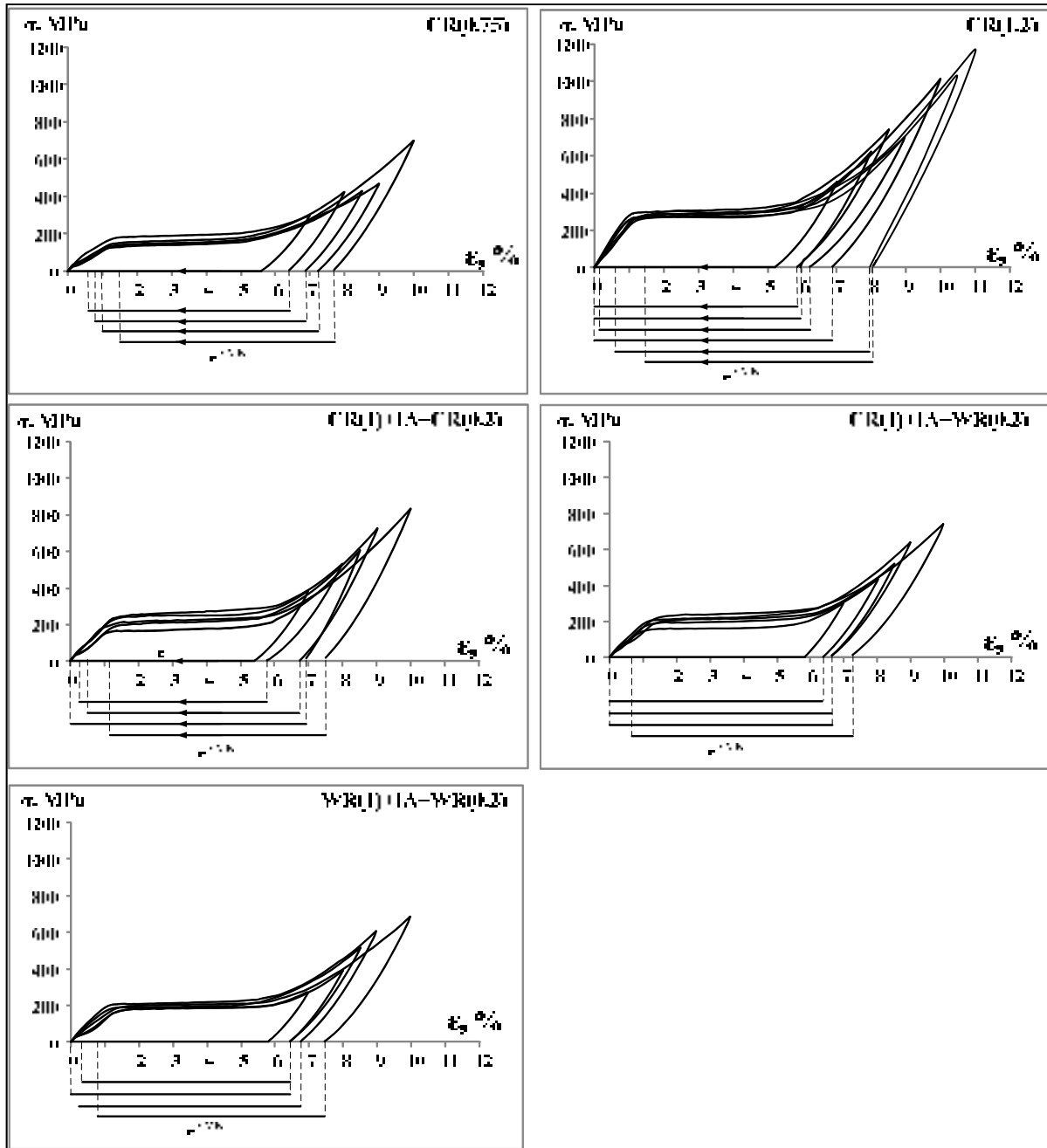


Figure 3.10 Characteristic loading-unloading diagrams of the Ti-50.26 at.%Ni alloy after different regimes of TMT

The residual strain arisen as a result of plastic deformation of samples upon tension increases with an increase in the total induced strain from 7 to 10% after all regimes of TMT. An increase in  $\epsilon_f$  after CR(0.75) is maximum in the entire range of the total induced strain in



comparison with other regimes of TMT and reaches a maximum value of 1.5% at the total induced strain of 10%.

The residual strain correlates with the values of the transformation yield stress  $\sigma_{tr}$  and the strain hardening  $\sigma_i$ , which is characterized here by the stress reached upon the tensile strain of 10%. After CR(0.75), the maximum value of  $\varepsilon_f$  corresponds to the smallest values of  $\sigma_i$  and  $\sigma_{tr}$ , while after CR(1.2) the smallest value of  $\varepsilon_f$  corresponds to the maximum values of  $\sigma_i$  and  $\sigma_{tr}$ .

Figure 3.11 and Table 3.5 present the results of determining the parameters of the shape recovery for the Ti–50.26 at.%Ni SMA. Here, in accordance with Figure 3.4a and Figure 3.4b,  $\varepsilon_t$  is the total induced strain,  $\varepsilon_i$  is the induced strain,  $\varepsilon_r$  is the complete recovery strain;  $\mathcal{E}_r^{SME}$  is the recovery strain that is realized by the mechanism of SME as a result of heating at 250°C,  $\mathcal{E}_r^{SE}$  is the recovery strain that is realized upon the unloading by the mechanism of superelasticity,  $\mathcal{E}_r^{\max}$  is the maximum recovery strain,  $\mathcal{E}_{r,l}^{\max}$  is the maximum completely recoverable strain, and  $\varepsilon_f$  is the residual recovery strain arising as a result of plastic deformation. It should be noted that the accuracy of determining  $\mathcal{E}_r^{SE}$  is acceptable, since a systematic difference in Young's moduli determined for the different regimes of TMT from the slope of the tangent to the unloading branch in its upper part is negligible (Table 3.6).

Table 3.5 Characteristics of the recovery strain of the Ti-50.26 at.%Ni SMA depending on the regimes of TMT and total induced strain  $\varepsilon_t$  (%)

Regimes of TMT	$\varepsilon_r$ , %							$\varepsilon_r^{\max}$ , %	$\varepsilon_{r,1}^{\max}$ , %
	$\varepsilon_t=7$	$\varepsilon_t=8$	$\varepsilon_t=8.5$	$\varepsilon_t=9$	$\varepsilon_t=10$	$\varepsilon_t=10.5$	$\varepsilon_t=11$		
CR(0.75)	6.0	6.15	6.5	6.67	6.57	-	-	6.67±0.15	6.1
CR(1.2)	5.71	6.25	6.64	6.93	8.0	7.71	7.27	8.00±0.32	8.0
CR(1)+IA+CR(0.2)	5.99	6.28	6.74	7.27	7.11	-	-	7.27±0.05	7.2
CR(1)+IA+WR(0.2)	6.05	6.7	7.1	7.37	7.1	-	-	7.37±0.12	7.3
WR(1)+IA+WR(0.2)	6.14	6.44	7.0	7.39	7.32	-	-	7.32±0.04	7.3

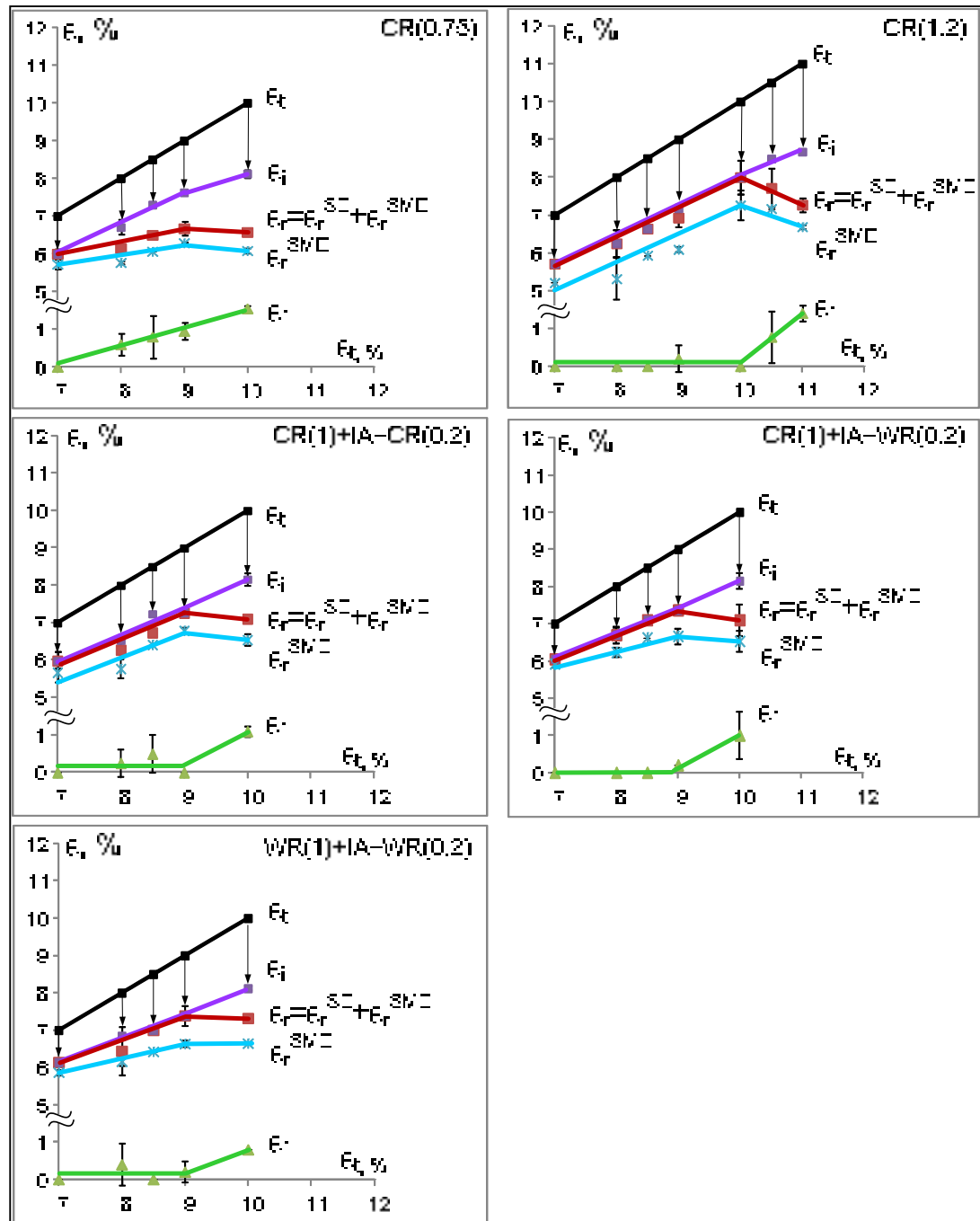


Figure 3.11 Variations in the induced ( $\epsilon_i$ ), recovery ( $\epsilon_r$ ) and residual ( $\epsilon_f$ ) strains of the Ti-50.26 at.%Ni SMA with an increase in the total induced strain ( $\epsilon_t$ ) after TMTs. The regimes of the TMT are indicated in the appropriate figures

The greatest values of the total recovery strain  $\mathcal{E}_r^{\max} = 8\%$  and of the recovery strain upon heating  $\mathcal{E}_r^{SME} = 7.3\%$  are attained in the case of TMT by the regime CR(1.2). After TMT via regimes that include combinations of CR, IA, and WR with the same accumulated strain  $e = 1.2$ , i.e., CR(1)+IA+CR(0.2), CR(1)+IA+WR(0.2), and WR(1)+IA+WR(0.2), these values are lower; i.e.,  $\mathcal{E}_r^{\max}$  is about 7.3% and  $\mathcal{E}_r^{SME}$  is about 6.6%. After TMT via the regime CR(0.75), which includes a much smaller accumulated strain, they are smallest, i.e.,  $\mathcal{E}_r^{\max} = 6.7\%$  and  $\mathcal{E}_r^{SME} = 6.3\%$ . Another important characteristic of the shape recovery of SMAs (the maximum completely recoverable strain) behaves similarly; moreover, after all regimes of TMT with the accumulated strain  $e = 1.2$ , it coincides with  $\mathcal{E}_r^{\max}$  in the limits of error and, for the regime CR(0.75), it is smaller (Table 3.5).

Now, we can compare the results of the experimental determination of the magnitude of the recovery strain (Table 3.5), as well as the results of the resource of the recovery strain calculated with allowance for texture (Table 3.4).

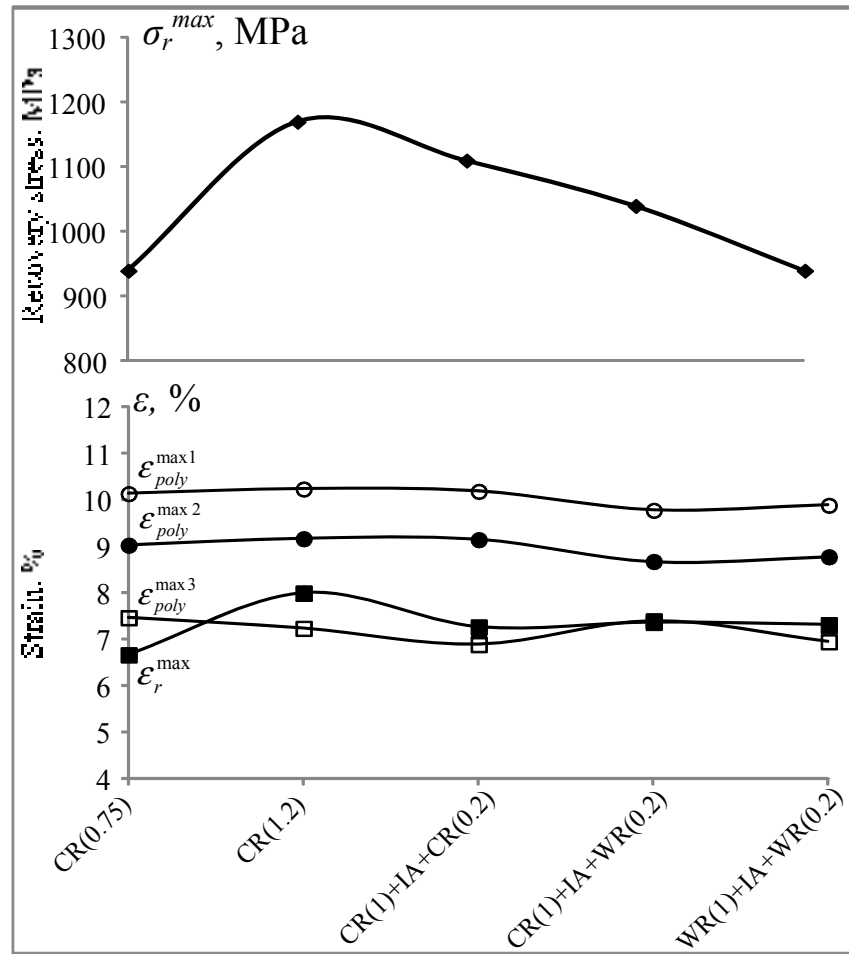


Figure 3.12 Comparison of the experimental values of the recovery strain (Table 3.5), its theoretical resource (calculated by different methods, Table 3.4), and recovery stress (borrowed from [24]) after TMT under different conditions

An analysis of the obtained results (summarized in Figure 3.12) makes it possible to draw the following conclusions:

-Allowance for the pole density of only three orientations ( $\langle 100 \rangle$ ,  $\langle 110 \rangle$ , and  $\langle 111 \rangle_{B2}$ ) does not give an adequate estimation of the resource of the recovery strain, since in three cases out of five (for the regimes CR(1.2), CR(1)+IA+WR(0.2), and WR(1)+IA+WR(0.2)), the experimentally measured maximum recovery strain exceeds the resource calculated by this simplified method.

-The values of the theoretical resource of the recovery strain calculated by other two methods, which take into account the pole densities of many directions ( $\varepsilon_{poly}^{max1}$  and  $\varepsilon_{poly}^{max2}$ ), are greater everywhere than the experimental maximum values of the recovery strain. Since the martensite transformation under the effect of a deformation that is capable of inducing SME occurs under the action of an external stress, we should take the quantity  $\varepsilon_{poly}^{max1}$  as the most adequate theoretical estimation of the resource of the recovery strain of polycrystalline material.

-The degree of resource realization of the recovery strain is greatest after TMT via the regime CR(1.2), which leads to the formation of the least sharp texture of the B2-austenite with the direction  $\langle 110 \rangle$  (coinciding with the rolling direction), but of the greatest amount of NC structures with the smallest grains (Fig. 5c). In the case of the smallest strain accumulated upon rolling (regime CR(0.75)) the ratio  $\varepsilon_r^{max}/\varepsilon_{poly}^{max1}$  is minimum; in the remaining cases, it has an intermediate value. The same ratio is characteristic of the amounts of the maximum completely recoverable strains  $\varepsilon_{r,1}^{max}$ .

-After TMT via all regimes except for CR(0.75), the values of  $\varepsilon_{r,1}^{max}$  and  $\varepsilon_r^{max}$  for this regime do not differ in the limits of error, while after CR(0.75), the value of  $\varepsilon_{r,1}^{max}$  is less than  $\varepsilon_r^{max}$ .

-After TMT via the regime CR(0.75), the residual strain  $\varepsilon_f$  arises at smaller values of  $\varepsilon_t$  than in the case of other regimes of TMT.

In order to understand the origin of the observed features of the thermomechanical behavior of the Ti–50.26 at.%Ni SMA, we have analyzed the relationship between the parameters of the loading–unloading diagram and the values of the maximum recovery stress after different treatments.

*Determination of the maximum recovery stress and the parameters of the loading–unloading diagrams.* Table 3.6 contains the averaged values of the following parameters of the loading–unloading diagrams of the Ti–50.26 at.%Ni SMA after TMT via different regimes:  $E_{unload}$  is the elasticity modulus determined as the slope of the tangent to the upper part of the descending branch of the diagram;  $\sigma_{tr}$  is the transformation yield stress (the critical stress for the start of the stress-induced martensite transformation or for the reorientation of the existing martensite);  $\sigma_i$  is the stress reached at  $\varepsilon_t = 10\%$ ; and  $\sigma_r^{max}$  is the maximum recovery stress (taken from [24]).

A comparison of these parameters after TMT performed via different regimes shows that all regimes that include IA and WR correspond to close force characteristics ( $\sigma_{tr}$  and  $\sigma_i$ ), and the Young's moduli after all regimes are identical in the limits of error. The values of  $\sigma_{tr}$  and  $\sigma_i$  differ from this level to the larger side for the regime CR(1.2) and to the smaller side for the regime CR(0.75).

Table 3.6 Parameters of the loading-unloading diagram of the Ti–50.26 at.%Ni SMA after TMT according to different regimes

Regime of TMT	$\sigma_{tr}$ , MPa	$E_{unload}$ , GPa	$\sigma_i$ , MPa (at $\varepsilon_t = 10\%$ )	$\sigma_r^{max}$ , MPa [24]
CR( 0.75)	144±14	34±2	690±30	940±40
CR(1.2)	238±12	39±3	860±50	1170±50
CR(1)+IA+CR(0.2)	189±24	38±2	740±30	1110±40
CR(1)+IA+WR(0.2)	178±28	37±3	705±35	1040±30
WR(1)+IA+WR(0.2)	170±17	36±3	750±60	940±30

It follows from Table 3.6 that, at identical accumulated strain (in our case,  $e = 1.2$ ), the most hardened state of the Ti–50.26 at.%Ni SMA is achieved through the use of only cold deformation before PDA at 400°C for 1h. The inclusion of warm deformation and intermediate annealing into the TMT schedule significantly decreases the hardening. Finally,

the decrease in the accumulated deformation from  $e = 1.2$  to 0.75 (even in the case of CR) minimizes the resulting strengthening.

### 3.6 Discussion

A comparative analysis of the characteristics of free shape recovery, force characteristics, and structure of the Ti–50.26 at.%Ni SMA makes it possible to consistently explain the observed features of the changes in the maximum recovery strain depending on the regime of a TMT and to estimate the role of the structural and textural factors in the realization of its resource with allowance for the following considerations.

The maximum structural hardening in combination with the least sharp texture in the case of the TMT according to the regime CR(1.2) leads to the formation of a predominantly nanocrystalline (NC) structure of the B2-austenite. This ensures the maximum values of the recovery strain ( $\mathcal{E}_r^{\max} = 8\%$ ) and degree of the realization of its crystallographic resource calculated with allowance for the real texture ( $\mathcal{E}_r^{\max}/\mathcal{E}_{poly}^{\max 1} = 0.79$ ). Obviously, this is a consequence of the effect of the NC structure, which ensures the maximum difference between the dislocation and transformation yield stresses and, correspondingly, the highest shape recovery rate [7].

The minimum structural hardening and, consequently, the minimum difference between the dislocation and transformation yield stresses is observed in the case of the TMT by the regime CR(0.75), which leads to the formation of a mixture of NC + NS structures in combination with a sharp texture. This ensures the minimum value of  $\mathcal{E}_r^{\max}$  (and  $\mathcal{E}_{r,l}^{\max}$ ) which is far from the theoretical resource calculated with taking into account the texture of the B2-austenite ( $\mathcal{E}_r^{\max}/\mathcal{E}_{poly}^{\max 1} = 0.66$ ).

The structural hardening of intermediate value in the case of the TMT by the regimes CR(1)+IA+CR(0.2), CR(1)+IA+WR(0.2), and WR(1)+IA+WR(0.2), which leads to the



formation of a mixed structure with a coarser nanograin of the NC structure, but with a larger dislocation density in the NS structure in combination with a sharp texture ensures intermediate values of  $\varepsilon_r^{\max}/\varepsilon_{poly}^{\max} = 0.72 - 0.75$ .

The incomplete realization of the calculated resource of the recovery strain in the experiment is explained by the fact that in the calculations there were used idealized concepts. The influence of some factors that impede the complete realization of the calculated theoretical resource was neglected. These are factors such as Taylor's condition, which is necessary to guarantee the compatibility of the deformation of adjacent grains and obviously requires the multiplication of the orientational variants of martensite in the near-boundary regions; the nonuniform distribution of deformation in the sample in the case of a relatively large tension, which leads to a local excess of the dislocation yield stress near the stress concentrators; and the formation of a developed dislocation substructure, which impedes the resource motion of the boundaries of crystals and twins.

On the whole, if we neglect these additional factors, the maximum value and the degree of the realization of the resource of the recovery strain is affected by two main factors.

The first, i.e., textural, factor (ODF) determines the theoretical resource of the recovery strain. Upon the appearance and sharpening of the texture in the initially anisotropic polycrystalline austenite, the following changes are possible: (1) if the texture ensures a resource of the recovery strain in the direction of tension that is larger than the resource of the recovery strain in the isotropic polycrystal, then the theoretical resource of the recovery strain will increase; (2) if the texture ensures a resource of the recovery strain in the direction of tension that is less than the resource of the recovery strain in the isotropic polycrystal, then the theoretical resource of the recovery strain will decrease; (3) if the ODF ensures a resource of the recovery strain in the direction of tension that is equal to the resource of the recovery strain in the isotropic polycrystal, then the theoretical resource of the recovery strain will not change.

The role of the second, i.e., structural, factor (lattice defects, which determine structural hardening and, most importantly, the difference between the dislocation and transformation yield stresses) is twofold. First, it determines the degree of the realization of this theoretical resource  $\varepsilon_r^{\max}/\varepsilon_{poly}^{\max}$  (and also the maximum completely recoverable strain  $\varepsilon_{r,l}^{\max}$ , the shape recovery rate  $\varepsilon_r/\varepsilon_i$ ). Second, it also affects the value of the theoretical resource, changing it due to a change in the lattice parameters of martensite [14].

It is obvious that the TMT according to the above regimes, which forms NC and NS structures in the B2-austenite of the Ti–Ni SMA, creates a texture of the same type, with the basic component  $\{100\}\langle 110 \rangle_{B2}$  with different sharpnesses. The corresponding ODFs are such that with all regimes of TMT the value of  $\varepsilon_{poly}^{\max}$  (9.75 – 10.18%) is less than that for the isotropic polycrystal (10.56%). At the same time, it is known that, in the case of the formation of stress-induced martensite from the recrystallized austenite, the characteristics of the shape recovery and the force characteristics of the Ti–Ni SMAs are much lower than those in the NS state and even more so in the NC state [7, 9, 22]. For example, the magnitude of  $\varepsilon_{r,l}^{\max}$  is about 2%, compared to 6.1–8% in the nanostructured states (Table 3.5). Thus, under real conditions, upon a TMT of the Ti–50.26 at.% Ni SMA, including CR, WR, IA, and PDA in different combinations, the basic influence on the amount of recovery strain is due to the structure factor. And the general conclusion is that, for the realization of the maximally high recovery strain, one should focus on to obtaining an NC structure in combination with a strong texture, the ODF of which ensures the maximum transformation deformation in the direction of tension.

### 3.7 Conclusions

Below, we formulate conclusions concerning the results of a comparative study of the structure, crystallographic texture, and functional properties of the Ti–50.26 at.%Ni shape memory alloy subjected to TMT under different conditions via the regimes including different combinations of cold rolling (CR) and warm rolling (WR) to different strains  $\varepsilon$ , and

intermediate annealing (IA), namely, CR( $e=0.75$ ), CR(1.0), CR(1.2), CR (1.0)+IA+CR(0.2), CR(1)+IA+WR(0.2), WR(1)+IA+WR(0.2), WR( $e=1.2$ ). The completing stage in all regimes was post-deformation annealing at 400°C for 1h for the formation of a nanostructure in the B2-austenite.

(1) The electron-microscopic examination revealed the following regularities in the formation of the final structure of the B2-phase of the Ti–50.26 at.%Ni alloy after a post-deformation annealing (PDA) at 400°C for 1h:

(a) the greater the contribution from the cold deformation to the deformation accumulated upon the TMT, the greater the fraction of an NC structure in comparison with the NS structure, and the lower the average dislocation density;

(b) the greater the contribution from the warm deformation (at 150°C) to the accumulated deformation, the greater the fraction of the NS structure in comparison with NC regions and the larger the size of grains, subgrains, and polygonized regions with an NS structure;

(c) the introduction of an intermediate annealing at 400°C for 1 h into the TMT schedule leads to a coarsening of the structure elements: to an increase in the size of NC grains and NS subgrains.

(2) The width of the XRD lines of the B2-austenite determined after PDA at 400°C for 1h increases with an increase in the degree of the accumulated strain upon CR from 0.75 to 1.2. In the case of the deformation accumulated at  $e = 1.2$ , the width of the austenite line is independent of the combination of the CR, WR, and IA treatments, since the contributions from the NC and NS structures to the line broadening under these conditions are approximately identical.

(3) Since the martensite transformation under the effect of an SME-inducing strain occurs under the action of an external stress, the adequate theoretical estimation of the resource of

the recovery strain both of isotropic and textured polycrystalline material must contain a condition necessary for the stress-induced realization of the most favorable orientational variant of martensite in each grain. The calculation of the pole density of only three orientations ( $\langle 100 \rangle$ ,  $\langle 110 \rangle$ , and  $\langle 111 \rangle_{B2}$ ) does not give an adequate estimation of the resource of the recovery strain; therefore, the resource of the recovery strain in a polycrystal should be calculated with the most complete allowance for the ODFs, e.g., as was done in this work, using 12500 orientations within the limits of the standard triangle.

(4) The lattice parameters of the B19'-martensite and the crystallographic resource of the recovery strain in the single-crystal approximation after TMT performed via different regimes do not differ between themselves, although they differ from the appropriate parameters of the martensite that is formed from quenched recrystallized austenite. In the latter case, the crystallographic resource of the recovery strain reaches 11.48%, compared to 10.5–10.88% after TMT. The difference between the resources of the recovery strain calculated in this approximation after usual quenching and TMT is caused by the differences in the lattice parameters of the martensites that are formed from the defect-free recrystallized and highly imperfect nanostructured austenite. The calculation of the theoretical resource of the recovery strain in the approximation of a polycrystal (isotropic after quenching and textured after TMT) according to the method that takes into account the realization of only the most favorable orientational variant of martensite in each grain of austenite yields a similar relationship, i.e., 10.56% after quenching and 9.75–10.18% after TMT.

(5) The basic component of the texture of the austenite of the Ti–50.26 at.%Ni alloy after TMT under all conditions was found to be  $\{100\}\langle 110 \rangle_{B2}$ . The TMT by the regime CR(1)+IA+WR(0.2) leads to the development of the strongest texture of the austenite. The texture of the austenite is much weaker after TMT via the regime CR(1.2); this is explained by the high percentage of arbitrarily oriented austenite grains that are formed upon the nanocrystallization of the amorphous structure in the course of PDA.

(6) The decrease in the strain level upon CR from  $e = 1.2$  to 0.75, just as the inclusion of warm rolling and intermediate annealing into the TMT schedule, leads to a decrease in the magnitude and in the degree of the realization of its resource. The greatest experimental value of the maximum recovery strain  $\varepsilon_r^{\max} = 8\%$  is observed after TMT by the regime CR(1.2); and the smallest value (6.7%), after CR(0.75). The intermediate values,  $\varepsilon_r^{\max} = 7.2\text{--}7.4\%$ , are observed after TMT under the other conditions. The same relationships are characteristic of the values of the degree of the resource realization of the recovery strain  $\varepsilon_r^{\max}/\varepsilon_{poly}^{\max l}$  (0.79: 0.66: 0.72–0.75) and the amount of the maximum completely recoverable strain  $\varepsilon_{r,l}^{\max}$  (8: 6.1: 7.3).

(7) The values of the maximum recovery stress and of the stress that corresponds to the strain by tension to 10%, which characterize the level of hardening of the Ti–50.26 at.%Ni SMA, are the greatest in the case of TMT by the regime CR(1.2) and smallest in the case of CR(0.75). After TMT, under other conditions, they take on intermediate values.

(8) The magnitude of the recovery strain resource and the degree of its realization in the polycrystalline SMA are affected by two basic factors. The textural factor (orientation distribution function) determines the theoretical resource of the recovery strain  $\varepsilon_{poly}^{\max l}$ . The role of the structural factor (lattice imperfection, which determines structural hardening and, first of all, the difference between the dislocation and transformation yields stresses) is twofold. First, it determines the degree of the realization of the theoretical resource of the recovery strain  $\varepsilon_r^{\max}/\varepsilon_{poly}^{\max l}$ , and also the maximum completely recoverable strain  $\varepsilon_{r,l}^{\max}$  and the degree of the shape recovery  $\varepsilon_r/\varepsilon_i$  and, second, it also influences the value of the theoretical resource, changing it via the changes in the lattice parameters of martensite.

(9) Under the real conditions of the TMT of the Ti–50.26 at.%Ni SMA, which includes CR, WR, IA and PDA in different combinations, the basic influence on the amount of the recovery strain comes from the structure factor. However, to achieve a maximally high

recovery strain, one should focus on obtaining an NC structure in combination with a strong texture, the ODF of which should ensure the maximum transformation deformation in the direction of tension.

### **3.8 Acknowledgments**

This work was supported in part by the Ministry of Education and Science of the Russian Federation and by the Natural Science and Engineering Research Council of Canada.

### **3.9 References**

1. Shape Memory Materials, Ed. by K. Otsuka and C. M. Wayman (Cambridge Univ., Cambridge, 1999).
2. Engineering Aspects of Shape Memory Alloys, Ed. By T. W. Duerig, K. N. Melton, D. Stockel, and C. M. Wayman (Butterworth-Heinemann, London, 1990).
3. Shape Memory Alloys: Fundamentals, Modeling and Applications, V. Brailovski, S. Prokoshkin, P. Terriault, and F. Trochu, Eds. (ETS, Montreal, 2003).
4. S. D. Prokoshkin, V. G. Pushin, E. P. Ryklina, and I. Y. Khmelevskaya, "Application of titanium nickelide-based alloys in medicine," *Phys. Met. Metallogr.* 97 (Suppl. 1), S56–S96 (2004).
5. Alloys with Shape Memory and Their Application in Medicine, Ed. by L. A. Monasevich (Nauka, Novosibirsk, 1992) [in Russian].
6. V. Brailovski, S. D. Prokoshkin, K. E. Inaekyan, and V. Demers, "Functional properties of nanocrystalline, submicrocrystalline and polygonized Ti–Ni alloys processed by cold rolling and post-deformation annealing," *J. Alloys Compd.* 509, 2066–2075 (2011).

7. V. Brailovski, S. D. Prokoshkin, I. Yu. Khmelevskaya, K. E. Inaekyan, V. Demers, S. V. Dobatkin, and E. V. Tatyannin, "Structure and properties of the Ti–50.0 at%Ni alloy after strain hardening and nanocrystallizing thermomechanical processing," *Mater. Trans.* 47, 795–804 (2006).
8. S. D. Prokoshkin, V. Brailovski, S. Turenne, I. Y. Khmelevskaya, A. V. Korotitskiy, and I. V. Trubitsyna, "Concentration, temperature and deformation dependences of martensite lattice parameters in binary Ti–Ni shape memory alloys," *J. Phys. IV* 112, 651–654 (2003).
9. S. D. Prokoshkin, V. Brailovski, K. E. Inaekyan, V. Demers, I. Yu. Khmelevskaya, S. V. Dobatkin, and E. V. Tatyannin, "Structure and properties of severely cold-rolled and annealed Ti–Ni shape memory alloys," *Mater. Sci. Eng., A* 481–482, 114–118 (2008).
10. S. D. Prokoshkin, V. Brailovski, I. Yu. Khmelevskaya, S. V. Dobatkin, J. E. Inaekyan, V. Yu. Turilina, V. Demers, and E. V. Tat'yannin, "Creation of substructure and nanostructure by thermomechanical treatment and control of properties of Ti–Ni alloys with shape memory effect," *Metal Sci. Heat Treatment* 47, 182–187 (2005).
11. S. D. Prokoshkin, V. Brailovski, S. Turenne, I. Yu. Khmelevskaya, A. V. Korotitskiy, and I. V. Trubitsyna, "On the lattice parameters of the B19-martensite in binary Ti–Ni shape memory alloys," *Phys. Met. Metallogr.* 96, 55–64 (2003).
12. S. D. Prokoshkin, A. V. Korotitskiy, V. Brailovski, D. Turenne, I. Yu. Khmelevskaya, and I. B. Trubitsyna, "On the lattice parameters of phases in binary Ti–Ni shape memory alloys," *Acta Mater.* 52, 4479–4492 (2004).
13. E. P. Ryklina, S. D. Prokoshkin, and A. Yu. Kreysberg, "Abnormally high recovery strain in Ti–Ni-based shape memory alloys," *J. Alloys Compd.* 577 (Suppl. 1) 255–258 (2013).

14. S. D. Prokoshkin, A. V. Korotitskiy, V. Brailovski, K. E. Inaekyan, and S. M. Dubinskiy. "Crystal lattice of martensite and the resource of recoverable strain of thermally and thermomechanically treated Ti–Ni shape-memory alloys," *Phys. Met. Metallogr.* 112, 170–188 (2011).
15. S. Miyazaki, S. Kimura, K. Otsuka, and Y. Suzuki, "The habit plane and transformation strains associated with martensitic transformation in Ti–Ni single crystals," *Scr. Metall.* 18, 883–888 (1984).
16. T. Saburi, M. Yoshida, and S. Nenno, "Deformation behavior of shape memory Ti–Ni alloy crystals," *Scr. Metall.* 18, 363–366 (1984).
17. T. E. Buchheit and J. A. Wert, "Modeling the effects of stress state and crystal orientation on the stress-induced transformation of NiTi single crystals," *Metall. Mater. Trans. A* 25, 2383–2389 (1994).
18. H. Inoue, N. Miwa, and N. Inakazu, "Texture and shape memory strain in TiNi alloy sheets," *Acta Mater.* 44, 4825–4834 (1996).
19. Y. C. Shu and K. Bhattacharya, "The influence of texture on the shape-memory effect in polycrystals," *Acta Mater.* 46, 5457–5473 (1998).
20. L. Zhao, P. F. Willemse, J. H. Mulder, J. Beyer, and W. Wei, "Texture development and transformation strain of a coldrolled Ti50–Ni45–Cu5 alloy," *Scr. Mater.* 39, 1317–1323 (1998).
21. S. Miyazaki, K. Otsuka, and C. M. Wayman, "The shape memory mechanism associated with the martensitic transformation in Ti–Ni alloys. I. Self-accommodation," *Acta Metall.* 37, 1873–1884 (1989).



22. V. Demers, V. Brailovski, S. Prokoshkin, and K. Inaekyan, "Thermomechanical fatigue of nanostructured Ti–Ni shape memory alloys," *Mater. Sci. Eng., A* 513–514, 185–196 (2009).
23. Y. Facchinello, V. Brailovski, T. Georges, S. D. Prokoshkin, and S. M. Dubinskiy, "Manufacturing of nanostructured Ti–Ni shape memory alloys by means of cold/warm rolling and annealing thermal treatment," *J. Mater. Proc. Technol.* 212, 2294–2304 (2012).
24. A. Kreitchberg, V. Brailovski, S. Prokoshkin, Y. Facchinello, K. Inaekyan, and S. Dubinskiy, "Microstructure and functional fatigue of nanostructured Ti–50.26 at % Ni alloy after thermomechanical treatment with warm rolling and intermediate annealing," *Mater. Sci. Eng., A* 562, 118–127 (2013).
25. A. Kreitchberg, V. Brailovski, S. D. Prokoshkin, and K. Inaekyan, "Influence of thermomechanical treatment on structure and crack propagation in nanostructured Ti–50.26 at. % Ni alloy," *Metallogr., Microstruct., Analysis* 3, 46–57 (2014).
26. H. J. Bunge, *Texture Analysis in Materials Science Mathematical Methods* (Butterworths, London, 1982).
27. S. D. Prokoshkin, V. Brailovskii, A. V. Korotitskii, K. E. Inaekyan, and A. M. Glezer, "Specific features of the formation of the microstructure of titanium nickelide upon thermomechanical treatment including cold plastic deformation to degrees from moderate to severe," *Phys. Met. Metallogr.* 110, 289–304 (2010).
28. S. D. Prokoshkin, I. Y. Khmelevskaya, S. V. Dobatkin, I. B. Trubitsyna, E. V. Tatyatin, V. V. Stolyarov, and E. A. Prokofiev, "Alloy composition, deformation temperature, pressure and post-deformation annealing effects in severely deformed Ti–Ni based shape memory alloys," *Acta Mater.* 53, 2703–2714 (2005).

29. D. L. Holt, "Dislocation cell formation in metals," *J. Appl. Phys.* 41, 3197–3201 (1970).
30. M. L. Bernshtein, S. V. Dobatkin, L. M. Kaputkina, and S. D. Prokoshkin, *Diagrams of Hot Deformation, Structure and Properties of Steels* (Metallurgiya, Moscow, 1989) [in Russian].

## CHAPTER 4

### ARTICLE #3

#### INFLUENCE OF THERMOMECHANICAL TREATMENT ON STRUCTURE AND CRACK PROPAGATION IN NANOSTRUCTURED Ti-50.26 at.%Ni ALLOY

A. Kreitchberg<sup>1,2</sup>, V. Brailovski<sup>1</sup>, S. Prokoshkin<sup>2</sup> and K. Inaekyan<sup>1</sup>

<sup>1</sup> Ecole de Technologie Supérieure, Montreal, Canada

<sup>2</sup> National University of Science and Technology “MISIS”, Moscow, Russia

This article was published

in *Metallography, Microstructure, and Analysis*, 2014, v. 3, no. 1, pp. 46-57.

#### 4.1 Summary

This article was focused on an in-depth study of interrelations between the rolling-induced damage, material structure and fatigue life of Ti-50.26 at.%Ni alloy subjected to different TMT routes selected from the first article. After PDA at 400°C (1h), the sample edges were polished to 60-90% of their initial width. The optical microscopy was used to measure the size and concentration of microcracks on the sample edges before and after mechanical polishing. The functional fatigue life was evaluated by superelastic and recovery stress generation-relaxation testing.

The mechanical polishing of sample edges led to a decrease of length and concentration of microcracks. However, this polishing does not result in the complete disappearance of edge cracks. Moreover, a so-called “small-crack behavior” was observed in the mixed nanocrystalline and nanosubgrained structures: when the crack length dropped under 15 µm in size, the smaller the crack length, the lower the fatigue life. On the contrary, the nanocrystalline structure showed higher tolerance to the small crack propagation than does the nanosubgrained structure.

## 4.2 Abstract

The fatigue propagation of processing-induced microcracks in severely deformed Ti-50.26 at.%Ni alloy's samples was investigated. The processing schedules included cold rolling with logarithmic strains of  $\varepsilon = 0.75$  and 1.2, and a combination of cold rolling ( $\varepsilon = 1$ ), intermediate annealing (400°C, 1h) and warm rolling ( $\varepsilon = 0.2$ ,  $T = 150^\circ\text{C}$ ). The final step of the thermomechanical processing schedules consisted of post-deformation annealing at 400°C, 1h. The resulting microstructures were studied using transmission electron microscopy. Using optical microscopy, the processing-induced edge cracks' lengths and concentrations were measured before and after multicycle superelastic and stress generation/relaxation testing. From the functional fatigue point of view, nanocrystalline microstructure demonstrated higher tolerance to small cracks than mixed nanocrystalline + nanosubgrained structure.

**Keywords:** rolling, electron microscopy, mechanical testing, optical microscopy, failure analysis.

## 4.3 Introduction

The current interest in nanocrystalline (NC) Ti–Ni shape memory alloys is justified by their high mechanical and functional properties, such as strength, hardness, and recovery strain/stress [1–4]. However, the fatigue life of NC Ti–Ni alloys remains insufficiently explored compared to that of their coarse (CG), fine (FG), or ultrafine-grained (UFG) counterparts, which is witnessed by a rather limited number of relevant publications [5–10]. In these publications, severe plastic deformation by rolling is used for nanostructure formation, with an evident detrimental impact on the surface quality and therefore on the functional fatigue life of the processed materials.

Generally, when a sample is subjected to cyclic loading, two mechanisms are responsible for fatigue failure: crack initiation and crack propagation. Under high-cycle fatigue conditions, the crack propagation phase dominates the fatigue lifetime to a large extent. Under low-cycle

fatigue conditions however, the crack initiation phase is a dominant factor of the fatigue life [11]. In order to enhance the fatigue resistance, either the crack initiation or the crack propagation (or both) should be hindered.

In many CG metals, fatigue crack initiation occurs frequently due to the formation of surface extrusions and intrusions caused by persistent slip bands. In NC metals, both internal and surface defects have been noted as nucleation sites for fatigue cracks. The internal crack initiation in NC materials depends on the dominant deformation mechanisms in these materials, and can be due to dislocation emission from grain boundaries [12–15], deformation twinning [12, 16–18], grain-boundary sliding [15, 16, 18], or grain rotation [17, 18].

Hanlon et al. [19, 20] showed that under stress-controlled fatigue testing conditions, crack initiation on the smooth surface of NC and UFG Ni samples is inhibited, which results in their higher endurance limit. However, in the case of pre-existing cracks in NC materials, as the grain size reduces, the resistance to crack propagation diminishes due to the reduction of crack path tortuosity and the diminishing contribution of the plasticity-induced crack closure-related phenomena [11]. As suggested by Rice and Thomson [21], at the crack tip, there is a competition between crack blunting (i.e., dislocation nucleation) and crack advancement. In NC materials, the emission of dislocations from the crack tip is limited by the small grain size due to dislocation repulsion and, therefore, the blunting is partially suppressed [22]. Consequently, the NC solids frequently tend to show brittle behavior.

However, the experimental results are not always in agreement with this simple explanation. For example, according to [19, 23, 24], for Ni and Ni–Co samples, the trend: the smaller the grain size, the greater the crack propagation rate, only appeared at higher load ratios ( $R > 0.3$ ), while being irrelevant at low load ratios ( $R = 0.1$ ).

In the case of Ti–Ni shape memory alloys, defect accumulation and crack initiation and propagation mechanisms are even more complicated than in the case of conventional metallic

materials. One study [25] found that stable martensite and austenite have similar threshold stress intensity factors (around  $\Delta K_{tr}=3 \text{ MPa}\sqrt{\text{m}}$ ) and that this value decreases as the load ratio increases. On the other hand, stable austenite and martensite have higher fatigue resistance than the same material subjected to repetitive stress-induced martensite transformation [25, 26]. Mechanical cycling through the strain range of direct and reverse martensitic transformations leads to transformation-induced hardening, oriented internal stress generation, permanent strain accumulation, stabilization of martensite, and austenite with an overall negative impact on the fatigue life.

Furthermore, crystallographic anisotropy in the region ahead of the advancing crack tip, i.e., the texture of the material, has a strong influence on crack propagation. For example, in polycrystalline Ti–50.8 at.%Ni alloy, transgranular cracks propagate more easily along the low Miller index planes as  $\{001\}$  and  $\{110\}$  of B2-austenite [27].

In conclusion, by considering the fatigue life of Ti–Ni alloys, the material microstructure, the surface quality, the deformation mechanisms during thermomechanical cycling, and the crystallographic texture should all be taken into account. The influence of the material structure [NC, nanosubgrained (NS), or their mixture] and of the processing-induced crack size and concentration on the number of superelastic cycles to failure of Ti–50.26 at.%Ni samples with the same texture component is analyzed in this study.

#### 4.4 Experimental

A Ti–50.26 at.%Ni alloy was studied. A 1 mm diameter as-drawn ( $\Delta F/F = 30\%$  of cold work) wire was primarily subjected to homogenization annealing (700°C, 1h) and then to various thermomechanical treatments (TMTs), which included cold rolling (CR), warm rolling (WR), intermediate annealing (IA), and post-deformation annealing (PDA) steps in different combinations. The rolling was performed using a four-high laboratory rolling mill under pulling tension corresponding to 10% of the material's yield stress at the mill's entry; the rolling speed was 10 mm/s. WR was carried out at 150°C ( $\sim 0.15 \cdot T_m$  [K]). This temperature

does not correspond to the conventionally accepted temperature of warm deformation (generally above  $0.3T_m$ ), but it is the highest deformation temperature for this alloy that allows the initiation of a pronounced strain-induced amorphization and therefore creation of various nanostructures after PDA. To reach this temperature, the wire was in-line heated by electrical current (Joule effect) using a custom heating unit (described in detail in [7]). Both the IA and PDA heat treatments were performed at 400°C (1h) using a heating furnace, with subsequent water-quenching at room temperature.

The following three TMT routes resulting in different Ti–Ni alloy's nanostructures—ranging from NS to NC - but manifesting competitive fatigue lives [8] were selected for this study (Figure 4.1):

- Routes 1-2, CR  $\varepsilon = 0.75$  (4 passes) and  $\varepsilon = 1.2$  (6 passes): CR(0.75) and CR(1.2); where  $\varepsilon$  is a true (logarithmic) strain.
- Route 3, CR  $\varepsilon = 1$  (5 passes)+IA+WR  $\varepsilon = 0.2$  (one pass): CR(1)+IA+WR(0.2).

Identical PDA (400 °C, 1h) was carried out following each of the TMT routes.

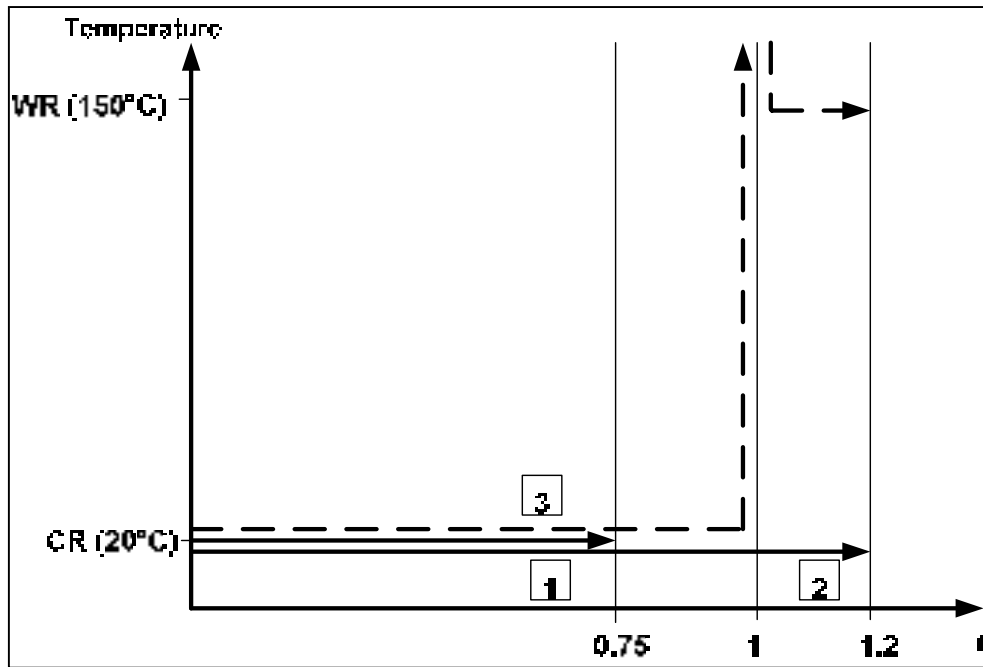


Figure 4.1 Schematic representation of the three processing routes

### Microstructure and crystallographic texture

Thin foils for electron microscopy were cut by the electroerosion method and then thinned by mechanical and electrolytical polishing.

The texture analysis was performed using an x-ray diffractometer with Cu  $K_{\alpha}$ -radiation. Samples were cut along the rolling direction and the surface layer was etched. The scanning for  $(110)_{B2}$ ,  $(200)_{B2}$ ,  $(211)_{B2}$  pole figures was carried out at  $A_f + 10^{\circ}\text{C}$  temperature with  $\Delta\alpha = \Delta\beta = 5^{\circ}$  azimuthal steps and with the radial angle of inclination  $\alpha_{max}$  varying from 0 to  $75^{\circ}$ . Both direct and inverse pole figure methods were used. The orientation distribution functions (ODF) were built in accordance with [28]. Since the width of each individual sample was about 1.6 mm, a side-by-side stack of 4-5 parallel samples was used for each measurement.



### Processing-induced crack size and concentration

To assess the degree of the processing-induced material damage (length and concentration of edge microcracks), the edges of 70-mm-long ribbons with different as-processed widths:  $h_0 = 1.6$  mm (after  $\varepsilon = 1.2$ ) and  $h_0 = 1.4$  mm (after  $\varepsilon = 0.75$ ) were gradually polished to 0.9, ..., 0.6 of their initial values (Figure 4.2). The final width of samples was therefore  $h_f = 1.6, 1.4, 1.2, 1.1, 1.0$ , and  $0.9$  mm (after  $\varepsilon = 1.2$ , Routes 2 and 3) and  $h_f = 1.4, 1.2, 1.1, 1.0, 0.84$ , and  $0.74$  mm (after  $\varepsilon = 0.75$ , Route 1). The metallographic analysis of the mechanically polished samples was performed. Using 30–40 mm sampling lengths, the edge crack length distribution, the average crack length ( $a$ , mm), and their concentration ( $N_c$ , cracks/mm) were evaluated using light microscopy with 50 $\times$  to 600 $\times$  magnifications (Figure 4.3). The number of cracks considered for this evaluation varied from 300 to 520 for each specimen.

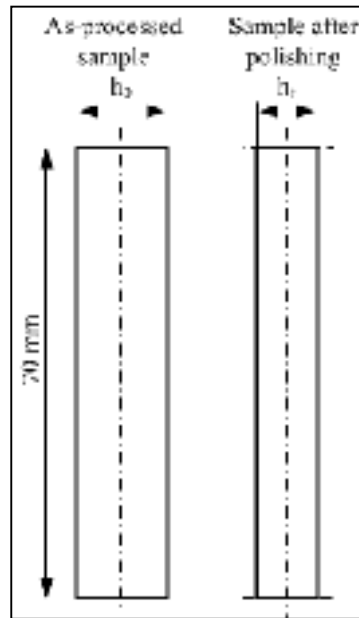


Figure 4.2  
Example of sample  
width reduction

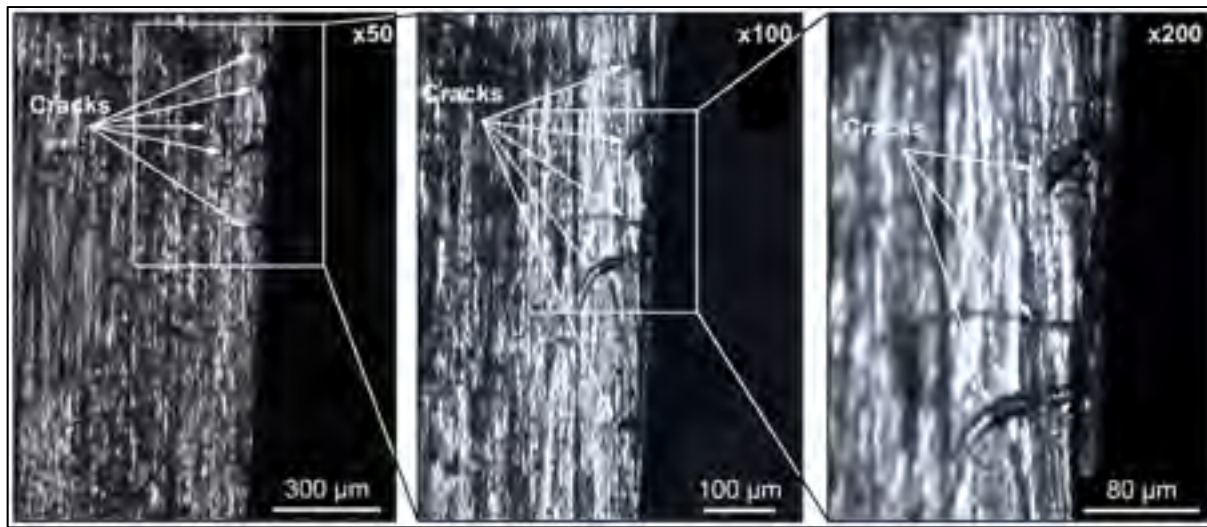


Figure 4.3 Example of crack measurement after CR(1.2)+PDA

### Multi-cycle testing

For multicycle superelastic and stress generation–relaxation thermomechanical testing, mechanically polished 70-mm-long samples were used. Four samples of each width were used for superelastic testing and one sample of each width was used for stress generation–relaxation testing.

The superelastic testing was carried out using a mechanical-testing machine equipped with a thermal chamber. The sample was heated up to  $A_f + 10^\circ\text{C}$  temperature, strained up to a total strain of  $\varepsilon_t = 3\%$  (Figure 4.4a, A–B), then unloaded (B–C). The test was repeated to sample failure, and the number of cycles to failure ( $N_f$ ) was noted.

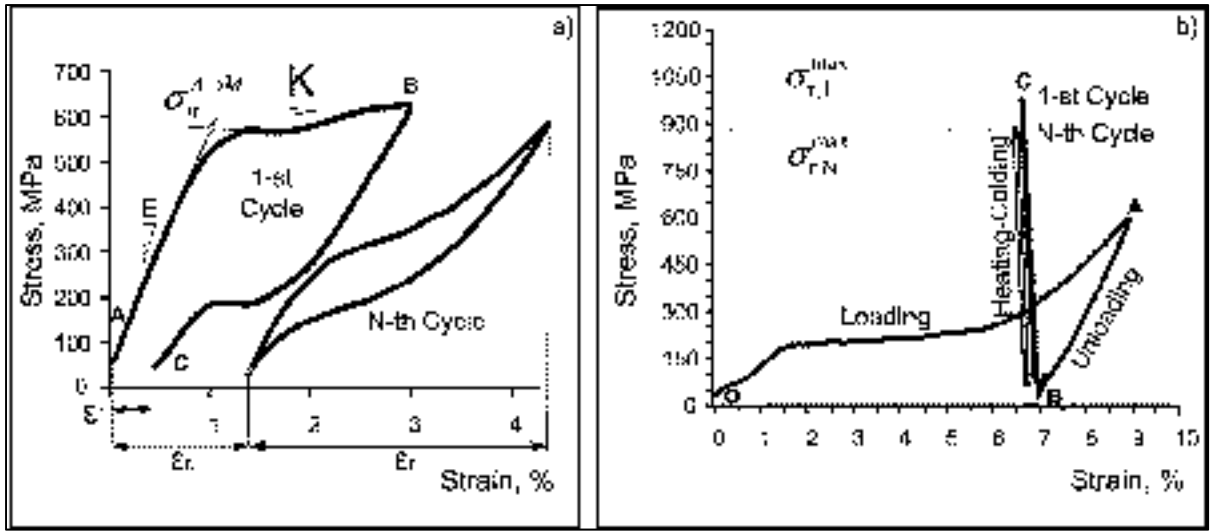


Figure 4.4 Stress-strain plots for the  $N=1$  and  $N^{\text{th}}$  cycles of Ti-50.26%Ni samples: a) superelastic testing after CR(1.2)+PDA (400°C, 1h), and b) stress generation-relaxation testing after CR(1.0)+IA+WR(0.2)+PDA (400°C, 1h)

The confidence error was calculated as:

$$\delta_{\bar{X}} = \frac{t_{0.95,(n-1)}}{\sqrt{n}} \cdot \left( \frac{\sum_{i=1}^n (\bar{X} - X_i)}{n-1} \right)^{\frac{1}{2}} \quad (4.1)$$

where  $X_i$  is the measured value of  $X$  in the  $i$ -th cycle,  $\bar{X}$  is the mean value,  $n$  is the number of measurements, and  $t_{0.95,(n-1)}$  is the Student's confidence coefficient probability  $P=0.95$ , and  $\kappa=n-1$  degrees of freedom.

The generation-relaxation (constrained recovery) testing was carried out using a custom made testing bench [5]. The sample was strained up to  $\varepsilon_t = 9\%$  (Figure 4.4b, O–A) at RT, then released to allow elastic springback (A–B). The initial (induced) strain was thus set at  $\varepsilon_i = 6\text{--}7\%$ . Afterward, the sample was kept fixed and then heated from room temperature to 200 °C to allow an almost complete reverse martensitic transformation and recovery stress generation,  $\sigma_r$  (B–C), and finally air-cooled to room temperature. The constrained

thermocycling in the RT–200°C range was repeated to sample failure, and the number of cycles to failure ( $N_f$ ) was noted.

### **Processing-induced crack size and concentration**

To assess the influence of the material structure on the crack propagation, all the samples were mechanically polished to an identical 1 mm width, irrespective of the processing conditions, and the edge crack length distribution and the average crack length were evaluated using the procedure described in “Processing-Induced Crack Size and Concentration” section. Afterward, the samples were subjected to 500-cycle superelastic testing (Figure 4.4a), and the edge crack length distribution and the average crack length were again evaluated.

## **4.5 Experimental results**

### **Electron microscopy study**

As the electron microscopy study shows, two types of nanostructure - in different proportions - are formed in B2-austenite after different processing routes: (a) a NS structure with nanosized ( $\leq 100$  nm) subgrains, i.e., structure elements surrounded by low-angle boundaries and formed as a result of polygonization of the dislocation substructure; (b) a NC structure with nanosized grains surrounded by high-angle boundaries and formed as a result of crystallization of the amorphous phase. Particular features of these nanostructures are discussed below.

#### *Route CR(0.75), Figure 4.5(a, b)*

With this processing, a mixed nanostructure is present after PDA. This structure includes alternating NS and NC regions (Figure 4.5a, b, respectively) in approximately equal quantities. The grain size in the NC structure is in the 15–80 nm range. The NS regions with average size of about 350 nm consist of closely oriented  $\leq 100$  nm subgrains and contain

high dislocation density. The microdiffraction patterns consist of fragmented arcs formed by closely located point-wise reflections (NS) (Figure 4.5a) or of individual reflections distributed along diffraction rings (NC) (Figure 4.5b). These TEM images and SAED patterns are typical for the NS and NC structures, as shown in detail in [29].

*Route CR(1.2), Figure 4.5(c)*

According to the bright- and dark-field images, a mainly NC structure with grain size in the 15–70 nm range is observed. Dark-field images indicate the presence of a relatively small amount (about 10–15%) of NS structure, which is identified as sparse “shining” nanosized (up to 150 nm) agglomerations containing several closely oriented (and therefore simultaneously shining) subgrains. Electron microdiffraction patterns contain dotted rings with a rather uniform orbital distribution of point-wise reflections, which is typical for NC structures.

*Route CR(1)+IA+WR(0.2), Figure 4.5(d, e)*

This TMT route results in a mostly NC structure, which is similar to CR(1.2). However, grain size after this route is in the 50–120 nm range, which is 1.5–2 times larger than after the CR(1.2) route. The NS structure is also present (conglomerates of subgrains sized under 200 nm), which means that this TMT route occupies an intermediate position between CR(0.75) and CR(1.2) as far as the resulting material microstructure ranges from NS to NC.

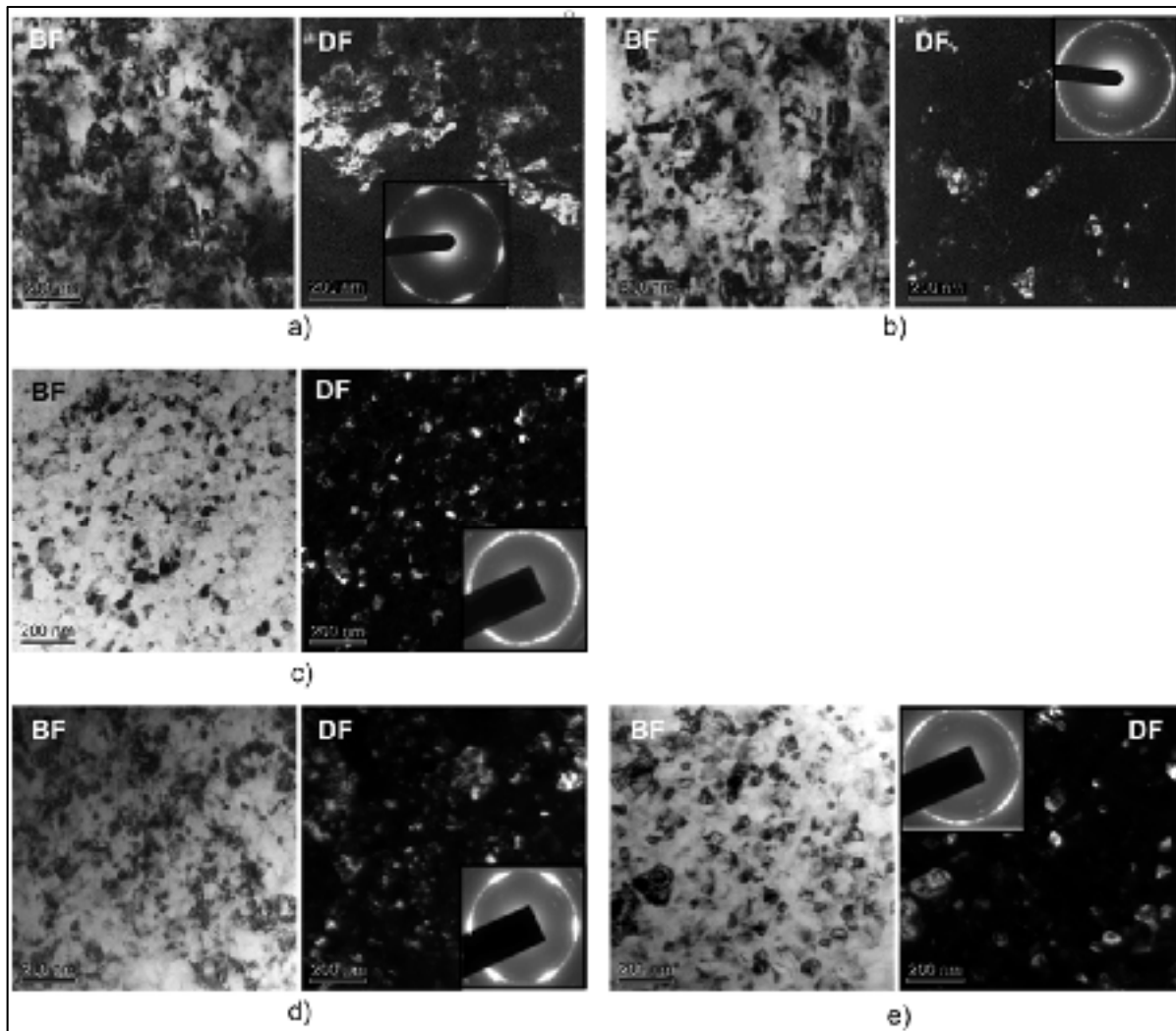


Figure 4.5 Structure of Ti-50.26%Ni alloy after selected TMT routes:  
a, b) CR(0.75); c) CR(1.2); and d, e) CR(1)+IA+WR(0.2). Left to right: bright-field image, dark-field image, electron diffraction pattern

### Texture Analysis

The ODFs and an inverse pole figure calculated on the basis of three pole figures: (110), (200), and (211), made it possible to conclude that the main austenite texture component in Ti-50.26 at.%Ni alloy after all the processing routes is  $\{100\}\langle 011 \rangle$  (Figure 4.6). This study is described in more detail in [8].

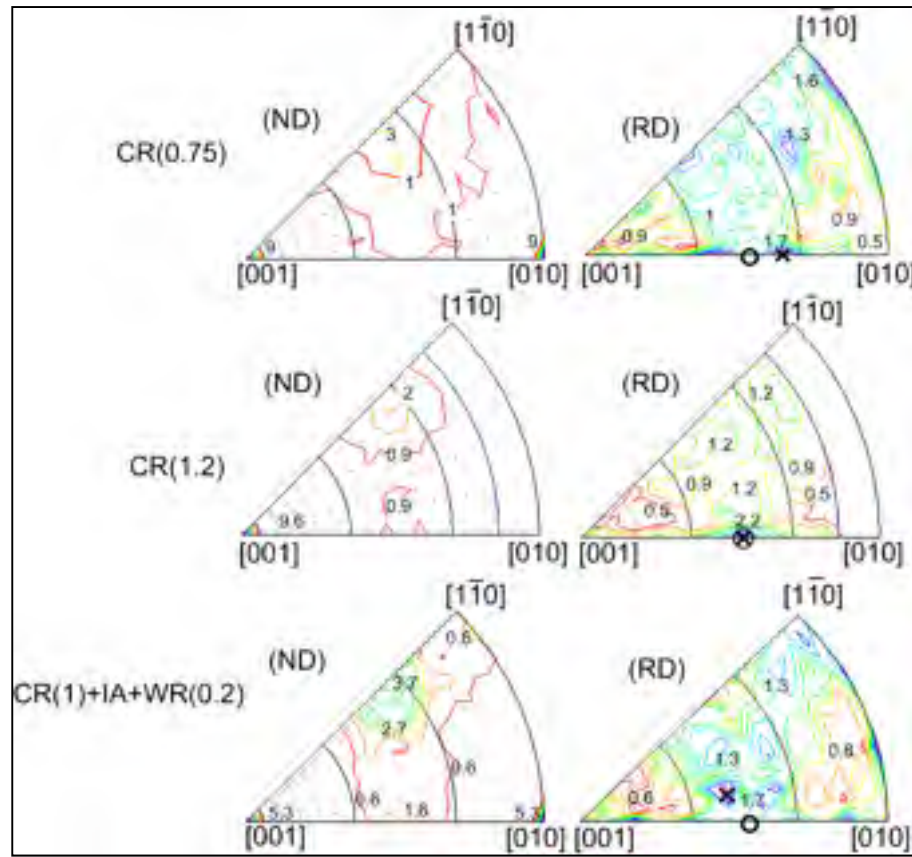


Figure 4.6 Texture of Ti-50.26 at.%Ni after CR(1.2), CR(0.75), and CR(1)+IA+WR(0.2): inverse pole figures corresponding to the normal direction (ND) and rolling direction (RD): x - [uvw] pole, o - [011]B2 pole

### Metallographic Analysis of the Processing-Induced Material Damage (Edge Microcracks)

A metallographic analysis of edge microcrack length and concentration after CR(0.75), CR(1.2), and CR(1)+IA+WR(0.2) routes was conducted. The results are collected in Figure 4.7. Just after CR(0.75), the average crack length was  $16 \pm 2 \mu\text{m}$ , and the crack concentration was  $19 \pm 3$  cracks/mm. The crack length (concentration) increased to  $25 \pm 3 \mu\text{m}$  ( $22 \pm 3$  cracks/mm) when CR intensity reached  $\varepsilon = 1.2$ . When IA was included in the TMT sequence, CR(1)+IA+WR(0.2), the crack length (concentration) reduced to  $17 \pm 2 \mu\text{m}$  ( $19 \pm 3$  cracks/mm).

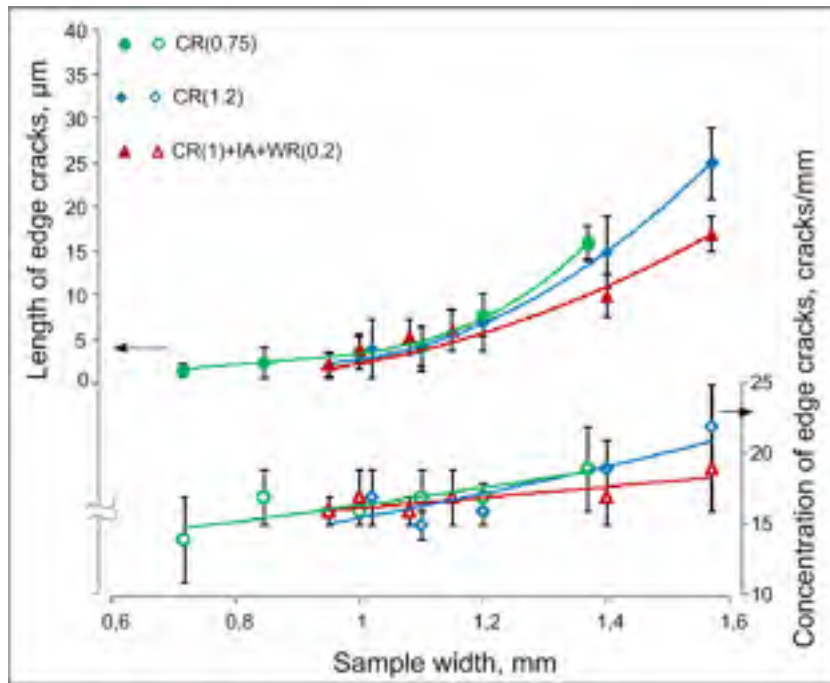


Figure 4.7 Variation of crack length and concentration after mechanical polishing of Ti-50.26 at.%Ni samples processed by different TMTs: CR(0.75), CR(1.2) and CR(1)+IA+WR(0.2)

After mechanical polishing of the samples' edges, the average crack length decreased exponentially for all the processing routes to reach a common 2–3  $\mu\text{m}$  length, when the samples' width approached 60% of their initial value (Figure 4.7). The average crack concentration also decreased, to reach 16–17 cracks/mm for all the TMT conditions (Figure 4.7). It should be noted that at the end of polishing, some cracks were still noticeable; further polishing did not lead to their total disappearance.

The crack length distributions for the as-processed and for the 1-mm width polished samples are compared in Figure 4.8. After CR(0.75), the majority of cracks (70%) are in the 5–30  $\mu\text{m}$  range; after CR(1.2), they are in the 20–90  $\mu\text{m}$  range and after CR(1)+IA+WR(0.2), in the 10–35  $\mu\text{m}$  range (Figure 4.8a). After polishing to 1 mm of width, the majority of cracks are situated in the 1–5  $\mu\text{m}$  range irrespective of the TMT conditions (Figure 4.8b).



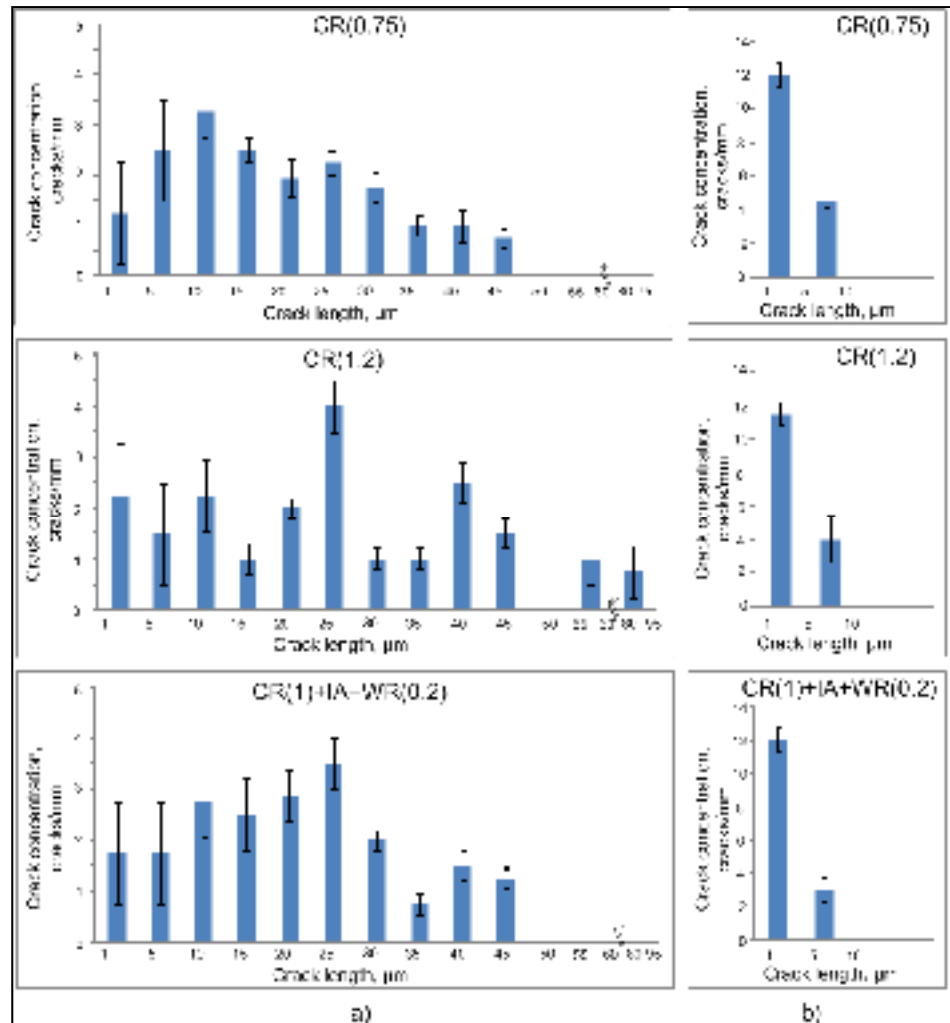


Figure 4.8 Distribution of crack length of Ti-50.26 at.%Ni alloy after CR(0.75), CR(1.2) and CR(1)+IA+WR(0.2): a) as-processed; b) after polishing to a 1.0 mm width

### Multicycle Testing

The results of the superelastic testing of the as-processed and polished samples after CR(0.75), CR(1.2), and CR(1)+IA+WR(0.2) TMT routes are shown in Figure 4.9(a). It can be seen that before polishing, the maximum numbers of cycles to failure ( $N_f = 2440 \pm 260$  and  $N_f = 2940 \pm 380$ , respectively) were observed after CR(0.75) and CR(1)+IA+WR(0.2), this number ( $N_f = 1680 \pm 50$ ) was significantly lower after the CR(1.2) processing schedule.

Surprisingly the polishing of the CR(0.75) and CR(1)+IA+WR(0.2)-processed samples led to a considerable decrease in their superelastic fatigue life, whereas the CR(1.2)-processed samples did not show any sensibility to the specimen width and therefore to crack length reduction caused by polishing. When the specimen width fell under 0.9 mm, CR(1.2)-processed specimens manifested the longest fatigue life, whereas CR(0.75) manifested the shortest fatigue life as compared to their competitors, which is contrary to what was observed with just-processed unpolished specimens (Figure 4.9a).

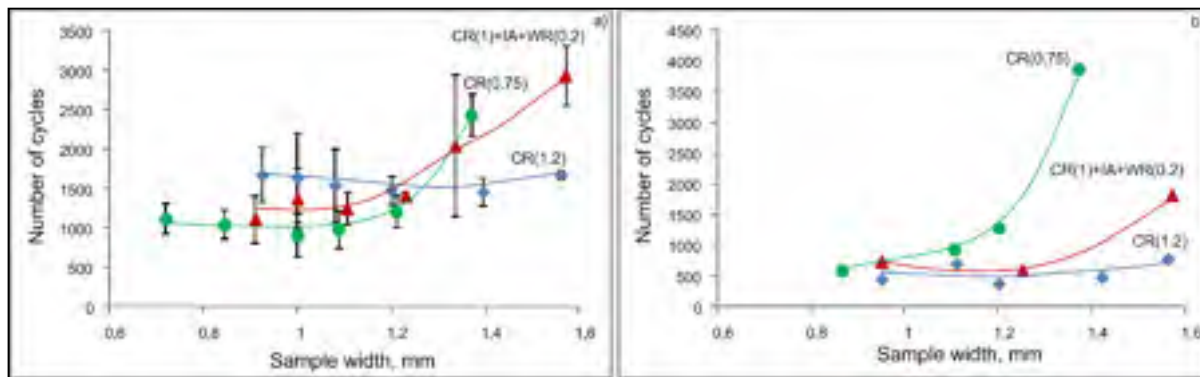


Figure 4.9 Fatigue life of Ti-50.26 at.%Ni samples as a function of the sample width (mechanical polishing): (a) superelastic testing; (b) constrained recovery testing

The results of the multiple cycle stress generation-relaxation testing before and after polishing are shown in Figure 4.9b and they corroborate the results obtained in superelastic testing. It can be observed that before mechanical polishing of the samples edges, the CR( $\epsilon = 0.75$ ) route resulted in the longest fatigue life among all the processing routes, whereas it became the shortest after CR( $\epsilon = 1.2$ ). CR(1)+IA+WR(0.2) resulted in an intermediate length of cycling life. As in the previous test, after polishing of CR(0.75) and CR(1)+IA+WR(0.2)-processed samples, their fatigue life dropped when the specimen width and therefore the crack length were reduced. On the contrary, the CR(1.2)-processed samples again showed an absence of sensitivity to the crack length reduction.

### **Crack propagation under superelastic cycling**

For the crack propagation testing, 1 mm width samples were used throughout, since with this sample width, the observable material damage became similar, irrespective of the TMT conditions: average crack length  $\sim 3 \mu\text{m}$  and average crack concentration  $\sim 15 \text{ crack/mm}$  (Figure 4.10a).

After superelastic testing of the CR(0.75)-processed samples, a significant crack length redistribution was observed compared to the post-processing conditions (Figure 4.10b). The number of small cracks ( $1\text{-}5 \mu\text{m}$ ) decreased, while the number of cracks longer than  $5 \mu\text{m}$  became greater, indicating the crack propagation during mechanical testing. In the CR(1.2)-processed samples, the concentration of small cracks ( $1\text{-}5 \mu\text{m}$ ) also decreased, but remained greater than that of the longer cracks. The CR(1)+IA+WR(0.2)-processed samples occupied an intermediate position between the CR(0.75) and the CR(1.2) TMTs.

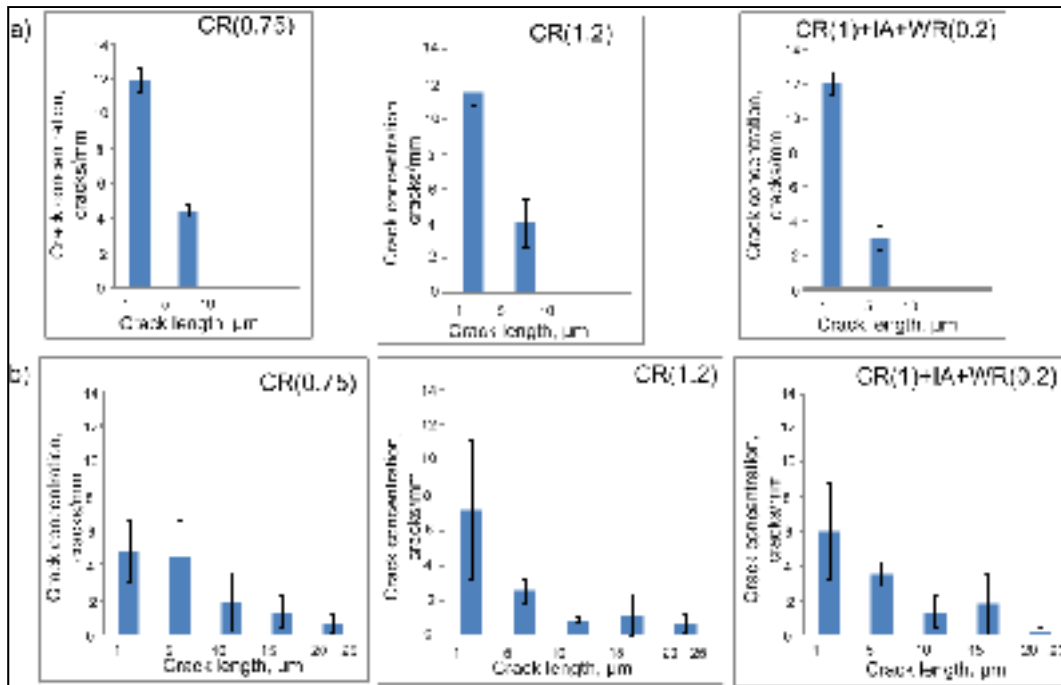


Figure 4.10 Evolution of crack length of the Ti-50.26 at.%Ni 1mm-width CR(0.75), CR(1.2) and CR(1)+IA+WR(0.2) - processed samples: a) before superelastic cycling; b) after 500 cycles of superelastic cycling

#### 4.6 Discussion

Various microstructures can be formed in Ti-50.26 at.%Ni SMA using thermomechanical processing, more specifically via a combination of rolling and annealing steps. In this study, the following features related to the structure formation were identified as functions of cold rolling strain ( $\epsilon=0.75$  to 1.2), partial replacement of CR by WR (at 150°C,  $\epsilon=0.2$ ) and introduction of intermediate annealing (400°C, 1h), each after PDA at 400°C, 1h: (1) The greater the CR contribution, the larger the fraction of nanocrystalline (NC) structure compared to the nanosubgrained (NS) structure, and the lower the average dislocation density; (2) When WR and IA are introduced in the technological schedule, the fraction of the NC structure decreases, and the NC and NS structural elements grow.

Consequently, after CR(0.75)+PDA, the B2-austenite contains a mixed NC (grain size  $\sim 75$  nm) + NS (size of nanosubgrained regions  $\sim 350$  nm) structure, at a  $\sim 40/60$  proportion. After CR(1.2)+PDA, the dominant structure is NC (grain size  $\sim 40$  nm), but NS substructure is still observed (size of nanosubgrained regions  $\sim 150$  nm), the proportion being 90/10. CR(1)+IA+WR(0.2)+PDA occupies an intermediate position resulting in a mixed NC (grain size  $\sim 75$  nm) + NS (size of nanosubgrained regions  $\sim 200$  nm) structure at a 60/40 proportion. The obtained microstructures are consistent with [8, 29, 30].

First, let us consider the nanosubgrained regions as grains of a submicrocrystalline structure (Figure 4.11). Then, let us use the rule of mixtures to calculate, for each TMT route, the average size ( $d_w$ ) of the weighted structural elements, and to range the microstructures obtained from the finest to the coarsest:  $\sim 50$  nm after CR(1.2),  $\sim 120$  nm after CR(1)+IA+WR(0.2) and  $\sim 240$  nm after CR(0.75).

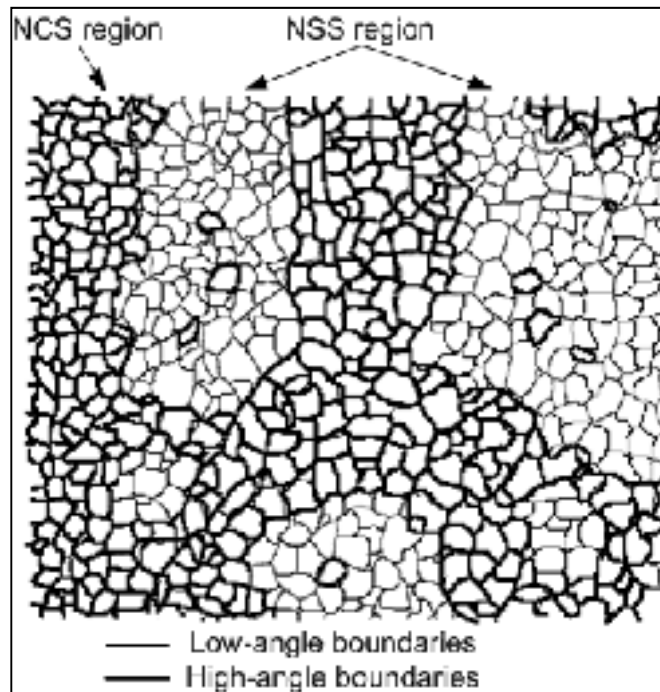


Figure 4.11 Schematic representation of a mixed nanocrystalline (NC) + nanosubgrained (NS) structure

The metallographic analysis shows that the degree of the processing-induced damage after each TMT route (CR(0.75), CR(1.2) or CR(1)+IA+WR(0.2)) is different. The greater the CR contribution to the TMT process, the greater the size of the cracks induced. CR(1.2) results in the largest number of cracks exceeding 25  $\mu\text{m}$ , with a few very large cracks of up to 90  $\mu\text{m}$ . The crack size distributions after the CR(0.75) and CR(1)+IA+WR(0.2) routes are similar. The majority of cracks are less than 25  $\mu\text{m}$ .

The mechanical polishing of the TMT-processed samples' edges allows a reduction of the edge crack length and concentration. However, this polishing does not result in the complete disappearance of edge crack: small 1-5  $\mu\text{m}$  cracks are still observed, and their concentration is sufficiently high (about 12-16 cracks/mm). The observed crack length evolution with the sample width reduction could be a result of two concurrent phenomena, the first clearly dominating the second: (1) length reduction of the pre-existing edge cracks, and (2) some processing-induced surface and internal cracks become visible on the sample edges as a result of polishing.

To summarize the multi-cycle test results, the fatigue life of the as-processed samples is inversely proportional to the post-processing crack length and concentration: the greater the material damage, the shorter the fatigue life. The CR(1.2) – processed sample has the lowest number of cycles to failure compared to the CR(0.75) and CR(1)+IA+WR(0.2) samples due to the largest crack sizes and concentration (Figure 4.11).

Since the crack lengths and concentration after each TMT route are not identical, their crack propagation rates cannot be directly compared. To make possible this comparison, the specimens were mechanically polished to gradually decrease the edge cracks' length and concentration, and then tested again. It was observed that the smaller the crack length, the lower the fatigue life of the CR(0.75) and CR(1)+IA+WR(0.2)-processed samples, whereas the CR(1.2)-processed samples showed no crack-length sensitivity (Figure 4.12).

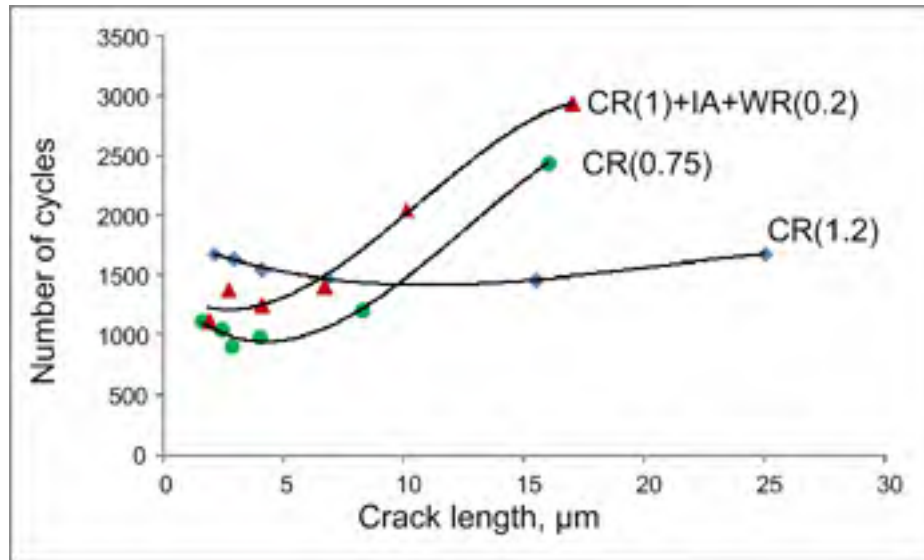


Figure 4.12 Number of superelastic cycles to failure as a function of the average crack length (to facilitate the observation, this figure is obtained from Figure 4.9a using only the average values of crack length and the numbers of cycles to failure).

The behavior observed in Figure 4.12 is associated with the difference between the long- and small-crack propagation mechanisms. It has already been shown that, under some specific conditions, small cracks could grow faster [31-38], and show larger scatter in their growth rate [34] than large cracks, due to a smaller amount of grains surrounding the crack-tip [37, 39] and therefore a smaller influence from the plasticity-induced crack closure mechanisms [22, 38].

Furthermore, the critical, or threshold, value of crack size corresponding to the transition from the long-crack behavior to the small-crack behavior depends on the size of the structure elements, and more specifically, on grain size. According to [31, 33], the smaller the grain size, the greater the number of grains surrounding the crack-tip and, therefore, the smaller the threshold crack size.

Consequently, for our study, the threshold value of the crack size can be ranged qualitatively from the largest to the smallest as a function of the processing conditions: CR(0.75) with  $d_w \sim 240 \text{ nm}$  > CR(1)+IA+WR(0.2) with  $d_w \sim 120 \text{ nm}$  > CR(1.2) with  $d_w \sim 50 \text{ nm}$ . From the

analysis of Figure 4.12, it appears that the edge crack length of the CR(0.75) and the CR(1)+IA+WR(0.2)–processed samples is already below their threshold values because they demonstrate small-crack-related behavior (an increase in the crack propagation rate with a decrease in crack size). First, the CR(0.75)–processed samples demonstrate a significant drop in fatigue life after a relatively small crack length reduction from 15 to 10  $\mu\text{m}$ . In the case of the CR(1)+IA+WR(0.2)–processed samples, this sudden drop in fatigue life corresponds to smaller crack lengths, from 6 to 4  $\mu\text{m}$ . On the other hand, polishing of the CR(1.2)–processed samples does not result in such a phenomenon: their fatigue life is fairly independent down to crack lengths as low as 2  $\mu\text{m}$ . The reason could be that for the finest NC structure corresponding to CR(1.2)+PDA, the smallest crack length reached at the final step of polishing is still larger than its threshold value.

The analysis of the crack length evolution after 500-cycle superelastic testing seems to corroborate this hypothesis. It appears that the crack propagation in the CR(0.75)–processed samples is faster than in the CR(1.2)–processed samples. After 500 cycles of mechanical testing, the first samples show a significant growth of  $\leq 5$   $\mu\text{m}$  cracks as compared to the second samples (Figure 4.10).

#### 4.7 Conclusions

The microstructure and processing-induced crack propagation in nanostructured Ti-50.26 at.%Ni SMA were studied after the following TMT routes: CR( $\varepsilon=0.75$ ), CR( $\varepsilon=1.2$ ) and CR( $\varepsilon=1$ )+IA+WR( $\varepsilon=0.2$ ), with final post-deformation annealing at 400°C(1h). CR( $\varepsilon=0.75$ ) processing of Ti-50.26 at.%Ni alloy results in a mixed NC<NS structure (average size of weighted structural elements,  $d_w = 240$   $\mu\text{m}$ ); CR( $\varepsilon=1.2$ ) results in a mainly NC structure ( $d_w = 50$   $\mu\text{m}$ ), and CR( $\varepsilon=1$ )+IA+WR( $\varepsilon=0.2$ ) results in a mixed NC>NS structure ( $d_w = 120$   $\mu\text{m}$ ); the finer the structure, the higher the processing-induced damage and the shorter the functional fatigue life.



The functional fatigue testing showed that Ti-50.26 at.%Ni alloy obeys the same rules as conventional metallic materials: a decrease in crack size under a certain threshold value results in an increase of the crack propagation rate (small crack phenomenon), and the smaller the grain size, the smaller this threshold value.

Ti-50.26 at.%Ni alloy with a mixed NC+NS structure ( $d_w$  ranging from 120 to 240 nm) manifests a strong sensitivity to the presence of processing-induced microcracks: the fatigue life shows a three-fold decrease when the crack length decreases from 15 to 2  $\mu\text{m}$ . Samples with mainly NC structure ( $d_w \sim 50$  nm) remain insensitive to the presence of cracks as small as 2  $\mu\text{m}$ , indicating that this crack size is still larger than the long-to-small crack transition threshold value for this microstructure.

From the functional fatigue point of view, a NC structure demonstrates a higher tolerance to small cracks, than a mixed NC-NS structure. However, severe flat rolling technology used in this work to produce NC Ti-Ni SMA results in unacceptable processing-induced damage, thus compromising the potential benefits of this microstructure for multi-cycle applications. If the comparable intensity of low-temperature plastic deformation could be achieved by other technological means with a higher-than-rolling level of hydrostatic stresses, such as equal-channel extrusion for example, it would become possible to further reduce the processing-induced damage while creating NC microstructures in Ti-Ni SMA, thus significantly improving their functional fatigue life.

#### **4.8 Acknowledgments**

The authors are grateful to the Natural Sciences and Engineering Research Council of Canada and to the Ministry of Education and Science of the Russian Federation for their financial support of the present work.

#### 4.9 References

- [1] V. Brailovski, S. D. Prokoshkin, I. Y. Khmelevskaya et al., Structure and properties of the Ti-50.0 at% Ni alloy after strain hardening and nanocrystallizing thermomechanical processing. *Mater. Trans.* 47(3), 795-804 (2006).
- [2] N. N. Kuranova, D. V. Gunderov, A. N. Uksusnikov et al., Effect of heat treatment on the structural and phase transformations and mechanical properties of TiNi alloy subjected to severe plastic deformation by torsion. *Phys. Met. Metall.* 108(6), 556-568 (2009).
- [3] A. V. Sergueeva, C. Song, R. Z. Valiev et al., Structure and properties of amorphous and nanocrystalline NiTi prepared by severe plastic deformation and annealing. *Mater. Sci. Eng. A.* A339(1-2), 159-65 (2003).
- [4] K. Tsuchiya, M. Ohnuma, K. Nakajima et al., Microstructures and enhanced properties of SPD-processed TiNi shape memory alloy. *Mater. Devices Smart Syst.* 3, 113-24 (2009).
- [5] V. Brailovski, S. Prokoshkin, K. Inaekyan et al., Functional properties of nanocrystalline, submicrocrystalline and polygonized Ti-Ni alloys processed by cold rolling and post-deformation annealing. *J. Alloys Compd.* 509(5), 2066-2075 (2011).
- [6] V. Demers, V. Brailovski, S. D. Prokoshkin et al., Thermomechanical fatigue of nanostructured Ti-Ni shape memory alloys. *Mater. Sci. Eng. A* 513-514 (1-7), 185-196 (2009).
- [7] Y. Facchinello, V. Brailovski, S. D. Prokoshkin et al., Manufacturing of nanostructured Ti-Ni shape memory alloys by means of cold/warm rolling and annealing thermal treatment. *J. Mater. Process. Technol.* 212 (11), 2294-2304 (2012).

- [8] A. Kreitchberg, V. Brailovski, S. Prokoshkin et al., Microstructure and functional fatigue of nanostructured Ti-50.26at%Ni alloy after thermomechanical treatment with warm rolling and intermediate annealing. *Mater. Sci. Eng. A* 562, 118-127 (2013).
- [9] S. Miyazaki, K. Mizukoshi, T. Ueki et al., Fatigue life of Ti-50 at.% Ni and Ti-40Ni-10Cu (at.%) shape memory alloy wires. *Mater. Sci. Eng. A* 273, 658-63 (1999).
- [10] N. Nayan, D. Roy, V. Buravalla et al., Unnotched fatigue behavior of an austenitic Ni-Ti shape memory alloy. *Mater. Sci. Eng. A* 497(1-2), 333-40 (2008).
- [11] H. A. Padilla Ii, B. L. Boyce: A review of fatigue behavior in nanocrystalline metals. *Proc. Soc. Exp. Mech.* 67, 5-23 (2010).
- [12] X. Z. Liao, Y. H. Zhao, Y. T. Zhu et al., Grain-size effect on the deformation mechanisms of nanostructured copper processed by high-pressure torsion. *J. Appl. Phys.* 96(1), 636-640 (2004).
- [13] X. Z. Liao, F. Zhou, E. J. Lavernia et al., Deformation mechanism in nanocrystalline Al: Partial dislocation slip. *Appl. Phys.* 83(4), 632-634 (2003).
- [14] V. H. Swygenhoven, P. M. Derlet, and A. G. Froseth, Stacking fault energies and slip in nanocrystalline metals. *Nat. Mater.* 3(6), 399-403 (2004).
- [15] D. Wolf, V. Yamakov, S. R. Phillpot et al., Deformation of nanocrystalline materials by molecular-dynamics simulation: relationship to experiments? *Acta Mater.* 53(1), 1-40 (2005).
- [16] K. S. Kumar, S. Suresh, M. F. Chisholm et al., Deformation of electrodeposited nanocrystalline nickel. *Acta Mater.* 51(2), 387-405 (2003).

- [17] X. Z. Liao, A. R. Kilmametov, R. Z. Valiev et al., High-pressure torsion-induced grain growth in electrodeposited nanocrystalline Ni. *Appl. Phys. Lett.* 88(2), 21909-1 (2006).
- [18] Z. Shan, E. A. Stach, J. M. K. Wiezorek et al., Grain boundary-mediated plasticity in nanocrystalline nickel. *Science* 305(5684), 654-657 (2004).
- [19] T. Hanlon, E. D. Tabachnikova, S. Suresh, Fatigue behavior of nanocrystalline metals and alloys. *Int. J. Fatigue* 27(10-12), 1147-1158 (2005).
- [20] T. Hanlon, Y. N. Kwon, S. Suresh, Grain size effects on the fatigue response of nanocrystalline metals. *Scripta Mater.* 49(7), 675-80 (2003).
- [21] J. R. Rice, and R. Thomson, Ductile versus brittle behaviour of crystals. *Philos. Mag.* 29(1), 73-97 (1974).
- [22] I. A. Ovid'ko, and A. G. Sheinerman, Grain size effect on crack blunting in nanocrystalline materials. *Scripta Mater.* 60(8), 627-630 (2009).
- [23] P. Cavaliere, Fatigue properties and crack behavior of ultra-fine and nanocrystalline pure metals. *Int. J. Fatigue* 31(10), 1476-1489 (2009).
- [24] M. D. Sangid, G. J. Pataky, H. Sehitoglu et al., Superior fatigue crack growth resistance, irreversibility, and fatigue crack growth-microstructure relationship of nanocrystalline alloys. *Acta Mater.* 59(19), 7340-55 (2011).
- [25] R. L. Holtz, K. Sadananda, M. A. Imam, Fatigue thresholds of Ni-Ti alloy near the shape memory transition temperature. *Int. J. Fatigue* 21, S137-S145 (1999).

- [26] K. N. Melton, and O. Mercier, Fatigue of NiTi thermoelastic martensites. *Acta Metall.* 27(1), 137-44 (1979).
- [27] J. F. Luo, S. C. Mao, X. D. Han et al., Crystallographic mechanisms of fracture in a textured polycrystalline TiNi shape memory alloy. *J. Appl. Phys.* 102(4), 043526-1 (2007).
- [28] Y. S. Umanskiy, Y. A. Skakov, A. N. Ivanov et al., *Crystallography, X-ray diffraction and electron microscopy.* (Metallurgy, Moscow, 1983).
- [29] S. D. Prokoshkin, V. Brailovski, A. V. Korotitskiy et al., Specific features of the formation of the microstructure of titanium nickelide upon thermomechanical treatment including cold plastic deformation to degrees from moderate to severe. *Phys. Met. Metall.* 110 (3), 289-303 (2010).
- [30] S. D. Prokoshkin, I. Y. Khmelevskaya, S. V. Dobatkin et al., Alloy composition, deformation temperature, pressure and post-deformation annealing effects in severely deformed Ti-Ni based shape memory alloys. *Acta Mater.* 53(9), 2703-2714 (2005).
- [31] R. L. Carlson, D. L. Steadman, D. S. Dancila et al., Fatigue growth of small corner cracks in aluminum 6061-T651. *Int. J. Fatigue* 19(1), 119-25 (1997).
- [32] M. F. Horstemeyer, D. Farkas, S. Kim et al., Nanostructurally small cracks (NSC): a review on atomistic modeling of fatigue. *Int. J. Fatigue* 32(9), 1473-502 (2010).
- [33] K. Tokaji, T. Ogawa, K. Ohya, The effect of grain size on small fatigue crack growth in pure titanium. *Int. J. Fatigue* 16(8), 571-8 (1994).

- [34] K. S. Ravichandran, L. Xu-Dong, Fracture mechanical character of small cracks in polycrystalline materials: concept and numerical K calculations. *Acta Mater.* 48(2), 525-40 (2000).
- [35] B. N. Leis, A. T. Hopper, J. Ahmad et al., Critical review of the fatigue growth of short cracks. *Eng. Fract. Mech.* 23(5), 883-898 (1986).
- [36] S. Pearson, Initiation of fatigue cracks in commercial aluminum alloys and the subsequent propagation of very short cracks. *Eng. Fract. Mech.* 7(2), 235-247 (1975).
- [37] K. S. Ravichandran, J. M. Larsen, Effects of crack aspect ratio on the behavior of small surface cracks in fatigue. II. Experiments on a titanium (Ti-8Al) alloy. *Metall. Mater. Trans. A* 28A(1), 157-69 (1997).
- [38] S. Suresh, R. O. Ritchie, Propagation of short fatigue cracks. *Int. Met. Rev.* 29(6), 445-76 (1984).
- [39] K. S. Ravichandran, Effects of crack aspect ratio on the behavior of small surface cracks in fatigue. I. Simulation. *Metall. Mater. Trans. A* 28A(1), pp. 149-56 (1997).

## CHAPTER 5

### ARTICLE #4

#### EFFECT OF THE GRAIN/SUBGRAIN SIZE ON THE STRAIN-RATE SENSITIVITY AND DEFORMABILITY OF Ti-50 at.%Ni ALLOY

A. Kreitchberg<sup>1,2</sup>, V. Brailovski<sup>2</sup>, S. Prokoshkin<sup>1</sup>, D. Gunderov<sup>3,4</sup>, M. Khomutov<sup>1</sup>,  
K. Inaekyan<sup>2</sup>

<sup>1</sup>National University of Science and Technology “MISiS”, Moscow, Russia

<sup>2</sup>Ecole de Technologie Supérieure, Montréal (Québec), Canada

<sup>3</sup>Ufa State Aviation Technical University, Ufa, Russia

<sup>4</sup>Institute of Molecule and Crystal Physics RAS, Ufa, Russia

This article was published

in *Materials Science and Engineering A*, 2015, v. 622, pp. 21-29.

### 5.1 Summary

This study was aimed at improving deformability of Ti-Ni alloys during SPD, thus promoting the nanocrystalline structure formation with minimum level of the processing-induced defects. The temperatures and strain rates which correspond to superplastic behavior of Ti-50.0 at.%Ni alloy with different grain size were identified by means of strain-rate jump and creep testing. The different initial structures were formed by means of ECAP at 400°C and 500°C followed by PDA at 350°C and 450°C (1h) respectively. The low-temperature deformability was studied by multi-pass CR to an accumulated logarithmic strain of 2. The microstructure features, martensitic transformation temperatures and microcrack lengths and concentrations after different processing routes were studied using transmission and scanning electron microscopies, differential scanning calorimetry and X-ray diffraction.

The strain-rate sensitivity and deformability of Ti-50.0 at.%Ni alloy were found to be improved with: (1) increasing temperature; (2) decreasing strain rate; and (3) structural refinement. The alloy with ultrafine-grained structure demonstrated significantly higher deformability compared to its coarse-grained counterpart and that at any deformation temperature. Moreover, the smaller the grain size, the lower the temperature and the higher the strain-rate leading to superplastic behavior. The obtained results showed the advantage of a combined TMT approach, comprising, for example, ECAP at elevated temperatures, for preliminary structure refinement, and CR, for the nanocrystalline structure formation with significantly reduced processing-related damage.

## 5.2 Abstract

The strain-rate sensitivity of coarse-grained (CG) and ultrafine-grained (UFG) Ti-50 at.%Ni alloys was studied in the 20 to 500°C temperature range. In the  $10^{-3}$ – $10^{-5}$  s<sup>-1</sup> strain rate range, the maximum strain-rate sensitivity exponent  $m$  was measured by the strain-rate-jump test, while in the  $10^{-5}$ – $10^{-6}$  s<sup>-1</sup> strain rate range,  $m$  has been measured by the stress-jump creep test. It was determined that the smaller the initial grain/subgrain size ( $d$ ), the lower the deformation temperature ( $T_d$ ) and the higher the strain rate ( $\dot{\epsilon}$ ) leading to superplasticity ( $m = 0.5$ ): for  $d = 250$  nm,  $T_d = 400^\circ\text{C}$  &  $\dot{\epsilon} \in [0.4 - 2.5] \cdot 10^{-5}$  s<sup>-1</sup>, while for  $d = 500$  nm,  $T_d = 500^\circ\text{C}$  &  $\dot{\epsilon} \in [0.1 - 3] \cdot 10^{-5}$  s<sup>-1</sup>. The low-temperature deformability of the CG and UFG Ti-Ni alloys have also been compared under conditions of severe cold rolling (accumulated strain of 2) by measuring the length and concentration of the processing-induced microcracks. The results of this study showed an increase in the low-temperature deformability of UFG Ti-Ni alloy compared to CG Ti-Ni alloy.

**Keywords:** nanostructured materials, shape memory alloys, equal channel angular processing, thermomechanical processing, superplasticity, grain refinement



### 5.3 Introduction

Ti-Ni shape memory alloys (SMA) have many current and potential engineering applications thanks to their shape memory and superelasticity properties [1, 2]. The functional properties of Ti-Ni SMA are structure-sensitive, and grain refinement represents one of the processing-related approaches to significantly improve the recoverable strain and recovery stress characteristics of these functional materials [3-5]. Severe plastic deformation (SPD) is commonly considered to be very efficient for grain refinement [6-8]. These benefits do come with a price tag: the drawbacks of some SPD techniques are the associated structural non-uniformity and an increasing risk of the processing-induced damage resulting in significant deterioration of the material fatigue resistance [9-12].

Some of the more frequently-used techniques for ultrafine structure formation in metals and metallic alloys are high pressure torsion (HPT), cold rolling (CR), and equal-channel angular pressing (ECAP) [6-8, 13, 14]. During HPT, a metal is deformed under the action of pressure and shear strain, and logarithmic strains of up to 10 or even more, can be applied without specimen destruction. The structural non-uniformity can however be observed across the specimen, which limits the use of HPT for the formation of desired structures in bulk and brittle materials [6-8]. In addition, this method makes it possible to produce small disk-shaped specimens only, the practical applicability of them is as yet very limited.

Cold rolling, on the other hand, is the simplest SPD technique capable of producing application-relevant semi-products, such as strips and plates, but inhomogeneous deformation during CR frequently leads to surface and subsurface microcracks, especially close to the product edges [4].

Finally, ECAP is capable of effectively producing uniform nano- and submicrocrystalline (NC and SMC) bulk semi-finished products of certain metals and alloys, such as Cu-based for example [13]. ECAP of Ti-Ni SMAs is commonly performed at elevated temperatures ( $0.4-0.5T_m$ ), since at lower temperatures, billet fragmentation has been observed [12, 15].

The ECAP-processed Ti-Ni SMAs mainly present a submicrocrystalline structure with grain/subgrain size ranging from 150 to 1000 nm [15-17]. (To the best of the authors' knowledge, no comprehensive information is published on the ECAP manufacturing of true nanocrystalline –grains smaller than 100 nm– Ti-Ni alloys.)

Since the manufacturing of nanocrystalline Ti-Ni alloys represents difficulties due to their limited deformability at low temperatures, some attempts have been undertaken to overcome this limitation, such as the use of multi-stage warm rolling and electropulsing rolling techniques [10, 11, 18, 19]. However, these approaches have resulted in microstructure coarsening and lower functional properties compared to their nanocrystalline counterparts [10].

It should be recalled that for a given deformation process, the deformability of a metallic alloy with a specific microstructure depends on the deformation temperature and the strain rate. For example, a strain rate sensitivity exponent of  $m \approx 0.5$  was found in the 470-530°C temperature range and in the  $[8 \cdot 10^{-6} - 2 \cdot 10^{-9}] \text{ s}^{-1}$  strain-rate range [20]. It was also found that the higher the deformation temperature, the higher the strain rates leading to appreciably high  $m$  values: at 950-1100°C,  $m \approx 0.4$  in the  $[10^{-5} - 10^{-6}] \text{ s}^{-1}$  strain-rate range [21]. In the same temperature range of 950-1100°C, when the strain rate increases,  $m$  decreases:  $m \approx 0.33$  in the  $[10^{-3} - 10^{-5}] \text{ s}^{-1}$  strain-rate range [22-24] and  $m = 0.2-0.17$ , in the  $[10^{-1} - 10^{-3}] \text{ s}^{-1}$  strain-rate range [25, 26]. Note however that these few studies on the Ti-Ni alloys strain rate sensitivity are mainly focused on the coarse-grained materials, and they do not explore the combined influence of the deformation conditions (temperature and strain rate) and microstructure (grain/subgrain size) on the strain rate sensitivity. This limitation represents the main incentive for this study, which verifies the hypothesis that for a given set of deformation conditions (stress state, deformation temperature and strain rate), the smaller the initial grain size of Ti-Ni SMAs, the higher their strain-rate sensitivity and deformability, even at low temperatures.

## 5.4 Experimental methodology

An as-drawn 19 mm-diameter Ti-50 at.%Ni alloy bar (“*Johnson Matthey*”) was primarily subjected to homogenization annealing (800°C, 1h), cut into 100 mm-long billets and ECAP-processed at 400°C (ECAP-400) and 500°C (ECAP-500) with a strain rate of 6.7 mm/s. The channels’ intersection angle was 120°, which gave a one-pass logarithmic strain of 0.68 and a total 8-pass strain of 5.44 (Figure 5.1a). After each pass, the billets were turned 90 degrees around their longitudinal axes to yield a uniform structure [13, 27, 28]. After ECAP, the specimens were annealed for 1h at 400°C (after ECAP-400) or at 500°C (after ECAP-500), and water-quenched.

For reference purposes, a certain number of specimens were reserved directly after homogenization annealing (RQ – reference quenched). The specimens’ designations are indicated in Table 5.1.

Table 5.1 Specimen designation and corresponding processing routes

Route	Identification	Step 1	Step 2	Step 3
1	RQ	Annealing at 800°C (1h) followed by water-quenching	-	-
2	ECAP-400		ECAP (400°C, $\epsilon=5.44$ )	PDA (350°C, 1 h)
3	ECAP-500		ECAP (500°C, $\epsilon=5.44$ )	PDA (450°C, 1 h)

The microscopy analysis was carried out using a “*Union*” optical microscope and a “*JEOL-2100*” transmission electron microscope. For electron microscopy, thin foils were cut by electro-discharging machining (EDM) and then thinned by mechanical grinding and polished by ion bombardment.

The X-ray diffraction analysis was performed at room temperature (RT) and at 150°C using a “*PANalytical X’Pert Pro*” diffractometer with  $Cu_{K\alpha}$  radiation. Prior to testing, the specimens were mechanically ground, polished and etched in 1HF:3HNO<sub>3</sub>:6H<sub>2</sub>O<sub>2</sub> solution.

The martensitic transformation temperatures were evaluated using a “*Perkin-Elmer Pyris*” differential scanning calorimeter with a 10°C/min cooling-heating rate in the -60 to 150°C temperature range.

In this work, a strain-rate sensitivity exponent  $m$  [29, 30] has been selected as an indicator of the alloy’s deformability. For example, when  $m$  situates in the 0.4-0.7 range, it is assumed that the material manifests superplasticity due to grain boundary sliding [30, 31].

In order to study the influence of the deformation conditions on the alloy’s strain-rate sensitivity, the strain-rate-jump and stress-jump creep tests [32-35] were performed concurrently. For these experiments, two types of specimens were prepared from the ECAP-processed and RQ billets: 1 x 0.25 x 4.5 (mm) gage-size dumbbell tensile specimens were EDM-cut from the billets’ cross sections, and 20 x 15 x 10 (mm) plane-strain compression testing specimens were EDM-cut along the billets’ axes (Figure 5.1b, c). Prior to testing, all the specimens were mechanically polished to remove the oxidized layer.

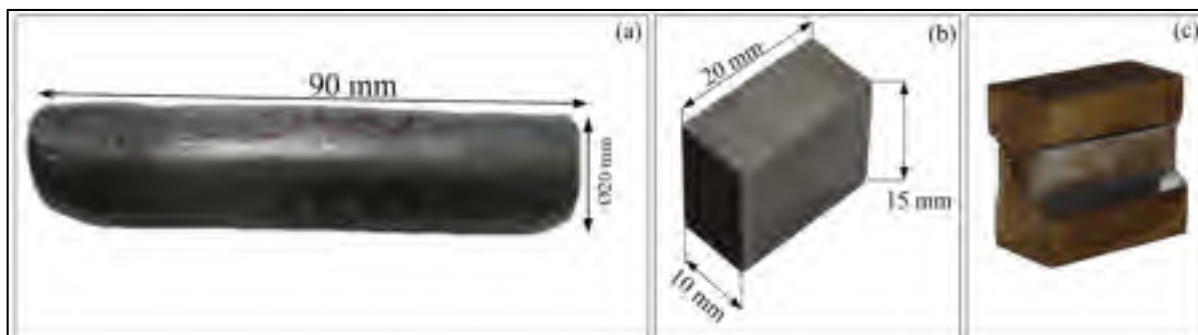


Figure 5.1 Plane-strain compression testing specimen at various preparation stages: a) ECAP-processed billet; (b) specimen before testing and (c) specimen after testing

For the preliminary assessment of the testing parameters, the *tensile strain-rate-jump tests* were performed at 20, 150, 250 and 400°C in the  $10^{-3}$  to  $10^{-4}$  s<sup>-1</sup> strain rate range using a custom-made testing machine equipped with a thermal chamber. The starting strain rate  $\dot{\epsilon}_1$  corresponded to  $10^{-3}$  s<sup>-1</sup>. When the steady-state flow stress  $\sigma_1$  was reached, the strain rate was decreased to  $\dot{\epsilon}_2$  of  $10^{-4}$  s<sup>-1</sup>. After reaching a new steady-state flow stress  $\sigma_2$ , the strain rate was reversed back to  $\dot{\epsilon}_1$ , and the test was repeated. The strain-rate sensitivity exponent  $m$  was calculated using equation (1) [30]:

$$m = \frac{\log(\sigma_1/\sigma_2)}{\log(\dot{\epsilon}_1/\dot{\epsilon}_2)} \quad (5.1)$$

The *compression strain-rate-jump tests* were performed using a thermomechanical simulator “Gleeble System 3800” under a plane-strain mode. The specimens were compressed to a total strain of 15% with a given strain rate, and the corresponding yield stress  $\sigma_y$  was measured (Figure 5.1c). Using this technique, the strain-rate sensitivity exponent  $m$  was determined at 400 and at 500°C in the  $[10^{-3} - 10^{-4}]$  s<sup>-1</sup> and  $[10^{-4} - 10^{-5}]$  s<sup>-1</sup> strain-rate ranges.

Since equipment limitations did not allow for strain-controlled experiments at strain rates under  $10^{-5}$  s<sup>-1</sup>, the next series of experiments were carried out using the stress-controlled creep mode and so-called *stress-jump creep* testing approach [36]. In this case, a given constant stress had to be applied to a specimen, and then the resulting creep strain rate measured. The stress-jump creep tests were performed at 400 and at 500°C under constant stresses corresponding to 0.4, 0.6, 0.7, 0.8 and (0.9-0.95)  $\sigma_y$ , where  $\sigma_y$  is the 0.2% offset yield stress measured at a corresponding temperature. The stress-jump creep plots obtained at different temperatures were then used to calculate the steady-state strain rates as slopes of the “strain-time” plots. The strain rates were finally utilized to calculate the strain-rate sensitivity exponent  $m$  as the slope of a  $\log(\sigma) - \log(\dot{\epsilon})$  plot, where  $\sigma$  is the constant stress and  $\dot{\epsilon}$  is the corresponding strain rate [37, 38].

Note that to avoid grain growth during high-temperature – low-strain-rate testing, it was decided to limit the maximum testing temperature by the corresponding ECAP temperature: so that the maximum testing temperatures were 400°C for ECAP-400 and 500°C for ECAP-500.

Finally, to compare the low-temperature deformability of Ti-Ni alloy after different processing routes, the 1 x 1.5 x 20 (mm) specimens cut from the cross-section of the RQ and ECAP-processed billets were multi-pass cold-rolled up to an accumulated logarithmic strain of 2 using a *FENN* laboratory rolling mill, and the length and concentration of microcracks on the specimens' edges measured using a *Hitachi TM3030* scanning electron microscope.

## 5.5 Results

### Optical and electron microscopy

The results of the metallographic analysis of the alloy annealed at 800°C (1h) followed by water-quenching show that the average B2-austenite grain size is 200-300  $\mu\text{m}$  (Figure 5.2a).

The TEM study reveals that ECAP creates a submicrocrystalline structure with different grain sizes depending on the deformation temperature. Post-ECAP annealing at temperatures 50° lower than the deformation temperature leads to stress relaxation and recovery of the dislocation substructure.

The specimens subjected to ECAP at 400°C and PDA at 350°C (1h) contain martensitic crystals with equiaxed structural elements of initial B2-austenite in the background (Figure 5.2b). Both the submicrocrystalline and submicrosubgrained regions can be observed. Compared to the as-quenched state, ECAP results in a significant structural refinement: the grain/subgrain size ( $d$ ) decreases from 200-300  $\mu\text{m}$  (grains) to 100-300 nm (grains+subgrains). The electron diffraction patterns consist of dotted rings with a non-uniform azimuthal distribution of point-like reflections. Such patterns in a combination with

dark-field image features are typical for a mixed grained/subgrained structure [39]. Indeed, the distribution of reflections along the rings and their small azimuthal broadening indicate the presence of high- and low-angle misorientations, i.e. grain boundaries and subboundaries. The dark field images (Figures 5.2b) show that some neighboring structure elements have close orientations, i.e. they are subgrains. After ECAP at 500°C and PDA at 450°C (1h), the alloy structure also consists of submicrograins and submicrosubgrains, however, in contrast to ECAP at 400°C, the structural elements are significantly coarser: 300-700 nm (Figure 5.2c).

To verify the grain size invariability during strain-rate sensitivity testing (~1-1.5 hours at elevated temperatures), the electron microscopy study of the ECAP-400 specimens was repeated after the stress-jump creep test: The corresponding bright- and dark-field images and electron diffraction patterns are represented in Figure 5.2d.

Comparing the alloy's microstructures before and after testing does not allow any conclusion to be made: after creep tests, the size of the structural elements (grains and subgrains) remains in the 100-300 nm range. The dislocation density inside both grains and subgrains is still high. Judging from the electron diffraction patterns and dark-field images, the low-angle and high-angle boundaries are present. The structure consists of a mixture of submicrocrystalline and submicrosubgrained regions, similar to [11, 39]. In this case, arc-like reflections from subgrains, with low-angle misorientation of their fragments in an azimuthal direction, superpose onto the pointed rings of reflections from individual grains of the submicrocrystalline structure. An example of an individual grain is presented in the dark-field image of Figure 5.2d. In the bright-field image of Figure 5.2d, a group of darker structural elements is visible on the left side; these structural elements are subgrains.

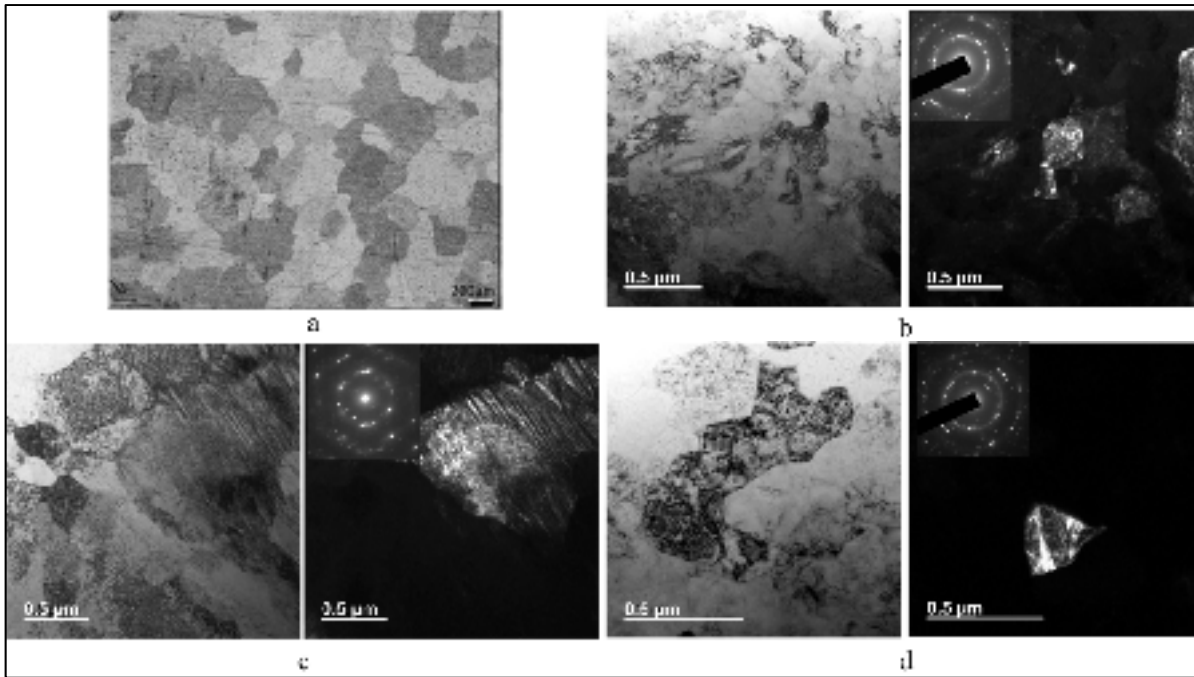


Figure 5.2 Alloy structure after TMT: a) RQ (optical microscopy); b) ECAP-400, c) ECAP-500 and d) ECAP-400 after creep test at 400°C (electron microscopy). In b, c and d: bright-field images are on the left, dark-field images on the right; SAED patterns are inserted into the dark-field images

## DSC

The martensitic transformation kinetics after RQ, ECAP-400 and ECAP-500 were studied using DSC. It was found that the peak transformation temperatures ( $A_p$  and  $M_p$ ) are not influenced by TMT (Figure 5.3): — the  $A \rightarrow M$  transformation peak temperatures are in the 39 to 45°C temperature range, and the  $M \rightarrow A$  transformation peak temperatures are in the 82 to 84°C range. After ECAP, however, the  $A \rightarrow M$  transformation range broadens,  $A_f$  temperatures shift toward higher temperatures, while  $A_s$  temperatures shift to lower temperatures, compared to the reference-quenched state. The transformation sequences change as well (Figure 5.3). After reference quenching, single-stage  $B19' \leftrightarrow B2$  transformation occurs upon heating and cooling, while after ECAP, an intermediate R-phase transformation ( $B2 \rightarrow R$  and  $R \rightarrow B19'$ ) is observed on cooling. The multi-stage transformation in the ECAP-processed alloy occurs as a consequence of the higher level of dislocation



density and internal stresses compared to their reference-quenched counterparts. The dislocation network offers a significant resistance to high-level lattice distortions associated with martensitic transformation, thus favoring the formation of an intermediate R-phase with significantly smaller transformation lattice strains [40, 41]. Therefore, the thermomechanical treatment changes the transformation path from  $B2 \rightarrow B19'$  into  $B2 \rightarrow R \rightarrow B19'$ . This effect was widely observed and extensively discussed in detail in [40, 41].

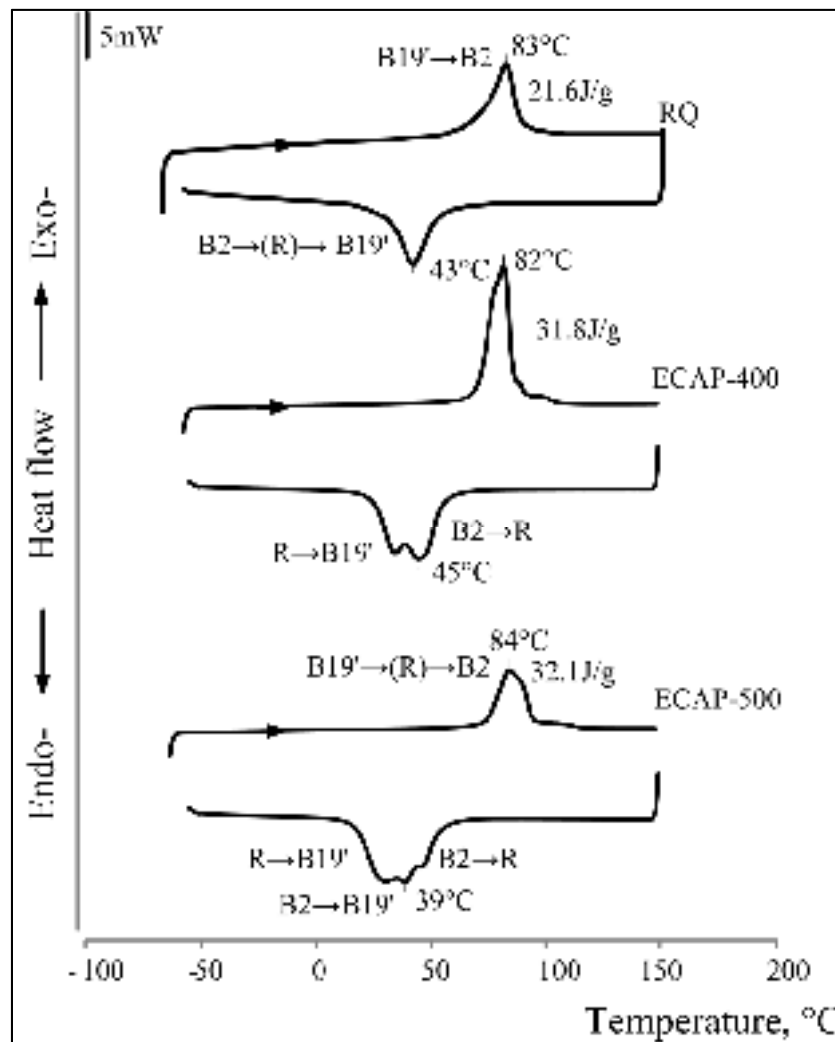


Figure 5.3 DSC plots after reference quenching and different TMT routes

### **X-ray diffraction analysis**

The X-ray diffractograms obtained at RT and 150°C analyses are collected in Figure 5.4. In the reference (RQ) alloy at RT, B19'-martensite and a small quantity (less than 5%) of retained B2-austenite are observed. Compared to the RQ, ECAP leads to a considerable broadening in the X-ray lines of both B19'-martensite (Figure 5.4a) and appearance of the intermediate R-phase lines instead of {110} line of B2-austenite (Figure 5.4b), due to an increase in dislocation density and the decrease in grain size. Moreover, visible shifts of the martensite X-ray lines from their positions for the quenched martensite are consistent with changes in the B19'-martensite lattice parameters [42, 43].

The lowering of the ECAP temperature from 500 to 400°C leads to an additional broadening of the B2-austenite and B19'-martensite X-ray lines, which correlate with the observed grain/subgrain refinement and increase in the dislocation density.

The observed particularities of the X-ray diffractograms correlate well with the known data on the effect of the highly-dislocated or nanostructured B2-austenites on their diffraction spectra [43]. Note that in the RQ alloy at 150°C, only three B2-austenite lines are observed, while after ECAP, (200)<sub>B2</sub> line becomes visible because of the processing-induced texture.

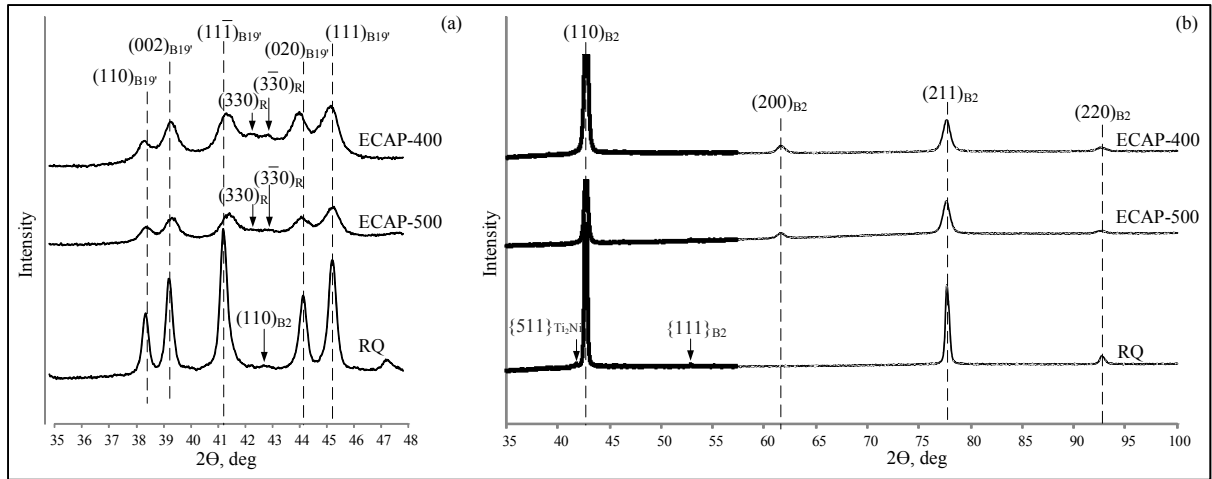


Figure 5.4 X-ray diffractions at RT (a) and 150°C (b) after RQ, ECAP-400 and ECAP-500

### Measurements of the strain-rate sensitivity exponent $m$

#### Strain-rate-jump tensile tests

The strain-rate-jump tensile test diagrams of the RQ and ECAP-400 specimens obtained in the  $[20 - 400]^{\circ}\text{C}$  and  $[10^{-3} - 10^{-4}] \text{ s}^{-1}$  temperature and strain rate ranges are presented in Figure 5.5. It can be seen that for the RQ specimens, the strain-sensitivity exponent  $m = 0.006$  at  $20^{\circ}\text{C}$ ; increasing to 0.028 when the deformation temperature increases from 20 to  $400^{\circ}\text{C}$  (Figure 5.5a-d). For the ECAP-400 specimens, the same trend is observed: the higher the testing temperature, the higher the  $m$  value, increasing from 0.011 to 0.05 when the testing temperature increases from 20 to  $400^{\circ}\text{C}$  (Figure 5.5e-h).

Given that under the same testing conditions,  $m$  after ECAP-400 was only slightly higher than after RQ, it was decided to perform subsequent tests at higher temperatures ( $400^{\circ}\text{C}$  for ECAP-400 and  $500^{\circ}\text{C}$ , for ECAP-500) and lower strain rates ( $10^{-4}$  and  $10^{-5} \text{ s}^{-1}$ ), using a compression testing mode.

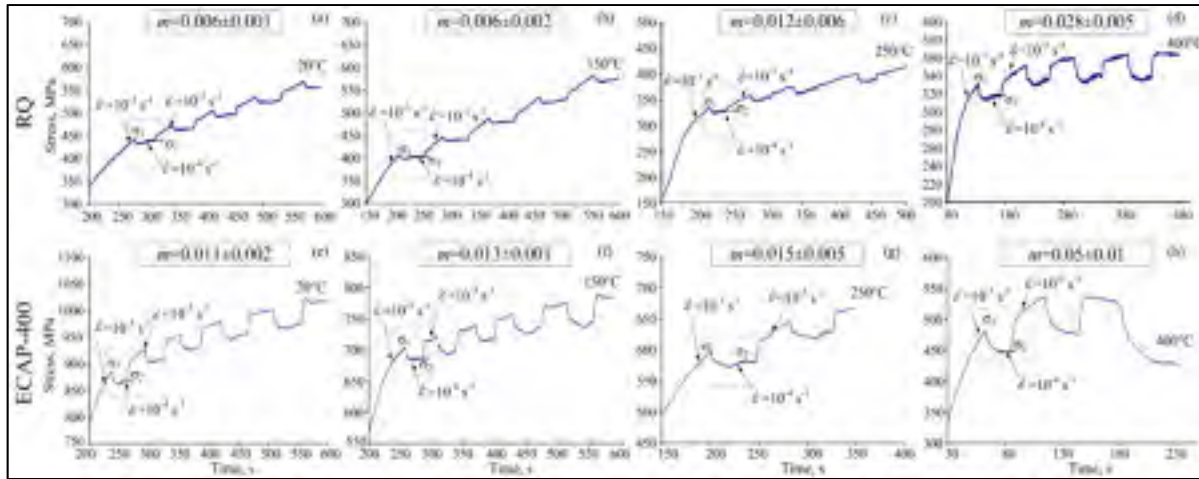


Figure 5.5 Strain-rate-jump tensile diagrams at 20, 150, 250 and 400°C in the  $[10^{-3} - 10^{-4}] \text{ s}^{-1}$  strain rate range: RQ (a) – (d) and ECAP-400 (e) – (h)

### Strain-rate-jump compression tests

Strain-rate-jump tests at elevated temperatures were performed using plane-strain compression mode. After ECAP, the specimens were subjected to deformation with a strain rate jumping from  $10^{-3}$  to  $10^{-4} \text{ s}^{-1}$  and then from  $10^{-4}$  to  $10^{-5} \text{ s}^{-1}$ . The stress-strain diagrams at 400°C and 500°C are presented in Figure 5.6 as functions of true strain, and the calculated strain-sensitivity exponents  $m$  are collected in Table 5.2. Note that to not alter the material microstructure by a long exposure at a temperature higher than that of processing, the ECAP-400 specimens were not tested at 500°C.

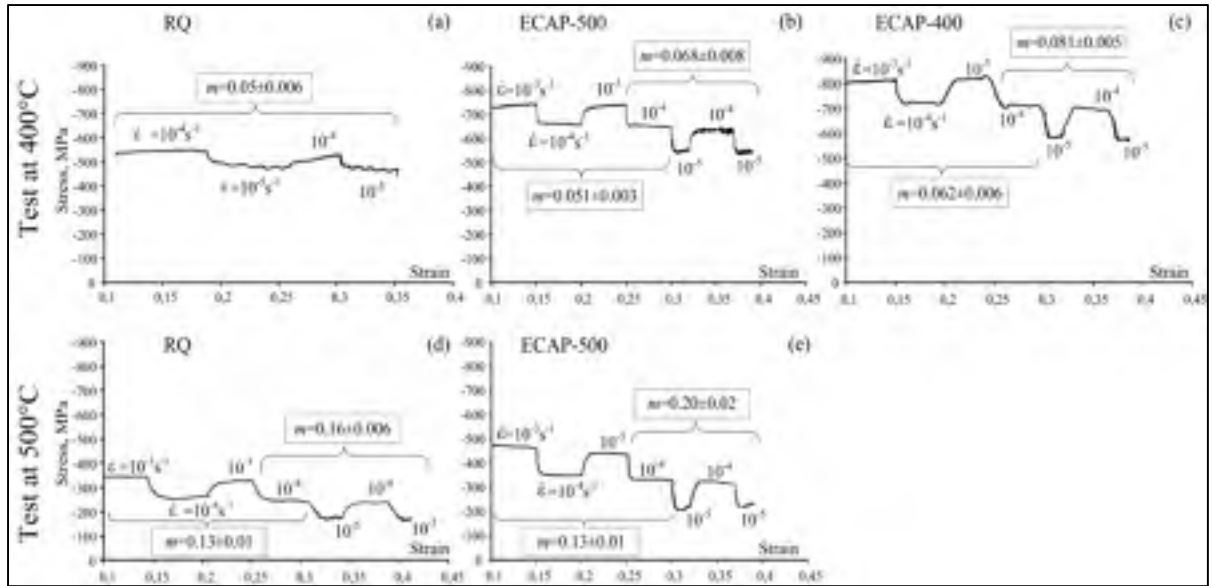


Figure 5.6 Strain-rate-jump compression diagrams: RQ (a, d); ECAP-500 (b, e); ECAP-400 (c)

Table 5.2 Strain-rate sensitivity exponent  $m$  measured by the strain-rate-jump compression test

Identification	Parameters	400°C		500°C	
	$\dot{\epsilon}$ , $s^{-1}$	$[10^{-3} - 10^{-4}] s^{-1}$	$[10^{-4} - 10^{-5}] s^{-1}$	$[10^{-3} - 10^{-4}] s^{-1}$	$[10^{-4} - 10^{-5}] s^{-1}$
RQ	$m$	-	$0.05 \pm 0.006$	$0.13 \pm 0.01$	$0.16 \pm 0.01$
ECAP-500		$0.051 \pm 0.003$	$0.068 \pm 0.008$	$0.13 \pm 0.01$	$0.20 \pm 0.02$
ECAP-400		$0.062 \pm 0.006$	$0.081 \pm 0.005$	-	-

It can be observed that the strain-rate sensitivity exponents measured in tension and compression of ECAP-400 specimens are close: for the same strain rate range of  $[10^{-3} - 10^{-4}] s^{-1}$ ,  $m = 0.05 \pm 0.01$  (Figure 5.5h, tension) and  $m = 0.062 \pm 0.006$  (Figure 5.6c, compression). This good agreement validates the possibility to apply these testing modes concurrently for strain-rate sensitivity measurements.

At the same testing temperature, the lower the strain-rate, the higher the strain-rate sensitivity exponent  $m$  (Figure 5.6a,b,c). For example for 400°C testing of ECAP-500, if the strain rate

range decreases from  $[10^{-3} - 10^{-4}] \text{ s}^{-1}$  to  $[10^{-4} - 10^{-5}] \text{ s}^{-1}$ ,  $m$  increased from 0.05 to 0.07, whereas for ECAP-400, after the same strain-rate jump,  $m$  increases from 0.06 to 0.08. For RQ and ECAP-500, an increase in testing temperature from 400 to 500°C leads to an approximately three-fold increase in the strain-rate sensitivity exponent  $m$  (Figure 5.6a,d and b,e). Note that at 500°C, in the  $[10^{-3} - 10^{-4}] \text{ s}^{-1}$  strain-rate range, the strain-rate sensitivity exponent  $m$  of RQ and ECAP-500 specimens are similar, thus reflecting the occurrence of the same plastic deformation mechanisms in both cases.

Finally, the maximum strain-rate sensitivity exponent of  $m = 0.2$  was obtained for ECAP-500 specimens at 500°C in the  $[10^{-4} - 10^{-5}] \text{ s}^{-1}$  strain rate range. This value remains, however, significantly lower than an  $m = 0.4-0.7$  corresponding to superplasticity. In the continuous quest for this phenomenon, it was decided to decrease the testing strain rate even more, since any increase in testing temperature was undesirable. The only testing mode offering this option was chosen: the stress-jump creep testing mode.

### **Stress-jump creep compression test**

The stress-jump creep tests were performed under constant stresses corresponding to 0.2, 0.4, 0.6, 0.7, 0.8 and 0.9 (0.95) of  $\sigma_y$ . To determine the yield stress at two testing temperatures (400 and 500°C), isothermal compression testing up to a strain of 0.15 was carried out on RQ and ECAP-500 specimens. After ECAP-400, the compression test was only performed at 400°C (see yield stress values in Table 5.3). It can be seen that after RQ, the yield stresses of B2-austenite are lower than those after ECAP at 400 and 500°C, and the higher the deformation temperature, the lower the  $\sigma_y$  value.

Using the Table 5.3 data (note that a 0.2% offset has been used to determine  $\sigma_y$ ), the stress-jump creep tests were carried out at 400 and 500°C on the RQ and ECAP-processed specimens, and the resulting strain-time plots are presented in Figure 5.7. Note that to perform these experiments, two opposing requirements had to be taken into account: the

holding time should be as short as possible to avoid grain growth, while it should be sufficiently long to allow the strain rate to reach a steady value.

Table 5.3 Yield stresses of B2-austenite at 400 and 500°C (0.2% offset).

Identification	$\sigma_y$ , MPa	
	400°C	500°C
RQ	320	210
ECAP-500	430	310
ECAP-400	500	-

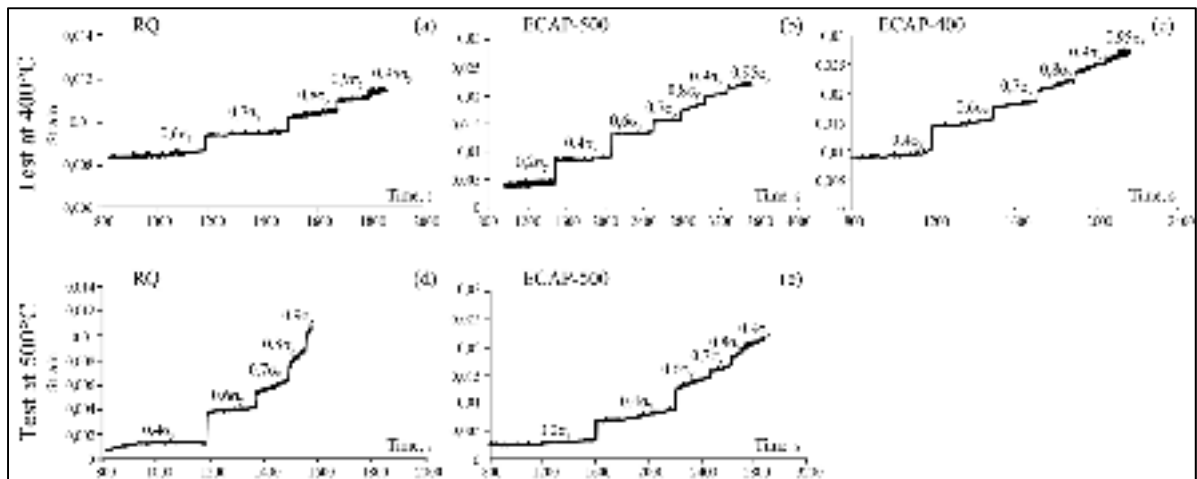


Figure 5.7 Stress-jump creep test diagrams: RQ (a, d), ECAP-500 (b, e), and ECAP-400 (c)

Using the stress-jump creep diagrams of Figure 5.7, strain rates were calculated as slopes of the “strain vs time” plots for each stress (Figure 5.8 and Table 5.4). Given that for RQ specimens at 400°C, creep strain rates under constant stresses of 0.2 and 0.4 $\sigma_y$  were too low to be measured, they were only measured for values of 0.6 $\sigma_y$  and higher. For the same reason, no data can be reported for 0.2 $\sigma_y$  in the case of ECAP-400 (400°C) and RQ (500°C).

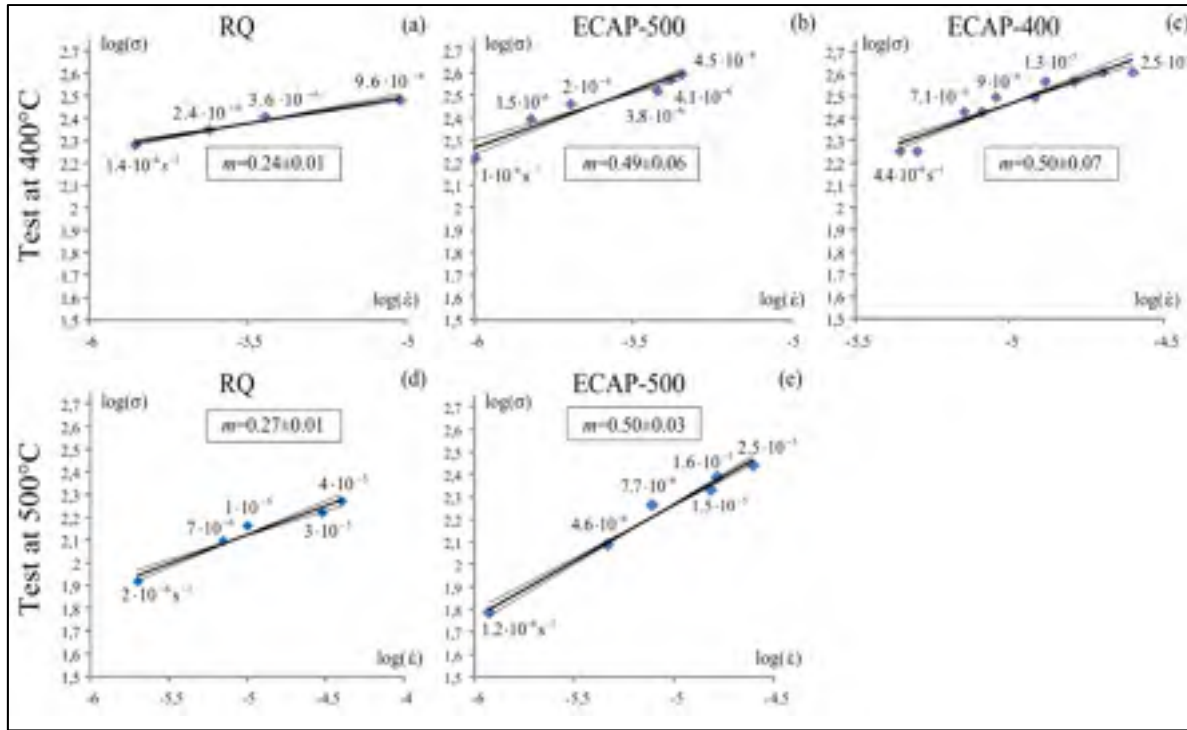


Figure 5.8 The  $\log(\sigma)$  vs  $\log(\dot{\epsilon})$  plots after RQ (a, d), ECAP-500 (b, e), and ECAP-400 (c)

The results presented in Figure 5.8 show an expected regularity: the higher the stress, the higher the creep strain rate. For RQ testing at 400°C, strain rate increases from  $1.4$  to  $9.6 \cdot 10^{-6} \text{ s}^{-1}$  when stress increases from 190 to 300 MPa. For ECAP-500, it increases from  $1$  to  $4.5 \cdot 10^{-6} \text{ s}^{-1}$  when stress increases from 170 to 390 MPa, and for ECAP-400, it increases from  $4.4 \cdot 10^{-6}$  to  $2.5 \cdot 10^{-5} \text{ s}^{-1}$  when stress increases from 180 to 410 MPa.

An increase in testing temperature from 400 to 500°C leads to an increase in creep strain rates under the same stresses. Thus, under the same stress of 180 MPa, when testing temperature increases from 400 to 500°C, the strain rate increases from  $1.4 \cdot 10^{-6}$  to  $4 \cdot 10^{-5} \text{ s}^{-1}$  (RQ), and from  $1.1 \cdot 10^{-6} \text{ s}^{-1}$  to  $7.7 \cdot 10^{-6} \text{ s}^{-1}$  (ECAP-500).



Table 5.4 Strain-rate sensitivity exponent  $m$  measured by stress-jump creep compression test.

Identification	Parameters	Testing at 400°C	Testing at 500°C
RQ	$\dot{\epsilon}, s^{-1}$	$[0.1 - 1] \cdot 10^{-5}$	$[0.2 - 4] \cdot 10^{-5}$
	$m$	$0.24 \pm 0.01$	$0.27 \pm 0.01$
ECAP-500	$\dot{\epsilon}, s^{-1}$	$[0.1 - 0.45] \cdot 10^{-5}$	$[0.1 - 3] \cdot 10^{-5}$
	$m$	$0.49 \pm 0.06$	$0.50 \pm 0.03$
ECAP-400	$\dot{\epsilon}, s^{-1}$	$[0.4 - 2.5] \cdot 10^{-5}$	-
	$m$	$0.50 \pm 0.07$	-

According to the results presented in Figure 5.8 and Table 5.4, the maximum strain rate sensitivity  $m$  at 400°C ranges from the lowest to the highest as follows: RQ ( $m=0.24$ ) → ECAP-500 and ECAP-400 ( $\sim 0.5$ ), and these  $m$  values are reached at higher strain rates for ECAP-400,  $[0.4 - 2.5] \cdot 10^{-5} s^{-1}$ , than for ECAP-500,  $[0.1 - 0.45] \cdot 10^{-5} s^{-1}$ .

Increasing the testing temperature from 400 to 500°C does not bring any significant improvement in the maximum strain-rate sensitivity of both RQ and ECAP-500 specimens. However, the higher the testing temperature, the higher the highest strain rate that maximizes  $m$ . For RQ, this strain rate increases from 1 to  $4 \cdot 10^{-5} s^{-1}$ , when temperature increases from 400 to 500°C, while for ECAP-500, it increases from 0.5 to  $3 \cdot 10^{-5} s^{-1}$ .

### Deformability

It is virtually impossible to use strain rates as low as  $10^{-5} s^{-1}$  during conventional plastic deformation processes. Furthermore, using deformation temperatures as high as 400°C would not allow the grain refinement targeted for practical applications of Ti-Ni SMA [3]. However, the results of the present work suggest that decreasing the grain size of Ti-Ni SMA to submicroscale level could eventually improve the deformability of these alloys at any temperature and any strain rate and, therefore, maintain advantages of low-temperature

severe plastic deformation, thereby creating ultrafine-grained (down to nanoscale) structures, while decreasing the risk of the processing-induced damage. One of the possible strategies could be to use ECAP for preliminary structural refinement (formation of submicrocrystalline structure), followed by severe cold or warm rolling to form nanosubgrain/nanograin structure.

With this hypothesis in mind, the RQ and ECAP-400 specimens were subjected to severe cold rolling (CR) with accumulated logarithmic strain of  $\varepsilon = 2$ . According to [4, 9, 14], the structure of Ti-Ni alloys after CR with  $\varepsilon > 1.9$  is a mixed nanocrystalline and amorphous structure, generally accompanied by a significant number of cold-work induced edge microcracks. To assess the influence of the proposed ECAP+CR processing strategy on this last aspect, the specimens' edges after RQ+CR ( $\varepsilon = 2$ ) and ECAP-400+CR ( $\varepsilon = 2$ ) were examined and the average edge crack length and concentration were calculated (Figure 5.9).

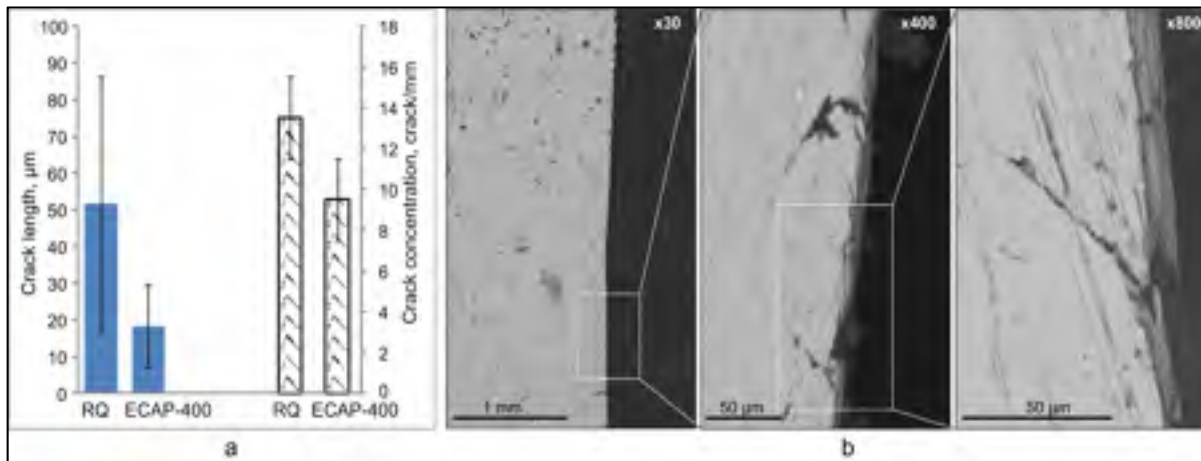


Figure 5.9 Microcracking after additional cold rolling. (a) Average length and concentration of microcracks for RQ and ECAP-400-processed specimens subjected to final CR( $\varepsilon=2$ ); microcrack views: (b) after RQ+CR( $\varepsilon=2$ ) and (c) after ECAP+CR( $\varepsilon=2$ )

It appears that application of a combined thermomechanical processing (ECAP+CR) decreases the severity of the CR-induced material damage. After RQ+CR, the average edge microcrack length is 51  $\mu\text{m}$ , while after ECAP+CR, it could be as low as 18  $\mu\text{m}$ . The same

trend is observed with the microcrack concentration: it decreases from  $\sim 14$  (RQ+CR) to  $\sim 10$  cracks/mm (ECAP+CR) (Figure 5.9).

## 5.6 Discussion

The Ti-50 at.%Ni alloy's microstructure is significantly affected by thermomechanical processing. A combination of ECAP with PDA being applied to this alloy makes it possible to create the material microstructures which differ radically from the as-quenched state. It was shown that the ECAP-PDA processing was responsible for different sizes of structure elements (grains and subgrains). After the reference quenching from 800°C (1 h), the average grain size ( $d$ ) was about 250  $\mu\text{m}$ , while after ECAP (accumulated strain of 5.44), a significant grain/subgrain refinement was observed:  $d = 500$  nm after ECAP at 500°C and  $d = 250$  nm after ECAP at 400°C.

The strain-rate sensitivity exponent  $m$  was measured using tensile and plane-strain compression strain-rate-jump and stress-jump creep tests in the wide temperature and strain-rate ranges: from 20 to 500°C and from  $10^{-3}$  to  $10^{-6}$   $\text{s}^{-1}$ , respectively (all the results are combined in Figure 5.10).

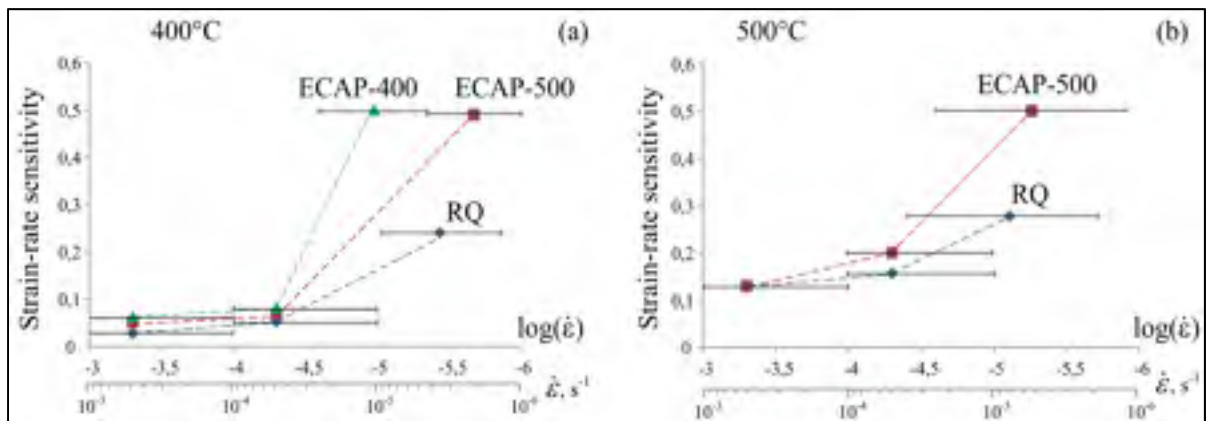


Figure 5.10 Strain-rate sensitivity exponent  $m$  as a function of strain rate and testing temperature after RQ, ECAP-400 and ECAP-500

The strain-rate-jump (tension and compression) tests in the 20-400°C temperature range and in the  $[10^{-3} - 10^{-4}] \text{ s}^{-1}$  strain rate range showed that the strain-rate sensitivity exponent  $m$  increases from 0.006 to 0.028 for  $d = 250 \text{ }\mu\text{m}$  (RQ) and from 0.011 to 0.05 for  $d = 250 \text{ nm}$  (ECAP-400), but it remains nevertheless very low compared to the  $m = 0.5$  value corresponding to superplastic behavior. It is only at strain rates as low as  $0.5 \cdot 10^{-5} \text{ s}^{-1}$  and temperatures as high as 400°C, the strain rate sensitivity starts to increase significantly. At the testing temperature of 400°C,  $m = 0.2$  for RQ ( $d = 250 \text{ }\mu\text{m}$ ), 0.5 for ECAP-400 ( $d = 250 \text{ nm}$ ), and 0.49 for ECAP-500 ( $d = 500 \text{ nm}$ ). A further increase in testing temperature does not really affect the maximum values of the strain rate sensitivity, but does increase the allowable strain rates, leading to these maximum values.

The lowest temperature and the highest strain rate leading to  $m = 0.5$  are 400°C and  $2.5 \cdot 10^{-5} \text{ s}^{-1}$ , and these results are obtained with the smallest grain/subgrain size  $d = 250 \text{ nm}$  resulted from the ECAP (400°C) + PDA (400°C, 1h) processing. Thus, it can be concluded that the smaller the grain size of Ti-Ni alloy, the lower the temperature and the higher the strain rate leading to superplasticity.

Generally, grain boundary sliding contributes to the superplastic behavior of metallic materials [30, 44, 45]. From our experiments, the activation volume  $\Delta V/b^3$  calculated as [46]:  $\Delta V/b^3 = \sqrt{3}kT/m\sigma b^3$  (where  $m$  is the strain-rate sensitivity exponent,  $k$  is the Boltzmann constant,  $T$  is the testing temperature,  $\sigma$  is the steady-state flow stress and  $b$  is the Burgers vector) (in our case  $b \approx 2.61 \text{ }\text{\AA}$  of B2-austenite), equals to 3-4 for the creep test at 400°C after ECAP-400, which corresponds to the diffusion and grain boundary sliding deformation mechanisms.

To compare the results obtained here with the existing data on the superelasticity of coarse-grained Ti-Ni alloys, two benchmark cases were taken from the literature: a) high temperature–high strain rate:  $[950 - 1100]^\circ\text{C}$  &  $[10^{-6} - 10^{-5}] \text{ s}^{-1}$ , and b) low temperature–low strain rate:  $[470 - 530]^\circ\text{C}$  &  $[2 \cdot 10^{-9} - 8 \cdot 10^{-6}] \text{ s}^{-1}$  [20, 21]. In our work, superplasticity has been observed at temperatures lower than the latter case and at strain rates higher than the former

case: 400°C &  $2.5 \cdot 10^{-5} \text{s}^{-1}$ , respectively, and this gain is explained by the grain refinement resulted from the ECAP+PDA processing.

Finally, it has been proven that grain refinement improves the strain-rate sensitivity and deformability of Ti-Ni alloys not only at elevated, but also at low temperatures. Based on the last outcome, it is possible to imagine a multi-step processing sequence consisting of a series of deformation–annealing steps with gradually decreasing deformation temperature, this decrease being coordinated with grain refinement after each step of this thermomechanical processing. Using this approach, the creation of truly nanocrystalline bulk Ti-Ni material free of processing-induced defects may soon become a reality.

## 5.7 Conclusions

1. The smaller the grain/subgrain size of parent B2-austenite in Ti-50 at.%Ni alloy, the lower the temperature and the higher the strain rate leading to superplasticity: this phenomena is observed at temperatures as low as 400°C and strain rates as high as  $2.5 \cdot 10^{-5} \text{s}^{-1}$  when submicrograin/subgrain size is reduced to 250 nm.
2. Thermomechanical processing consisting of ECAP (400°C) and PDA (400°C, 1h) leads to a significant grain/subgrain refinement of the Ti-Ni structure down to submicron scale, as well as a significant improvement of the Ti-Ni alloy low-temperature deformability. The latter is manifested in this works by a radical decrease in microcrack size and concentration in the process of severe cold rolling of submicrograined/subgrained Ti-50 at.%Ni alloy.

## 5.8 Acknowledgments

The authors wish to indicate their appreciation for the financial support provided by the Natural Sciences and Engineering Research Council of Canada 227549-2009 and by the Ministry of Education and Science of the Russian Federation in the frame work of the

Increase Competitiveness Program of NUST "MISIS", grant No. K3-2014-017, and Federal Targeted Program "Research and development in priority directions of scientific and technological complex of Russia for 2014-2020", Agreement No. 14.575.21.0094.

## 5.9 References

- [1] V. Brailovski, S.D. Prokoshkin, P. Terriault, F. Trochu, Shape memory alloy: Fundamentals, modeling and applications, École de technologie supérieure, 2003.
- [2] K. Otsuka, C.M. Wayman, Shape memory materials, Cambridge University Press, Cambridge, United Kingdom, 1998.
- [3] V. Brailovski, S.D. Prokoshkin, I.Y. Khmelevskaya, K.E. Inaekyan, V. Demers, S.V. Dobatkin, E.V. Tatyannin, Materials Transactions, 47 (2006) 795-804.
- [4] V. Demers, V. Brailovski, S.D. Prokoshkin, K.E. Inaekyan, Materials Science and Engineering A 513-514 (2009) 185-196.
- [5] S.D. Prokoshkin, V. Brailovski, K.E. Inaekyan, V. Demers, I.Y. Khmelevskaya, S.V. Dobatkin, E.V. Tatyannin, Materials Science and Engineering: A, 481-482 (2008) 114-118.
- [6] R.Z. Valiev, V.G. Pushin, V.V. Stolyarov, T.C. Lowe, Y.T. Zhu, Materials Science and Engineering A 410-411 (2005) 386-389.
- [7] R.Z. Valiev, Metals 1 (2004) 15-21.
- [8] R.Z. Valiev, R.K. Islamgaliev, I.V. Alexandrov, Progress in Materials Science, 45 (2000) 103-189.
- [9] V. Demers, V. Brailovski, S.D. Prokoshkin, K.E. Inaekyan, Journal of Materials Processing Technology, 209 (2009) 3096-3105.
- [10] A. Kreitchberg, V. Brailovski, S. Prokoshkin, Y. Facchinello, K. Inaekyan, S. Dubinskiy, Materials Science and Engineering A, 562 (2013) 118-127.
- [11] A. Kreitchberg, V. Brailovski, S. Prokoshkin, K. Inaekyan, Metallography, Microstructure, and Analysis, 3 (2014) 46-57.

- [12] H. Shahmir, M. Nili-Ahmadabadi, M. Mansouri-Arani, T.G. Langdon, *Materials Science and Engineering A*, 576 (2013) 178-184.
- [13] V.M. Segal, *Material Science and Engineering*, 197 (1995) 157-164.
- [14] V. Brailovski, S. Prokoshkin, K. Inaekyan, V. Demers, *Journal of Alloys and Compounds*, 509 (2011) 2066-2075.
- [15] V.V. Stolyarov, E.A. Prokofev, S.D. Prokoshkin, S.B. Dobatkin, I.B. Trubitsyna, I.Y. Khmelevskaya, V.G. Pushin, R.Z. Valiev, *Physics of Metals and Metallography*, 100 (2005) 608-618.
- [16] V.G. Pushin, D.V. Gunderov, N.I. Kourov, L.I. Yurchenko, E.A. Prokofiev, V.V. Stolyarov, Y.T. Zhu, R.Z. Valiev, in: *Ultrafine Grained Materials 3 Symposium*, TMS, Warrendale, PA, USA, 2004, pp. 481-486.
- [17] V.G. Pushin, R.Z. Valiev, in: *Interfacial Effects and Novel Properties of Nanomaterials*, 2003, Trans Tech Publications Ltd, Warsaw, Poland, 2003, pp. 13-24.
- [18] V.V. Stolyarov, *Materials Science and Engineering A*, 503 (2009) 18-20.
- [19] V.V. Stolyarov, *Journal of Alloys and Compounds*, 577 (2013) S274-S276.
- [20] G. Eggeler, J. Khalil-Allafi, K. Neuking, A. Dlouhy, *Zeitschrift fur Metallkunde*, 93 (2002) 654-660.
- [21] S.M. Oppenheimer, A.R. Yung, D.C. Dunand, *Scripta Materialia*, 57 (2007) 377-380.
- [22] C. Llexcellent, P. Robinet, J. Bernardini, D.L. Beke, P. Olier, Wiley-VCH Verlag, 2005, pp. 509-512.
- [23] A.K. Mukherjee, *Symposium on TiNi and Associated Compounds*, 3 April 1967, 1968, pp. 2201-2204.
- [24] H. Kato, T. Yamamoto, S. Hashimoto, S. Miura, *Materials Transactions, JIM*, 40 (1999) 343-350.
- [25] E. Kobus, K. Neuking, G. Eggeler, I. Wittkamp, *Praktische Metallographie*, 39 (2002) 177-186.

- [26] M. Morakabati, M. Aboutalebi, S. Kheirandish, A. Karimi Taheri, S.M. Abbasi, *Intermetallics*, 19 (2011) 1399-1404.
- [27] V.V. Stolyarov, Y. Theodore Zhu, I.V. Alexandrov, T.C. Lowe, R.Z. Valiev, *Materials Science and Engineering A*, 299 (2001) 59-67.
- [28] T.G. Langdon, M. Furukawa, M. Nemoto, Z. Horita, in: *International Conference on Superplasticity in Advanced Materials (ICSAM-2000)*, Trans Tech Publications, Switzerland, 2001, pp. 489-498.
- [29] J.E. Dorn, *Journal of the Mechanics and Physics of Solids*, 3 (1955) 85-116.
- [30] A.K. Mukherjee, R.S. Mishra, *Encyclopedia of materials: Science and Thechnology*, 2 (2001) 8977-8981.
- [31] A.K. Mukherjee, in: *Rate Processes in Plastic Deformation II: Towards a Unified Constitutive Theory of Deformation*, TMS Fall Meeting 2000, Elsevier, Switzerland, 2002, pp. 1-22.
- [32] F.A. Mohamed, T.G. Langdon, *Acta Metallurgica*, 23 (1975) 117-124.
- [33] F.A. Mohamed, S. Shen-Ann, T.G. Langdon, *Acta Metallurgica*, 23 (1975) 1443-1450.
- [34] P.N. Comley, *Journal of Materials Engineering and Performance*, 17 (2008) 183-186.
- [35] Y.M. Haddad, in: *Kluwer Academic Publishers, The Netherlands*, 2001.
- [36] N.Q. Chinh, A. Juhász, P. Tasnádi, I. Kovács, *Acta Universitatis Carolinae. Mathematica et Physica*, 32 (1991) 17-23.
- [37] T.G. Langdon, in: *Symposium on the Mechanical, Microstructural and Fracture Processes in Superplasticity*, USA, 1982, pp. 689-701.
- [38] H. Watanabe, F. Ono, K. Higashi, *Material Science Forum*, 447-448 (2004) 189-196.
- [39] S.D. Prokoshkin, V. Brailovski, A.V. Korotitskiy, K.E. Inaekyan, A.M. Glezer, *Physics of Metals and Metallography*, 110 (2010) 289-303.



- [40] X. Ren, N. Miura, J. Zhang, K. Otsuka, K. Tanaka, M. Koiwa, T. Suzuki, Y.I. Chumlyakov, M. Asai, *Materials Science and Engineering: A*, 312 (2001) 196-206.
- [41] K. Otsuka, X. Ren, *Progress in Materials Science*, 50 (2005) 511-678.
- [42] S.D. Prokoshkin, A.V. Korotitskiy, V. Brailovski, S. Turenne, I.Y. Khmelevskaya, I.B. Trubitsyna, *Acta Materialia*, 52 (2004) 4479-4492.
- [43] S.D. Prokoshkin, A.V. Korotitskiy, V. Brailovski, K.E. Inaekyan, S.M. Dubinskiy, *Physics of Metals and Metallography*, 112 (2011) 170-187.
- [44] J.-P. Poirier, *Diffusion creep, grain-boundary sliding and superplasticity. Creep of crystals*, Cambridge University Press, Cambridge, London, New York, New Rochelle, Melbourne, Sydney, 1985.
- [45] O.A. Kaibyshev, *Materials Science and Engineering A*, 324 (2002) 96-102.
- [46] P. Rodriguez, in: *Third TMS/ASM Symposium on "Dynamic Behavior of Materials"*, ASM Int, USA, 2004, pp. 2697-2705.



## CONCLUSION

The principal research objectives of this project were to study the interrelations between the processing conditions, damageability during processing, microstructure and functional properties of Ti-Ni SMAs and to optimize the processing conditions of nanocrystalline Ti-Ni SMAs with the aim of improving their long-term functional performance.

In respect to the first objective of this project, the following TMTs were performed: CR( $e=0.75$ ), CR( $e=1.0$ ), CR( $e=1.2$ ), CR( $e=1$ )+IA+CR( $e=0.2$ ), CR( $e=1$ )+IA+WR( $e=0.2$ ), WR( $e=1$ )+IA+WR( $e=0.2$ ) and WR( $e=1.2$ ). All the processing routes were followed by a PDA at 400°C (1h). The main features of structure and texture formation of Ti-50.26 at.%Ni alloy as a result of these TMTs are the following:

- The amount of nanosubgrained structure increases at the expense of nanocrystalline structure; grain/subgrain size increases and dislocation density increases as well when CR true strain decreases from  $e=1.2$  to 0.75 and WR and IA are introduced to the TMT with total accumulated strain  $e=1.2$ . After CR( $e=1.2$ ) and PDA (400°C, 1h) the mainly nanocrystalline structure forms.
- Using inverse pole figure and orientation distribution functions, the main texture component of B2-austenite after all processing routes was determined as  $\{100\}\langle 011\rangle$ . Moreover, this texture component is the sharpest after the CR( $e=1$ )+IA+WR( $e=0.2$ ) processing route.

The fatigue life was significantly improved in two cases: either when WR and AI were introduced in the TMT processing or when CR strain was decreased from  $e=1.2$  to 0.75 as a consequence of reduced processing-induced damage and development of a favorable B2-austenite texture. However, this fatigue life improvement came with a price tag: inferior performances of the mixed nanocrystalline and nanosubgrained structures compared to the

nanocrystalline structures, in terms of their maximum recovery strains and stresses, cycling stability and tolerance to small-crack propagation.

Thus, when comparing the nanocrystalline with the mixed nanocrystalline and nanosubgrained structures, the former ensured higher functional properties and, therefore, still remained a target. However, to draw an entire benefit from the property-enhancement potential of nanocrystalline structures, the conditions leading to the improved deformability of Ti-Ni SMAs were still to be found.

As of the second objective of this project, it was shown that the deformability of Ti-Ni SMAs could be improved. The preliminary structural refinement of these alloys to a micro-scale promoted their deformability at any temperature and strain rate. The proposed TMT consisting of ECAP at elevated temperatures followed by severe cold rolling was found beneficial to minimize processing-induced damage, while creating the necessary conditions for the nanostructure formation.

## **RECOMENDATIONS**

The following research directions can be recommended for the sequel of this project:

- Development of nanocrystalline Ti-Ni alloys using novel TMTs schedules, such as, for example, combinations of ECAP with CR and/or WR. It will allow the inherent potential of these alloys to be entirely exploited, as far as it concerns their static and fatigue functional characteristics.
- In-depth analysis of the microcrack formation during rolling and their preexistence in the supplied as-drawn wire to validate our conclusions about higher tolerance of nanocrystalline Ti-Ni alloys to small crack propagation.
- A detailed study of the functional fatigue resistance of Ti-Ni alloys with structure varying from coarse grained to nanocrystalline.



## APPENDIX I

### EFFECT OF INITIAL RECOVERY STRESS ON THE FATIGUE LIFE OF Ti-50.26 at.%Ni ALLOY

In the first article the fatigue life of Ti-50.26 at.%Ni alloy subjected to CR and/or WR and IA was studied using a recovery stress generation-relaxation (constrained recovery) test. A sample was strained up to  $\varepsilon_f=9\%$ , then released to allow the elastic springback. The initial (induced) strain was thus set at  $\varepsilon_f=6-7\%$ . Afterwards, the sample was kept fixed and then heated from room temperature to 200°C to allow almost complete reverse martensitic transformation and recovery stress generation,  $\sigma_r$ , and finally air-cooled to room temperature. The test was repeated until sample failure.

The maximum recovery stress (1170 MPa) and the highest stability were observed after the CR( $e=1.2$ ) route when number of cycles to failure was the lowest (780 cycles). Introduction of WR and IA, CR( $e=1$ )+IA+WR( $e=0.2$ ), provided an increase in the fatigue life by 2-2.5 times and a decrease in the maximum recovery stress to 1030 MPa. The maximum cycles up to failure (3870 cycles) were observed after the CR( $e=0.75$ ) route when the maximum recovery stress (940 MPa) and stability were the lowest.

Figure A.1 summarizes the results obtained in the first article following constrained recovery testing of the three processing routes (where  $\sigma_{r,1}^{max}$  is maximum recovery stress in first cycle,  $\sigma_{r,N}^{max}$  is maximum recovery stress in the last cycle before failure,  $\Delta\sigma_r$  is degradation of recovery stress during cycling and  $N_f$  is number of cycles to failure).

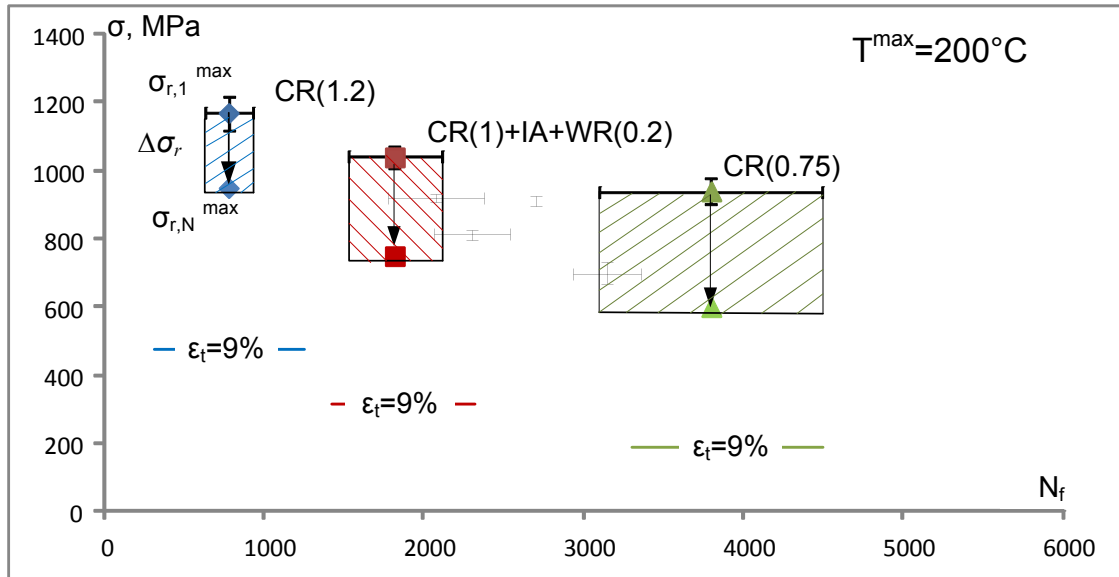


Figure A.1 Fatigue life of Ti-50.26 at.%Ni alloy at different recovery stress in the first cycle

According to the obtained results, after CR( $e=0.75$ ) the number of cycles to failure (3800 cycles) exceeds  $N_f$  of the processed CR( $e=1.2$ ) and CR( $e=1$ )+IA+WR( $e=0.2$ ) samples (1820 and 780 cycles, respectively). It can be explained by comparing maximum recovery stress after these routes: the processed CR( $e=1.2$ ) and CR( $e=1$ )+IA+WR( $e=0.2$ ) samples were tested at higher stress rates than CR(0.75). Therefore, to confirm or contradict the superiority of CR( $e=0.75$ ) routes in terms of fatigue life, the following tests were performed when either the maximum recovery stresses  $\sigma_{r,1}^{max}$  in the first cycle or the maximum recovery stresses  $\sigma_{r,N}^{max}$  in the last cycle were close in cases of these processing routes. From this point of view, the maximum target of  $\sigma_{r,1}^{max}$  and  $\sigma_{r,N}^{max}$  will be 940 MPa and 600 MPa, which corresponds to a maximum  $\sigma_{r,1}^{max}$  and  $\sigma_{r,N}^{max}$  obtained after CR(0.75).

The maximum recovery stress value can be decreased using the following methods: (1) reduction in maximum heating temperature ( $<200^\circ\text{C}$ ); or (2) reduction in total induced strain  $\epsilon_t$  ( $< 9\%$ ) in recovery stress generation-relaxation testing.

The following results were obtained in this case:



- (1) According to the first method, the samples were strained up to  $\varepsilon_f=9\%$ , then released to allow elastic springback, as in the previous test. Afterwards, the sample was kept fixed and then heated from room temperature to a temperature below  $200^\circ\text{C}$  (Figure A.2). In this case, the reverse martensite transformation was incomplete (as compared to the previous one).

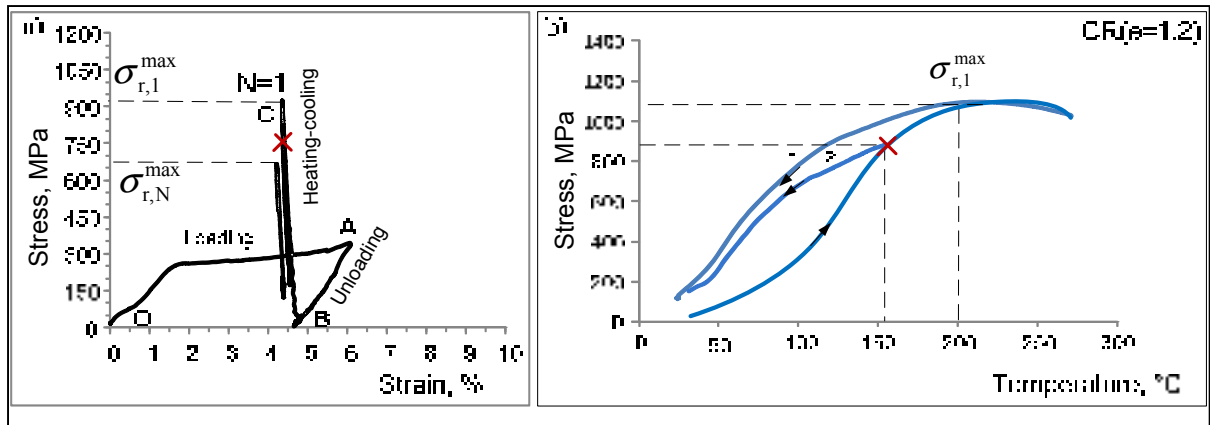


Figure A.2 Method of recovery stress lowering based on heating temperature decrease from  $200^\circ\text{C}$  (1) to  $T < 200^\circ\text{C}$  (2) for Ti-50.26 at.%Ni alloy after CR(1.2). Stress-strain plot (a); and recovery stress-temperature plot (b) of constrained recovery test

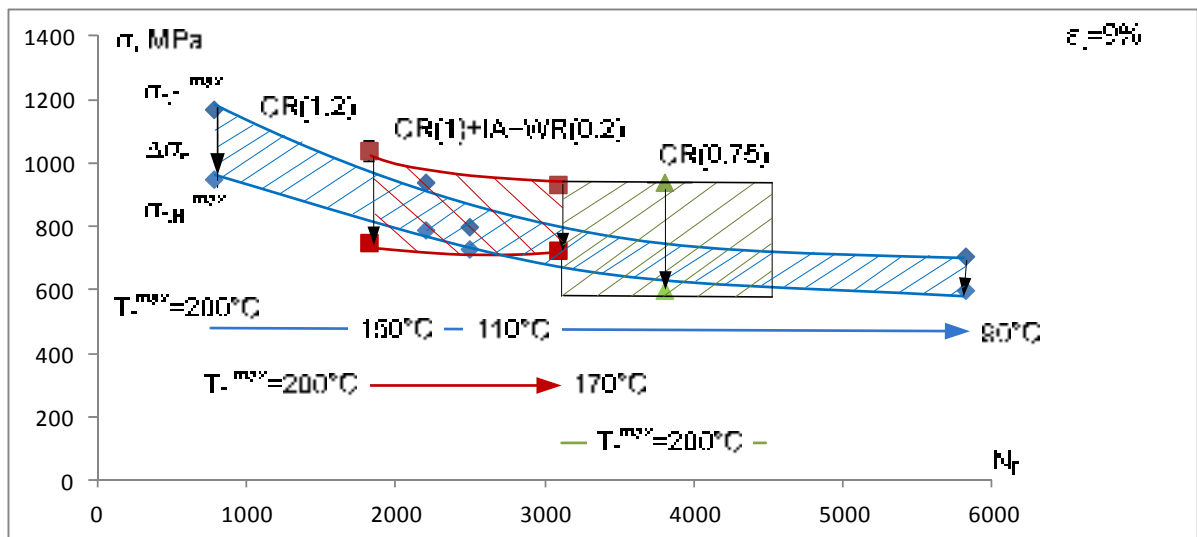


Figure A.3 Fatigue life of Ti-50.26 at.%Ni alloy after three TMTs as a function of heating temperature

The decrease in the maximum temperature from 200°C to 110-150°C (for CR(1.2) route) and to 170°C (for CR(1)+IA+WR(0.2)) ensured the maximum recovery stress of 940 MPa after these TMTs as a consequence of an incomplete martensitic transformation (Figure A.3). In this case, the fatigue life of CR(1.2) samples was improved threefold (2200 cycles) and CR(1)+IA+WR(0.2) samples were improved 1.5 times (3090 cycles). Furthermore, the incomplete reverse martensitic transformation led to an enhancement of the recovery stress stability due to the lower transformation-related hardening. Therefore, the less incompleteness of reverse martensitic transformation, the higher the recovery stress stability.

Thus, the decrease in the maximum heating temperature and, consequently, in the maximum recovery stress  $\sigma_{r,l}^{max}$  improves the functional fatigue performance. However, note that the new  $N_f$  in CR(1.2) and CR(1)+IA+WR(0.2) samples is still lower than the  $N_f$  of the CR(0.75) sample under the same value of  $\sigma_{r,l}^{max}$ .

The next step of this study consisted of the further decrease in  $\sigma_{r,N}^{max}$  to 600 MPa in the last cycle. This value corresponds to the  $\sigma_{r,N}^{max}$  of CR(0.75) samples after heating to 200°C, while after CR(1.2) it is 800 MPa. In this case, the maximum heating temperature was decreased to 90°C which provided a sixfold improvement of the fatigue life, 6020 cycles (1.5 times higher than after the CR(0.75) route).

(2) Following application of the second method, the total induced strain decreased from 9% to 6%, 5.7% and 5% for CR(1.2) samples and to 8% and 7.5% for CR(1)+IA+WR(0.2) as shown in Figure A.4.

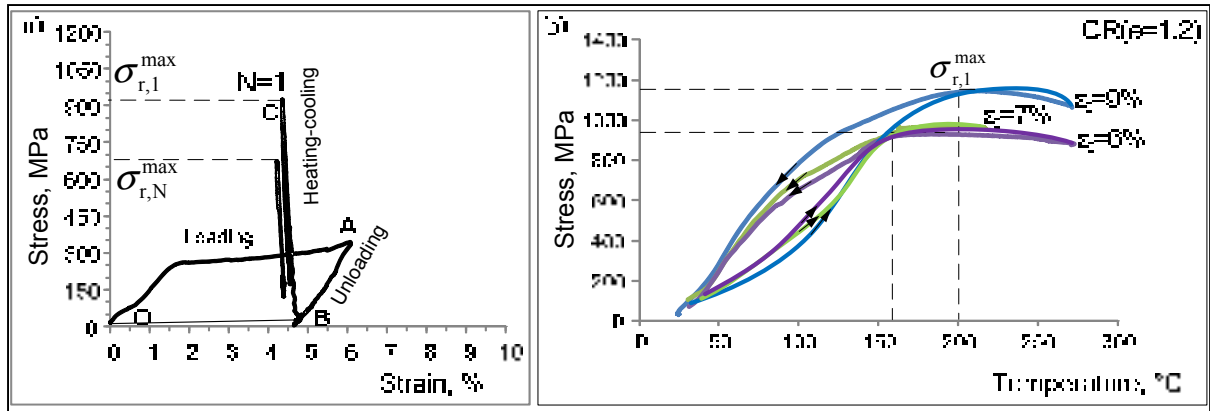


Figure A.4 Method of recovery stress lowering based on total induced strain decrease from 9% to  $\varepsilon_i < 9\%$  for Ti-50.26 at.%Ni alloy after CR(1.2). Stress-strain plot (a); and recovery stress/temperature plot (b) of constrained recovery testing

The maximum recovery stress of 910-920 MPa was obtained at  $\varepsilon_i=6\%$  for CR(1.2) samples and at  $\varepsilon_i=8\%$  for CR(1)+IA+WR(0.2) samples. However, the lower the  $\varepsilon_i$  value, the lower the temperature at which an irreversible plastic deformation is involved in the deformation mechanism of austenite during heating. Since the plastic deformation negatively affects the fatigue life due to increase in an unrecoverable strain, to prevent the plastic deformation, the maximum heating temperature should be lowered as well.

Generally speaking, when the recovery stress/temperature curve reaches “plateau” (the increase in recovery stress value is insignificant during heating), plastic deformation occurs (Figure A.4b). The preliminary analysis of recovery stress/temperature curves allows determination of maximum heating temperature to prevent the beginning of plastic deformation (Table A.1).

Table A.1      Recovery stress as a function of temperature and total induced strain for Ti-50.26 at.%Ni alloy after CR(1.2) and CR(1)+IA+WR(0.2)

TMT	Parameters	Values			
CR(1.2)	$\varepsilon_t$ , %	9	6	5.7	5
	$T$ , °C	200	160-165	150-145	130
	$\sigma_{r,l}^{max}$ , MPa	1170	920	810	700
CR(1)+IA +WR(0.2)	$\varepsilon_t$ , %	9	8	7.5	
	$T$ , °C	200	170-165	160	
	$\sigma_{r,l}^{max}$ , MPa	1030	910	860	

Figure A.5 displays the results of fatigue life as a function of recovery stress and total induced strain

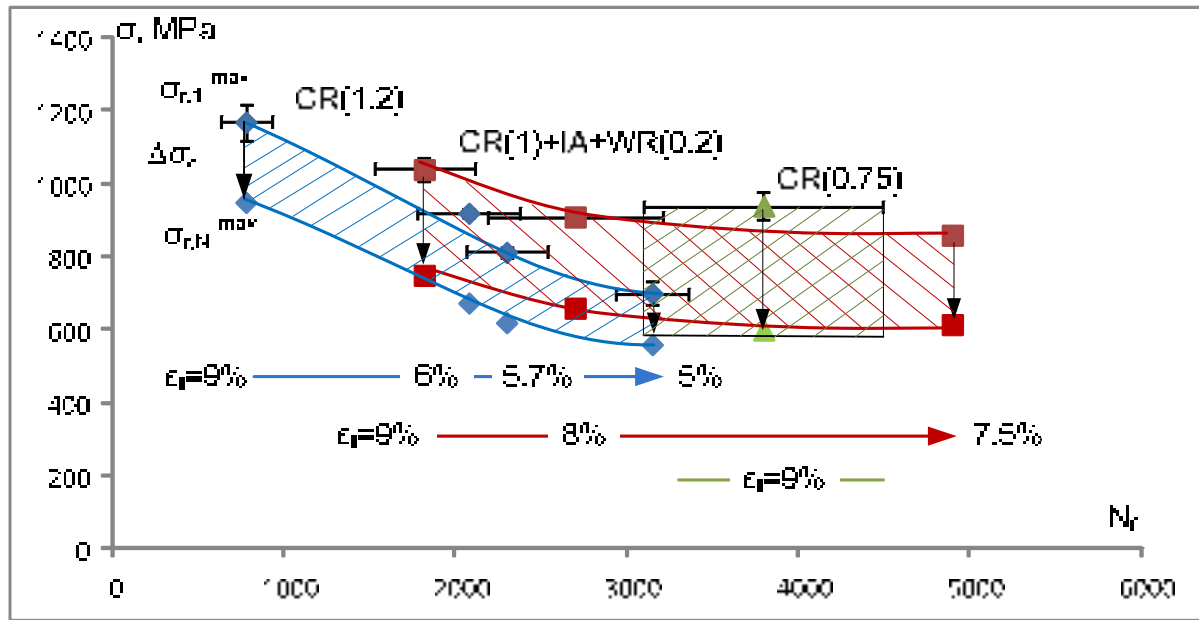


Figure A. 5 Fatigue life of Ti-50.26 at.%Ni alloy after three TMTs as function of total induced strain

The decrease in total induced strain  $\varepsilon_t$  and, consequently, in  $\sigma_{r,l}^{max}$  to 910-920 MPa leads to a significant increase in fatigue life: by 2.5 times (2080 cycles) for CR(1.2) samples and by 1.5

times (2700 cycles) for CR(1)+IA+WR(0.2) samples. However, as compared to previous testing, the stability of recovery stress, in this case, is not enhanced.

The decrease in recovery stress  $\sigma_{r,N}^{max}$  in the last cycle to 600 MPa promotes the further improvement of fatigue life: by 3.5 times (to 3000 cycles) at  $\varepsilon_t=5\%$  for CR(1.2) samples and by 2.5 times (to 4900 cycles) at  $\varepsilon_t=7.5\%$  for CR(1)+IA+WR(0.2). Moreover, in this case, the  $N_f$  after CR(1)+IA+WR(0.2) is higher by 1.2 times than  $N_f$  after CR(0.75).

Thus, the recovery stress value significantly affects the fatigue life of samples. Under similar deformation conditions, the greatest number of cycles to failure is observed after CR(1)+IA+WR(0.2) and CR(0.75) routes. However, the recovery stress stability of CR(1)+IA+WR(0.2) samples is significantly higher than that following CR(0.75) and it can be improved by lowering maximum heating temperature in the constrained recovery test.



## LIST OF REFERENCES

- [1] Brailovski, V., S. D. Prokoshkin, I. Yu Khmelevskaya, K. E. Inaekyan, V. Demers, E. Bastarache, S. V. Dobatkin et E. V. Tatyatin. 2006. «Interrelations between the properties and structure of thermomechanically-treated equiatomic Ti-Ni alloy». *Materials Science and Engineering A*, vol. 438-440, p. 597-601.
- [2] Demers, V., V. Brailovski, S. D. Prokoshkin et K. E. Inaekyan. 2009. «Thermomechanical fatigue of nanostructured Ti-Ni shape memory alloys». *Materials Science and Engineering A*, vol. 513-514, no 1-7, p. 185-96.
- [3] Facchinello, Y., Brailovski V., Georges T. et Prokoshkin S. D. 2012. «Functional properties of nanostructured Ti-Ni SMA produced by a combination of cold, warm rolling and annealing». In *7th International Conference on Processing and Manufacturing of Advanced Materials, THERMEC'2011*, August 1, 2011 - August 5, 2011. (Quebec City, QC, Canada) Vol. 409, p. 615-620.
- [4] Karaman, I., Karcka H. E., Maier H. J. et Luo Z. P.. 2003. «The effect of severe marforming on shape memory characteristics of a Ti-rich NiTi alloy processed using equal channel angular extrusion». *Metallurgical and Materials Transactions A*, vol. 34A, no 11, p. 2527-39.
- [5] Brailovski, V., S. Prokoshkin, K. Inaekyan et V. Demers. 2011. «Functional properties of nanocrystalline, submicrocrystalline and polygonized Ti-Ni alloys processed by cold rolling and post-deformation annealing». *Journal of Alloys and Compounds*, vol. 509, no 5, p. 2066-75.
- [6] Inaekyan, K., V. Brailovski, S. Prokoshkin, A. Korotitskiy et A. Glezer. 2009. «Characterization of amorphous and nanocrystalline Ti-Ni-based shape memory alloys». *Journal of Alloys and Compounds*, vol. 473, no 1-2, p. 71-8.
- [7] Prokoshkin, S. D., V. Brailovski, A. V. Korotitskiy, K. E. Inaekyan et A. M. Glezer. 2010. «Specific features of the formation of the microstructure of titanium nickelide upon thermomechanical treatment including cold plastic deformation to degrees from moderate to severe». *Physics of Metals and Metallography*, vol. 110, no 3, p. 289-303.
- [8] Facchinello, Yann. 2011. «Development de la technologie de laminage à tiède pour la production d'alliage à mémoire de forme Ti-Ni». Montreal, ETS.
- [9] Facchinello, Y., Brailovski V., Prokoshkin S. D., Georges T. et Dubinskiy S. M.. 2012. «Manufacturing of nanostructured Ti-Ni shape memory alloys by means of cold/warm rolling and annealing thermal treatment». *Journal of Materials Processing Technology*, vol. 212, no 11, p. 2294-2304.

- [10] Schey, J.A. 2000. Introduction to Manufacturing Processes.
- [11] Gorelic, S.S. 2002. X-ray and electron optical analyse. Moscow MISIS.
- [12] Paula, A. S., Mahesh, K. K., Schell N. et Femandes F. M. B.. 2010. «Textural modifications during recovery in Ti-rich Ni-Ti shape memory alloy subjected to low level of cold work reduction». Materials Science Forum, vol. 636-637, p. 618-23.
- [13] Mulder, Jan H., Paul E. Thoma et Jeno Beyer. 1993. «Anisotropy of the shape memory effect in tension of cold-rolled 50.8 Ti 49.2 Ni (at.%) sheet». Zeitschrift fuer Metallkunde/Materials Research and Advanced Techniques, vol. 84, no 7, p. 501-508.
- [14] Paula, A. S., Mahesh, K. K. et Braz Fernandes, F.M. 2009. «Texture evolution by multiple steps of marformaing in Ti-rich Ni-Ti shape memory alloy». In ESOMAT. (2009).
- [15] Zhao, L., Willemse, P. F., Mulder, J. H., Beyer, J. et Wei, W. 1998. «Texture development and transformation strain of a cold-rolled Ti50-Ni45-Cu5 alloy». Scripta Materialia, vol. 39, no 9, p. 1317-23.
- [16] Khantachawana, A., Miyazaki, S., Iwai, H. et Kohl, M. 1999. «Effect of heat-treatment on the texture and anisotropy of transformation strain in Ti-Ni-Fe rolled thin plates». In ICOMAT 98. International Conference on Martensitic Transformations, 7-11 Dec. 1998. (Switzerland), vol. A273-275, p. 763-8.
- [17] Monasevich, L. A., Paskal, Yu I., Prib, V. E., Timonin, G. D. et Chernov, D. B. 1979. «Effect of texture on the shape memory effect in titanium nickelide». Metal Science and Heat Treatment, vol. 21, no 9-10, p. 735-7.
- [18] Zel'dovich, V. I., Sobyana, G. A., Rinkevich, O. S. et Gundyrev, V. M. 1996. «Shape memory effects, thermal expansion, and texture of B19' martensite in titanium nickelide». Technical Physics, vol. 41, no 11, p. 1158-62.
- [19] Inoue, H., Miwa N. et Inakazu, N. 1996. «Texture and shape memory strain in TiNi alloy sheets». Acta Materialia, vol. 44, no 12, p. 4825-34.
- [20] Yuan, W. Q., et Yang, S. Q. 2002. «Effect of texture on elastic modulus and pseudo-elastic strain of Ti-Ni shape memory alloys». Journal of Materials Science Letters, vol. 21, no 6, p. 443-5.
- [21] Yuan, W. Q., et Yi, S. 1999. «Pseudo-elastic strain estimation of textured TiNi shape memory alloys». Materials Science and Engineering A, vol. A271, no 1-2, p. 439-48.
- [22] Liu, Y., Xie, Z. L., Humbeeck, J. Van et Delaey, L. 1999. «Effect of texture orientation on the martensite deformation of NiTi shape memory alloy sheet». Acta Materialia, vol. 47, no 2, p. 645-60.



- [23] Li, D. Y., Wu, X. F. et Ko, T. 1990. «The texture of Ti-51.5 at.%Ni rolling plate and its effect on the all-round shape memory effect». *Acta Metallurgica et Materialia*, vol. 38, no 1, p. 19-24.
- [24] Gundyrev, V. M., et Zel'dovich, V. I. 2003. «On the texture and crystal structure of the B19' martensite in single-crystal titanium nickelide». *Physics of Metals and Metallography*, vol. 96, no 1, p. 86-91.
- [25] Mulder, J. H., Thoma, P. E. et Beyer, J. 1994. «Anisotropy of thermal fatigue properties of cold-rolled TiNi sheet». *Materials Characterization*, vol. 32, no 3, p. 161-8.
- [26] Valiev, R. Z., Islamgaliev, R. K. et Alexandrov, I. V. 2000. «Bulk nanostructured materials from severe plastic deformation». *Progress in Materials Science*, vol. 45, no 2, p. 103-89.
- [27] Ryklina, E. P., I. Yu Khmelevskaya, S. D. Prokoshkin, S. M. Dubinskii, A. Yu Kreitsberg et V. A. Sheremet'ev. 2011. «Production, structure, and properties of bulk nanostructural and ultrafine-grain alloys with shape memory». *Steel in Translation*, vol. 40, no 11, p. 954-960.
- [28] Segal, V.M. 1995. «Materials processing by simple shear». *Material Science and Engineering*, vol. 197, p. 157-164.
- [29] Stolyarov, Vladimir V., Y. Theodore Zhu, Igor V. Alexandrov, Terry C. Lowe et Ruslan Z. Valiev. 2001. «Influence of ECAP routes on the microstructure and properties of pure Ti». *Materials Science and Engineering A*, vol. 299, no 1-2, p. 59-67.
- [30] Langdon, T. G., M. Furukawa, M. Nemoto et Z. Horita. 2001. «Using severe plastic deformation for grain refinement and superplasticity». In *International Conference on Superplasticity in Advanced Materials (ICSAM-2000)*, 1-4 Aug. 2000. (Switzerland) Vol. 357-359, p. 489-98.
- [31] Yongbo, Xu, Zhang Jinghua, Bai Yilong et M. A. Meyers. 2008. «Shear localization in dynamic deformation: microstructural evolution». *Metallurgical and Materials Transactions A* vol. 39, no 4, p. 811-43.
- [32] Maynadier, Anne, Dorian Depriester, Karine Lavernhe-Taillard et Olivier Hubert. 2011. «Thermo-mechanical description of phase transformation in Ni-Ti Shape Memory Alloy». In *11th International Conference on the Mechanical Behavior of Materials, ICM11*, June 5, 2011 - June 9, 2011. (Como, Italy) Vol. 10, p. 2208-2213.
- [33] Watanabe, S., K. Kawata, T. Kokie, T. Suda, S. Ohnuki, H. Takahashi, Y. Matsukawa et M. Kiritani. 2003. «Non-equilibrium local phase formation by high-speed deformation in NiTi». *Materials Science and Engineering A*, vol. A350, no 1-2, p. 145-9.

- [34] Stolyarov, V. V., E. A. Prokofiev, S. D. Prokoshkin, S. B. Dobatkin, I. B. Trubitsyna, I. Yu Khmelevskaya, V. G. Pushin et R. Z. Valiev. 2005. «Structural features, mechanical properties, and the shape-memory effect in TiNi alloys subjected to equal-channel angular pressing». *Physics of Metals and Metallography*, vol. 100, no 6, p. 608-18.
- [35] Pushin, V. G., D. V. Gunderov, N. I. Kourov, L. I. Yurchenko, E. A. Prokofiev, V. V. Stolyarov, Y. T. Zhu et R. Z. Valiev. 2004. «Nanostructures and phase transformations in TiNi shape memory alloys subjected to severe plastic deformation». In *Ultrafine Grained Materials 3 Symposium*, 14-18 March 2004. (Warrendale, PA, USA), p. 481-6.
- [36] Pushin, V. G., et R. Z. Valiev. 2003. «The nanostructured TiNi shape-memory alloys: New properties and applications». In *Interfacial Effects and Novel Properties of Nanomaterials*, September 14, 2003 - September 18, 2003. (Warsaw, Poland) Vol. 94, p. 13-24.
- [37] Pushin, V. G., V. V. Stolyarov, R. Z. Valiev, T. C. Lowe et Y. T. Zhu. 2005. «Nanostructured TiNi-based shape memory alloys processed by severe plastic deformation». *Materials Science and Engineering A*, vol. 410-411, p. 386-389.
- [38] Popov, N. N., A. I. Korshunov, A. A. Aushev, M. Yu Sidorkin, T. I. Sysoeva, I. V. Kostylev, A. E. Gusarov et V. V. Stolyarov. 2006. «Effect of nanostructuring and rate of inducing deformation on the structural and thermomechanical characteristics of a titanium nickelide-based alloy». *Physics of Metals and Metallography*, vol. 102, no 4, p. 432-8.
- [39] Fan, Zhiguo, et Chaoying Xie. 2008. «Phase transformation behaviors of Ti-50.9at.% Ni alloy after Equal Channel Angular Extrusion». *Materials Letters*, vol. 62, no 6-7, p. 800-803.
- [40] Noskov, N.I., et R.R. Mulukov. 2003. *Submicrocrystalline and nanocrystalline metals and alloys*. Ekaterinburg: Uro RAN, 279 p.
- [41] Zhang, Xiaoning, Jie Song, Chenglong Huang, Baoyu Xia, Bin Chen, Xiaogang Sun et Chaoying Xie. 2011. «Microstructures evolution and phase transformation behaviors of Ni-rich TiNi shape memory alloys after equal channel angular extrusion». *Journal of Alloys and Compounds*, vol. 509, no 6, p. 3006-3012.
- [42] Tong, Y. X., B. Guo, F. Chen, B. Tian, L. Li, Y. F. Zheng, Egor A. Prokofiev, Dmitry V. Gunderov et Ruslan Z. Valiev. 2012. «Thermal cycling stability of ultrafine-grained TiNi shape memory alloys processed by equal channel angular pressing». *Scripta Materialia*, vol. 67, no 1, p. 1-4.
- [43] Khmelevskaya, I. Yu, S. D. Prokoshkin, I. B. Trubitsyna, M. N. Belousov, S. V. Dobatkin, E. V. Tatyagin, A. V. Korotitskiy, V. Brailovski, V. V. Stolyarov et E. A. Prokofiev. 2008. «Structure and properties of Ti-Ni-based alloys after equal-channel angular pressing and high-pressure torsion». *Materials Science and Engineering A*, vol. 481-482, p. 119-22.

- [44] Karaman, I., A. V. Kulkarni et Z. P. Luo. 2005. «Transformation behaviour and unusual twinning in a NiTi shape memory alloy ausformed using equal channel angular extrusion». *Philosophical Magazine*, vol. 85, no 16, p. 1729-45.
- [45] Shahmir, Hamed, Mahmoud Nili-Ahmadabadi, Mojtaba Mansouri-Arani et Terence G. Langdon. 2013. «The processing of NiTi shape memory alloys by equal-channel angular pressing at room temperature». *Materials Science and Engineering A*, vol. 576, no 0, p. 178-184.
- [46] Brailovski, V., S. D. Prokoshkin, I. Yu Khmelevskaya, K. E. Inaekyan, V. Demers, S. V. Dobatkin et E. V. Tatyannin. 2006b. «Structure and properties of the Ti-50.0 at%Ni alloy after strain hardening and nanocrystallizing thermomechanical processing». *Materials Transactions*, vol. 47, no 3, p. 795-804.